Fall 12-16-2022

Engineering the Spectrum of Near-Field Thermal Radiation

Saman Zare
University of Maine, saman.zare@maine.edu

ENGINEERING THE SPECTRUM OF NEAR-FIELD THERMAL RADIATION

By

Saman Zare

B.S. Ferdowsi University of Mashhad, 2012

M.S. Ferdowsi University of Mashhad, 2016

A DISSERTATION

Submitted in Partial Fulfillment of the

Requirements for the Degree of

Doctor of Philosophy

(in Mechanical Engineering)

The Graduate School

The University of Maine

December 2022

Advisory Committee:

Sheila Edalatpour, Associate Professor of Mechanical Engineering, University of Maine, Advisor

Carl P. Tripp, Professor of Chemistry, University of Maine

Mathieu Francoeur, Associate Professor of Mechanical Engineering, University of Utah

Yingchao Yang, Assistant Professor of Mechanical Engineering, University of Maine

Olivier Putzeys, Lecturer of Mechanical Engineering, University of Maine

ENGINEERING THE SPECTRUM OF NEAR-FIELD THERMAL RADIATION

By Saman Zare

Dissertation Advisor: Dr. Sheila Edalatpour

An Abstract of the Dissertation Presented
in Partial Fulfillment of the Requirements for the
Degree of Doctor of Philosophy
(in Mechanical Engineering)
December 2022

Thermal emission observed at sub-wavelength distances from the thermal source is referred to as near-field thermal radiation. Thermal radiation in the near-field regime can exceed Planck's blackbody limit by orders of magnitude and be quasi-monochromatic. Due to these unique properties, near-field thermal radiation is very promising for several thermal management and energy harvesting applications. Many of these applications, such as nanogap thermophotovoltaics and thermal rectification, require near-field spectra that are not found among natural materials. Artificial metamaterials, which are engineered at the sub-wavelength scale, have been theoretically proposed for tuning the spectrum of near-field thermal radiation. However, engineering the near-field spectra using metamaterials has not been experimentally demonstrated mostly due to the complexities associated with guiding the near-field evanescent waves to an FTIR spectrometer located in the far zone. Additionally, the possibility of tuning the near-field spectra by engineering materials at length scales much smaller than the thermal wavelength, i.e., atomic length scales, has not been explored theoretically or experimentally.

In this dissertation, a new technique is proposed and implemented for measuring the near-field thermal spectra. The proposed technique is verified against the theoretical predictions of near-field thermal radiation from natural materials. This technique is then utilized for measuring the near-field

spectra thermally emitted by metamaterials made of silicon carbide nanopillars, and the tunability of the near-field thermal spectra by changing the dimensions of the nanopillars at the sub-wavelength scale is demonstrated. Using numerically-exact simulations, it is shown that the effective medium theory, commonly used for theoretical study of the near-field thermal spectra of nanopillar metamaterials, is not valid in the near-field regime. Additionally, the tunability of near-field spectra by using spherically-shaped sub-wavelength particles is theoretically investigated by developing analytical expressions for predicting the energy density emitted by spherical particles. Lastly, near-field thermal radiation from quantum dots, which have a length scale comparable to the atomic scales, is theoretically studied for the first time. It is shown that the near-field thermal radiation is highly impacted by the size-dependent quantum confinement effect that arises at the atomic length scales, thus providing a new mechanism for tuning the near-field thermal emission spectra.

ACKNOWLEDGEMENTS

I would like to express my deepest gratitude to my advisor, Dr. Sheila Edalatpour, for her invaluable advice, unwavering support, and patience during the past five years. Her immense knowledge and insight helped me in all the time of my research and writing of this dissertation. I could not have imagined a more dedicated and supportive advisor and mentor for my Ph.D. study.

I would also like to thank Dr. Carl P. Tripp whose expertise and support was truly influential in shaping my experimental methods and critiquing my results. In addition, my gratitude extends to Dr. Mathieu Francoeur, Dr. Yingchao Yang, and Dr. Olivier Putzeys who agreed to be a part of my Ph.D. committee. I am also grateful to my fellow lab mates and research team, Ramin Pourya, Behrad Zeinali Tajani, Mehran Habibzadeh, Md. Shofiqul Islam, and Md. Jahid Hasan Sagor, for their collaborative efforts and technical support. Furthermore, I gratefully acknowledge the Department of Mechanical Engineering and the Graduate School at the University of Maine for providing resources and support for my research studies.

Last but not least, I would like to give my sincere appreciation to my parents, Masoud and Tayebeh, my wife, Mahnaz, and my siblings, Saeid and Simin, for all the unconditional love and encouragement they have shown me all through my Ph.D. study. Without their tremendous understanding and encouragement in the past few years, it would have been impossible for me to undertake this journey.

TABLE OF CONTENTS

LIST OF FIGURES

CHAPTER 1

INTRODUCTION

1.1. Introduction to Thermal Radiation and Its Regimes

All materials with a temperature greater than zero Kelvin emit electromagnetic waves known as thermal radiation. Thermal radiation is generated by thermally-driven stochastic fluctuations of charged particles inside the emitting material. When the distance from the emitting medium is greater than the dominant wavelength of thermal radiation, λ_{max}, radiation of thermally-generated waves is referred to as the far-field thermal radiation. The magnitude of λ_{max}, which is ~10 μm at room temperature, varies with the absolute temperature of the emitting medium, T, according to Wien's displacement law as [1]:

$$\lambda_{max} T = 2898\,\mu\text{m.K} \tag{1.1}$$

In the far-field regime, thermal radiation is described by Planck's theory [2,3] and is limited to thermal radiation by a perfect emitter, known as a blackbody. Far-field thermal radiation by a blackbody has a broadband emission spectrum and is traditionally considered spatially incoherent [4]. The Planck's theory only accounts for the contribution of propagating waves, which have a parallel component of wavevector (k_ρ) smaller than the wavevector in the free space (k_0) and can travel to far-field distances from the surface of the thermal emitter. Additionally, the wave interference is not accounted for in the Planck's theory of thermal radiation.

Thermal emission observed at distances comparable to or smaller than λ_{max} from the emitting medium is referred to as the near-field thermal radiation. In the near-field regime, thermal radiation is dominated by the contribution from evanescent waves which exponentially decay in a distance approximately equal to λ_{max} from the surface of the thermal emitter (see Fig. 1.1). Due to the contribution of evanescent waves to the near-field regime, near-field thermal radiation exceeds the far-field blackbody limit, as described by Planck's law, by orders of magnitude [5]. Moreover, unlike blackbody emission, near-field thermal

radiation can be quasi-monochromatic and be highly spatial coherent when resonance modes such as surface phonon and plasmon polaritons are emitted [4].

The thermally-emitted evanescent waves can include frustrated modes and surface modes, which are schematically shown in Fig. 1.1 for a medium emitting in the free space. While frustrated modes are propagating inside the emitter, they are evanescent in the free space, i.e., they have $k_0 < k_\rho < n_E k_0$ where n_E is the refractive index of the emitter. These waves reach the emitter-vacuum interface at an incident angle (θ_I) greater than the critical angle [$\theta_{cr} = 1/\sin^{-1}(n_E)$]. As such, they experience total internal reflection at the free space-emitter interface and are evanescent inside the free space. Frustrated modes result in broadband enhancement of thermal radiation in the near-field regime. Surface modes are evanescent in both the emitter and the free space as these waves have k_ρs greater than the wavevector in both media (i.e. $k_\rho > k_0$ and $k_\rho > n_E k_0$). Resonant oscillations of free electrons (in metallic and doped semiconducting materials) or optical phonons (in polar dielectric materials) give rise to thermal emission of resonant surface modes referred to as surface plasmon polaritons (SPPs) and surface phonon polaritons (SPhPs), respectively. Thermal emission of SPPs or SPhPs result in a quasi-monochromatic enhancement of thermal radiation in the near-field regime [4].

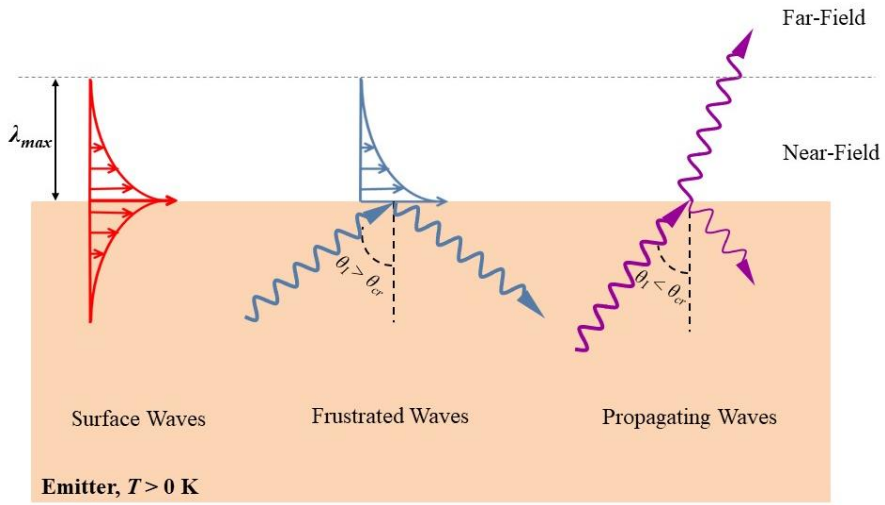

Figure 1.1 – Schematic of thermal emission of propagating, frustrated, and surface waves from a medium at a temperature greater than zero Kelvin.

1.2. Description of Near-Field Thermal Radiation

Thermal radiation in the near-field regime is described by the framework of fluctuational electrodynamics [6]. In fluctuational electrodynamics, a stochastic current density, $\mathbf{J}^{fl}$, is added to Maxwell equations to account for the random, thermally-driven motions of charged particles in a non-magnetic emitting medium [7]:

$$\nabla \times \mathbf{E}(\mathbf{r},\omega) = i\omega\mu_0 \mathbf{H}(\mathbf{r},\omega) \tag{1.2a}$$

$$\nabla \times \mathbf{H}(\mathbf{r},\omega) = -i\omega\varepsilon \mathbf{E}(\mathbf{r},\omega) + \mathbf{J}^{fl}(\mathbf{r},\omega) \tag{1.2b}$$

$$\nabla \cdot \mathbf{E}(\mathbf{r},\omega) = 0 \tag{1.2c}$$

$$\nabla \cdot \mathbf{H}(\mathbf{r},\omega) = 0 \tag{1.2d}$$

where ω is the angular frequency, μ_0 is the permeability of the free space, ε is the permittivity of the medium, and **E** and **H** are the electric and magnetic fields at an observation point **r** in the free space, respectively. For a non-magnetic medium, the first moment (i.e., the ensemble average) of $\mathbf{J}^{fl}$ is zero. The second moment (i.e., the ensemble average of spatial correlation function) of $\mathbf{J}^{fl}$ is linked to the temperature and material properties of the emitting medium using fluctuation-dissipation theorem as [6]:

$$\left\langle J_\alpha^{fl}(\mathbf{r},\omega) J_\beta^{fl\dagger}(\mathbf{r}',\omega) \right\rangle = \frac{4}{\pi}\omega\varepsilon_0 \,\mathrm{Im}[\varepsilon]\Theta(\omega,T)\delta(\mathbf{r}-\mathbf{r}')\delta_{\alpha\beta} \tag{1.3}$$

where ε_0 is the permeability of the free space, Θ is the mean energy of an electromagnetic state, T is the temperature of the medium, superscript $\dagger$ indicates the Hermitian operator, subscripts α and β are the orthogonal components, $\delta_{\alpha\beta}$ is the Kronecker delta, and $\delta(\mathbf{r}-\mathbf{r}')$ is the Dirac delta function.

Equations 1.2(a) to 1.2(d), which are referred to as the stochastic Maxwell equations, are solved to obtain **E** and **H** [7] and the spectral energy density, u, at the observation point **r** can be found from the emitted fields as [8]:

$$u(\mathbf{r},\omega) = \frac{1}{4}\varepsilon_0 \mathrm{Trace}\left\langle \mathbf{E}(\mathbf{r},\omega) \otimes \mathbf{E}(\mathbf{r},\omega) \right\rangle + \frac{1}{4}\mu_0 \mathrm{Trace}\left\langle \mathbf{H}(\mathbf{r},\omega) \otimes \mathbf{H}(\mathbf{r},\omega) \right\rangle \tag{1.4}$$

where $\otimes$ represents the outer product. The electric and magnetic fields for simple geometries, such as planar media, can be found analytically using the dyadic Green's functions, while numerical simulations of stochastic Maxwell's equations are required in more complex geometries. Once the dyadic Green's functions are available for a given geometry, the electric and magnetic fields can be found as [7]:

$$\mathbf{E}(\mathbf{r},\omega) = i\omega\mu_0 \int_V \overline{\overline{\mathbf{G}}}^{E}(\mathbf{r},\mathbf{r}',\omega)\cdot\mathbf{J}^{fl}(\mathbf{r}',\omega)\,dV' \tag{1.5a}$$

$$\mathbf{H}(\mathbf{r},\omega) = \int_V \overline{\overline{\mathbf{G}}}^{H}(\mathbf{r},\mathbf{r}',\omega)\cdot\mathbf{J}^{fl}(\mathbf{r}',\omega)\,dV' \tag{1.5b}$$

By substituting Eqs. (1.3) and (1.5) into Eq. (1.4), the spectral energy density due to thermal radiation by the emitting medium can be written as:

$$u(\mathbf{r},\omega) = \frac{k_0^2}{\pi\omega}\,\mathrm{Im}[\varepsilon]\Theta(\omega,T)\int_V \mathrm{Trace}\left[k_0^2\,\overline{\overline{\mathbf{G}}}^{E}(\mathbf{r},\mathbf{r}').\overline{\overline{\mathbf{G}}}^{E^\dagger}(\mathbf{r},\mathbf{r}') + \overline{\overline{\mathbf{G}}}^{H}(\mathbf{r},\mathbf{r}').\overline{\overline{\mathbf{G}}}^{H^\dagger}(\mathbf{r},\mathbf{r}')\right]dV' \tag{1.6}$$

The radiative heat transfer between two media separated by a near-field distance can also be found by calculating the Poynting vector, **S**, which gives the energy flux transferred by the thermally emitted waves. The time-averaged Poynting vector is given as [7]:

$$\langle \mathbf{S}(\mathbf{r},\omega)\rangle = \frac{1}{2}\mathrm{Re}\left[\langle \mathbf{E}(\mathbf{r},\omega)\times\mathbf{H}^{\dagger}(\mathbf{r},\omega)\rangle\right] \tag{1.7}$$

By substituting Eqs. (1.3) and (1.5) into Eq. (1.7), the time-averaged Poynting vector can be written as:

$$\langle \mathbf{S}(\mathbf{r},\omega)\rangle = \frac{2}{\pi}k_0^2\,\mathrm{Im}[\varepsilon]\Theta(\omega,T)\,\mathrm{Re}\left[i\int_V G^{E}_{m\alpha}(\mathbf{r},\mathbf{r}',\omega)G^{H\dagger}_{n\beta}(\mathbf{r},\mathbf{r}',\omega)\,dV'\right] \tag{1.8}$$

where the subscripts *m* and *n* represent the orthogonal components and k_0 is the magnitude of the wavevector in the free space. The radiative heat flux between two media can be calculated from Eq. (1.8) once the dyadic Green's functions are known for the system.

1.3. Applications of Near-Field Thermal Radiation

Near-field thermal radiation have attracted significant attention for many potential applications in near-field thermophotovoltaic (TPV) energy conversion [9-26], thermal management of electronic devices [27-

29], thermal rectification [30-44], and imaging [45,46]. When the emitter and the TPV cell of a thermophotovoltaic device is reduced to a near-field distance, evanescent waves, in addition to propagating waves, contribute to power generation and the power output of the device enhances significantly due to this extraneous contribution [9-26]. In addition, the significant enhancement of thermal radiation over the blackbody limit in the near-field regime provides a noncontact method for cooling down localized hotspots in micro- and nanostructures and can be employed in radiative cooling of electronic devices [27-29]. Another promising application of near-field thermal radiation is in thermal rectifiers in which the magnitude of radiative heat transfer between two media depends on the direction of the temperature bias [30-44]. The proposed near-field thermal rectifiers are based on the variation of dielectric functions of the two media with temperature. The temperature dependence of the dielectric functions results in variation of the resonance frequency of near-field thermal radiation by each medium and leads to the asymmetry of radiative heat flux between two media when the temperature difference is reversed. Moreover, near-field thermal radiation has been utilized in thermal radiation scanning tunneling microscopy (TRSTM) for high-resolution imaging [45,46]. In TRSTM technique, the evanescent waves thermally emitted by a heated sample are scattered to the far field using a sharp tip of an atomic force microscope (AFM) brought in near-field distances from the sample. The scattered fields provide local information about the material and geometry properties of the sample and enables thermal imaging of nanostructured surfaces without any external illumination.

1.4. Spectral Tuning of Near-Field Thermal Radiation

Many of the near-field applications, such as near-field thermophotovoltaics and thermal rectification, require tuning the spectrum of near-field thermal radiation from the emitting medium to match the desired application. Spectrally-selective near-field thermal radiation plays an important role in increasing the efficiency [19,20,22,23,26] and power output of the TPV devices [9-26]. The frequencies at which the emitter thermally radiates should be higher than the bandgap of the PV cell to generate electron-hole pairs (and thus, electricity) and the emission at frequencies below the bandgap of the PV should be suppressed. Hence, a spectrally-selective emitter with desired near-field radiation spectrum is required for maximizing

the electron-hole generation, which can be possible using quasi-monochromatic near-field radiation. In addition, the rectification factor in near-field thermal rectifiers, i.e., the ratio of heat flux in one direction to that in opposite direction, depends on matching and mismatching of the resonance frequencies between two media in different directions of temperature bias. Thermal rectification is enhanced when the resonance frequencies of two media overlap in the forward temperature bias while there is no overlap between resonance frequencies in the reverse temperature bias. As such, it is of great importance to tune the near-field radiation spectra of the media such that the desired rectification factor is achieved in near-field thermal rectifiers [30-44].

The required near-field spectra are usually not found among natural materials. Artificial man-made materials, which are engineered at the sub-wavelength scale and are also referred to as metamaterials, have been theoretically proposed for tailoring the near-field spectra [47-131]. The radiative properties of metamaterials can be controlled by varying the material properties and the geometry and can be significantly different from those of their constituent materials. Various types of metamaterials, such as hyperbolic metamaterials [47-77], periodic gratings [78-98], photonic crystals [99-105], and double-negative metamaterials [106-131], have been theoretically proposed for tailoring the spectrum of near-field thermal radiation.

Despite numerous theoretical studies on metamaterials, spectral tuning of near-field thermal radiation using metamaterials has not been experimentally demonstrated yet. Indeed, experimental measurements of the spectrum of near-field thermal emission are even sparse. Most of the experimental studies on near-field thermal radiation has focused on total radiative heat transfer between two bodies, such as two flat surfaces [20,132-144], a sphere and a flat surface [145-149], a probe and a flat surface [150-159], and two microcavities [136] separated by sub-wavelength gaps. Since total radiative heat transfer is spectrally integrated over all frequencies, it does not provide insight into the spectrum (i.e. the frequency dependence) of near-field thermal radiation. The main challenge in measuring the spectrum of near-field thermal radiation is the fact that the evanescent waves present in the near-field distances from the emitter do not propagate to the far-field distances, and thus, cannot be captured by a detector located in the far

region. As such, the evanescent waves need to be converted into propagating waves to reach the far region.

So far, this process, which is referred to as coupling the evanescent waves to the far-field radiation, has been experimented in a few studies on natural materials using a probe-based spectroscopy technique [47,155,160,161]. In this method, a sharp tip of an atomic force microscope (AFM) is brought into a near-field distance from an emitting medium. The near-field evanescent waves thermally emitted from the medium are scattered by the AFM tip to the far field. The scattered waves are then collected using a Fourier transform infrared (FTIR) spectrometer where their spectrum is recorded. Using the AFM-based spectroscopy technique, the spectrum of near-field thermal radiation has been measured for a few natural materials such as silica, quartz, silicon carbide, and polytetrafluoroethylene [47,155,160,161]. However, experimental demonstration of spectral tuning of near-field thermal radiation by utilizing metamaterials has not been addressed in the literature so far. In this dissertation, we propose and implement a new, simple and robust technique utilizing an internal reflection for measuring the spectrum of near-field thermal radiation. Using this new experimental technique, the spectrum of near-field thermal radiation from metamaterials made of nanopillar arrays is measured. It is demonstrated that the near-field spectra for the nanopillar arrays are significantly different from that of the bulk material and that the spectrum of near-field thermal radiation can be tuned by varying the geometry of the nanopillars.

Accurate prediction of near-field thermal radiation from metamaterials is also of great importance for designing the desired near-field spectra. Due to complex geometries, the near-field spectra for metamaterials cannot be predicted analytically. Most of the theoretical studies on the spectrum of near-field thermal radiation from metamaterials have been performed using an approximate method known as the effective medium theory (EMT) [50,64,67,70,85,86,88,89,93,123,127,162-171]. In EMT, metamaterials are approximated as an anisotropic homogeneous film with effective dielectric functions along different directions [172-175]. It is shown that the EMT can provide an adequate approximation of the near-field thermal radiation from metamaterials such as multilayered metamaterials [50,86,162-164]. In this thesis, we study the validity of the EMT for predicting the near-field thermal radiation from

nanopillar arrays, and we show that the EMT cannot accurately predict the magnitude and the spectrum of near-field radiation by arrays of nanopillars that support localized surface phonons in the infrared region of the electromagnetic spectrum.

Spherical nanoparticles are the building blocks of man-made materials such as Mie-resonance-based metamaterials. The near-field spectrum for the Mie-resonance-based metamaterials is greatly dependent on thermal emission from individual spherical nanoparticles, which can support resonance modes such as localized surface phonons [114,115,123,125]. In this dissertation, analytical expressions are developed for predicting the spectrum of near-field thermal emission from spherical particles, as characterized by their spectral energy density.

Finally, a new mechanism for tailoring the near-field radiation spectrum is proposed in this dissertation. Metamaterials that have been proposed so far for tuning the near-field radiation spectrum rely on engineering the emitting medium at the sub-wavelength scale (micrometer scale) which is much greater than the atomic length scales (a few nanometers). When the dimensions of the emitting medium are comparable to the atomic length scales the quantum confinement effect arises and the electronic structure of the emitter becomes size-dependent. This provides an opportunity for engineering the spectrum of near-field thermal radiation. In this dissertation, we explore the possibility of tuning the near-field thermal radiation spectrum by exploiting the size-dependence of quantum confinement effect in emitters with sizes comparable to the atomic length scales.

1.5. Dissertation Outline

The outline of this dissertation is presented as follows. In Chapter 2, a new spectroscopy method based on an internal reflection element is presented and verified for measuring the spectrum of near-field thermal radiation. This new experimental technique is utilized in Chapter 3 to measure the near-field thermal radiation spectrum for SiC nanopillars fabricated on a SiC substrate and to provide experimental demonstration of spectral tuning of near-field thermal radiation using metamaterials. In Chapter 4, the validity of the EMT is examined for predicting near-field thermal radiation in metamaterials made of nanopillar arrays. The magnitude and spectrum of near-field energy density found from the EMT is

compared with that found using a numerically exact method, namely the thermal discrete dipole approximation (T-DDA), for an array of nanopillars with various filling factors, heights and diameters. In Chapter 5, analytical expressions are developed for predicting the energy density and spatial correlation function of thermal radiation by spherical particles of various sizes and materials. Using the developed framework, the effect of sphere size and material on the spectrum of near-field thermal radiation emitted by a sphere is explored. Also, the spatial coherence of field thermally emitted by a sphere is quantified in radial and polar directions at near-field and far-field distances from the sphere. In Chapter 6, the near-field radiation spectra for arrays of quantum dots (QDs) made of lead chalcogenides with various diameters are calculated using the T-DDA, and it is shown that the spectral location of the peak of near-field thermal radiation can be tuned significantly (by up to ~4500 cm^{-1}) by varying the size of QDs by only a few nanometers. Finally, a summary of the work described in this dissertation and some recommendations for future studies are presented in Chapter 7.

1.6. References

[1] M. F. Modest, Fundamentals of Thermal Radiation (Academic Press, 2013).

[2] M. Planck, The Theory of Heat Radiation (Blakiston, 1914).

[3] J. R. Howell, M. P. Mengüç, K. Daun, and R. Siegel, Thermal Radiation Heat Transfer (CRC press, 2020).

[4] K. Joulain, J.-P. Mulet, F. Marquier, R. Carminati, and J.-J. Greffet, Surf. Sci. Rep. 57, 59 (2005).

[5] Z. M. Zhang, Nano/Microscale Heat Transfer (McGraw-Hill, 2007).

[6] S. M. Rytov, Y. A. Kravtsov and V. Tatarskii, Principles of Statistical Radiophysics 3: Elements of Random Fields (Springer, 1989).

[7] M. Francoeur, M. P. Mengüç, and R. Vaillon, J J. Quant. Spectrosc. Radiat. Transf. 110, 2002 (2009).

[8] J. D. Jackson, Classical Electrodynamics (John Wiley & Sons, 1999).

[9] R. S. DiMatteo, P. Greiff, S. L. Finberg, K. A. Young-Waithe, H. K. H. Choy, M. M. Masaki, and C. G. Fonstad, Appl. Phys. Lett. 79, 1894 (2001).

[10] M. D. Whale and E. G. Cravalho, IEEE Trans. Energy Convers. 17, 130 (2002).

[11] A. Narayanaswamy and G. Chen, Appl. Phys. Lett. 82, 3544 (2003).

[12] M. Laroche, R. Carminati, and J. J. Greffet, J. Appl. Phys. 100, 63704 (2006).

[13] K. Park, S. Basu, W. P. King, and Z. M. Zhang, J. Quant. Spectrosc. Radiat. Transf. 109, 305 (2008).

[14] M. Francoeur, R. Vaillon, and M. P. Mengüç, M. P. IEEE Trans. Energy Convers. 26, 686 (2011).

[15] O. Ilic, M. Jablan, J. D. Joannopoulos, I. Celanovic, and M. Soljačić, Opt. Express 20, A366 (2012).

[16] M. P. Bernardi, O. Dupré, E. Blandre, P. O. Chapuis, R. Vaillon, and M. Francoeur, Sci. Rep. 5, 11626 (2015).

[17] S. Molesky and Z. Jacob, Phys. Rev. B 91, 205435 (2015).

[18] J. Z. J. Lau, V. N. S. Bong, and B. T. Wong, B. T. J. Quant. Spectrosc. Radiat. Transf. 171, 39 (2016).

[19] R. St-Gelais, G. R. Bhatt, L. Zhu, S. Fan, and M. Lipson, ACS Nano 11, 3001 (2017).

[20] N. Vongsoasup, M. Francoeur, and K. Hanamura, Int. J. Heat Mass Transfer 115, 326 (2017).

[21] A. Fiorino, L. Zhu, D. Thompson, R. Mittapally, P. Reddy, and E. Meyhofer, Nat. Nanotechnol. 13, 806 (2018).

[22] M. Lim, J. Song, J. Kim, S. S. Lee, I. Lee, and B. J. Lee, J. Quant. Spectrosc. Radiat. Transf. 210, 35 (2018).

[23] P. Sabbaghi, Y. Yang, J. Y. Chang, and L. Wang, J. Quant. Spectrosc. Radiat. Transf. 234, 108 (2019).

[24] G. R. Bhatt, B. Zhao, S. Roberts, I. Datta, A. Mohanty, T. Lin, J. M. Hartmann, R. St-Gelais, S. Fan and M. Lipson, Nat. Commun. 11, 2545 (2020).

[25] D. Milovich, J. Villa, E. Antolin, A. Datas, A. Marti, R. Vaillon, and M. Francoeur, J. Photonics Energy 10, 025503 (2020).

[26] C. Lucchesi, D. Cakiroglu, J. Perez, T. Taliercio, E. Tournié, P. Chapuis, and R. Vaillon, Nano Lett. 21, 4524 (2021).

[27] B. Guha, C. Otey, C. B. Poitras, S. Fan, and M. Lipson, Nano Lett. 12, 4546 (2012).

[28] K. Chen, P. Santhanam, and S. Fan, Phys. Rev. Appl. 6, 024014 (2016).

[29] L. Zhu, A. Fiorino, D. Thompson, R. Mittapally, E. Meyhofer, and P. Reddy, Nature 566, 239 (2019).

[30] C. R. Otey, W. T. Lau, and S. Fan, Phys. Rev. Lett. 104, 154301 (2010).

[31] S. Basu and M. Francoeur, Appl. Phys. Lett. 98, 113106 (2011).

[32] H. Iizuka and S. Fan, J. Appl. Phys. 112, 024304 (2012).

[33] L. P. Wang and Z. M. Zhang, Nanoscale Microscale Thermophys. Eng. 17, 337 (2013).

[34] Y. Yang, S. Basu, and L. Wang, Appl. Phys. Lett. 103, 163101 (2013).

[35] K. Joulain, Y. Ezzahri, J. Drevillon, B. Rousseau, and D. D. S. Meneses, Opt. Express 23, A1388 (2015).

[36] A. Ghanekar, J. Ji, and Y. Zheng, Appl. Phys. Lett. 109, 123106 (2016).

[37] Z. Zheng, X. Liu, A. Wang, and Y. Xuan, Int. J. Heat Mass Transfer 109, 63 (2017).

[38] A. Fiorino, D. Thompson, L. Zhu, R. Mittapally, S. A. Biehs, O. Bezencenet, N. El-Bondry, S. Bansropun, P. Ben-Abdallah, E. Meyhofer, and P. Reddy, ACS Nano 12, 5774 (2018).

[39] A. Ghanekar, Y. Tian, M. Ricci, S. Zhang, O. Gregory, and Y. Zheng, Opt. Express 26, A209 (2018).

[40] S. Wen, X. Liu, S. Cheng, Z. Wang, S. Zhang, and C. Dang, J. Quant. Spectrosc. Radiat. Transf. 234, 1 (2019).

[41] F. Chen, X. Liu, Y. Tian, and Y. Zheng, Adv. Eng. Mater. 23, 2000825 (2020).

[42] G. Xu, J. Sun, H. Mao, and T. Pan, Int. J. Therm. Sci. 149, 106179 (2020).

[43] R. Mittapally, B. Lee, L. Zhu, A. Reihani, J. W. Lim, D. Fan, S. R. Forrest, P. Reddy, and E. Meyhofer, Nat. Commun. 12, 4346(2021).

[44] S. Landrieux, P. Ben-Abdallah, R. Messina, Appl. Phys. Lett. 120, 143502 (2022).

[45] Y. De Wilde, F. Formanek, R. Carminati, B. Gralak, P.A. Lemoine, K. Joulain, J.P. Mulet, Y. Chen, and J.J. Greffet, Nature 444, 740 (2006).

[46] A.C. Jones and M.B. Raschke, Nano Lett. 12, 1475 (2012).

[47] S. A. Biehs and M. Tschikin, Phys. Rev. Lett. 109, 104301 (2012).

[48] Y. Guo, C. L. Cortes, S. Molesky, and Z. Jacob, Appl. Phys. Lett. 101, 131106 (2012).

[49] Y. Guo and Z. Jacob, Opt. Express 21, 15014 (2013).

[50] X. L. Liu, R. Z. Zhang, and Z. M. Zhang, Appl. Phys. Lett. 103, 213102 (2013).

[51] B. Liu and S. Shen, Phys. Rev. B 87, 115403 (2013).

[52] C. Simovski, S. Maslovski, I. Nefedov, and S. Tretyakov, Opt. Express 21, 14988 (2013).

[53] M. Tschikin, S. A. Biehs, R. Messina, and P. Ben-Abdallah, J. Opt. 15, 105101 (2013).

[54] T. J. Bright, X. L. Liu, and Z. M. Zhang, Opt. Express 22, A1112 (2014).

[55] S. Lang, M. Tschikin, S. A. Biehs, A. Y. Petrov, and M. Eich, Appl. Phys. Lett. 104, 121903(2014).

[56] X. Liu, R. Z. Zhang, and Z. Zhang, ACS Photonics 1, 785 (2014).

[57] B. Liu, J. Shi, K. Liew, and S. Sheng, Opt. Commun. 314, 57 (2014).

[58] Y. Bai, Y. Jiang, and L. Liu, J. Quant. Spectrosc. Radiat. Transf. 158, 61 (2015).

[59] S. A. Biehs, S. Lang, A. Y. Petrov, M. Eich, and P. Ben-Abdallah, Phys. Rev. Lett. 115, 174301

(2015).

[60] J. Y. Chang, S. Basu, and L. Wang, J. Appl. Phys. 117, 054309 (2015).

[61] J. Y. Chang, Y. Yang, and L. Wang, Int. J. Heat Mass Transf. 87, 237 (2015).

[62] J. Liu and E. Narimanov, Phys. Rev. B 91, 041403 (2015).

[63] M. Tschikin, S. A. Biehs, P. Ben-Abdallah, S. Lang, A. Y. Petrov, and M. Eich, J. Quant. Spectrosc. Radiat. Transf. 158, 17 (2015).

[64] S. Jin, M. Lim, S. S. Lee, and B. J. Lee, Opt. Express 24, A635 (2016).

[65] R. Messina, P. Ben-Abdallah, B. Guizal, M. Antezza, and S. A. Biehs, Phys. Rev. B 94, 104301 (2016).

[66] S. A. Biehs, and P. Ben-Abdallah, Z. Naturforsch. A, 72, 115 (2017).

[67] T. Ikeda, K. Ito, and H. Iizuka, J. Appl. Phys. 121, 013106 (2017).

[68] K. Shi, F. Bao, and S. He, ACS Photonics 4, 971 (2017).

[69] B. Zhao, B. Guizal, Z. M. Zhang, S. Fan, and M. Antezza, Phys. Rev. B 95, 245437 (2017).

[70] L. Ge, Y. Cang, K. Gong, L. Zhou, D. Yu, and Y. Luo, AIP Adv. 8, 085321 (2018).

[71] Q. M. Zhao, T. B. Wang, D. J. Zhang, W. X. Liu, T.B. Yu, Q. H. Liao, and N. H. Liu, Chin. Phys. B 27, 094401 (2018).

[72] A. Ghanekar, Y. Tian, X. Liu, and Y. Zheng, J. Photonics Energy 9, 032706 (2019).

[73] J. Y. Chang, P. Sabbaghi, and L. Wang, Int. J. Heat Mass Transf. 158, 120023 (2020).

[74] W. Du, J. Yang, S. Zhang, N. Iqbal, Y. Dang, J. B. Xu, and Y. Ma, Nano Energy, 78, 105264 (2020).

[75] J. Song, Q. Cheng, L. Lu, B. Li, K. Zhou, B. Zhang, Z. Luo, X. Zhou, Phys. Rev. Appl. 13, 024054 (2020).

[76] X. Wu, and C. Fu, J. Quant. Spectrosc. Radiat. Transf. 258, 107337 (2021).

[77] R. Liu, C. Zhou, Y. Zhang, Z. Cui, X. Wu, and H. Yi, Int. J. Extreme Manuf. 4, 032002 (2022).

[78] S. A. Biehs, F. S. S. Rosa, and P. Ben-Abdallah, Appl. Phys. Lett. 98, 243102 (2011).

[79] R. Guérout, J. Lussange, F. S. S. Rosa, J. P. Hugonin, D. A. R. Dalvit, J. J. Greffet, A. Lambrecht, and S. Reynaud, Phys. Rev. B 85, 180301 (2012).

[80] J. Lussange, R. Guérout, F. S. S. Rosa, J. J. Greffet, A. Lambrecht, and S. Reynaud, Phys. Rev. B 86, 085432 (2012).

[81] X. L. Liu and Z. M. Zhang, Appl. Phys. Lett. 104, 251911 (2014).

[82] X. L. Liu, R. Z. Zhang, and Z. M. Zhang, Int. J. Heat Mass Transf. 73, 389 (2014).

[83] J. Dai, S. A. Dyakov, and M. Yan, Phys. Rev. B 92, 035419 (2015).

[84] A. Didari and M. P. Mengüç, Opt. Express 23, A1253 (2015).

[85] X. Liu, B. Zhao, and Z. M. Zhang, Phys. Rev. A 91, 062510 (2015).

[86] J. Dai, S. A. Dyakov, S. I. Bozhevolnyi, and M. Yan, Phys. Rev. B 94, 125431 (2016).

[87] Y. Yang and L. Wang, Phys. Rev. Lett. 117, 044301 (2016).

[88] V. Fernández-Hurtado, F. J. García-Vidal, S. Fan, and J. C. Cuevas, Phys. Rev. Lett. 118, 203901 (2017).

[89] K. Isobe, D. Hirashima, and K. Hanamura, Int. J. Heat Mass Transf. 115, 467 (2017).

[90] D. Lu, A. Das, and W. Park, Opt. Express 25, 12999 (2017).

[91] J. I. Watjen, X. L. Liu, B. Zhao, and Z. M. Zhang, J. Heat Transf. 139, 052704(2017).

[92] Y. Yang, P. Sabbaghi, and L. Wang, Int. J. Heat Mass Transf. 108, 851 (2017).

[93] H. Yu, D. Liu, Z. Yang, and Y. Duan, Sci. Rep. 7, 1 (2017).

[94] A. Didari, E. B. Elçioğlu, T. Okutucu-Özyurt, and M. P. Mengüç, J. Quant. Spectrosc. Radiat. Transf. 212, 120 (2018).

[95] J. Shen, X. Liu, H. He, W. Wu, and B. Liu, J. Quant. Spectrosc. Radiat. Transf. 211, 1 (2018).

[96] Y. H. Kan, C. Y. Zhao, and Z. M. Zhang, Phys. Rev. B 99, 035433 (2019).

[97] M. J. He, H. Qi, Y. T. Ren, Y. J. Zhao, and M. Antezza, Int. J. Heat Mass Transf. 150, 119305 (2020).

[98] F. R. Chen, G. An, and Z. G. Xu, J. Quant. Spectrosc. Radiat. Transf. 258, 107395 (2021).

[99] W. T. Lau, J. T. Shen, G. Veronis, S. Fan, and P. V. Braun, Appl. Phys. Lett. 92, 103106 (2008).

[100] P. Ben-Abdallah, K. Joulain, and A. Pryamikov, Appl. Phys. Lett. 96, 143117 (2010).

[101] A. Rodriguez, O. Ilic, P. Bermel, I. Celanovic, J. D. Joannopoulos, M. Soljačić, and S. Johnson Phys. Rev. Lett. 107, 114302 (2011).

[102] M. Tschikin, P. Ben-Abdallah, and S. A. Biehs, Phys. Lett. A 376, 3462 (2012).

[103] T. Inoue, T. Asano, and S. Noda, Phys. Rev. B 95, 125307 (2017).

[104] M. Elzouka, and S. Ndao, J. Quant. Spectrosc. Radiat. Transf. 204, 56 (2018).

[105] T. Inoue, T. Asano, and S. Noda, Opt. Express 26, 32074 (2018).

[106] K. Joulain and J. Drevillon, Phys. Rev. B 81, 165119 (2010).

[107] S. Basu and M. Francoeur, Appl. Phys. Lett. 99, 143107 (2011).

[108] M. Francoeur, S. Basu, and S. J. Petersen, Opt. Express 19, 18774 (2011).

[109] Z. Zheng and Y. Xuan, Int. J. Heat Mass Transf. 54, 1101 (2011).

[110] Z. Zheng and Y. Xuan, Chi. Sci. Bull. 56, 2312 (2011).

[111] L. Cui, Y. Huang, and J. Wang, J. Appl. Phys. 112, 084309 (2012).

[112] S. Basu and L. Wang, Appl. Phys. Lett. 102, 053101 (2013).

[113] L. Cui, Y. Huang, J. Wang, and K. Y. Zhu, Appl. Phys. Lett. 102, 053106 (2013).

[114] S. J. Petersen, S. Basu, and M. Francoeur, Photonics Nanostructures: Fundam. Appl. 11, 167 (2013).

[115] S. J. Petersen, S. Basu, B. Raeymaekers, and M. Francoeur, J. Quant. Spectrosc. Radiat. Transf. 129, 277 (2013).

[116] S. Basu and M. Francoeur, Opt. Lett. 39, 1266 (2014).

[117] D. Drosdoff, A. D. Phan, and L. M. Woods, Adv. Opt. Mater. 2, 1038 (2014).

[118] H. Iizuka and S. Fan, J. Quant. Spectrosc. Radiat. Transf. 148, 156 (2014).

[119] Y. Bai, Y. Jiang, and L. Liu, J. Phys. D: Appl. Phys. 47, 445304 (2014).

[120] Y. Bai, Y. Jiang, and L. Liu, J. Quant. Spectrosc. Radiat. Transf. 158, 36 (2015).

[121] S. Basu, Y. Yang, and L. Wang, Appl. Phys. Lett. 106, 033106 (2015).

[122] A. Didari and M. P. Mengüç, Opt. Express 23, A547 (2015).

[123] A. Ghanekar, L. Lin, J. Su, H. Sun, and Y. Zheng, Opt. Express 23, A1129 (2015).

[124] N. Zhou and X. Xu, J. Quant. Spectrosc. Radiat. Transf. 167, 156 (2015).

[125] A. Ghanekar, L. Lin, and Y. Zheng, Opt. Express 24, A868 (2016).

[126] A. Didari and M. P. Mengüç, J. Quant. Spectrosc. Radiat. Transf. 197, 95 (2017).

[127] A. Ghanekar, Y. Tian, S. Zhang, Y. Cui, and Y. Zheng, Materials 10, 885 (2017).

[128] Q. Zhao, T. Zhou, T. Wang, W. Liu, J. Liu, T. Yu, Q. Liao, and N. Liu, J. Phys. D: Appl. Phys. 50, 145101 (2017).

[129] K. Isobe and K. Hanamura, Int. J. Heat Mass Transf. 134, 807 (2019).

[130] Y. Taniguchi, K. Isobe, and K. Hanamura, Appl. Therm. Eng. 183, 116041 (2021).

[131] C. Su and C. Fu, Int. J. Heat Mass Trans. 196, 123235 (2022).

[132] L. Hu, A. Narayanaswamy, X. Chen, and G. Chen, Appl. Phys. Lett. 92, 133106 (2008).

[133] R. S. Ottens, V. Quetschke, S. Wise, A. A. Alemi, R. Lundock, G. Mueller, D. H. Reitze, D. B. Tanner, and B. F. Whiting, Phys. Rev. Lett. 107, 14301 (2011).

[134] S. Shen, A. Mavrokefalos, P. Sambegoro, and G. Chen, Appl. Phys. Lett.100, 233114 (2012).

[135] T. Kralik, P. Hanzelka, M. Zobac, V. Musilova, T. Fort, and M. Horak, Phys. Rev. Lett.109, 3 (2012).

[136] T. Ijiro and N. Yamada, Appl. Phys. Lett. 106, 23103 (2015).

[137] M. Lim, S. S. Lee, and B. J. Lee, Phys. Rev. B 91, 195136 (2015).

[138] B. Song, D. Thompson, A. Fiorino, Y. Ganjeh, P. Reddy, and E. Meyhofer, Nat. Nanotechnol. 11, 509 (2016).

[139] R. St-Gelais, L. Zhu, S. Fan, and M. Lipson, Nat. Nanotechnol.11, 515 (2016).

[140] M. P. Bernardi, D. Milovich, and M. Francoeur, Nat. Commun. 7, 12900 (2016).

[141] J. L. Watjen, B. Zhao, and Z. M. Zhang, Appl. Phys. Lett. 109, 203112 (2016).

[142] S. Lang, G. Sharma, S. Molesky, P. U. Kränzien, T. Jalas, Z. Jacob, A. Y. Petrov, and M. Eich, Sci. Rep. 7, 13916 (2017).

[143] M. Ghashami, H. Geng, T. Kim, N. Iacopino, S. K. Cho, and K. Park, Phys. Rev. Lett. 120, 175901 (2018).

[144] J. Yang, W. Du, Y. Su, Y. Fu, S. Gong, S. He, and Y. Ma, Nat. Commun. 9, 4033 (2018).

[145] S. Shen, A. Narayanaswamy, and G. Chen, Nano Lett. 9, 2909 (2009).

[146] E. Rousseau, A. Siria, G. Jourdan, S. Volz, F. Comin, J. Chevrier, and J. J. Greffet, Nat. Photonics 3, 514 (2009).

[147] J. Shi, P. Li, B. Liu, and S. Shen, Appl. Phys. Lett. 102, 183114 (2013).

[148] B. Song, Y. Ganjeh, S. Sadat, D. Thompson, A. Fiorino, V. Fernández-Hurtado, J. Feist, F. J. García-Vidal, J. C. Cuevas, P. Reddy, and E. Meyhofer. Nat. Nanotechnol. 10, 253 (2015).

[149] D. Thompson, L. Zhu, R. Mittapally, S. Sadat, Z. Xing, P. McArdle, M. M. Qazilbash, P. Reddy, and E. Meyhofer, E. Hundred-Fold Enhancement in Far-Field Radiative Heat Transfer over the Blackbody Limit. Nature 561, 216 (2018).

[150] A. Kittel, W. Müller-Hirsch, J. Parisi, S. A. Biehs, D. Reddig, and M. Holthaus, Phys. Rev. Lett. 95, 224301 (2005).

[151] U. F. Wischnath, J. Welker, M. Munzel, and A. Kittel, Rev. Sci. Instrum. 79, 073708 (2008).

[152] A. Kittel, U. F. Wischnath, J. Welker, O. Huth, F. Rüting, and S. A. Biehs, Appl. Phys. Lett. 93, 2006 (2008).

[153] L. Worbes, D. Hellmann, and A. Kittel, Phys. Rev. Lett. 110, 134302 (2013).

[154] K. Kloppstech, N. Konne, S. A. Biehs, A. W. Rodriguez, L. Worbes, D. Hellmann, and A. Kittel, Nat. Commun. 8, 14475 (2017).

[155] A. Babuty, K. Joulain, P. O. Chapuis, J. J. Greffet, and Y. De Wilde, Phys. Rev. Lett. 110, 146103 (2013).

[156] K. Kim, B. Song, V. Fernández-Hurtado, W. Lee, W. Jeong, L. Cui, D. Thompson, J. Feist, M. T. H. Reid, F. J. García-Vidal, J. C. Cuevas, E. Meyhofer, and P. Reddy, Nature 528, 387 (2015).

[157] L. Cui, W. Jeong, V. Fernández-Hurtado, J. Feist, F. J. García-Vidal, J. C. Cuevas, E. Meyhofer,

and P. Reddy, Nat. Commun. 8, 14479 (2017).

[158] F. Peragut, L. Cerruti, A. Baranov, J. P. Hugonin, T. Taliercio, Y. De Wilde, and J. J. Greffet, Optica 4, 1409 (2017).

[159] A. Jarzembski, C. Shaskey, and K. Park, Front. Energy 12, 43 (2018).

[160] B. T. O'Callahan, W. E. Lewis, A. C. Jones, and M. B. Raschke, Phys. Rev. B 89, 245446 (2014).

[161] B. T. O'Callahan and M. B. Raschke, APL Photonics 2, 021301 (2017).

[162] Y. Guo and Z. Jacob, J. Appl. Phys. 115, 234306 (2014).

[163] X. L. Liu, T. J. Bright and Z. M. Zhang, J. Heat Transfer 136, 092703 (2014).

[164] M. S. Mirmoosa, F. Rüting, I. S. Nefedov and C. R. Simovski, J. Appl. Phys. 115, 234905 (2014).

[165] X. Liu and Z. M. Zhang, ACS Photonics 2, 1320 (2015).

[166] X. Liu and Z. M. Zhang, Appl. Phys. Lett. 107, 143114 (2015).

[167] Y. Yang, J. Y. Chang, P. Sabbaghi and L. Wang, J. Heat Transfer 139, 052701 (2017).

[168] M. Lim, J. Song, S. S. Lee and B. J. Lee, Nat. Commun. 9, 4302 (2018).

[169] H. Iizuka and S. Fan, Phys. Rev. Lett. 120, 063901 (2018).

[170] H. Yu, Y. Duan and Z. Yang, Int. J. Heat Mass Transf. 123, 67 (2018).

[171] J. E. Pérez-Rodríguez, G. Pirruccio and R. Esquivel-Sirvent, Phys. Status Solidi B 257, 1900498 (2020).

[172] J. C. Maxwell-Garnett, Philos. Trans. R. Soc. Lond. B 203, 385 (1904).

[173] D. A. G. Bruggeman, Ann. Phys. (Leipzig) 24, 636 (1935).

[174] T. C. Choy, Effective Medium Theory: Principles and Applications 2 ed. (Oxford University Press, New York, 2016).

[175] V. A. Markel, J. Opt. Soc. Am. A 33(7), 1244-56 (2016).

CHAPTER 2

MEASUREMENT OF NEAR-FIELD THERMAL EMISSION SPECTRA USING AN INTERNAL REFLECTION ELEMENT

This chapter has been reproduced from a previous publication in Physical Review B: *S. Zare, C. P. Tripp, and S. Edalatpour, Phys. Rev. B **100**, 235450 (2019).*

2.1. Abstract

We describe a simple and robust method using an internal reflection element to measure the spectra of near-field thermal emission. We experimentally demonstrate the spectrally narrow peaks of near-field thermal emission by isotropic media due to the excitation of surface phonon polaritons in quartz and amorphous silica and due to the frustrated total-internal-reflection modes in amorphous silica and polytetrafluoroethylene. Additionally, we demonstrate the broadband near-field thermal emission of hyperbolic modes in hexagonal boron nitride, which is an anisotropic uniaxial medium. We also present a theoretical approach based on the fluctuational electrodynamics and dyadic Green's functions for one-dimensional layered media for accurately modeling the measured spectra.

2.2. Introduction

Many near-field applications, such as nano-gap thermophotovoltaic power generation [1-8] and thermal rectification [9-21], rely on spectrally selective thermal emission in the near field. Most of the experimental studies on near-field thermal radiation have measured the total (spectrally integrated) heat transfer which does not provide information about the spectrum of heat transfer [7,22-49]. Narrow peaks can be observed in the near-field thermal emission by isotropic media due to the excitation of surface phonon- and plasmon-polaritons (SPhPs and SPPs, respectively) as well as frustrated total-internal-reflection modes. In addition to surface and frustrated modes, anisotropic media can support hyperbolic modes that enhance near-field thermal emission in a broadband manner. Measuring the spectrum of near-field thermal emission is challenging because the evanescent waves in the near-field need to be converted to propagating waves to reach a Fourier-transform infrared (FTIR) spectrometer located in the far zone.

So far, the SPhP modes of near-field thermal emission have been measured for silica [50,51], quartz [52], silicon carbide (SiC) [50,52-54], and for a thin film of hexagonal boron nitride (hBN) on gold and silica substrates [54]. The frustrated total-internal-reflection modes thermally emitted by polytetrafluoroethylene (PTFE) have also been measured [52,54]. However, the broadband near-field thermal emission due to hyperbolic modes has not been experimentally observed.

Most of the measured near-field spectra are obtained using scanning optical microscopes [50,52-54]. In this spectroscopic technique, the thermal near field of an emitting sample is scattered to the far zone by bringing the sharp tip of the microscope to a sub-wavelength distance from the sample. The measured peaks using this technique are redshifted (from 3 to 63 cm^{-1}) and broadened relative to the theoretical predictions using the fluctuational electrodynamics [50-56]. It is shown experimentally [53], and theoretically [56], that the spectral redshift and broadening of the peaks are strongly dependent on the geometry of the probe. For example, three different values of 898, 923, and 943 cm^{-1} were obtained for the SPhP resonance of SiC when different probes were used in the same experimental setup [53]. The reason for the three different values for the resonance arises from the difficulty in precisely controlling and measuring the geometry of the probe. Furthermore, computationally expensive numerical models are required for relating the measured signal to the near-field thermal emission by the sample.

In this study, we present a simple and robust spectroscopy technique which does not involve multiscale, complex-shape probes and specialized optical instruments. In addition to SPhP and frustrated modes for quartz, silica and PTFE, we experimentally demonstrate broadband hyperbolic thermal emission for hBN. The measured spectra are reproducible, and the redshift and broadening of the peaks can accurately be predicted using a theoretical model based on the fluctuational electrodynamics and dyadic Green's functions (DGFs) for one-dimensional layered media.

2.3. Experimental Setup

A schematic of the experimental setup for near-field thermal emission spectroscopy is shown in Fig. 2.1(a). An internal reflection element (IRE) which has low infrared losses is brought into contact with an emitting sample. Due to surface roughness, several sub-wavelength air gaps are formed between the two

surfaces. The air gap due to surface roughness is represented by d in Fig. 2.1(b) where a close-up view of the sample-IRE interface is shown. The emitted evanescent waves with parallel component of the wavevector, k_ρ, between k_0 and $n_I k_0$ (k_0 and n_I are vacuum wavevector and IRE refractive index, respectively) are converted into propagating waves in the IRE due to the increase of the wavevector [Fig. 2.1(b)]. These propagating waves cannot escape the parallel surfaces of the IRE as they experience total internal reflections. Instead, these modes travel through the IRE toward its beveled ends which make an angle of α with the surface normal. The coupled modes with k_ρ between k_0 and $\sin(90° - \alpha + \theta_{cr}) n_I k_0$, where $\theta_{cr} = \sin^{-1}(1/n_I)$ is the critical angle for the IRE-air interface, hit the IRE beveled ends with an angle smaller than the critical angle (see Sec. A.1 of the Appendix [57]). These modes exit from IRE's beveled ends and are sent to an FTIR spectrometer where their spectrum is recorded. The higher the refractive index and the bevel angle of the IRE, the larger the number of evanescent modes that can couple to the IRE. Since the IRE is transparent in the infrared, its thermal emission is negligible compared to the sample. The arrangement shown in Fig. 2.1(b) is similar to the inverse of the Kretschmann configuration used for exciting SPPs at the interface of a metallic thin film and the free space using an external illumination [58].

The sample is mounted on a metal ceramic heater with an output of 24 W at 24 V (Thorlabs, HT24S), which is connected to a power supply (KEPCO, ABC 36-3DM) with a maximum voltage of 36 V. The sample temperature is measured using a K-type thermocouple and is read using a digital thermometer (OMEGA, HH-52). The sample-heater assembly is adhered to a ceramic base using a nickel-base metallic adhesive (Cotronics Corp., Durabond 952 FS). A zinc selenide (ZnSe) IRE with a trapezoidal cross section and a bevel angle of $\alpha = 45°$ is selected for the experiment (Harrick, EM2122). The IRE dimensions are 50 (length) × 10 (width) × 2 (thickness) mm. ZnSe has a refractive index of $n_I \approx 2.4$ and is transparent between 700 and 15000 cm^{-1}. The IRE is placed on the sampling surface of a multiple-reflection horizontal Attenuated Total Reflection (ATR) accessory (Harrick, HorizonTM). The base-heater-sample assembly is put in contact with the IRE while two elastic posts made of 0.005"-thick

stainless-steel plates acting as a spring are placed between the base and the sampling plate of the ATR accessory. A pressure applicator is used to press the base toward the IRE for near-field measurements. For far-field measurements, the pressure is released from the base such that the elastic posts push the sample away and keep it at a 1-mm distance from the IRE. The signal exiting one of the IRE beveled ends is collected by the ATR accessory and transferred into the emission port of an FTIR spectrometer using an *f*/4 parabolic mirror. The FTIR is an ABB-Bomem MB1552E equipped with a broadband mercury-cadmium-telluride detector (InfraRed Associates Inc.).

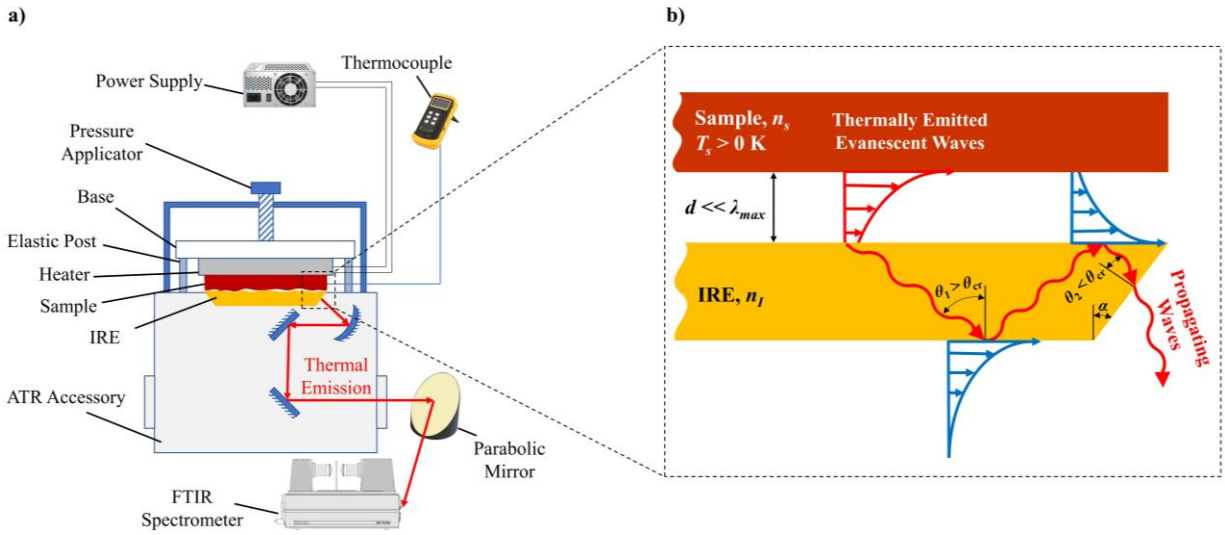

Figure 2.1 – (a) A schematic of the experimental setup for near-field thermal emission spectroscopy. (b) A close-up view of the sample-IRE interface. The distance *d* represents the air gap between the sample and the IRE due to surface roughness. Thermally emitted evanescent waves with k_ρ between k_0 and $\sin(90° - \alpha + \theta_{cr})n_1k_0$ exit the IRE's beveled ends after several total internal reflections, and are collected using an FTIR spectrometer.

2.4. Results and Discussion

Near-field and far-field thermal spectra are measured for quartz, silica, PTFE, and hBN at a temperature of approximately 160°C (see Sec. A.2 of the Appendix [57]). The silica, hBN, and PTFE samples are 1-mm thick, while the thicknesses of the quartz sample is 0.5 mm. It is verified experimentally and

theoretically that all samples are optically thick. A spectral resolution of 4 cm^{-1} is selected for the FTIR spectrometer. The background thermal emission is measured by blocking the sample emission from reaching the FTIR via placing a thick film of stainless steel (which is opaque in the infrared) at the exit of the ATR accessory. The background thermal emission is subtracted from the measured signals. The near-field spectra are normalized by the far-field thermal emission to compensate for the wavenumber-dependent responsivity of the photodetector, absorption by the internal parts of the ATR accessory and ambient gases, as well as modulation efficiency of the FTIR spectrometer (see Sec. A.3 of the Appendix [57]). The normalized near-field spectra are shown in Fig. 2.2(a) to 2.2(d). To ensure that the experiments are reproducible, the measurements were repeated three times for each sample. In each repetition, the IRE, the sample, and the heater are disassembled and reinstalled. As an example, the three measured spectra for the quartz sample are plotted in Fig. 2.2(a). This level of repeatability was observed for all samples.

To compare measurements with theory, the energy density emitted by the samples in free space (integrated over k_ρ from 0 to infinity) is calculated using the fluctuational electrodynamics and the DGFs for a semi-infinite bulk [59-62]. The near-field and far-field energy densities are calculated at 200 nm (approximately equal to the surface flatness of the samples) and 1 mm above the samples, respectively. The dielectric functions of quartz, silica, PTFE, and hBN are obtained from literature [63-65] and are plotted in Sex. A.4 of the Appendix [57]. It should be noted that hBN is an anisotropic uniaxial medium and is described using a parallel and a perpendicular (to the optical axis) dielectric function. The calculated near-field spectra normalized by their far-field value are plotted in Figs. 2.2(e) to 2.2(h). Peaks in near-field thermal spectra occur when $\varepsilon_s + 1 \to 0$ (due to the excitation of SPhPs) and $\mathrm{Im}[\varepsilon_s] \to \infty$ (due to the contribution of frustrated total-internal-reflection modes), where $\varepsilon_s = n_s^2$ is the dielectric function of the sample [66]. Additionally, thermal emission by uniaxial media can be enhanced in a broadband manner when $\mathrm{Re}[\varepsilon_{s,\parallel}]\mathrm{Re}[\varepsilon_{s,\perp}] < 0$ ($\varepsilon_{s,\parallel}$ and $\varepsilon_{s,\perp}$ are the dielectric functions of the sample in the

parallel and perpendicular directions relative to the optical axis, respectively) due to the excitation of hyperbolic modes.

The near-field energy density for quartz [Fig. 2.2(e)] has three peaks at 806, 1155, and 1189 cm^{-1} due to the excitation of surface phonon polaritons (Re[ε_s] = -0. 5, -1.4, and -1.0, respectively). The three SPhP resonances are captured in the measured quartz spectrum [Fig. 2.2(a)]. The SPhP resonances are redshifted and broadened in the experiments compared to the theoretical predictions. The origin of the redshift and broadening of the peaks will be discussed later using a theoretical model. The theoretical energy density for silica [Fig. 2.2(f)] shows two peaks at 809 and 1149 cm^{-1} which both are measured [Fig. 2.2b]. The low-wavenumber peak is due to the symmetric Si-O-Si stretching vibrations (frustrated modes), while the high-wavenumber peak is because of the excitation of SPhPs (Re[ε_s] = -1.2). The theoretical spectrum for PTFE [Fig. 2.2(g)] has two peaks at 1163 and 1225 cm^{-1}, which are due to the symmetric and asymmetric C-F stretching vibrations (frustrated modes). These peaks are also captured in the measured spectrum [Fig. 2.2(c)]. The experimental and theoretical spectra of near-field thermal emission by hBN are shown in Figs. 2.2(d) and 2.2(h), respectively. Hexagonal boron nitride has two hyperbolic bands at 780–835 cm^{-1} and 1400–1600 cm^{-1}. These two hyperbolic bands are captured in the measured spectrum of hBN in Fig. 2.2(d). The increase of the measured signal near 700 cm^{-1} is due to thermal emission by ZnSe which becomes opaque around this wavenumber.

The measured near-field peaks are broadened and exhibit redshifts ranging from 8 to 42 cm^{-1}. Peak broadening and redshifts up to 105 cm^{-1} are also observed in previously measured spectra [50-56]. The redshift and broadening in our measurements can be predicted by modeling energy density in the IRE due to thermal emission by the sample. The energy density at distance Δ in the IRE due to thermal emission by an anisotropic uniaxial medium separated by an air gap of size d from the IRE [see the inset of Fig. 2.2(e)] is derived in Sec. A.5 of the Appendix [57]. The energy density in the IRE is derived using the fluctuational electrodynamics and the DGFs for a one-dimensional layered media. We have verified that an air gap exists between the sample and the IRE, and that the gap can be adjusted by depositing

polystyrene nanoparticles on the IRE (see Secs. A.6 and A.7 of the Appendix [57]). The energy density of the modes exiting the IRE beveled ends, i.e., modes with k_ρ between $\sin(20.4°)n_I k_0$ and $\sin(69.6°)n_I k_0$ (see Sec. A.1 of the Appendix [57]), is derived as:

$$\left\langle u\left(\Delta,\omega\right)\right\rangle = \frac{\Theta\left(\omega,T_s\right)\omega}{2c_0^2\pi^2}\int_{\sin(20.4°)n_I k_0}^{\sin(69.6°)n_I k_0} k_\rho \int_0^{t_s}\Bigg(k_I^2 \mathrm{Trace}\left[\bar{\bar{\mathbf{g}}}^E\left(k_\rho,\Delta,z',\omega\right)\cdot \mathrm{Im}\left[\bar{\bar{\boldsymbol{\varepsilon}}}_{\mathbf{s}}\right]\cdot \bar{\bar{\mathbf{g}}}^{E^\dagger}\left(k_\rho,\Delta,z',\omega\right)\right] + \mathrm{Trace}\left[\bar{\bar{\mathbf{g}}}^H\left(k_\rho,\Delta,z',\omega\right)\cdot \mathrm{Im}\left[\bar{\bar{\varepsilon}}_s\right]\cdot \bar{\bar{\mathbf{g}}}^{H^\dagger}\left(k_\rho,\Delta,z',\omega\right)\right]\Bigg) dz' dk_\rho \tag{2.1}$$

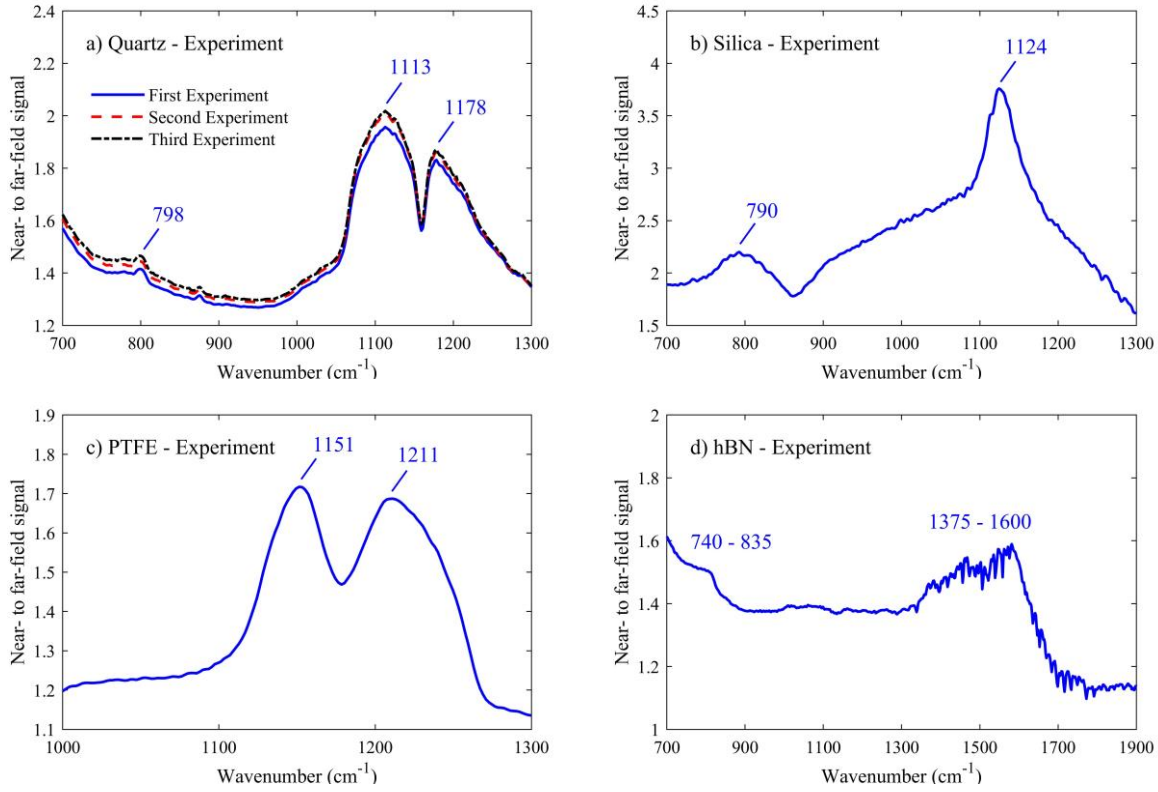

Figure 2.2 – The near-field thermal emission spectra normalized by the far-field value for quartz, silica, PTFE, and hBN. Panels (a) to (d) show the measured spectra, while Panels (e) to (h) display theoretically predicted spectra. In Panels (e) to (h), red dashed lines show the energy density at distance *d* in the free space, while the solid blue lines show the energy density at distance Δ in the IRE due to the modes with k_ρ between $\sin(20.4°)n_I k_0$ and $\sin(69.6°)n_I k_0$.

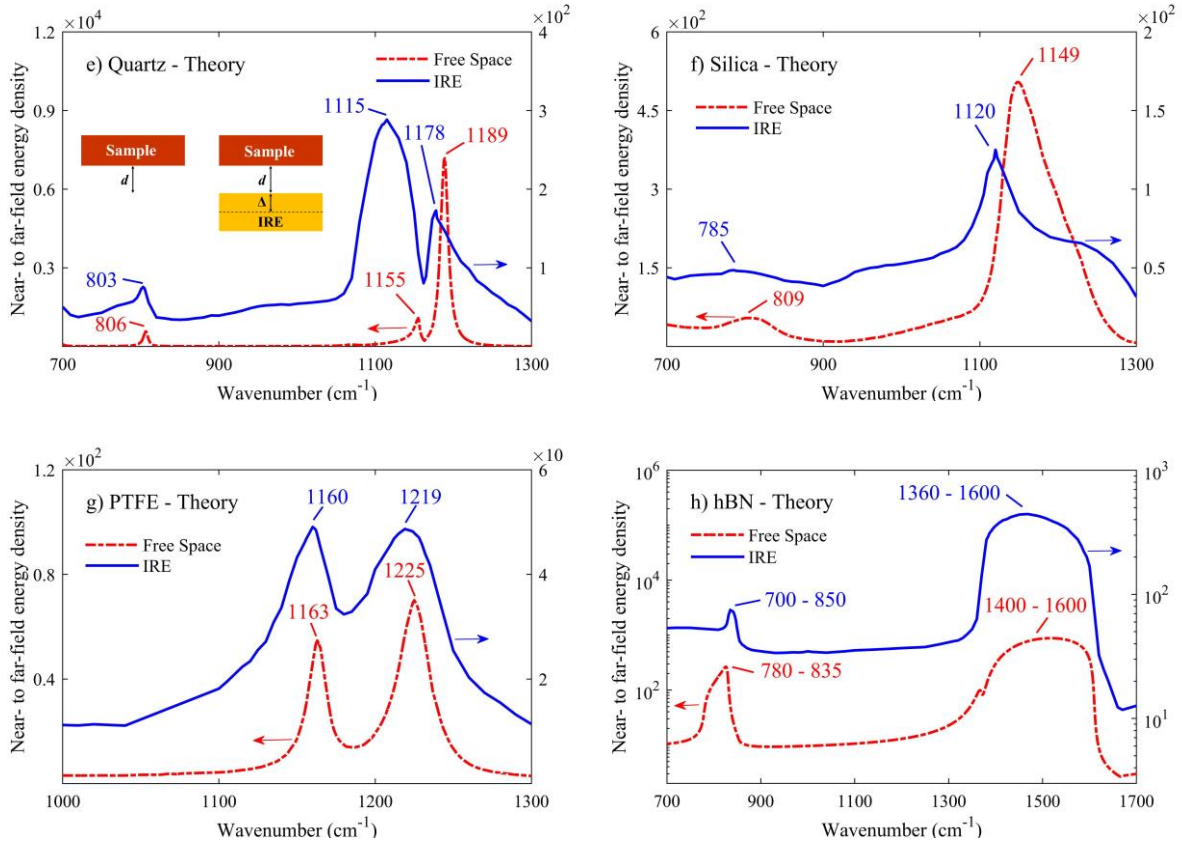

Figure 2.2 (contd.) – The near-field thermal emission spectra normalized by the far-field value for quartz, silica, PTFE, and hBN. Panels (a) to (d) show the measured spectra, while Panels (e) to (h) display theoretically predicted spectra. In Panels (e) to (h), red dashed lines show the energy density at distance d in the free space, while the solid blue lines show the energy density at distance Δ in the IRE due to the modes with k_ρ between $\sin(20.4°)n_I k_0$ and $\sin(69.6°)n_I k_0$.

In Eq. (2.1), u is the energy density, ω is the angular frequency, Θ is the mean energy of an electromagnetic state [60], $< >$ represents ensemble average, c_0 is the speed of light in the free space, T_s is the sample temperature, t_s is the thickness of the sample, k_I is the wavevector in the IRE, z' is the vertical (to the surface) position of a thermally emitting source in the sample, the superscript $\dagger$ indicates the Hermitian operator, $\overline{\overline{\boldsymbol{\varepsilon}}}_s$ (= diag[$\varepsilon_{s,\perp}$; $\varepsilon_{s,\perp}$; $\varepsilon_{s,\parallel}$]) is the dielectric-function tensor for the sample, and $\overline{\overline{\mathbf{g}}}^E$

and $\overline{\overline{\mathbf{g}}}^{H}$ are the Weyl components of the electric (*E*) and magnetic (*H*) DGFs for an emitting anisotropic medium, respectively. The Weyl components of the DGFs are derived using the scattering matrix method [67] in Sec. A.5 of the Appendix [57].

The energy density in the middle of the IRE (where the signal is collected using the ATR accessory) is calculated in the near and far fields for a sample temperature of 160°C. The ratio of the near-field and far-field energy densities is shown in Figs. 2.2(e) to 2.2(h) for the four samples. The calculated spectra are in great agreement with the measurements showing that Eq. (2.1) can be used for predicting the redshift and broadening of the near-field peaks. These redshifts and broadening arise from the multiple reflections of the thermally emitted waves between the sample and the IRE as well as the fact that a portion of the near-field evanescent waves are captured in the measurements. However, all the SPhP, frustrated and hyperbolic modes are captured in the measured spectra. The number of captured modes can be increased by using an IRE with a higher refractive index or using a hemispherical IRE (see Sec. A.1 of the Appendix [57]).

2.5. Conclusions

In summary, we experimentally demonstrated narrow peaks of near-field thermal emission due to the excitation of SPhPs (for quartz and silica) and frustrated total-internal-reflection modes (for silica and PTFE), as well as the broadband thermal emission of hyperbolic modes in the near field (for hBN). We derived an analytical expression for the energy density inside the IRE due to thermal emission by an anisotropic medium that can be used for predicting the redshift and broadening of the measured near-field peaks.

2.6. Acknowledgment

The authors acknowledge support from the National Science Foundation under Grant No. CBET-1804360.

2.7. References

[1] R. S. DiMatteo, P. Greiff, S. L. Finberg, K. A. Young-Waithe, H. K. H. Choy, M. M. Masaki, and C. G. Fonstad, Appl. Phys. Lett. 79, 1894 (2001).

[2] M. D. Whale and E. G. Cravalho, IEEE Trans. Energy Convers. 17, 130 (2002).

[3] M. Laroche, R. Carminati, and J.-J. Greffet, J. Appl. Phys. 100, 63704 (2006).

[4] K. Park, S. Basu, W. P. King, and Z. M. Zhang, J. Quant. Spectrosc. Radiat. Transf. 109, 305 (2008).

[5] M. Francoeur, R. Vaillon, and M. P. Mengüç, IEEE Trans. Energy Convers. 26, 686 (2011).

[6] M. P. Bernardi, O. Dupré, E. Blandre, P.-O. Chapuis, R. Vaillon, and M. Francoeur, Sci. Rep. 5, 11626 (2015).

[7] A. Fiorino, L. Zhu, D. Thompson, R. Mittapally, P. Reddy, and E. Meyhofer, Nat. Nanotechnol. 13, 806 (2018).

[8] E. Tervo, E. Bagherisereshki, and Z. Zhang, Front. Energy 12, 5 (2018).

[9] C. R. Otey, W. T. Lau, and S. Fan, Phys. Rev. Lett. 104, 154301 (2010).

[10] S. Basu and M. Francoeur, Appl. Phys. Lett. 98, 113106 (2011).

[11] P. J. Van Zwol, K. Joulain, P. Ben Abdallah, J.-J. Greffet, and J. Chevrier, Phys. Rev. B 83, 201404 (2011).

[12] H. Iizuka and S. Fan, J. Appl. Phys. 112, 24304 (2012).

[13] Y. Yang, S. Basu, and L. Wang, Appl. Phys. Lett. 103, 163101 (2013).

[14] L. P. Wang and Z. M. Zhang, Nanoscale Microscale Thermophys. Eng. 17, 337 (2013).

[15] K. Ito, K. Nishikawa, H. Iizuka, and H. Toshiyoshi, Appl. Phys. Lett. 105, 253503 (2014).

[16] K. Joulain, Y. Ezzahri, J. Drevillon, B. Rousseau, and D. D. S. Meneses, Opt. Express 23, A1388 (2015).

[17] A. Ghanekar, J. Ji, and Y. Zheng, Appl. Phys. Lett. 109, 123106 (2016).

[18] Z. Zheng, X. Liu, A. Wang, and Y. Xuan, Int. J. Heat Mass Transf. 109, 63 (2017).

[19] K. Ito, K. Nishikawa, A. Miura, H. Toshiyoshi, and H. Iizuka, Nano Lett. 17, 4347 (2017).

[20] M. Elzouka and S. Ndao, Sci. Rep. 7, 44901 (2018).

[21] A. Fiorino, D. Thompson, L. Zhu, R. Mittapally, S.-A. Biehs, O. Bezencenet, N. El-Bondry, S. Bansropun, P. Ben-Abdallah, E. Meyhofer, and others, ACS Nano 12, 5774 (2018).

[22] A. Kittel, W. Müller-Hirsch, J. Parisi, S.-A. Biehs, D. Reddig, and M. Holthaus, Phys. Rev. Lett. 95, 224301 (2005).

[23] L. Hu, A. Narayanaswamy, X. Chen, and G. Chen, Appl. Phys. Lett. 92, 133106 (2008).

[24] U. F. Wischnath, J. Welker, M. Munzel, and A. Kittel, Rev. Sci. Instrum. 79, 73708 (2008).

[25] A. Kittel, U. F. Wischnath, J. Welker, O. Huth, F. Rueting, and S.-A. Biehs, Appl. Phys. Lett. 93, 193109 (2008).

[26] S. Shen, A. Narayanaswamy, and G. Chen, Nano Lett. 9, 2909 (2009).

[27] E. Rousseau, A. Siria, G. Jourdan, S. Volz, F. Comin, J. Chevrier, and J.-J. Greffet, Nat. Photonics 3, 514 (2009).

[28] R. S. Ottens, V. Quetschke, S. Wise, A. A. Alemi, R. Lundock, G. Mueller, D. H. Reitze, D. B. Tanner, and B. F. Whiting, Phys. Rev. Lett. 107, 14301 (2011).

[29] S. Shen, A. Mavrokefalos, P. Sambegoro, and G. Chen, Appl. Phys. Lett. 100, 233114 (2012).

[30] T. Kralik, P. Hanzelka, M. Zobac, V. Musilova, T. Fort, and M. Horak, Phys. Rev. Lett. 109, 224302 (2012).

[31] J. Shi, P. Li, B. Liu, and S. Shen, Appl. Phys. Lett. 102, 183114 (2013).

[32] L. Worbes, D. Hellmann, and A. Kittel, Phys. Rev. Lett. 110, 134302 (2013).

[33] B. Song, Y. Ganjeh, S. Sadat, D. Thompson, A. Fiorino, V. Fernández-Hurtado, J. Feist, F. J. García-Vidal, J. C. Cuevas, P. Reddy, and Others, Nat. Nanotechnol. 10, 253 (2015).

[34] T. Ijiro and N. Yamada, Appl. Phys. Lett. 106, 23103 (2015).

[35] M. Lim, S. S. Lee, and B. J. Lee, Phys. Rev. B 91, 195136 (2015).

[36] K. Kim, B. Song, V. Fernández-Hurtado, W. Lee, W. Jeong, L. Cui, D. Thompson, J. Feist, M. T. H. Reid, F. J. García-Vidal, and Others, Nature 528, 387 (2015).

[37] S. A. Dyakov, J. Dai, M. Yan, and M. Qiu, J. Phys. D: Appl. Phys. 48, 305104 (2015).

[38] B. Song, D. Thompson, A. Fiorino, Y. Ganjeh, P. Reddy, and E. Meyhofer, Nat. Nanotechnol. 11, 509 (2016).

[39] R. St-Gelais, L. Zhu, S. Fan, and M. Lipson, Nat. Nanotechnol. 11, 515 (2016).

[40] M. P. Bernardi, D. Milovich, and M. Francoeur, Nat. Commun. 7, 12900 (2016).

[41] J. I. Watjen, B. Zhao, and Z. M. Zhang, Appl. Phys. Lett. 109, 203112 (2016).

[42] S. Lang, G. Sharma, S. Molesky, P. U. Kränzien, T. Jalas, Z. Jacob, A. Y. Petrov, and M. Eich, Sci. Rep. 7, 13916 (2017).

[43] K. Kloppstech, N. Könne, S.-A. Biehs, A. W. Rodriguez, L. Worbes, D. Hellmann, and A. Kittel, Nat. Commun. 8, 14475 (2017).

[44] L. Cui, W. Jeong, V. Fernández-Hurtado, J. Feist, F. J. García-Vidal, J. C. Cuevas, E. Meyhofer, and P. Reddy, Nat. Commun. 8, 14479 (2017).

[45] F. Peragut, L. Cerruti, A. Baranov, J. P. Hugonin, T. Taliercio, Y. De Wilde, and J. J. Greffet, Optica 4, 1409 (2017).

[46] D. Thompson, L. Zhu, R. Mittapally, S. Sadat, Z. Xing, P. McArdle, M. M. Qazilbash, P. Reddy, and E. Meyhofer, Nature 561, 216 (2018).

[47] M. Ghashami, H. Geng, T. Kim, N. Iacopino, S. K. Cho, and K. Park, Phys. Rev. Lett. 120, 175901 (2018).

[48] J. Yang, W. Du, Y. Su, Y. Fu, S. Gong, S. He, and Y. Ma, Nat. Commun. 9, 4033 (2018).

[49] A. Jarzembski, C. Shaskey, and K. Park, Front. Energy 12, 43 (2018).

[50] A. Babuty, K. Joulain, P.-O. Chapuis, J.-J. Greffet, and Y. De Wilde, Phys. Rev. Lett. 110, 146103 (2013).

[51] J. K.-K. Tong, Photonic Engineering of Near-and Far-Field Radiative Heat Transfer, Massachusetts Institute of Technology, 2016.

[52] A. C. Jones and M. B. Raschke, Nano Lett. 12, 1475 (2012).

[53] B. T. O'Callahan, W. E. Lewis, A. C. Jones, and M. B. Raschke, Phys. Rev. B 89, 245446 (2014).

[54] B. T. O'Callahan and M. B. Raschke, APL Photonics 2, 21301 (2017).

[55] V. Hatamipour, S. Edalatpour, and M. Francoeur, Phys. Rev. Appl. 10, 54047 (2018).

[56] S. Edalatpour, V. Hatamipour, and M. Francoeur, Phys. Rev. B 99, 165401 (2019).

[57] See Supplemental Material at http://link.aps.org/supplemental/ 10.1103/PhysRevB.100.235450 for determination of the modes exiting the IRE; measurement of the temperature of the sample; background subtraction and normalization of the near-field spectra; dielectric functions of the samples; derivation of energy density inside the IRE; and verification and adjustment of the air gap between the sample and the IRE..

[58] S. A. Maier, Plasmonics: *Fundamentals and Applications* (Springer Science & Business Media, 2007).

[59] S. M. Rytov, Y. A. Kravtsov and V. Tatarskii, *Principles of Statistical Radiophysics 3: Elements of Random Fields* (Springer, New York, 1989).

[60] K. Joulain, J.-P. Mulet, F. Marquier, R. Carminati, and J.-J. Greffet, Surf. Sci. Rep. 57, 59 (2005).

[61] Y. Guo and Z. Jacob, J. Appl. Phys. 115, 234306 (2014).

[62] S. Lang, M. Tschikin, S. A. Biehs, A. Y. Petrov, and M. Eich, Appl. Phys. Lett., 104, 121903 (2014).

[63] E. D. Palik, *Handbook of Optical Constants of Solids* (Academic Press, 1997).

[64] E. H. Korte and A. Röseler, Anal. Bioanal. Chem. 382, 1987 (2005).

[65] Y. Cai, L. Zhang, Q. Zeng, L. Cheng, and Y. Xu, Solid State Commun. 141, 262 (2007).

[66] J.-P. Mulet, K. Joulain, R. Carminati, and J.-J. Greffet, Microscale Thermophys. Eng. 6, 209 (2002).

[67] M. Francoeur, M. P. Mengüç, and R. Vaillon, J. Quant. Spectrosc. Radiat. Transf. 110, 2002 (2009).

CHAPTER 3

PROBING NEAR-FIELD THERMAL EMISSION OF LOCALIZED SURFACE PHONONS FROM SILICON CARBIDE NANOPILLARS

This chapter has been submitted to be published in ACS Photonics as an article. Coauthors of this paper are Saman Zare, Ramin Pouria, Philippe K. Chow, Tom Tiwald, Carl P. Tripp, and Sheila Edalatpour.

3.1. Abstract

Thermal emission of localized surface phonons (LSPhs) from nanostructures of polaritonic materials is a promising mechanism for tuning the spectrum of near-field thermal radiation. Previous studies have theoretically shown that thermal emission of LSPhs results in narrow-band peaks in the near-field spectra, whose spectral locations can be modulated by changing the dimensions of the nanostructure. However, near-field thermal emission of LSPhs has not been experimentally explored yet. In this study, we measure the spectrum of near-field thermal radiation from arrays of 6H-silicon carbide (6H-SiC) nanopillars using an internal-reflection-element based spectroscopy technique. We present experimental demonstration of thermal emission of the transverse dipole, quadrupole, and octupole, as well as longitudinal monopole from 6H-SiC nanopillars at a near-field distance from the array. We show that the spectral location of the longitudinal monopole and transverse dipole are significantly affected by the near-field coupling between neighboring nanopillars as well as the intercoupling of the nanopillars and the substrate. We also experimentally demonstrate that the spectrum of near-field thermal radiation from 6H-SiC nanopillar arrays can be tuned by varying the dimensions of the nanopillars, providing an opportunity for designing emitters with tailored near-field thermal radiation.

3.2. Introduction

Thermal radiation in the near-field regime, i.e., at sub-wavelength distances from the emitting medium, can exceed the blackbody limit by several orders of magnitude and be quasi-monochromatic. These unique properties of near-field thermal radiation have attracted significant attention for many promising

applications, such as power generation using thermophotovoltaic devices [1,2], near-field photonic cooling [3], thermal management of electronic devices [4,5], and thermal rectification [6,7]. Most of these applications require spectral tuning of the near-field thermal radiation. It has been theoretically proposed that the near-field spectra can be tailored via using metamaterials engineered at the sub-wavelength scale [8-37]. Among the proposed metamaterials, are nanostructures made of polaritonic materials such as silicon carbide (SiC) [9,11,15-18,23,27,30,36]. Polaritonic materials have negative permittivity in their Reststrahlen band bounded by the transverse and longitudinal optical phonon frequencies. The Reststrahlen band of polaritonic materials is located in the infrared part of the electromagnetic spectrum38, where thermal emission is commonly spectrally located. It is theoretically shown that metamaterials made of nanoparticles of polaritonic materials can emit localized surface phonons (LSPhs) in their Reststrahlen band, causing narrow-band peaks in the near-field spectra [9,15,39]. It is proposed that the spectral location of the thermally emitted LSPhs can be modulated by varying the size and shape of the nanoparticles [9,15,39]. However, near-field thermal emission of LSPhs from polaritonic metamaterials has not been experimentally demonstrated yet. A limited number of studies have experimentally explored the near-field response of polaritonic metamaterials to an external illumination using scattering-scanning near-field optical microscopy [40-42]. However, the studied near-field spectra are dependent on the direction and polarization of the incident electromagnetic wave and do not represent the spectrum of near-field thermal radiation.

In this paper, we provide measurements of the spectrum of near-field thermal radiation from periodic arrays of 6H-SiC nanopillars. We experimentally demonstrate that thermal emission of LSPhs results in narrow peaks in the near-field spectrum of 6H-SiC nanopillars. In addition, the effect of the nanopillar height on the spectral location of LSPhs is investigated, and it is experimentally shown that the spectral location of LSPhs in the near-field spectrum can be modulated by varying the height of the nanopillars. The spectral measurements provided in this study, which agree with theoretically predicted spectra, can pave the way for developing tunable emitters for near-field thermal radiation applications.

3.3. Results and Discussion

To demonstrate thermal emission of LSPhs in the near-field regime, two periodic arrays of 6H-SiC nanopillars with a similar pitch, *L*, of 1 μm are fabricated using inductively-coupled plasma reactive ion etching (see Sec. B.1 of the Appendix for fabrication details). Scanning electron microscope (SEM) images of the fabricated samples (labeled as Sample A and B) are shown in Figs. 3.1(a) and 3.1(b), respectively. The fabricated nanopillars have a conical frustum shape. The bottom and top diameters of the nanopillars in Sample A are ~700 nm and ~500 nm, respectively, while the nanopillars in Sample B have a bottom diameter of ~650 nm and a top diameter of ~500 nm. The interpillar spacing, defined as the bottom-to-bottom gap between two adjacent nanopillars, for Samples A and B are ~300 nm and ~350 nm, respectively. The height of the nanopillars in Sample A is ~1 μm, while the nanopillars in Sample B have a larger height of ~1.6 μm. A conical trench is formed around each nanopillar in both samples. The height and width of the trench is ~50 nm in Sample A [see the inset of Fig. 3.2(b)] while the dimensions of the trench in Sample B are about half of those in Sample A [see the inset of Fig. 3.4(b)].

The spectra of near-field thermal radiation from the fabricated samples are measured using an experimental technique which utilizes an internal reflection element (IRE) for guiding the evanescent waves to a Fourier-transform infrared (FTIR) spectrometer [43] (see Sec. B.2 of the Appendix for setup details). The spectra measured for Sample A and a flat 6H-SiC sample are shown in Fig. 3.2(a) at a temperature of 150ºC and a distance of ~100 nm from the surface of the samples. The experimental near-field spectra in Fig. 3.2(a) are normalized by the far-field thermal radiation measured for a carbon nanotube (CNT) sample, acting as a blackbody thermal emitter at the same temperature. The CNT sample has an emissivity of ~0.97-0.99 in the wavenumber range of interest, i.e., 750-1000 cm^{-1} (see the Sec. B.2 of the Appendix section for details of measuring the emissivity of the CNT sample). The spectrum of the flat SiC has a peak at 935 cm^{-1} corresponding to thermal emission of propagating surface phonon polaritons (SPhPs) in the Reststrahlen band of 6H-SiC (~796-965 cm^{-1}). The near-field spectrum of Sample A is quite different from that of the flat surface, and it has five peaks in the considered spectral region. These peaks are located at 777, 843, 876, 910, and 933 cm^{-1}.

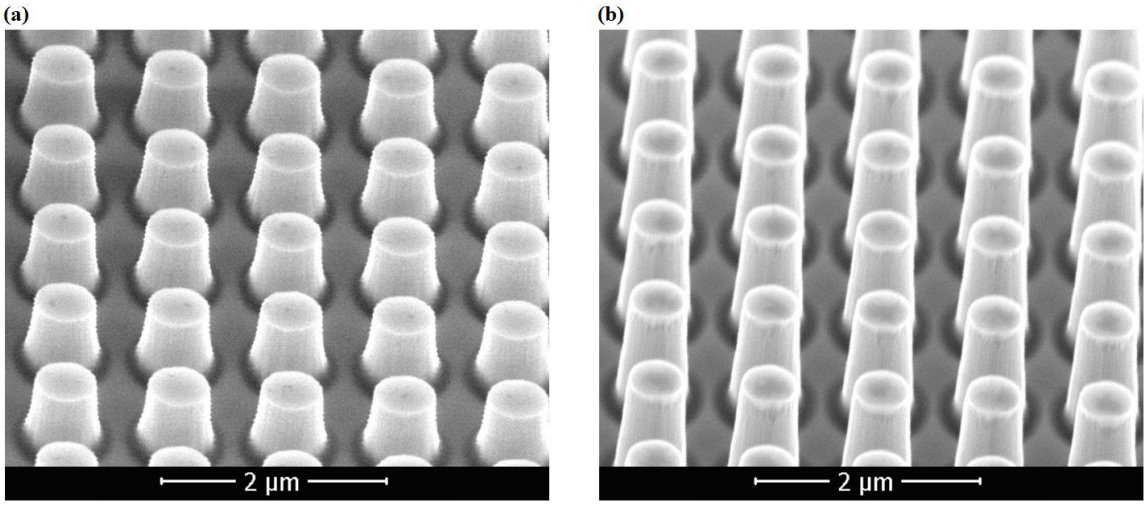

Figure 3.1 - SEM images of the fabricated 6H-SiC nanopillar arrays: (a) Sample A, and (b) Sample B.

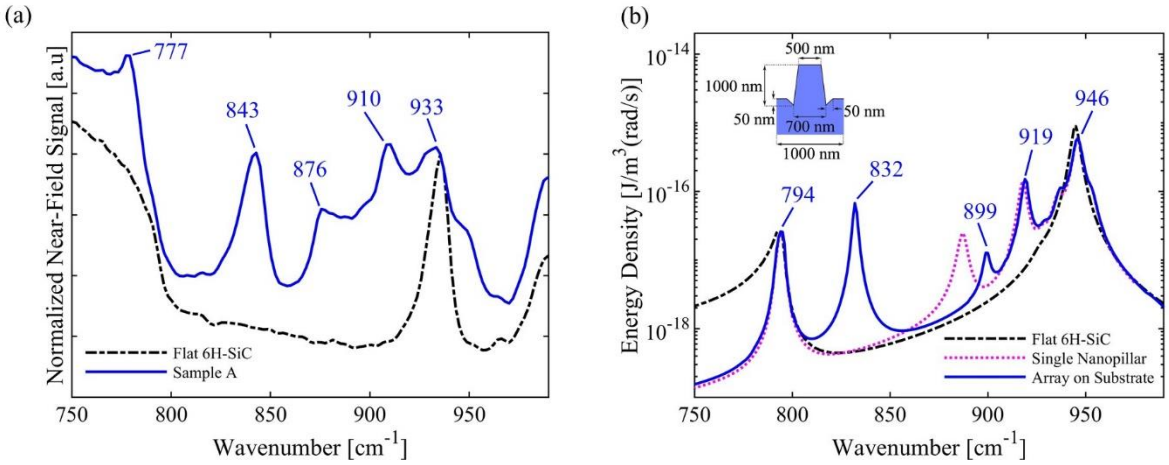

Figure 3.2 – (a) Measured near-field thermal radiation spectra for Sample A and a flat 6H-SiC sample at 150°C and a distance of 100 nm above the samples. The near-field spectra are normalized by the far-field thermal emission measured for a CNT sample at the same temperature. (b) Theoretically predicted near-field energy density for Sample A, a flat 6H-SiC sample, and a single free-standing nanopillar at a temperature of 150°C and a distance of 100 nm. The dimensions of the modeled unit cell of Sample A are shown in the inset.

For comparison with theory, the spectral energy density emitted by Sample A into the free space is calculated using the SCUFF-LDOS tool of the SCUFF-EM electromagnetic solver [44] and is shown in Fig. 3.2(b). A temperature of 150°C is assumed in the simulations, and the near-field energy density is calculated in the free space at a distance of 100 nm above the nanopillars along their central axis. The ordinary dielectric function of 6H-SiC measured using an ellipsometry technique at a close temperature of 200°C is used in the SCUFF-LDOS simulations (see Sec. B.3 of the Appendix for details of ellipsometry measurements). The near-field spectral energy density is also calculated for a single, free-standing nanopillar (using the SCUFF-LDOS) and a flat 6H-SiC bulk (using scattering matrix approach [45]) at the same temperature and distance and are shown in Fig. 3.2(b). The theoretical spectrum for Sample A also has five dominant peaks corresponding to those experimentally measured. The peaks in the theoretical spectrum are located at 794, 832, 899, 919, and 946 cm^{-1}. The measured locations of the peaks are shifted (by up to 23 cm^{-1}) in comparison to the theoretical data. Different factors contribute to the observed shift. This shift is partly due to the assumption of an isotropic dielectric function for 6H-SiC when modeling the energy density using SCUFF-LDOS. As mentioned before, the ordinary dielectric function is used in the SCUFF-LDOS simulations. Another factor is related to the fact that the measured spectra only include thermally-emitted electromagnetic waves with a parallel component of the wavevector, k_ρ, in the range of $\sin(20.4°)n_I k_0 < k_\rho < \sin(69.6°)n_I k_0$ (where n_I and k_0 are the refractive index of the IRE and the magnitude of the wavevector in free space, respectively), while the simulated energy density includes contributions from all k_ρs [43]. Furthermore, the measured electromagnetic waves go through multiple reflections between the sample and the IRE before being captured by the FTIR spectrometer, while the theoretical energy density is simulated in a free space above the samples [43]. The peak predicted at 794 cm^{-1} for Sample A is outside the Reststrahlen band of the 6H-SiC and is due to the large value of the imaginary part of the dielectric function at this wavenumber. The peaks predicted at 919 cm^{-1} and 946 cm^{-1} are also observed in the theoretical spectrum of the single free-standing nanopillar. To understand the physical origin of these two peaks, the charge density on the surface of the single free-standing nanopillar when illuminated by a *p*-polarized planar wave is simulated using the SCUFF-SCATTER tool of the SCUFF-

EM solver [46]. The *k*-vector of the incoming wave lies in the *x*-*z* plane with an angle of 25° from the central axis of the nanopillar [see Fig. 3.3(a)]. The simulated surface charge densities, ρ, at 919 cm^{-1} and 946 cm^{-1} are plotted in Figs. 3.3(a) and 3.3(b), respectively. It is seen from these figures that the peak at 919 cm^{-1} corresponds to thermal emission of the transverse quadruple mode with $m = 2$ (m being the order of the mode), while the peak at 946 cm^{-1} is associated with the transverse octupole mode with a higher order of $m = 4$. Since the spectral locations of these two transverse modes are the same for Sample A and the single free-standing nanopillar, it is concluded that transverse quadrupole and octupole modes are affected by neither the near-field interactions between neighboring nanopillars nor the presence of the substrate. The near-field spectrum for a single nanopillar also has a peak at 887 cm^{-1} and a shoulder at 911 cm^{-1} [see the close-up view of the shoulder in the inset of Fig. 3.3(e)]. The surface charge density for the single nanopillar at these two wavenumbers, presented in Figs. 3.3(c) and 3.3(d), respectively, shows that the peak at 887 cm^{-1} is due to thermal emission of the longitudinal monopole with $m = 0$, while the shoulder at 911 cm^{-1} is associated with the transverse dipole mode with $m = 1$. For an on-substrate array (i.e., for Sample A), the locations of the longitudinal monopole and transverse dipole are redshifted to 832 cm^{-1} and 899 cm^{-1}, respectively. To find the factors contributing to this redshift, the spectral energy density above free-standing and on-substrate arrays of nanopillars is simulated in the spectral range of 800-915 cm^{-1} for various array pitches, L, ranging from 3 μm to 1 μm (interpillar spacing of 2300 nm to 300 nm), as shown in Fig. 3.3(e). For a free-standing array with $L = 3$ μm, where the interpillar spacing is ~3 times the nanopillars largest diameter, the near-field interactions between neighboring nanopillars are weak and the spectral locations of the longitudinal monopole and transverse dipole are the same as those for a single nanopillar. As the nanopillars get closer to each other with decreasing L to 1.25 μm and 1 μm, the interactions between neighboring nanopillars become stronger, resulting in redshift of the longitudinal monopole and transverse dipole modes. In the presence of a substrate, these two modes are further redshifted (the longitudinal mode by up to ~44 cm^{-1} and the transverse dipole by up to ~12 cm^{-1}) for all array pitches [see Fig. 3.3(e)].

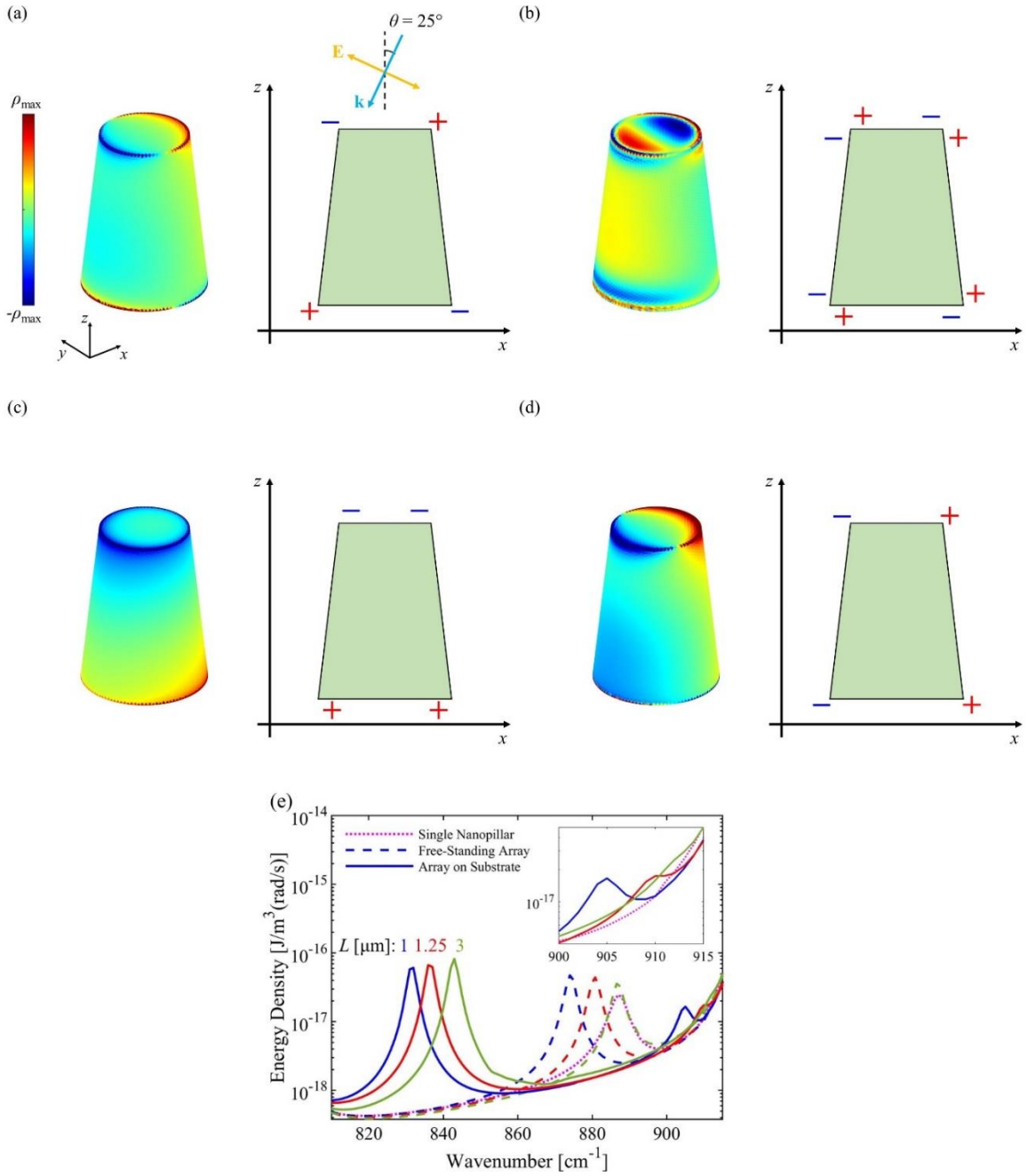

Figure 3.3 - Simulated surface charge density, ρ, over the surface of a single free-standing nanopillar at (a) 919 cm^{-1}, (b) 946 cm^{-1}, (c) 887 cm^{-1}, and (d) 911 cm^{-1}. For each mode, the schematic of the charge distribution in the *x*-*z* plane is also shown. (e) Predicted near-field energy density emitted by a single nanopillar, a free-standing array of nanopillars, and an on-substrate array of nanopillars for various array pitches, *L*. The inset is a close-up view of the energy density in the spectral range of 900-915 cm^{-1}, where transverse dipole mode is emitted.

The measured near-field spectrum for Sample B is compared with that for Sample A in Fig. 3.4(a). The simulated spectra for both samples are also shown in Fig. 3.4(b). The theoretical near-field spectrum for Sample B has six peaks which are detected in the measurements. The spectral locations of the measured and predicted peaks are specified in Figs. 3.4(a) and 3.4(b). The peaks due to the large imaginary part of the dielectric function, transverse quadrupole, and transverse octupole are almost unchanged as the height of the nanopillars increases from 1 μm in Sample A to 1.6 μm in Sample B. To find the physical origin of the peaks predicted at 810 cm^{-1} and 875 cm^{-1} for Sample B, the energy densities emitted from a single free-standing nanopillar, a free-standing array of nanopillars with pitch L (L = 1 and 3 μm), as well as an on-substrate nanopillar array with the same pitch L are simulated and presented in Fig. 3.4(c). It is seen that the spectrum of the single nanopillar has two peaks at 859 cm^{-1} and 908 cm^{-1}. Based on the charge density distributions in Figs. 3.4(d) and 3.4(e), these two peaks, respectively, correspond to the longitudinal monopole and transverse dipole modes of the nanopillar which are redshifted with increasing the height of the nanopillar to 1.6 μm. As for Sample A, the spectral locations of these modes are further redshifted for an on-substrate nanopillar array due to the near-field coupling between neighboring pillars and the presence of the substrate [see Fig. 3.4(c)]. The theoretical near-field spectrum for Sample B also shows a small peak at 903 cm^{-1}, which is not observed in the spectra of the single nanopillar and free-standing array, indicating that this peak is caused by the coupling between the nanopillars and the substrate. This peak is detected in the measured spectrum. The observed differences between the measured spectra for Samples A and B, which are in agreement with the theoretical predictions, demonstrate that the spectrum of near-field thermal radiation from nanopillar arrays of polaritonic materials can be modulated by varying the dimensions of the nanopillars.

3.4. Conclusions

The spectra of near-field thermal emission from periodic arrays of 6H-SiC frustum-shaped nanopillars with nanoscale interpillar spacings fabricated on a 6H-SiC substrate were experimentally explored. Two periodic arrays of different heights were considered. Near-field thermal emission of the transverse dipole, quadrupole, and octupole as well as longitudinal monopole from the nanopillar arrays is experimentally

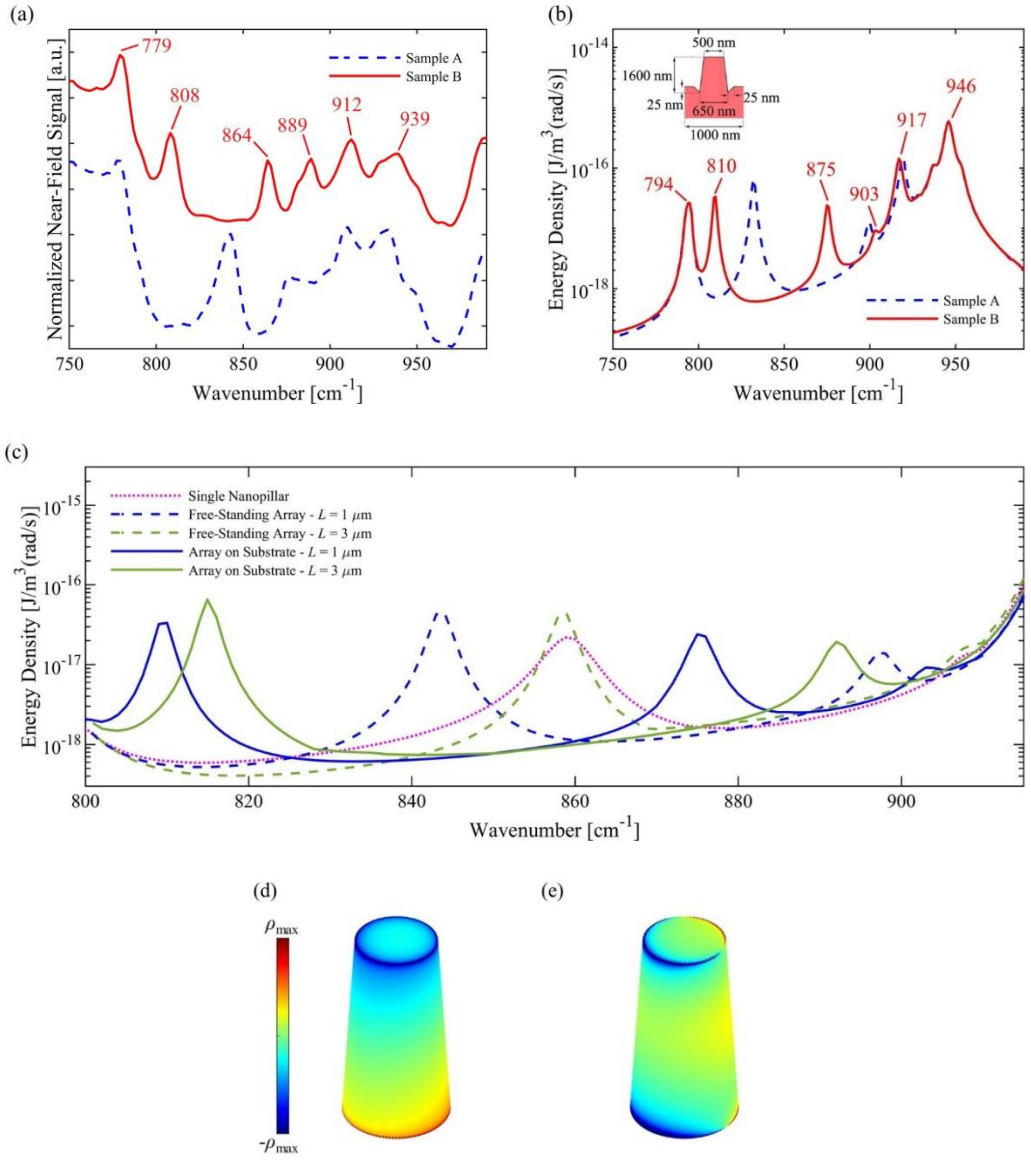

Figure 3.4 - (a) Measured spectrum for near-field thermal radiation from Sample B at 150°C and a distance of 100 nm in comparison with that from Sample A. The spectrum of Sample B is offset vertically for clarity. (b) The near-field energy density predicted for Samples A and B at 150°C and a distance of 100 nm. The inset shows the dimensions of the simulated unit cell for Sample B. (c) Theoretical near-field energy density for a single free standing nanopillar, a free-standing array of nanopillars with pitch L (L = 1 μm and 3 μm), and an on-substrate array of nanopillars with the same pitch. (d,e) Simulated charge density over the surface of a single, free-standing nanopillar corresponding to Sample B at (d) 859 cm^{-1} and (e) 908 cm^{-1}.

demonstrated. It is shown that the spectral locations of the transverse quadrupole and octupole do not change with increasing the height of the nanopillars, while the longitudinal monopole and transverse dipole modes of the nanopillars are redshifted as their height increases. Our measured spectra show that near-field thermal emission from nanostructures can be very different from the one for flat surfaces and that the near-field spectra can be modulated by engineering the materials at the sub-wavelength scale.

3.5. Acknowledgments

This work is financially supported by the National Science Foundation under Grant No. CBET-1804360.

3.6. References

[1] R. DiMatteo, P. Greiff, S. Finberg, K. Young-Waithe, H. Choy, M. Masaki, and C. Fonstad, Appl. Phys. Lett. 79, 1894 (2001).

[2] C. Lucchesi, D. Cakiroglu, J. Perez, T. Taliercio, E. Tournié, P. Chapuis, and R. Vaillon, Nano Lett. 21, 4524 (2021).

[3] L. Zhu, A. Fiorino, D. Thompson, R. Mittapally, E. Meyhofer, and P. Reddy, Nature 566, 239 (2019).

[4] B. Guha, C. Otey, C. Poitras, S. Fan, and M. Lipson, Nano Lett. 12, 4546 (2012).

[5] K. Chen, P. Santhanam, and S. Fan, Phys. Rev. Appl. 6, 024014 (2016).

[6] C. Otey, W. Lau, and S. Fan, Phys. Rev. Lett. 104, 154301 (2010).

[7] A. Fiorino, D. Thompson, L. Zhu, R. Mittapally, S. Biehs, O. Bezencenet, N. El-Bondry, S. Bansropun, P. Ben-Abdallah, E. Meyhofer, and P. Reddy, ACS Nano 12, 5774 (2018).

[8] P. Ben-Abdallah, K. Joulain, and A. Pryamikov, Appl. Phys. Lett. 96, 143117 (2010).

[9] M. Francoeur, S. Basu, and S. Petersen, Optics Express 19, 18774 (2011).

[10] A. Rodriguez, O. Ilic, P. Bermel, I. Celanovic, J. Joannopoulos, M. Soljačić, and S. Johnson, Phys. Rev. Lett. 107, 114302 (2011).

[11] S. Biehs, M. Tschikin, and P. Ben-Abdallah, Phys. Rev. Lett. 109, 104301 (2012).

[12] R. Guérout, J. Lussange, F. Rosa, J. Hugonin, D. Dalvit, J. Greffet, A. Lambrecht, and S. Reynaud, Phys. Rev. B 85, 180301 (2012).

[13] X. Liu, R. Zhang, and Z. Zhang, Int. J. Heat Mass Transf. 73, 389 (2014).

[14] X. Liu and Z. Zhang, Appl. Phys. Lett. 104, 251911 (2014).

[15] Y. Bai, Y. Jiang, and L. Liu, J. Quant. Spectrosc. Radiat. Transf. 158, 61 (2015).

[16] S. Basu, Y. Yang, and L. Wang, Appl. Phys. Lett. 106, 033106 (2015).

[17] A. Didari and M. Mengüç, Optics Express 23, A1253 (2015).

[18] M. Tschikin, S. Biehs, P. Ben-Abdallah, S. Lang, A. Petrov, and M. Eich, J Quant. Spectrosc. Radiat. Transf. 158, 17 (2015).

[19] N. Zhou and X. Xu, J Quant. Spectrosc. Radiat. Transf. 167, 156 (2015).

[20] S. Biehs and P. Ben-Abdallah, Zeitschrift für Naturforschung A 72, 115 (2016).

[21] J. Dai, S. Dyakov, S. Bozhevolnyi, and M. Yan, Phys. Rev. B 94, 125431 (2016).

[22] Y. Yang and L. Wang, Phys. Rev. Lett. 117, 044301 (2016).

[23] A. Didari, M. Mengüç, J Quant. Spectrosc. Radiat. Transf. 197, 95 (2017).

[24] V. Fernández-Hurtado, F. García-Vidal, S. Fan, and J. Cuevas, Phys. Rev. Lett. 118, 203901 (2017).

[25] K. Isobe, D. Hirashima, and K. Hanamura, Int. J. Heat Mass Transf. 115, 467 (2017).

[26] J. Watjen, X. Liu, B. Zhao, and Z. Zhang, J. Heat Transf. 139, 052704 (2017).

[27] Y. Yang, P. Sabbaghi, and L. Wang, Int. J. Heat Mass Transf. 108, 851 (2017).

[28] H. Yu, D. Liu, Z. Yang, and Y. Duan, Sci. Rep. 7, 1026 (2017).

[29] B. Zhao, B. Guizal, Z. Zhang, S. Fan, and M. Antezza, Phys. Rev. B 95, 245437 (2017).

[30] A. Didari, E. Elçioğlu, T. Okutucu-Özyurt, M. Mengüç, J. Quant. Spectrosc. Radiat. Transf. 212, 120 (2018).

[31] M. Elzouka and S. Ndao, J. Quant. Spectrosc. Radiat. Transf. 204, 56 (2018).

[32] T. Inoue, T. Asano, and S. Noda, Optics Express 26, 32074 (2018).

[33] H. Yu, Y. Duan, and Z. Yang, Int. J. Heat Mass Transf. 123, 67 (2018).

[34] K. Isobe and K. Hanamura, Int. J. Heat Mass Transf. 134, 807 (2019).

[35] Y. Kan, C. Zhao, and Z. Zhang, Phys. Rev. B 99, 035433 (2019).

[36] J. Song, Q. Cheng, L. Lu, B. Li, K. Zhou, B. Zhang, Z. Luo, and X. Zhou, Phys. Rev. Appl. 13, 024054 (2020).

[37] Y. Taniguchi, K. Isobe, and K. Hanamura, Appl. Therm. Eng. 183, 116041 (2021).

[38] S. Foteinopoulou, G. Devarapu, G. Subramania, S. Krishna, D. Wasserman, Nanophotonics 8, 2129 (2019).

[39] S. Zare and S. Edalatpour, Phys. Rev. B 101, 165424 (2020).

[40] T. Wang, P. Li, D. Chigrin, A. Giles, F. Bezares, O. Glembocki, J. Caldwell, and T. Taubner, ACS Photonics 4, 1753 (2017).

[41] A. Mancini, C. Gubbin, R. Berté, F. Martini, A. Politi, E. Cortés, Y. Li, S. De Liberato, and S. A. Maier, ACS Nano 14, 8508 (2020).

[42] X. Hu, T. Lo, A. Mancini, C. Gubbin, F. Martini, J. Zhang, Z. Gong, A. Politi, S. De Liberato, X. Zhang, D. Lei, S. A. Maier, Appl. Phys. Rev. 9, 021414 (2022).

[43] S. Zare, C. Tripp, and S. Edalatpour, Phys. Rev. B 100, 235450 (2019).

[44] M. T. H. Reid, Computing the Photonic Local Density of States with SCUFF-LDOS http://homerreid.github.io/scuff-em-documentation/applications/scuff-ldos/scuff-ldos/.

[45] M. Francoeur, M. Mengüç, and R. Vaillon, J. Quant. Spectrosc. Radiat. Transf. 110, 2002 (2009).

[46] M. T. H. Reid, Solving Electromagnetic Scattering Problems with SCUFF-SCATTER http://homerreid.github.io/scuff-em-documentation/applications/scuff-scatter/scuff-scatter/.

CHAPTER 4

VALIDITY OF THE EFFECTIVE MEDIUM THEORY FOR MODELING NEAR-FIELD THERMAL EMISSION BY NANOWIRE ARRAYS

This chapter has been reproduced from a previous publication in Journal of Quantitative Spectroscopy and Radiative Transfer: *S. Zare, R. Pouria, and S. Edalatpour, J. Quant. Spectrosc. Radiat. Transfer* ***261****, 107482 (2021).*

4.1. Abstract

Nanowire arrays are promising man-made materials for tuning the spectrum and the magnitude of near-field thermal radiation. Near-field radiative properties of nanowire arrays are often studied using the effective medium theory (EMT). In this paper, we inspect the validity of the Maxwell-Garnett (MG) and Bruggeman (BR) EMTs for predicting near-field thermal emission by quartz and indium tin oxide (ITO) nanowire arrays. The near-field energy density predicted using the EMTs is compared with numerical simulations obtained using the thermal discrete dipole approximation. For quartz nanowire arrays, which support localized surface phonons in the infrared region, neither MG nor BR EMT can accurately predict the spectrum and the magnitude of near-field thermal emission even at distances, z_o, greater than the array pitch, L over π. Based on the performed simulations, the EMT agrees the best with the T-DDA when $1 < \frac{L}{z_o} < \pi$. It is also shown that MG EMT is slightly more consistent with numerical simulations than the BR EMT. For the ITO array, which does not support localized surface plasmons in the infrared region, the MG EMT provides an acceptable estimations of near-field thermal radiation. Finally, it is observed that near-field emission can vary by a factor of two in lateral directions which cannot be captured in the EMT.

4.2. Introduction

Man-made materials engineered at the sub-wavelength scale (the dominant wavelength of thermal radiation at room temperature is about 10 μm) offer great potential for tuning the magnitude and the

spectrum of near-field thermal emission. A class of man-made materials that has attracted significant attention is nanowire arrays. Nanowire arrays can support hyperbolic modes resulting in a broadband enhancement of thermal emission as well as surface phonons resulting in sharp (narrow-band) peaks in the spectrum of the emitted energy. So far, near-field thermal emission by nanowire arrays has been mostly studied using the effective medium theory (EMT) [1-19]. In this theory, the nanowire array is modeled as an anisotropic (uniaxial), homogeneous film with effective parallel (to the optical axis which is along the nanowires axis) and perpendicular dielectric functions determined from those of the nanowires and the free space. Maxwell-Garnett (MG) [20-22] and Bruggeman (BR) [21-23] EMTs are used for determining the effective dielectric function. The EMT is assumed to be valid for in the long wavelength regime (i.e., when the nanowires and the array pitch are much smaller than the thermal wavelength in the free space) and at observation distances greater than the array pitch divided by π [1,11,13,15,18]. Although the validity of the EMT for modeling near-field thermal radiation of man-made materials such as multilayer media [24-33], gratings [34-38], nanoparticles on a flat surface [39-41], and nanoholes [42,43] has been investigated, the applicability of the EMT to nanowire arrays has not been thoroughly inspected. Mirmoosa et al. [44] studied the applicability of the EMT for modeling metallic nanowires and concluded that the EMT can be used qualitatively for predicting the magnitude of the radiative heat transfer. In this study, the transverse-magnetic (TM) polarized transfer function (instead of radiative heat transfer) was calculated using ANSYS HESS and compared with the EMT for a few frequencies and parallel components of the wavevector, k_ρ, smaller than the wavevector in the substrate. As such, the validity of the EMT for predicting near-field thermal emission integrated over all k_ρ modes and the near-field spectrum (and thus the location of the peaks and hyperbolic bands) was not analyzed. Yu et al. [43] studied how radiative heat transfer between a bulk Drude emitter and a bulk gallium antimonide (semiconductor) absorber is affected if the surface of the absorber is patterned into nanowires. It was found that the EMT can only qualitatively predict the spectral locations of the peaks in the radiative heat transfer, and it cannot provide an accurate estimation of the magnitude of heat transfer even when the

size of the nanowires is smaller than the wavelength. However, the validity of the EMT for modeling near-field thermal radiation of nanowire-array emitters made of dielectric and metallic materials is still unverified.

In this paper, the validity of the MG and BR EMTs for modeling near-field thermal emission by periodic arrays of quartz and indium tin oxide (ITO) nanowires is investigated by comparing these models against the thermal discrete dipole approximation (T-DDA) simulations. The T-DDA is a numerically exact solution of the Maxwell equations augmented by the thermally fluctuating current given by the fluctuation dissipation theorem [45]. Near-field emission by arrays with various filling factors, nanowire heights and diameters at different perpendicular and lateral observation distances is considered. Quartz nanowire arrays support both hyperbolic and surface phonon-polariton modes in the infrared portion of the electromagnetic spectrum, where these modes can be thermally excited. The ITO nanowires do not support surface plasmon-polariton and hyperbolic modes in the infrared region.

This paper is structured as follows. The problem under consideration, the MG and BR EMTs, and the T-DDA approach for modeling periodic arrays are presented in Sec. 4.3. The EMT results for the energy density are compared with the T-DDA simulations in Sec. 4.4, and the concluding remarks are provided in Sec. 4.5.

4.3. Near-Field Thermal Emission by Periodic Arrays of Nanowires

4.3.1. Description of the Problem

A schematic of the problem under consideration is shown in Fig. 4.1(a). A periodic array of nanowires is at temperature T and emits in the free space. The nanowires have a diameter of D, a height of H, and they are separated by a gap of size d such that the array has a pitch of $L = D + d$. The energy density thermally emitted by the array at observation point $\mathbf{r_o} = (x_o, y_o, z_o)$ is desired.

4.3.2. Effective Medium Theory

In the effective medium theory, the periodic array of the nanowires is modeled as a homogenous film with an anisotropic effective dielectric function as shown in Fig. 4.1(b). Two EMTs, namely Maxwell-Garnett

(MG) and Bruggeman (BR) EMTs, are commonly used for finding the effective dielectric function of the homogenized thin film.

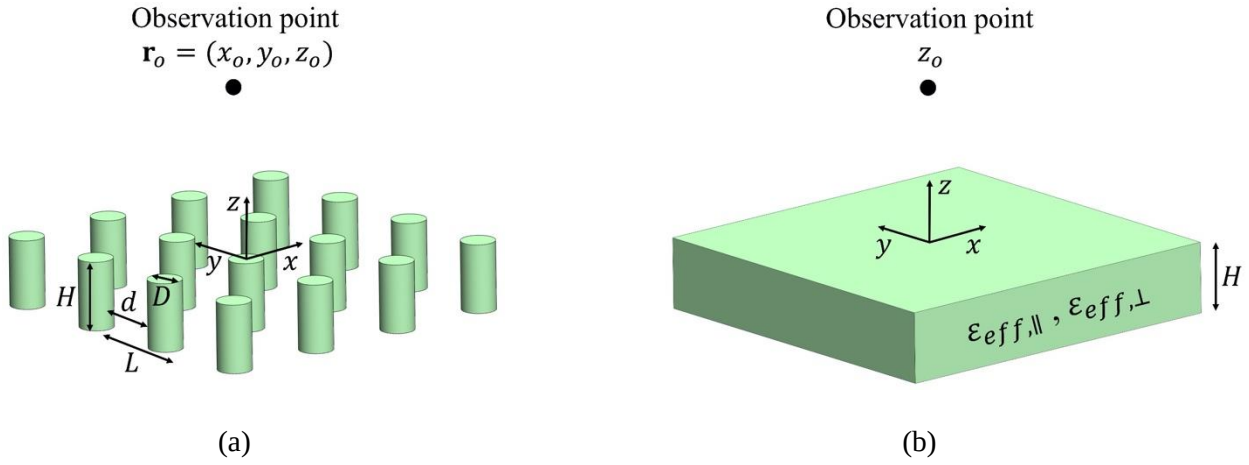

(a) (b)

Figure 4.1 – (a) A periodic array of nanowires with diameter D, height H, and interwire distance d thermally emits in the free space. (b) In the EMT, the array is modeled as a homogeneous thin film with height H and effective parallel and perpendicular dielectric functions $\varepsilon_{eff,\parallel}$ and $\varepsilon_{eff,\perp}$, respectively.

The MG EMT is derived by assuming the nanowires as single dipoles. This assumption is valid only in the quasi-static regime, i.e., when the nanowires are much smaller than the wavelength in the free space, the wavelength in the nanowires, the interwire spacing, and the observation distance. Then, the total dipole moment of the array due to illumination of an external field, $\mathbf{E}^{ext}$, is obtained by summing up the dipole moment of the individual nanowires, i.e.,

$$\mathbf{p}_{\alpha}^{tot} = N_w \alpha_{w,\alpha} \mathbf{E}^{ext} \tag{4.1}$$

where the subscript α refers to the direction (α = ∥ or ⊥) with respect to the optical axis of the nanowire array, $\mathbf{p}_{\alpha}^{tot}$ is the total dipole moment of the array in direction α, N_w is the number of the nanowires in the array, and $\alpha_{w,\alpha}$ is the nanowire polarizability in direction α [22]. Equation (4.1) is obtained by assuming that the external incident field is the same for all nanowires. This assumption is only valid in the long-wavelength regime (i.e., when $L \ll \lambda_v$ with λ_v being the wavelength in the free space) where it can be

assumed that the phase of the external field remains constant. An effective electric susceptibility, $\chi_{eff,\alpha}$, can be assigned to the nanowire array and is found as [46]:

$$\chi_{eff,\alpha} = \frac{\mathbf{p}_{\alpha}^{tot}/V}{\mathbf{E}_{\alpha}^{in}} \tag{4.2}$$

where V is the volume of the array, $\mathbf{p}_{\alpha}^{tot}/V$ is the average electric polarization of the array, and $\mathbf{E}_{\alpha}^{in}$ is the average electric field inside the array. Substituting Eq. (4.2) into Eq. (4.1) results in:

$$\chi_{eff,\alpha} = \frac{\alpha_{w,\alpha}}{V_{uc}} \frac{\mathbf{E}^{ext}}{\mathbf{E}_{\alpha}^{in}} \tag{4.3}$$

where $V_{uc} = V/N_w$ is the volume of the unit cell of the array. For finding the effective susceptibility of the array using Eq. (4.3), a relation between the external and internal fields should be established. Assuming negligible interactions between the nanowires, the electric field inside the array is given by [22]:

$$\mathbf{E}_{\alpha}^{in} = \left(1 - \frac{4\pi g_{\alpha}}{\varepsilon_v} \frac{\alpha_{w,\alpha}}{V_{uc}}\right) \mathbf{E}^{ext} \tag{4.4}$$

where $\varepsilon_v = 1$ is the dielectric function of the free space, and g_{α} is the geometry-dependent depolarization factor for cylindrical nanowires in direction α. The depolarization factor g_{α} in Eq. (4.4) can be calculated as [47]:

$$g_{\perp} = \frac{1}{2}\cos\theta - i\frac{k_v^3}{6\pi} V_w \tag{4.5a}$$

$$g_{\parallel} = 1 - \cos\theta - \frac{k_v^2}{6\pi} V_w C_z - i\frac{k_v^3}{6\pi} V_w \tag{4.5b}$$

where i is the imaginary unit, k_v is the magnitude of the wavevector in the free space, $\theta = \tan^{-1}(D/H)$, $V_w = \pi H D^2/4$ is the volume of a nanowire, and $C_z = \frac{3}{2H} ln\left|\frac{1+E}{1-E}\right|$ with $E = 1 + \left(\frac{D}{H}\right)^2$ [47].

Equation (4.4) is only valid for very dilute arrays as it is obtained by assuming negligible interaction between nanowires. Using Eq. (4.4) and substituting for the polarizability of the nanowires ($\alpha_{w,\alpha} =$

$\frac{vV_w}{4\pi}\frac{\varepsilon_v(\varepsilon_w-\varepsilon_v)}{\varepsilon_v+g_\alpha(\varepsilon_w-\varepsilon_v)}$, where ε_w is the dielectric function of the nanowires [22]), the effective susceptibility of the array in Eq. (4.3) can be written as:

$$\chi_{eff,\alpha} = \frac{1}{4\pi}\frac{f\varepsilon_v\left(\varepsilon_w-\varepsilon_v\right)}{\varepsilon_v+g_\alpha\left(1-f\right)\left(\varepsilon_w-\varepsilon_v\right)} \tag{4.6}$$

The parameter f in Eq. (4.6) is the filling factor of the array given by $f=\frac{V_w}{V_{uc}}$. The effective dielectric function of the array is related to the susceptibility as $\varepsilon_{eff,\alpha}=\varepsilon_v+4\pi\chi_{eff,\alpha}$ [46]; thus, the effective dielectric function can be found as:

$$\varepsilon_{eff,\alpha} = \varepsilon_v + f\frac{\varepsilon_v\left(\varepsilon_w-\varepsilon_v\right)}{\varepsilon_v+g_\alpha\left(1-f\right)\left(\varepsilon_w-\varepsilon_v\right)} \tag{4.7}$$

Equation (4.7) is referred to as the MG EMT. The MG EMT suffers from the shortcoming that it is not symmetric with respect to the inclusions and the host medium [21,22]. In other words, if the array is assumed as free-space holes in a host medium made of the same material as the nanowires, a different effective dielectric function is found compared to the case where nanowires are assumed as inclusions in a free-space host medium. This asymmetry of the effective dielectric function is particularly drastic when the difference between the filling factors or the dielectric functions of the two media is large [21,22].

In the BR EMT, the nanowires and the free-space medium are treated in a symmetrical manner. However, this does not mean that the BR EMT is more accurate the MG EMT [22]. The BR EMT is obtained by embedding the nanowire array in an infinite medium with the same dielectric function as the effective film. If the infinite medium and the nanowire array have the same dielectric function, the polarization of the nanowire array should be zero. The BR formula can be obtained by replacing the dielectric function of the host medium in the generalized MG formula (i.e., the formula generalized to account for more than one inclusion) by the effective dielectric function [21,22]:

$$f\frac{\varepsilon_w-\varepsilon_{eff,\alpha}}{\varepsilon_{eff,\alpha}+g_\alpha\left(\varepsilon_w-\varepsilon_{eff,\alpha}\right)}+(1-f)\frac{\varepsilon_v-\varepsilon_{eff,\alpha}}{\varepsilon_{eff,\alpha}+g_a\left(\varepsilon_v-\varepsilon_{eff,\alpha}\right)}=0 \tag{4.8}$$

An explicit expression for the BR effective dielectric function cannot be obtained. In this case, Eq. (4.8) can be written as the following quadratic equation:

$$\left(1-g_\alpha\right)\varepsilon_{eff,\alpha}^2+\left[\left(g_\alpha-f\right)\varepsilon_w-\left(1-f-g_\alpha\right)\right]\varepsilon_{eff,\alpha}-g_\alpha\varepsilon_w=0 \tag{4.9}$$

The solution of Eq. (4.9) that results in a non-negative value for the imaginary part of $\varepsilon_{eff,\alpha}$ is selected as the effective dielectric function.

Once the effective dielectric function is found, the energy density, u, emitted by the anisotropic thin film can be calculated at distance z_o above the film in the free space as [48]:

$$u\left(\omega,T\right)=\frac{\Theta\left(\omega,T\right)}{4\pi^2\omega}\left(k_v^2\int_0^{k_v}\frac{k_\rho}{\left|k_{z,v}\right|}\sum_{\gamma=TE,TM}\left(1-\left|R^\gamma\right|^2-\left|T^\gamma\right|^2\right)dk_\rho+2\int_{k_v}^{\infty}\frac{k_\rho^3}{\left|k_{z,v}\right|}\sum_{\gamma=TE,TM}\mathrm{Im}\left[R^\gamma\right]e^{-2\left|k_{z,v}\right|z_o}dk_\rho\right) \tag{4.10}$$

where ω is the angular frequency, Θ is the mean energy of an electromagnetic state, k_ρ is the parallel (to the film interface) component of the wavevector, and $k_{z,v}$ is the perpendicular component of the wavevector in the free space. In Eq. (4.10), R^γ and T^γ represent the reflection and transmission coefficients of the film for γ-polarization (γ = transverse electric (TE) or magnetic (TM)), respectively, and are calculated as [49]:

$$R^\gamma=\frac{r_{vf}^\gamma+r_{fv}^\gamma e^{2iHk_{z,f}^\gamma}}{1+r_{vf}^\gamma r_{fv}^\gamma e^{2iHk_{z,f}^\gamma}} \tag{4.11a}$$

$$T^\gamma=\frac{t_{vf}^\gamma t_{fv}^\gamma e^{iHk_{z,f}^\gamma}}{1+r_{vf}^\gamma r_{fv}^\gamma e^{2iHk_{z,f}^\gamma}} \tag{4.11b}$$

where the subscript f and v correspond to the film and the free space, respectively, and $k_{z,f}^\gamma$ is the perpendicular component of the wavevector in the film for γ-polarization which is given by [25]:

$$k_{z,f}^{TE}=\sqrt{\varepsilon_{eff,\perp}k_v^2-k_\rho^2} \tag{4.12a}$$

$$k_{z,f}^{TM}=\sqrt{\varepsilon_{eff,\perp}k_v^2-\frac{\varepsilon_{eff,\perp}}{\varepsilon_{eff,\parallel}}k_\rho^2} \tag{4.12b}$$

The parameters r_{ij}^{γ} and t_{ij}^{γ} in Eq. (4.11) are respectively the Fresnel reflection and transmission coefficients at the interface of layers i and j for γ-polarization. The Fresnel coefficients are given by [25]:

$$r_{ij}^{TE} = \frac{k_{z,i}^{TE} - k_{z,j}^{TE}}{k_{z,i}^{TE} + k_{z,j}^{TE}} \tag{4.13a}$$

$$r_{ij}^{TM} = \frac{\varepsilon_{j,\perp} k_{z,i}^{TM} - \varepsilon_{i,\perp} k_{z,j}^{TM}}{\varepsilon_{j,\perp} k_{z,i}^{TM} + \varepsilon_{i,\perp} k_{z,j}^{TM}} \tag{4.13b}$$

$$t_{ij}^{TE} = \frac{2k_{z,i}^{TE}}{k_{z,i}^{TE} + k_{z,j}^{TE}} \tag{4.13c}$$

$$t_{ij}^{TM} = \frac{2\varepsilon_{j,\perp} k_{z,i}^{TM}}{\varepsilon_{j,\perp} k_{z,i}^{TM} + \varepsilon_{i,\perp} k_{z,j}^{TM}} \sqrt{\frac{\varepsilon_{j,\perp}}{\varepsilon_{j,\parallel}}} \tag{4.13d}$$

It should be noted that the free space is an isotropic medium, and thus $\varepsilon_{v,\perp} = \varepsilon_{v,\parallel} = \varepsilon_v$ and $k_{z,v}^{TE} = k_{z,v}^{TM} = k_{z,v}$.

4.3.3. Thermal Discrete Dipole Approximation

Numerical simulations of thermal emission by the nanowire array is done using the periodic thermal discrete dipole approximation (T-DDA) [50-52]. The periodic T-DDA requires discretizing only one period of the array, and thus is computationally practicable. In this method, a nanowire, referred to as the unit cell, is discretized into N cubical sub-volumes. The sub-volumes should be much smaller than the nanowires (D and H), their separation distance (d), the observation distance (z_o), and the wavelength (λ). In this case, the variation of the electric field within the sub-volumes is negligible such that the sub-volumes behave as electric point dipoles. The array can be constructed by replicating the unit cell along the x- and y-directions. The replicas of the unit cell are numbered as (m, n), where m and n show the row and the column number of a replica, respectively. The energy density at the observation point $\mathbf{r}_o$ due to thermal emission by the nanowire array can be calculated using the electric and magnetic dyadic Green's functions of the array as [52]:

$$u(\mathbf{r}_o,\omega)=\frac{2k_v^2}{\pi\omega}\sum_{j=1}^{N}V_j\varepsilon''\Theta(\omega,T)\sum_{m=0}^{N_{kx}}\sum_{n=0}^{N_{ky}}Trace\left[k_v^2\mathbf{G}^E_{jmn,o}\otimes\mathbf{G}^E_{jmn,o}+\mathbf{G}^H_{jmn,o}\otimes\mathbf{G}^H_{jmn,o}\right] \tag{4.14}$$

where V_j is the volume of sub-volume j, ε'' is the imaginary part of the dielectric function of the nanowires, $\otimes$ is the outer product, $N_{k\beta}$ ($\beta = x, y$) is the number of mathematical wave vectors selected for discretizing the Brillouin zone along β-direction, the subscript o refers to the observation point, and the subscript jmn refers to replica (m,n) of the sub-volume j in the unit cell. Additionally, $\mathbf{G}^{E(H)}_{jmn,o}$ represents the dyadic electric (magnetic) Green's function of the array which relates the electric (magnetic) field at the observation point $\mathbf{r}_o$ to the thermally generated fluctuating current at sub-volume jmn. The dyadic Green's function of the array can be obtained by integrating the wavevector-dependent Green's function over the Brillouin zone as [52]:

$$\mathbf{G}^E_{jmn,o}=\frac{L^2}{(2\pi)^2}\int_{-\frac{\pi}{L}}^{\frac{\pi}{L}}\int_{-\frac{\pi}{L}}^{\frac{\pi}{L}}\mathbf{g}^{\xi}_{jmn,o}\left(k_x,k_y\right)dk_y dk_x\,, \qquad \xi = E \text{ or } H \tag{4.15}$$

where $\mathbf{g}^{\xi}_{jmn,o}$ is the wavevector-dependent Green's function of the array between sub-volume jmn and the observation point. The Green's function $\mathbf{g}^{\xi}_{jmn,o}$ is only phase shifted relative to $\mathbf{g}^{\xi}_{j00,o}$. As such, $\mathbf{g}^{\xi}_{jmn,o}$ can be related to $\mathbf{g}^{\xi}_{j00,o}$ as [52]:

$$\mathbf{g}^{\xi}_{jmn,o}=\mathbf{g}^{\xi}_{j00,o}e^{i\left(mLk_x+nLk_y\right)}, \qquad m,n=0,\pm1,\pm2,\ldots,\ j=1,2,3,\ldots,N \tag{4.16}$$

where $\mathbf{g}^{\xi}_{j00,o}$ is found by solving the following system of equations [52]:

$$\frac{1}{\alpha_j}V_j\varepsilon_v\left(\varepsilon-1\right)\mathbf{g}^{\xi}_{j00,o}-k_v^2\sum_{l=1}^{N}V_l\left(\varepsilon-1\right)\mathbf{G}^{0E,P}_{j,l}\cdot\mathbf{g}^{\xi}_{l00,o}=\mathbf{G}^{0\xi,P}_{j,o},\ j=1,2,3,\ldots,N \tag{4.17}$$

where α_j is the polarizability of sub-volume j, ε_v is the free space permittivity, and $\mathbf{G}^{0\xi,P}_{j,l}$ represents the periodic free-space dyadic Green's function between sub-volume j in the unit cell and point l (where l refers to either the observation point or a sub-volume in the unit cell). The periodic free-space dyadic Green's function between j and l, $\mathbf{G}^{0\xi,P}_{j,l}$, is defined as [53]:

$$\mathbf{G}_{j,l}^{0\xi,P} = \sum_{m=-\infty}^{\infty} \sum_{n=-\infty}^{\infty} G_{j00,lmn}^{0\xi} e^{i\left(mLk_x + nLk_y\right)} \tag{4.18}$$

In Eq. (4.18), $\mathbf{G}_{j00,lmn}^{0\xi}$ is the free-space dyadic Green's function between sub-volume j in the unit cell and the point lmn (i.e., the replica (m,n) of point l). By substituting Eq. (4.18) into Eq. (4.17) and solving the system of equations, $\mathbf{g}_{j00,o}^{\xi}$ is found. Then, using $\mathbf{g}_{j00,o}^{\xi}$ and Eqs. (4.14)-(4.15), the energy density emitted by the periodic array of nanowires is calculated.

4.4. Results

Thermal emission by periodic arrays of quartz and ITO nanowires is considered. Based on the EMT, quartz nanowires support both surface and hyperbolic modes, while thermal emission by ITO nanowires does not exhibit any resonances. The non-approximate simulations of the energy density are done using the periodic T-DDA, and the results are compared with those predicted by MG and BR EMTs. The periodic T-DDA and the EMT results are compared for different perpendicular and lateral observation distances, filling factors, and nanowire heights and diameters.

4.4.1. Comparison of the EMT with the T-DDA for Various Perpendicular Observation Distances and Filling Factors

The energy density emitted by three arrays of quartz nanowires is considered. The arrays all have a diameter D of 100 nm and a height H of 20 nm, while they have different nanowire spacings. The nanowires are separated by a distance d of 200 nm in the first array, 62 nm in the second array, and 20 nm in the third one. The filling factor f of these arrays is 0.09, 0.30, and 0.55, respectively, such that they correspond to a dilute, a medium-density, and a dense array. The energy density for each array is calculated at three perpendicular observation distances z_o of 20 nm ($L/z_o > \pi$), 100 nm ($L/z_o < \pi$), and 500 nm ($L/z_o \ll \pi$) above the array on the central axis of the nanowires (i.e., at $x_o = y_o = 0$). The arrays are emitting at a temperature T of 400 K.

The energy density emitted by the array with f = 0.09 is shown in Fig. 4.2(a). The real part of the effective dielectric function of the array in the parallel ($\varepsilon'_{eff,\parallel}$) and perpendicular ($\varepsilon'_{eff,\perp}$) directions as

predicted using the MG and BR EMTs is also shown in Fig. 4.2(b). As it is seen from Fig. 4.2(b), the MG and BR EMTs predict different values for $\varepsilon'_{eff,\parallel}$ in the spectral band of 1000 – 1141 cm^{-1} and for $\varepsilon'_{eff,\perp}$ in the spectral band of 1168 – 1244 cm^{-1}, where quartz has metallic behavior ($\varepsilon' < 0$). Based on the MG EMT, the array has a hyperbolic band ($\varepsilon'_{eff,\parallel} \cdot \varepsilon'_{eff,\perp} < 0$) at 1101 – 1122 cm^{-1}, while the BR EMT does not predict any hyperbolic thermal emission for the array. The energy densities predicted by the MG and BR EMTs do not agree in the spectral band of 1000 – 1222 cm^{-1}. Neither of EMTs can accurately predict the magnitude and the spectrum of the energy density. The EMT models underestimate the total (spectrally-integrated) energy density by a factor of ~7 at z_o = 20 nm and a factor of ~2.6 at z_o = 100 nm, while they overestimate the energy density at z_o = 500 nm by a factor of ~1.4. The spectrum of the energy density as predicted using the EMT has several peaks, and it remains almost the same when the observation distance increases from 20 nm to 500 nm. The energy density emitted by the effective film is dominated by the contribution of transverse-magnetic (TM) polarized electromagnetic waves, and it resonantly increases when $\mathrm{Im}[r^{TM}]$ is maximum. In the quasistatic limit (i.e., when $k_\rho \gg k_0$), $\mathrm{Im}\left[r^{TM} \right] \approx 2\,\mathrm{Im}\left[\varepsilon_{eff,\parallel} \sqrt{\varepsilon^*_{eff,\parallel} / \varepsilon^*_{eff,\perp}} \right] / \left| \varepsilon_{eff,\parallel} + \sqrt{\varepsilon_{eff,\parallel} / \varepsilon_{eff,\perp}} \right|^2$. Peaks in the EMT energy density are observed at wavenumbers for which $\mathrm{Im}\left[\varepsilon_{eff,\parallel} \sqrt{\varepsilon^*_{eff,\parallel} / \varepsilon^*_{eff,\perp}} \right]$ has local maxima or when $\varepsilon_{eff,\parallel} \to -\sqrt{\varepsilon_{eff,\parallel} / \varepsilon_{eff,\perp}}$. The peaks at 697, 801, 1163, and 1225 cm^{-1} in the MG and BR EMT spectra are due to the former condition, while the high energy density around 1110 cm^{-1} in the MG spectrum is due to hyperbolic thermal emission in the spectral range of 1101 – 1122 cm^{-1}.

Unlike the EMT, the T-DDA predicts distance-dependent spectra for the energy density. At z_o = 20 nm, the T-DDA spectrum of the energy density is almost the same as that for a single nanowire. This is because the observation distance is much smaller than the array pitch ($L/z_o = 15$) such that the energy density is mostly dominated by the contribution of the single nanowire located directly below the observation point. Also, thermal emission by the single nanowire is very similar to that for a thin film of quartz (rather than a film with effective dielectric function) with a thickness equal to the height of the

array except for in the spectral range of 1090-1153 cm^{-1} where the dipole mode of the nanowire resonantly emits. The nanowire below the observation point acts similar to a thin film since its diameter is much greater than the observation distance ($D/z_o = 5$). The peaks in the T-DDA energy density are located at 699, 807, 1110, 1153, 1181, and 1197 cm^{-1}. These peaks except for the one at 1110 cm^{-1} can be accurately predicted by modeling the wire as a thin film of quartz. The peak at 1110 cm^{-1} is associated with the dipole mode of the nanowire. The nanowire can be modeled as an oblate spheroidal dipole with semi-axes equal to 50 nm ($D/2$) and 10 nm ($H/2$). Thermal emission by the nanowire is proportional to the imaginary part of the polarizability of the spheroidal dipole given by $\mathrm{Im}\left[\alpha_j\right] = \varepsilon_v V \varepsilon'' / \left|1 + L_j\left(\varepsilon - 1\right)\right|^2$ where L_j is the geometrical factor of the spheroid along j-direction ($j = x, y, z$) [54]. When $\varepsilon = \left(L_j - 1\right)/L_j$, $\mathrm{Im}\left[\alpha_j\right] \to \infty$ and thermal emission by the dipole resonantly increases due to the excitation of localized surface phonons (LSPhs). The peak at 1110 cm^{-1} is associated with the resonant polarizability along the *x*- and *y*-directions. At z_o = 100 nm, the energy density is still similar to that for a single nanowire since L/z_o is large ($L/z_o = 3$). However, the nanowire cannot be considered as a film of quartz anymore as D and z_o are comparable ($D/z_o = 1$). At z_o = 500 nm, where the distance is greater than the pitch size of the array ($L/z_o = 0.6$), the cumulative effect of the nanowires becomes significant such that the spectrum of the energy density cannot be predicted using the one for a single nanowire anymore. In this case, the energy density by the array is about an order of magnitude larger than that for a single nanowire. Figure 4.2(a) shows that none of the EMTs can accurately model the cumulative thermal emission by the nanowires, even though it is assumed that the EMT is valid when $L/z_o < \pi$. The EMTs significantly overestimate the energy density at z_o = 500 nm. Among the two EMTs, the MG EMT spectrum agrees more with the T-DDA at z_o = 500 nm. Nevertheless, the difference between the MG EMT and the T-DDA is non-negligible. It should also be mentioned that the hyperbolic thermal emission in the spectral band of 1101 – 1122 cm^{-1} which is predicted by the MG EMT is not observed in the T-DDA energy density. Instead, the T-DDA energy density in this spectral band peaks at 1110 cm^{-1} due to the excitation of the LSPhs.

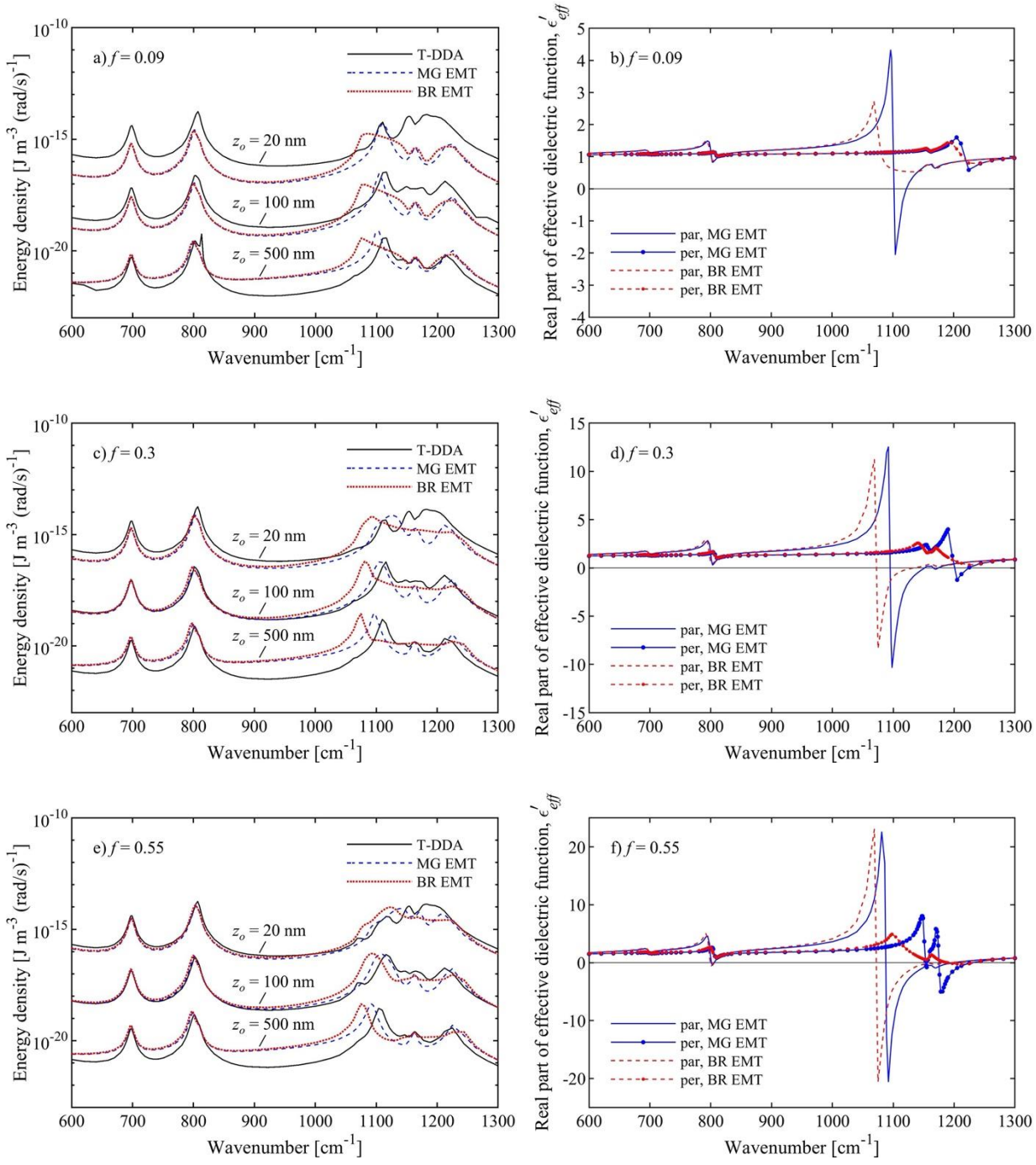

Figure 4.2 - Energy density and the real part of the effective dielectric function for arrays of quartz nanowires with D = 100 nm, H = 20 nm, and three filling factors of f = 0.09, 0.30, and 0.55. The arrays emit at 400 K.

The EMT is compared with the T-DDA for a larger filling factor of f = 0.30 in Fig. 4.2(c). The real part of the effective dielectric function in the parallel and perpendicular directions predicted by the MG and BR EMTs is shown in Fig. 4.2(d). Based on the MG EMT, the array has two wide hyperbolic bands at 1095 – 1151 cm^{-1} and 1200 – 1225 cm^{-1}. The BR EMT predicts one hyperbolic band at 1072 – 1133 cm^{-1}. The T-DDA energy density at z_o = 20 nm is still very similar to a single nanowire since the observation distance is much smaller than the array pitch (L/z_o = 8.1). The MG EMT energy density at z_o = 20 nm shows a broadband hyperbolic thermal emission around 1127 cm^{-1}, while the BR EMT displays a hyperbolic emission around 1092 cm^{-1}. This disagrees with the T-DDA energy density at z_o = 20 nm where thermal emission is dominated by the contribution of the LSPh mode of the single nanowire in this spectral band. At z_o = 100 nm (L/z_o = 1.6) and 500 nm (L/z_o = 0.3), the T-DDA energy density deviates from that for the single nanowire. At these two distances, the cumulative thermal emission by the nanowires enhances the energy density particularly at the LSPh resonance wavenumber. The cumulative thermal emission at z_o = 100 nm is captured well using the MG EMT expect for in the spectral band of 1000 – 1244 cm^{-1} where quartz has mostly metallic behavior. The MG EMT does not agree with the T-DDA at z_o = 500 nm as for the case with f = 0.09. It should also be mentioned that the EMT spectra do not show broadband emissions at z_o = 100 nm and 500 nm since the number of contributing hyperbolic modes decreases with the distance as z_o^{-2} [1].

The filling factor of the array is further increased to f = 0.55 in Fig. 4.2(e). The real part of the effective dielectric function predicted using the MG and BR EMTs is shown in Fig. 4.2(f). The T-DDA energy density at z_o = 20 nm (L/z_o = 6) does not vary significantly with increasing the filling factor, and it is still very similar to that for a single nanowire. The BR EMT has a broad hyperbolic band from 1072 cm^{-1} to 1230 cm^{-1} resulting in a broadband thermal emission at this spectral region. The MG EMT has three hyperbolic bands causing enhanced thermal emission around 1142 cm^{-1}, 1170 cm^{-1} and 1205 cm^{-1}. This is while the T-DDA energy density at z_o = 20 nm, which is dominated by the contribution of only one nanowire, does not show any hyperbolic emission. At z_o = 100 nm (L/z_o = 1.2) and 500 nm (L/z_o =

0.24), the T-DDA energy density is significantly affected by the collective contribution of the nanowires such that the energy density increases by factors of 2.2 and 40.2, respectively, relative to the one for a single nanowire at the same distance. Similar to the case of f = 0.30, the MG EMT agrees the most with the T-DDA at z_o = 100 nm while deviating significantly from the T-DDA for z_o = 500 nm.

4.4.2. Effect of Height

The validity of the EMT is tested against the T-DDA for quartz nanowires of greater height in this sub-section. The nanowires height is increased by one order of magnitude from 20 nm to 200 nm, while the diameter of the nanowires is kept at 100 nm. The energy density emitted by an array with $f = 0.3$ ($d = 62$ nm) is shown in Fig. 4.3(a) for two observation distances of $z_o = 100$ nm ($L/z_o = 1.6$) and 500 nm ($L/z_o = 0.3$). The real part of the effective dielectric function of the array is also shown in Fig. 4.3(b). The BR EMT predicts a hyperbolic band of 1075 cm^{-1} – 1133 cm^{-1} for the array, while the array has two hyperbolic bands at 1098 cm^{-1} – 1147 cm^{-1} and 1176 cm^{-1} – 1197 cm^{-1} based on the MG EMT. Single nanowires of the same height and diameter support a sharp LSPh peak at 1110 cm^{-1}. However, this peak is not observed in the T-DDA energy density of the array. Instead, the T-DDA energy density shows a broadband behavior around this wavenumber at z_o = 100 nm and does not show any enhancement at z_o = 500 nm (the contribution of hyperbolic modes decays with distance as z_o^{-2}). Comparing the EMT and T-DDA energy densities in Fig. 4.3(a), the same conclusions as for the array with H = 20 nm can be made about the accuracy of the EMT. The MG EMT agrees more with the T-DDA than BR EMT. The best agreement is obtained for z_o = 100 nm ($L/z_o = 1.6$), and both EMTs greatly overestimate thermal emission at z_o = 500 nm ($L/z_o = 0.3$).

4.4.3. Effect of Lateral Observation Distance

In the EMT, it is assumed that the energy density emitted by the array is uniform along the *x*- and *y*-directions. To verify this assumption, the energy density emitted by an array of quartz nanowires with $D = 100$ nm, H = 200 nm, and f = 0.30 at a distance of z_o = 100 nm (for which the EMT agrees the most

with the T-DDA) is calculated at three values of x_o equal to 0 nm, 50 nm, and 81 nm using the T-DDA. The T-DDA results are compared to the MG and BR EMT predictions in Fig. 4.4. The simulations are done for y_o = 0. It is seen from the T-DDA simulations that the locations of the peaks in the energy density spectra remain the same as x_o increases. However, the hyperbolic emission around 1110 cm^{-1} decreases with increasing x_o. Additionally, the magnitude of the energy density decreases by a factor of 2 as x_o increases from 0 nm to 81 nm. Clearly, these effects are not captured in the EMT energy density.

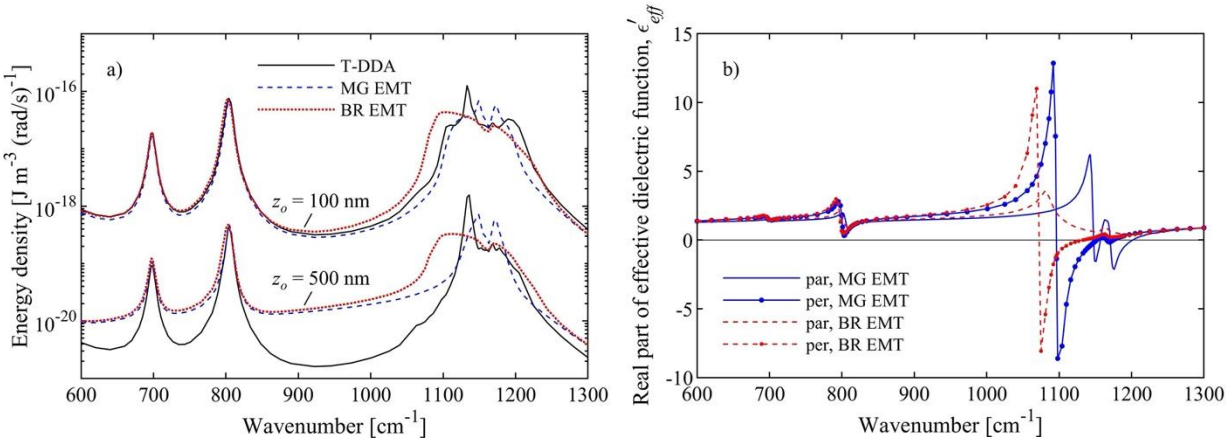

Figure 4.3 - (a) Energy density emitted by an array of quartz nanowires with D = 100 nm, H = 200 nm, and f = 0.30 at two observation distances z_o of 100 nm and 500 nm. (b) The real part of the effective dielectric function of the array as predicted by the MG and BR EMTs.

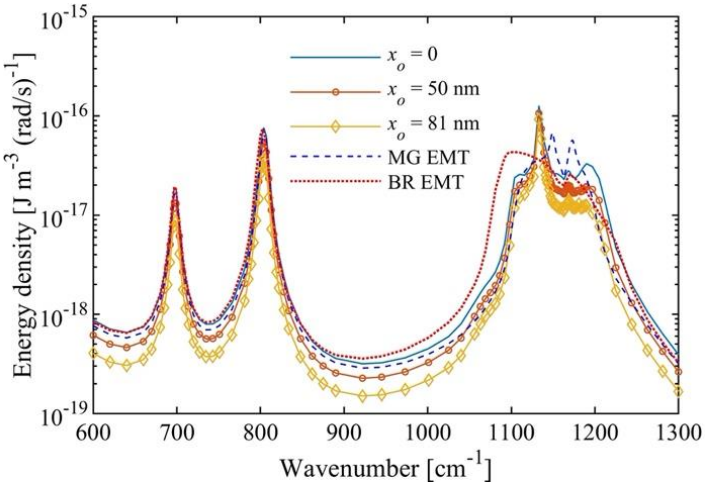

Figure 4.4 - Energy density emitted by an array of quartz nanowires with D = 100, H = 200 nm, and f = 0.30 at a distance z_o of 100 nm and three lateral distances x_o of 0 nm, 50 nm, and 81 nm. y_o = 0.

4.4.4. Effect of Diameter

In this sub-section, the validity of the EMT is tested for quartz nanowires of a smaller diameter. Figure 4.5 shows the spectral energy density emitted by an array of nanowires with diameter D = 20 nm, height H = 20 nm at distance z_o = 100 nm above the array. The array has a filling factor of f = 0.09 (d = 40 nm) in Fig. 4.5(a) and a filling factor of f = 0.30 (d = 12 nm) in Fig. 4.5(b). In both cases, $L/z_o \ll \pi$ such that the EMT is said to be valid. However, as it is seen from Fig. 4.5, none of the EMT models accurately predicts the magnitude and the spectrum of the energy density. The nanowires in Fig. 4.5(a) are much smaller than the thermal wavelength, the nanowire spacing as well as the observation distance such that the nanowires can be modeled as cylindrical dipoles. Even in this simple case, the EMT is not able to accurately model near-field thermal emission by the array.

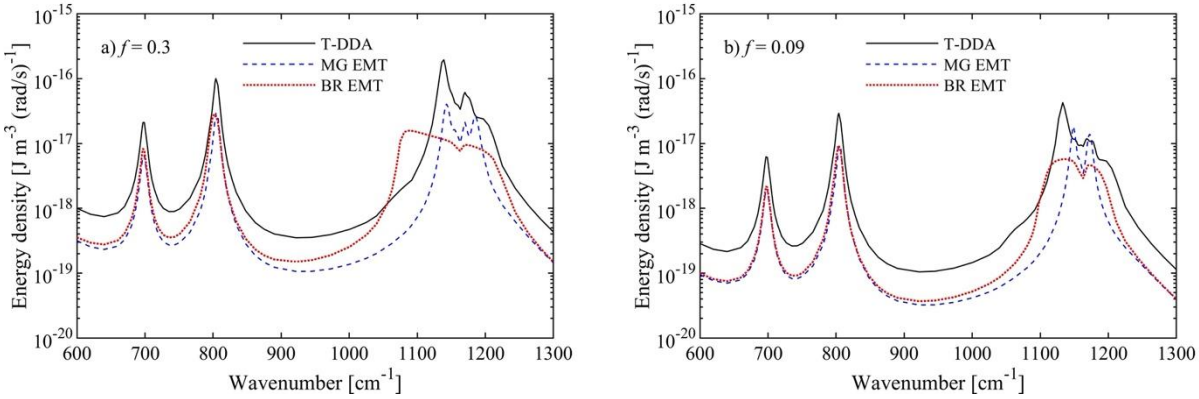

Figure 4.5 - The energy density emitted by arrays of quartz nanowires of diameter D = 20 nm and height H = 20 nm at an observation distance of z_o= 100 nm. The filling factor f is equal to 0.3 in Panel (a) and 0.09 in Panel (b).

4.4.5. Effect of Material

The validity of the EMTs for predicting near-field thermal emission by nanowire arrays made of a plasmonic material, namely ITO, is tested in this section. The nanowires have a diameter D = 100 nm and a height of H = 200 nm, and the filling factor of the array is f = 0.3. The dielectric function of the ITO is modeled using the Drude equation as $\varepsilon_{ITO} = \varepsilon_\infty - \omega_p^2/(\omega^2 + i\gamma\omega)$, where ε_∞ = 3.95, ω_p = 2 eV, and γ

= 0.11 eV. The energy density as computed using the T-DDA is compared with the EMTs results at an observation distances of z_o = 50 nm in Fig. 4.6(a) and z_o = 100 nm in Fig. 4.6(b). As it can be seen from these figures, the MG EMT provides acceptable estimation of the energy density particularly at shorter wavenumbers, while the BR EMT significantly overestimates (by up to an order of magnitude) thermal emission at shorter frequencies. Both EMTs converge to the same results at higher wavenumbers. Additionally, as the distance increases to z_o = 100 nm, the EMT results get closer to the T-DDA simulations. While the total energy density precited by the MG EMT at z_o = 50 nm is different from the T-DDA by 31%, the EMT results differ from the T-DDA solution only by 18%. This observation is consistent with previous findings that modeling resonant materials, such as quartz, using the EMTs is more challenging than non-resonant materials such as ITO [55,56].

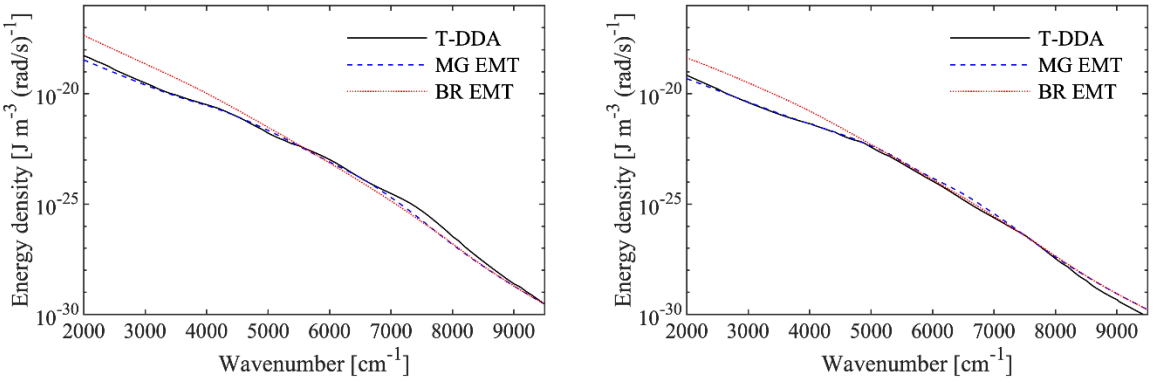

Figure 4.6 - The energy density emitted by an array of ITO nanowires of diameter D = 100 nm, height H = 200 nm, and filling factor f = 0.3 at an observation distance of (a) z_o= 50 nm and (b) z_o= 100.

4.5. Conclusions

The validity of the MG and BR EMTs for modeling near-field thermal emission by nanowire arrays was inspected. Near-field energy density emitted by various quartz nanowires was computed using the EMTs and was compared to numerical simulations using the T-DDA. It was concluded that the EMT cannot accurately predict the energy density magnitude and spectrum for quartz nanowires. Although it is

assumed that the EMT is valid when $\frac{L}{z_o} < \pi$, it was shown that this theory deviates significantly from the T-DDA when $\frac{L}{z_o} < 1$. Among the two theories, the MG EMT agrees the most with the T-DDA. The MG EMT predictions are closest to the T-DDA simulations when $1 < \frac{L}{z_o} < \pi$. For the ITO nanowires, which do not support any resonances in the infrared portion of the electromagnetic spectrum, the MG EMT provides an acceptable estimation of energy density. It was also shown that the EMTs cannot capture the variation of near-field thermal emission in lateral directions for any materials which can be very significant.

4.6. Acknowledgments

The authors acknowledge support from the National Science Foundation under Grant No. CBET-1804360.

4.7. References

[1] S. A. Biehs, M. Tschikin and P. Ben-Abdallah, Phys. Rev. Lett. 109, 104301 (2012).

[2] G. D'Aguanno, N. Mattiucci, A. Alù, C. Argyropoulos, J. V. Foreman, and M. J. Bloemer, Opt. Express 20, 9784 (2012).

[3] X. J. Wang, J. L. Abell, Y-P. Zhao and Z. M. Zhang, Appl. Opt. 51, 1521 (2012).

[4] S. Basu and L. Wang, Appl. Phys. Lett. 102, 053101 (2013).

[5] X. L. Liu, L. P. Wang and Z. M. Zhang, J. Heat Transf. 135, 061602 (2013).

[6] X. L. Liu, R. Z. Zhang and Z. M. Zhang, Appl. Phys. Lett. 103, 213102 (2013).

[7] C. Simovski, S. Maslovski, I. Nefedov and S. Tretyakov, Opt. Express 21, 14988 (2013).

[8] H. Wang, X. Liu, L. Wang and Z. M. Zhang, Int. J. Therm. Sci. 65, 62 (2013).

[9] S. Lang, M. Tschikin, S. A. Biehs, A. Y. Petrov and M. Eich, Appl. Phys. Lett. 104, 121903 (2014).

[10] X. L. Liu, R. Z. Zhang and Z. M. Zhang, Int. J. Heat Mass. Transf. 73, 389 (2014).

[11] X. L. Liu, R. Z. Zhang and Z. M. Zhang, ACS Photonics 1, 785 (2014).

[12] J. Y. Chang, S. Basu and L. Wang, J. Appl. Phys. 117, 054309 (2015).

[13] J. Y. Chang, Y. Yang and L. Wang, Int. Int. J. Heat Mass. Transf. 87, 237 (2015).

[14] R. Z. Zhang, X. Liu and Z. M. Zhang, AIP Adv. 5, 053501 (2015).

[15] X. J. Hong, J. W. Li, T. B. Wang, D. J. Zhang, W. X. Liu, Q. H., Liao, T. B. Yu and N. H. Liu, Jpn. J. Appl. Phys. 57, 045001 (2018).

[16] Z. Shen, H. Wu and H. Wang, Appl. Sci. 8, 2023 (2018).

[17] H. Wang, D. Qi and H. Wu, J. Photonics Energy 9, 015501 (2019).

[18] W. B. Zhang, C. Y. Zhao and B. X. Wang, Phys. Rev. B 100, 075425 (2019).

[19] J. Y. Chang , P. Sabbaghi, Y. S. Weng, Y. B. Chen and L. Wang, J. Heat Transfer 142(7) (2020).

[20] J. C. Maxwell-Garnett, Philos. Trans. R. Soc. Lond. B 203, 385 (1904).

[21] T. C. Choy, Effective Medium Theory: Principles and Applications 2 ed. (Oxford University Press, New York, 2016).

[22] V. A. Markel, J. Opt. Soc. Am. A 33(7), 1244-56 (2016).

[23] D. A. G. Bruggeman, Ann. Phys. (Leipzig) 24, 636 (1935).

[24] Y. Guo and Z. Jacob, Opt. Express 21, 15014 (2013).

[25] Y. Guo and Z. Jacob, J. Appl. Phys. 115, 234306 (2014).

[26] X. L. Liu, T. J. Bright and Z. M. Zhang, J. Heat Transfer 136, 092703 (2014).

[27] M. Tschikin, S. A. Biehs, P. Ben-Abdallah, S. Lang, A. Y. Petrov and M. Eich, J. Quant. Spectrosc. Radiat. Transf. 158, 17 (2015).

[28] S. A. Biehs and P. Ben-Abdallah, Z. Naturforsch. A 72, 115 (2017).

[29] Y. Yang, J. Y. Chang, P. Sabbaghi and L. Wang, J. Heat Transfer 139, 052701 (2017).

[30] B. Zhao, B. Guizal, Z. M. Zhang, S. Fan and M. Antezza, Phys. Rev. B 95, 245437 (2017).

[31] M. Lim, J. Song, S. S. Lee and B. J. Lee, Nat. Commun. 9, 4302 (2018).

[32] H. Iizuka and S. Fan, Phys. Rev. Lett. 120, 063901 (2018).

[33] J. E. Pérez-Rodríguez, G. Pirruccio and R. Esquivel-Sirvent, Phys. Status Solidi B 257, 1900498 (2020).

[34] X. Liu, B. Zhao and Z. M. Zhang, Phys. Rev. A 91, 062510 (2015).

[35] X. Liu and Z. M. Zhang, ACS Photonics 2, 1320 (2015).

[36] X. Liu and Z. M. Zhang, Appl. Phys. Lett. 107, 143114 (2015).

[37] Y. Yang and L. Wang, Phys. Rev. Lett. 117, 044301 (2016).

[38] Y. Yang, P. Sabbaghi and L. Wang, Int. J. Heat Mass Transf. 108, 851 (2017).

[39] A. Didari and M. P. Mengüç, Opt. Express 23, A547 (2015).

[40] A. Didari and M. P. Mengüç, Opt. Express 23, A1253 (2015).

[41] A. Didari and M. P. Mengüç, J. Quant. Spectrosc. Radiat. Transf. 197, 95 (2017).

[42] V. Fernández-Hurtado, F. J. García-Vidal, S. Fan and J. C. Cuevas, Phys. Rev. Lett. 118, 203901 (2017).

[43] H. Yu, Y. Duan and Z. Yang, Int. J. Heat Mass Transf. 123, 67 (2018).

[44] M. S. Mirmoosa, F. Rüting, I. S. Nefedov and C. R. Simovski, J. Appl. Phys. 115, 234905 (2014).

[45] S. M. Rytov, Y. A. Kravtsov and V. Tatarskii, Principles of Statistical Radiophysics 3: Elements of Random Fields (Springer, New York, 1989).

[46] C.A. Balanis, Advanced Engineering Electromagnetics 2 ed. (John Wiley & Sons, Inc., New Jersey, 2012).

[47] A. O. Silva and J. C. Costa, J. Microw. Optoelectron. Electromagn. Appl. 13, 10 (2014).

[48] M. Francoeur, M. P. Menguc and R. Vaillon, J. Quant. Spectrosc. Radiat. Transfer 110, 2002 (2009).

[49] M. Francoeur, M. P. Menguc and R. Vaillon, J. Phys. D: Appl. Phys. 43, 075501 (2010).

[50] S. Edalatpour and M. Francoeur, J. Quant. Spectrosc. Radiat. Transfer 133, 364 (2014).

[51] S. Edalatpour, M. Čuma, T. Trueax, R. Backman and M. Francoeur, Phys. Rev. E 91, 063307 (2015).

[52] S. Edalatpour, Phys. Rev. E 99, 063308 (2019).

[53] L. Tsang, J. A. Kong, K. Ding and C. O. Ao, Scattering of Electromagnetic Waves: Numerical Simulations (John Wiley & Sons, Inc., New York, 2002).

[54] C. F. Bohren and D. R. Huffman, Absorption and Scattering of Light by Small Particles (Wiley, New York, 1998).

[55] P. Sheng, Introduction to Wave Scattering, Localization and Mesoscopic Phenomena 2 ed. (Springer, 2006).

[56] X. Zhang and Y. Wu, Sci. Rep. 5, 7892 (2015).

CHAPTER 5

SPATIAL COHERENCE OF THE THERMAL EMISSION OF A SPHERE

This chapter has been reproduced from a previous publication in Physical Review B: *S. Zare and S. Edalatpour, Phys. Rev. B* ***101****, 165424 (2020).*

5.1. Abstract

Analytical expressions for calculating the energy density and spatial correlation function of thermal emission by a homogeneous, isothermal sphere of arbitrary size and material are presented. The spectral distribution and the power law governing the distance-dependent energy density are investigated in the near-field and far-field regimes for silicon carbide (dielectric), silicon (semiconducting), and tungsten (metallic) spheres of various size parameters ranging from X = 0.002 to 5. The spatial coherence of the thermal field emitted by spheres of different size and material is also studied in both radial and polar directions, and the effect of localized surface phonons (LSPhs) on the correlation length and angle is elucidated. It is shown that the energy density follows a power law of d^{-2} (d is the observation distance) in the far field independent of the size and material of the sphere. The power law in the near field is strongly dependent on the material, size parameter, and the ratio $\frac{d}{a}$ (a is the sphere radius). In the near field, the energy density follows a power law of d^{-6} when $X \ll 1$ and $\frac{d}{a} \gg 1$ (similar to an electric point dipole). With increasing X or decreasing $\frac{d}{a}$, the contribution of multipoles to the energy density increases resulting in an increase in the power of d until the power law converges to that for a semi-infinite medium ($d^{-2.5}$, $d^{-0.5}$, and $d^{-3.5}$ for silicon carbide, silicon and tungsten, respectively, in the intermediate near field, and $d^{-3.5}$, $d^{-3.5}$, and $d^{-2.5}$ for silicon carbide, silicon and tungsten, respectively, in the extreme near field.). It is also found that the spatial correlation length in the radial direction is approximately on the order of λ, 0.1λ, and 0.001λ in the far-field, intermediate near-field, and extreme near-field regimes, respectively,

when the multipolar LSPhs are not supported. The correlation angle in the extreme near field is strongly dependent on the sphere size parameter, such that it decreases by three orders of magnitude (from 0.5π to 0.001π) when X increases from 0.002 to 5. The dependence of the correlation angle on X decreases significantly in the intermediate near-field and far-field regimes, and the correlation angle retains the same order of magnitude ($0.15\pi - 0.7\pi$) for all considered Xs in these two regimes. While the excitation of dipolar LSPhs does not affect the correlation length and angle of the thermal field, the multipolar LSPhs reduce the spatial coherence in both directions.

5.2. Introduction

Thermal radiation is traditionally considered to be spatially incoherent. However, this is not entirely true as the thermally generated electromagnetic waves can exhibit a high degree of spatial coherence in both near-field ($d \leq \lambda$, where d and λ are the observation distance and thermal wavelength, respectively) and far-field ($d > \lambda$) regimes.

While far-field blackbody radiation is spatially correlated over a distance on the order of $\lambda/2$ [1], highly correlated far-field emission can be achieved by engineering materials at the sub-wavelength scale [2-11], for example, using gratings [2,3,5,7,11] or multilayers of thin films [4,8,9].

Thermal radiation in the near field can have various coherence behaviors depending on the geometry, material properties, and crystalline structure of the source as well as the observation distance. The coherence of thermal near field is mostly studied within the framework of fluctuational electrodynamics [12], and most of these studies are focused on planar media, i.e., semi-infinite media [1,5,13-15], thin films [16,17], and multilayer hyperbolic media [18]. For a semi-infinite planar source, the spatial coherence of the thermal near field has been studied in the intermediate near-field ($d \leq \lambda$) and extreme near-field ($d \ll \lambda$) regimes. When the source does not support surface polaritons, the coherence length in the intermediate regime has the same order of magnitude as the minimum of the skin depth, δ, and the wavelength [13]. As such, a coherence length much smaller than the thermal wavelength is found for metals which have small skin depths. The excitation of surface polaritons significantly modifies the

coherence of the thermal field in the intermediate regime. In this case, the fields are correlated over a distance on the scale of the propagation length of the surface polariton [1,5,13,14]. The coherence length in the extreme near-field regime is much smaller than that in the intermediate regime. In this case, the coherence length is equal to the observation distance from the source, d [1]. The spatial coherence of thermal emission has also been studied for dielectric and metallic thin films [16,17]. In the intermediate regime, the waveguide modes of a dielectric (heavily-doped silicon) thin film result in a long-range coherence (1.34λ) for the thermal field [16]. In the extreme near-field regime, a very small coherence length ($1.13\times10^{-4}\lambda$) is obtained for the thermal field. The short coherence length of the thermal emission in this regime is attributed to the divergence of the electric field in the vicinity of point charges induced at the source surface. The spatial coherence of the thermal field emitted by metallic thin films has been studied in the extreme near-field regime [17]. The coherence length in the polariton frequency band increases due to the excitation of surface plasmon polaritons, while the coherence length outside this band is $\lambda/2$. In the polariton frequency band, the coherence length strongly depends on the film thickness and can be larger than 10λ. Spatial coherence of the thermal near field has also been studied for a multilayer hyperbolic ($\varepsilon_{\parallel}\varepsilon_{\perp}<0$, where $\varepsilon_{\parallel}$ and $\varepsilon_{\perp}$ are the dielectric functions parallel and perpendicular to the optical axis, respectively) semi-infinite medium [18]. The correlation length of thermal emission by a type I ($\varepsilon_{\parallel}<0$ and $\varepsilon_{\perp}>0$) hyperbolic semi-infinite medium, which cannot support surface polaritons, is on the order of 0.1λ and λ in the extreme and intermediate near-field regimes, respectively. Unlike type I, a type II ($\varepsilon_{\parallel}>0$ and $\varepsilon_{\perp}<0$) hyperbolic medium can support surface polaritons resulting in a large correlation length on the order of 10λ in the intermediate near field. In the extreme near field, however, the correlation length for a type II hyperbolic medium is the same as that for the type I, i.e., on the order of 0.1λ. The nonlocal effects on the spatial correlation of thermal emission in the extreme near-field regime have been studied for semi-infinite planar media using approximate macroscopic models [15]. The coherence length of the extreme near field is calculated for polar crystals and an electron plasma. For

polar crystals, a correlation length equal to the lattice constant is obtained for thermal emission at sub-nanometer distances. For electron plasma, the minimum coherence length is set by the Thomas-Fermi screening length [15].

While spatial coherence of thermal emission by planar media has been extensively studied, spatial coherence for finite, nonplanar media is almost unexplored. In the only study concerned with nonplanar media [19], the spatial coherence of an incident electric field scattered by a single lossless (non-emitting) sphere with $X = 1$ (X is the size parameter) and a chain of spheres with $X = 0.3$ is studied. The scattering of incident field by the spheres is studied using electromagnetic multiple-scattering theory. The single sphere has a constant (with wavelength) and real dielectric function (thus it does not emit thermal radiation), and it does not support localized surface modes. A coherence length on the order of several wavelengths ($\sim 5\lambda$) is found at the near-field distances from dielectric spheres. It is also shown that spheres with larger dielectric function show a higher degree of coherence. The spatial correlation of the thermal field is also studied for a chain of lossless silicon nanospheres with $X = 0.3$ as well as for a chain of metallic nanospheres of the same size with a dielectric function given by the Drude model. In both cases, the coherence length varies significantly with the observation location from the chain.

Spatial coherence of thermal emission by spheres is of significance as they are used for engineering thermal emission in man-made materials such as Mie-resonance-based metamaterials [20-23]. However, the spatial coherence of the thermal field emitted by a single sphere is not fully understood yet. The spatial correlation function for an emitting sphere has not been formulated so far, and the effects of the localized surface phonons (LSPhs), material, and sphere size parameter on spatial coherence in the extreme near-field, intermediate near-field, and far-field regimes have not been investigated yet. Additionally, while the far-field emissive power of spheres with various size parameters is discussed in several studies [24-27], there has not been any analysis of the near-field thermal emission by a sphere.

In this paper, we use the analytical expressions of the electric and magnetic fields thermally emitted by a sphere [24] to calculate the energy density and spatial correlation function. The spectrum and the power laws governing near-field and far-field energy density for spheres of various size parameters and

materials are studied. Silicon carbide (SiC), silicon (Si), and tungsten (W) are considered in this study. The spatial coherence of the thermal field emitted by a sphere is also investigated in both radial and polar directions. The effects of size parameter, LSPhs, and material on the spatial coherence of thermal emission are discussed, and the correlation length and angle in the extreme near-field, intermediate near-field, and far-field regimes are quantified.

This paper is organized as follows. Analytical expressions for energy density and spatial correlation function of the thermal field are presented in Sec. 5.3. These expressions are then used in Sec. 5.4 to study the spectral and total (spectrally-integrated) energy density. The spatial coherence along radial and polar directions is discussed in Sec. 5.5, and the concluding remarks are provided in Sec. 5.6.

5.3. Mathematical Derivation of Spatial Correlation Function

The problem under consideration is schematically shown in Fig. 5.1. A sphere with an arbitrary radius, *a*, and temperature, *T*, is thermally emitting in free space. The sphere is described by a local, complex, and frequency-dependent dielectric function $\varepsilon = \varepsilon' - i\varepsilon''$ ($e^{i\omega t}$ dependence is used for the time harmonic fields), and it is assumed that the sphere is homogeneous, nonmagnetic, and in local thermodynamic equilibrium. The spatial coherence of thermal electric fields at two arbitrary points $\mathbf{r}_1$ and $\mathbf{r}_2$ located in free space, which is characterized using the spatial correlation function, is of interest. The spatial correlation function is defined as [16,28,29]

$$\overleftrightarrow{\mathbf{W}}(\mathbf{r}_1, \mathbf{r}_2, \omega)\delta(\omega - \omega') = \left\langle \mathbf{E}(\mathbf{r}_1, \omega) \otimes \mathbf{E}^*(\mathbf{r}_2, \omega') \right\rangle \tag{5.1}$$

where $\mathbf{E}(\mathbf{r}_1,\omega)$ and $\mathbf{E}(\mathbf{r}_2,\omega)$ are the thermally emitted electric fields at points $\mathbf{r}_1$ and $\mathbf{r}_2$, respectively; $\otimes$ denotes the direct product of two vectors; the superscript $*$ represents the complex conjugate; and $\langle\ \rangle$ is the ensemble average. The electric field emitted by the sphere can be obtained using fluctuational electrodynamics [12,24]. The electric field at point $\mathbf{r}$ in free space can be expanded in vector spherical harmonics as [24,30]

$$\mathbf{E}(\mathbf{r}, \omega) = \sum_{n=1}^{\infty} \sum_{m=-n}^{n} \left(Q_{nm} \mathbf{M}_{nm}(\mathbf{r}, \omega) + S_{nm} \mathbf{N}_{nm}(\mathbf{r}, \omega) \right) \tag{5.2}$$

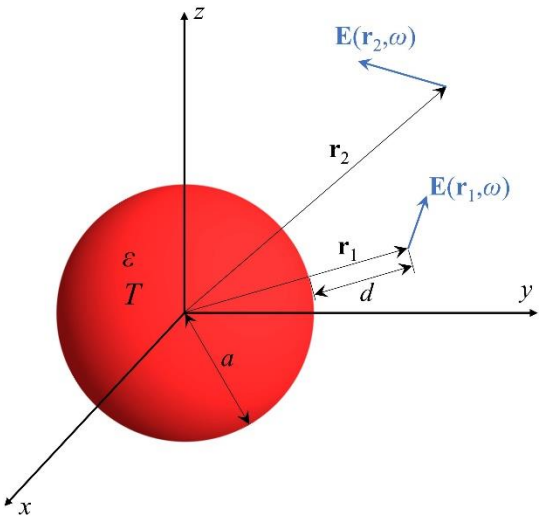

Figure 5.1 – A homogeneous sphere of radius *a*, temperature *T*, and dielectric function ε is emitting in free space. The spatial correlation of the thermal electric fields at points $\mathbf{r}_1$, $\mathbf{E}(\mathbf{r}_1,\omega)$, and $\mathbf{r}_2$, $\mathbf{E}(\mathbf{r}_2,\omega)$, is of interest. Parameter *d* shows the distance of observation point $\mathbf{r}_1$ from the sphere surface.

In Eq. (5.2), $\mathbf{M}_{nm}$ and $\mathbf{N}_{nm}$ are the vector spherical harmonics that are given by the following equations [24]:

$$\mathbf{M}_{nm} = h_n(k_0 r)\left(\frac{im}{\sin\theta}P_n^{|m|}\hat{\theta} - P_n'^{|m|}\hat{\varphi}\right)e^{im\varphi} \tag{5.3a}$$

$$\mathbf{N}_{nm} = \left\{\frac{n(n+1)}{k_0 r}h_n(k_0 r)P_n^{|m|}\hat{r} + \frac{1}{k_0 r}\frac{\partial}{\partial r}\left[rh_n(k_0 r)\right]P_n'^{|m|}\hat{\theta} + \frac{im}{k_0 r\sin\theta}\frac{\partial}{\partial r}\left[rh_n(k_0 r)\right]P_n^{|m|}\hat{\varphi}\right\}e^{im\varphi} \tag{5.3b}$$

where k_0 is the magnitude of the wavevector in free space, h_n is the spherical Hankel function of the second order, *i* is the imaginary unit, (r,θ,φ) are the components of vector **r** in spherical coordinates, $\hat{r}$, $\hat{\theta}$, and $\hat{\varphi}$ are the unit vectors in spherical coordinates, $P_n^{|m|}$ is the associated Legendre polynomial defined as $P_n^{|m|} \equiv P_n^{|m|}(\cos\theta)$, and $P_n'^{|m|} = \frac{\partial P_n^{|m|}}{\partial\theta}$. It should be noted that Gaussian units are used in this paper. The coefficients Q_{nm} and S_{nm} in Eq. (5.2) are given by [24]

$$Q_{nm} = -\tilde{A}_{nm} / qa^2 \left[h_n(k_0 a)\, j_n'(qa) - h_n'(k_0 a)\, j_n(qa) \right] \tag{5.4a}$$

$$S_{nm} = \tilde{B}_{nm} / k_0 a \left\{ \varepsilon \left[a h_n(k_0 a) \right]' \, j_n(qa) - h_n(k_0 a) \left[a j_n(qa) \right]' \right\} \tag{5.4b}$$

where $q = \sqrt{\varepsilon} k_0$, j_n is the spherical Bessel function of the first kind, the prime denotes differentiation with respect to *a*, and the coefficients $\tilde{A}_{nm}$ and $\tilde{B}_{nm}$ are found as [24]

$$\tilde{A}_{nm} = \int_0^a \frac{k_0 (\varepsilon - 1)(qr)^2 j_n(qr)}{2\pi \gamma_{nm} \sqrt{\varepsilon}} \int_{-\pi}^{\pi} e^{-im\varphi} d\varphi \int_0^{\pi} \left(\frac{im}{\sin\theta} P_n^{|m|} K_\theta + P_n'^{|m|} K_\varphi \right) \sin\theta \, d\theta \, dr \tag{5.5a}$$

$$\begin{aligned} \tilde{B}_{nm}(r) = &- \int_0^a \frac{q k_0 r (\varepsilon - 1)}{2\pi \gamma_{nm} \sqrt{\varepsilon}} \frac{\partial (r j_n(qr))}{\partial r} \int_{-\pi}^{\pi} e^{-im\varphi} d\varphi \int_0^{\pi} \left(K_\theta P_n'^{|m|} \sin\theta - im K_\varphi P_n^{|m|} \right) d\theta \, dr \\ &- \int_0^a \frac{(\varepsilon - 1) q^2 r j_n(qr)}{2\pi \varepsilon \rho_{nm}} \int_{-\pi}^{\pi} e^{-im\varphi} d\varphi \int_0^{\pi} K_r P_n^{|m|} \sin\theta \, d\theta \, dr \end{aligned} \tag{5.5b}$$

where γ_{nm} and ρ_{nm} in Eq. (5.5) are defined as

$$\gamma_{nm} = \frac{2n(n+1)(n+|m|)!}{(2n+1)(n-|m|)!} \tag{5.6a}$$

$$\rho_{nm} = \frac{2(n+|m|)!}{(2n+1)(n-|m|)!} \tag{5.6b}$$

In Eq. (5.5), $\left(K_r, K_\theta, K_\varphi \right)$ are the spherical components of vector $\mathbf{K}$, where $(\varepsilon - 1)\mathbf{K} / 4\pi$ is the thermally fluctuating electric moment per unit volume [24]. The ensemble average of the spatial correlation function of the spherical components of vector $\mathbf{K}$ is given by the fluctuation-dissipation theorem as [12,24]

$$\left\langle K_\alpha (\mathbf{r}, \omega) K^*_\beta (\mathbf{r}', \omega') \right\rangle = \frac{2\hbar}{r^2 \sin\theta} \coth\left(\frac{\hbar\omega}{2k_B T} \right) \mathrm{Im}\left(\frac{1}{\varepsilon - 1} \right) \delta_{\alpha\beta} \delta(\mathbf{r} - \mathbf{r}') \delta(\omega - \omega') \tag{5.7}$$

where $\hbar$ and k_B are the reduced Plank and Boltzmann constants, respectively.

Inserting Eq. (5.2) into Eq. (5.1) results in

$$W_{\alpha\beta}\left(\mathbf{r}_1,\mathbf{r}_2,\omega\right)=\sum_{n=1}^{\infty}\sum_{m=-n}^{n}\sum_{n'=1}^{\infty}\sum_{m'=-n'}^{n'}\left\langle\left(Q_{nm}M_{nm_\alpha}\left(\mathbf{r}_1,\omega\right)+S_{nm}N_{nm_\alpha}\left(\mathbf{r}_1,\omega\right)\right)\right.$$
$$\left.\times\left(Q^*_{n'm'_\beta}M^*_{n'm'_\beta}\left(\mathbf{r}_2,\omega'\right)+S^*_{n'm'_\beta}N^*_{n'm'_\beta}\left(\mathbf{r}_2,\omega'\right)\right)\right\rangle \tag{5.8}$$

where $\alpha,\beta=r,\theta,\varphi$. The vector spherical harmonics are deterministic. As such, they can be taken out of the ensemble average, and Eq. (5.8) can be rewritten as follows

$$W_{\alpha\beta}\left(\mathbf{r}_1,\mathbf{r}_2,\omega\right)=\sum_{n=1}^{\infty}\sum_{m=-n}^{n}\sum_{n'=1}^{\infty}\sum_{m'=-n'}^{n'}\left[\left\langle Q_{nm}Q^*_{n'm'}\right\rangle M_{nm_\alpha}\left(\mathbf{r}_1,\omega\right)M^*_{n'm'_\beta}\left(\mathbf{r}_2,\omega'\right)\right.$$
$$+\left\langle S_{nm}S^*_{n'm'}\right\rangle N_{nm_\alpha}\left(\mathbf{r}_1,\omega\right)N^*_{n'm'_\beta}\left(\mathbf{r}_2,\omega'\right)$$
$$+\left\langle Q_{nm}S^*_{n'm'}\right\rangle M_{nm_\alpha}\left(\mathbf{r}_1,\omega\right)N^*_{n'm'_\beta}\left(\mathbf{r}_2,\omega'\right)$$
$$\left.+\left\langle S_{nm}Q^*_{n'm'}\right\rangle N_{nm_\alpha}\left(\mathbf{r}_1,\omega\right)M^*_{n'm'_\beta}\left(\mathbf{r}_2,\omega'\right)\right] \tag{5.9}$$

The ensemble average of the products of coefficients *S* and *Q* in Eq. (5.9) are obtained using the following equations:

$$\left\langle Q_{nm}Q^*_{n'm'}\right\rangle=\frac{k_0^2\hbar}{\pi\gamma_{nm}\left|D_n\right|^2}\coth\left(\frac{\hbar\omega}{2k_BT}\right)\mathrm{Im}\left(j^*_n\left(qa\right)j'_n\left(qa\right)\right)\delta_{nn'}\delta_{mm'} \tag{5.10a}$$

$$\left\langle S_{nm}S^*_{n'm'}\right\rangle=\frac{k_0{}^2\hbar}{\pi\gamma_{nm}\left|E_n\right|^2}\coth\left(\frac{\hbar\omega}{2k_BT}\right)\mathrm{Im}\left\{\varepsilon^*\left(\frac{\left|j_n\left(qa\right)\right|^2}{a}+j^*_n\left(qa\right)j'_n\left(qa\right)\right)\right\}\delta_{nn'}\delta_{mm'} \tag{5.10b}$$

$$\left\langle Q_{nm}S^*_{n'm'}\right\rangle=\left\langle S_{nm}Q^*_{n'm'}\right\rangle=0 \tag{5.10c}$$

where

$$D_n=a\left[h_n(k_0a)j'_n\left(qa\right)-h'_n(k_0a)j_n\left(qa\right)\right] \tag{5.11a}$$

$$E_n=\varepsilon\left[ah_n(k_0a)\right]'j_n\left(qa\right)-h_n(k_0a)\left[aj_n\left(qa\right)\right]' \tag{5.11b}$$

Using Eq. (5.10c) and the properties of the Kronecker delta function in Eqs. (5.10a) and (5.10b), the correlation function in Eq. (5.9) is reduced to

$$W_{\alpha\beta}\left(\mathbf{r}_1,\mathbf{r}_2,\omega\right)=\sum_{n=1}^{\infty}\sum_{m=-n}^{n}\Big[\left\langle\left|Q_{nm}\right|^2\right\rangle M_{nm_\alpha}\left(\mathbf{r}_1,\omega\right)M^{*}{}_{nm_\beta}\left(\mathbf{r}_2,\omega'\right) + \left\langle\left|S_{nm}\right|^2\right\rangle N_{nm_\alpha}\left(\mathbf{r}_1,\omega\right)N^{*}{}_{nm_\beta}\left(\mathbf{r}_2,\omega'\right)\Big] \tag{5.12}$$

Equation (5.12) combined with Eqs. (5.3) and (5.10) provide the spatial correlation function of the electric fields at points $\mathbf{r}_1$ and $\mathbf{r}_2$. These equations can also be used for finding the energy density emitted by the sphere in free space. The electric energy density, u^E, at point **r** in free space is given by [31]

$$u^E\left(\mathbf{r},\omega\right)=\frac{1}{8\pi}\left\langle\left|\mathbf{E}(\mathbf{r},\omega)\right|^2\right\rangle \tag{5.13}$$

where based on Eq. (5.1), $\left\langle\left|\mathbf{E}(\mathbf{r},\omega)\right|^2\right\rangle$ can be obtained by taking the trace of $\ddot{\mathbf{W}}\left(\mathbf{r}_1,\mathbf{r}_2,\omega\right)$ for $\mathbf{r}_1=\mathbf{r}_2=\mathbf{r}$, i.e.,

$$u^E\left(\mathbf{r},\omega\right)=\frac{1}{8\pi}Tr\left[\ddot{\mathbf{W}}\left(\mathbf{r},\mathbf{r},\omega\right)\right] \tag{5.14}$$

Substituting for $\ddot{\mathbf{W}}$ from Eq. (5.12), the electric energy density can then be written as:

$$u^E\left(\mathbf{r},\omega\right)=\frac{1}{8\pi}\sum_{\alpha=r,\theta,\varphi}\sum_{n=1}^{\infty}\sum_{m=-n}^{n}\left[\left\langle\left|Q_{nm}\right|^2\right\rangle\left|M_{nm_\alpha}\left(\mathbf{r},\omega\right)\right|^2+\left\langle\left|S_{nm}\right|^2\right\rangle\left|N_{nm_\alpha}\left(\mathbf{r},\omega\right)\right|^2\right] \tag{5.15}$$

The magnetic energy density, u^H, can be obtained in a similar way as the electric energy density. The magnetic energy density at point **r** in free space is found using the magnetic field at this point as [31]

$$u^H\left(\mathbf{r},\omega\right)=\frac{1}{8\pi}\left\langle\left|\mathbf{H}(\mathbf{r},\omega)\right|^2\right\rangle \tag{5.16}$$

The magnetic field at point **r** can be expanded in vector spherical harmonics as [24]

$$\mathbf{H}\left(\mathbf{r},\omega\right)=i\sum_{n=1}^{\infty}\sum_{m=-n}^{n}\left(S_{nm}\mathbf{M}_{nm}\left(\mathbf{r},\omega\right)+Q_{nm}\mathbf{N}_{nm}\left(\mathbf{r},\omega\right)\right) \tag{5.17}$$

Using Eq. (5.17) and following the same steps as those taken for deriving the electric energy density, the magnetic energy density is obtained as

$$u^H(\mathbf{r},\omega)=\frac{1}{8\pi}\sum_{\alpha=r,\theta,\varphi}\sum_{n=1}^{\infty}\sum_{m=-n}^{n}\left[\left\langle\left|S_{nm}\right|^2\right\rangle\left|M_{nm_\alpha}(\mathbf{r},\omega)\right|^2+\left\langle\left|Q_{nm}\right|^2\right\rangle\left|N_{nm_\alpha}(\mathbf{r},\omega)\right|^2\right] \tag{5.18}$$

Finally, the spectral energy density is found by adding Eq. (5.18) and Eq. (5.15) as

$$u(\mathbf{r},\omega)=\frac{1}{8\pi}\sum_{\alpha=r,\theta,\varphi}\sum_{n=1}^{\infty}\sum_{m=-n}^{n}\left(\left\langle\left|S_{nm}\right|^2\right\rangle+\left\langle\left|Q_{nm}\right|^2\right\rangle\right)\left(\left|M_{nm_\alpha}(\mathbf{r},\omega)\right|^2+\left|N_{nm_\alpha}(\mathbf{r},\omega)\right|^2\right) \tag{5.19}$$

5.4. Energy Density

The total (spectrally-integrated) and the spectral energy density emitted by single spheres made of SiC (dielectric), Si (semiconductor), and W (metal) is calculated at an observation distance, $d=r-a$, using the formalism described in Sec. 5.3. The total energy density is shown in Fig. 5.2 versus the observation distance normalized by the dominant wavelength of thermal radiation at 300 K ($\lambda_{\max}$ = 9.66 μm), $\frac{d}{\lambda_{\max}}$, for four size parameters ($X=\frac{2\pi a}{\lambda_{\max}}$) of 0.002, 0.02, 0.2, and 5. The energy density emitted by a semi-infinite medium [14] as well as an electric point dipole [14] is also shown in Fig. 5.2 for comparison. The energy density for all materials increases with increasing the size parameter and decreasing the observation distance.

In the far-field region ($\frac{d}{\lambda_{\max}}>10$), the spheres behave as electric point dipoles when their size is much smaller than the wavelength inside the material (i.e., λ/n where n is the refractive index of the sphere). As shown in Fig. 5.2, the far-field energy density for SiC and Si spheres agrees well with that predicted using the dipole approximation when $X < 1$. For W spheres, which have a large refractive index, the agreement between the energy density of the sphere and the dipole approximation is observed in the far field only for X = 0.002. The energy density for all spheres follows a power law of d^{-2} in the far field ($\frac{d}{\lambda_{\max}}>10$) regardless of the size and material of the sphere, which is similar to the far-field behavior of an electric point dipole. The electric field generated by a dipole is proportional to d^{-1} in the far field [32].

Consequently, based on Eq. (5.13) (magnetic energy density is negligible), the energy density of an electric dipole is proportional to d^{-2} in the far field.

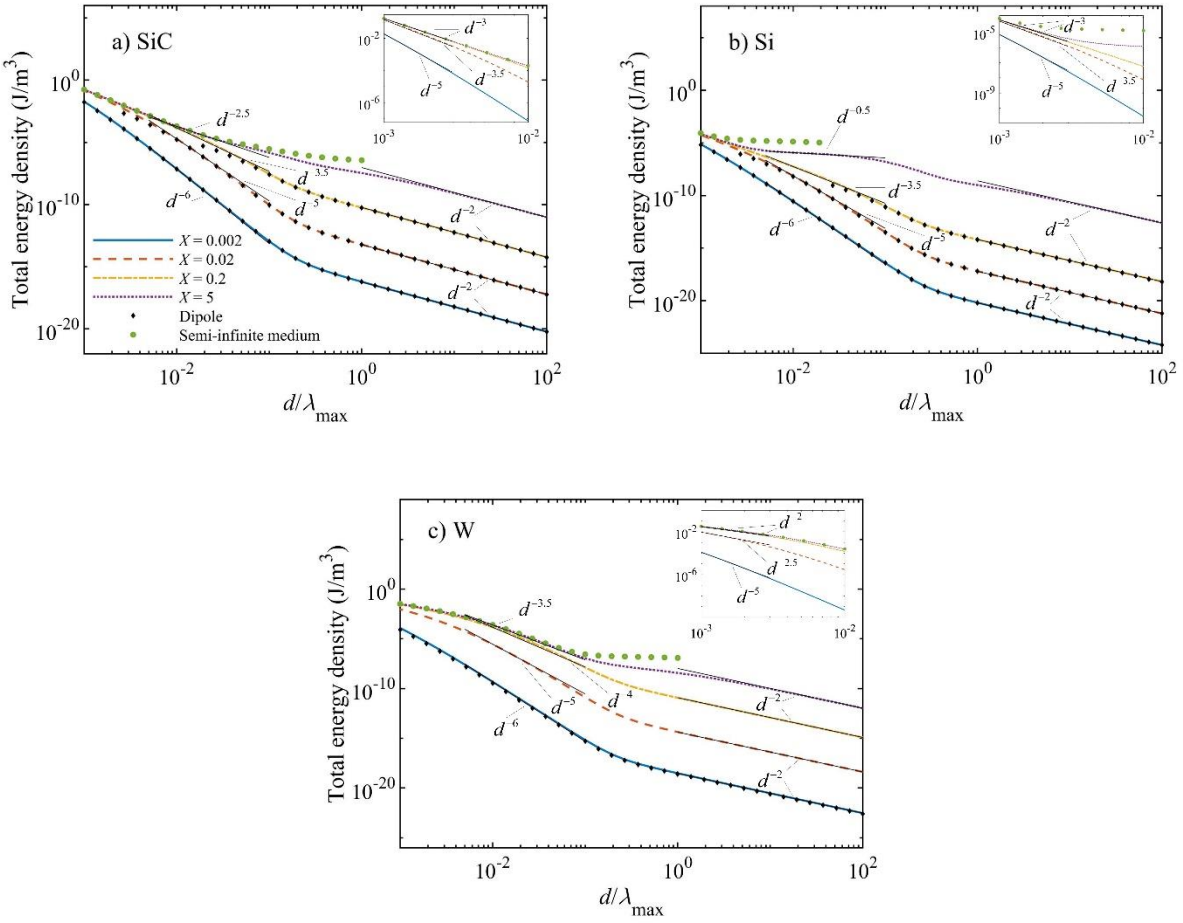

Figure 5.2 – Total energy density emitted by a (a) SiC, (b) Si, and (c) W sphere versus observation distance d normalized by λ_{max} (= 9.66 μm). The insets show the total energy density in the extreme near-field distances ($\frac{d}{\lambda_{max}} < 0.01$).

In the intermediate near-field distances ($0.01 \le \frac{d}{\lambda_{max}} \le 0.1$), the energy density of a sphere with X = 0.002 varies with distance as d^{-6} similar to the behavior of an electric point dipole. For an electric dipole, the electric field follows a power law of d^{-3} in the intermediate near field [32,33], and thus the energy

density has a d^{-6} distance dependence. This similarity to a dipole in distance dependence is because $X \ll 1$ and $a \ll d$ in the intermediate near-field distances from a sphere with X = 0.002. As the size of the sphere increases, the energy density starts deviating from that of an electric dipole. In this region, the energy density is governed by a d^{-5} power law for SiC, Si, and W spheres with X = 0.02. With further increase in the size, the power of d becomes material dependent and further increases until it converges to that for a semi-infinite medium ($X \to \infty$) when X = 5. For X = 5, the power laws are $d^{-2.5}$, $d^{-0.5}$, and $d^{-3.5}$ for SiC, Si, and W spheres, respectively.

In the extreme near-field region ($\frac{d}{\lambda_{\max}} < 0.01$), the behavior of the energy density for a sphere with X = 0.002, where still $a < d$, is similar to that for a point dipole and the energy density is governed by a power law of d^{-5} for all three materials. With increasing the size parameter, however, the size of the spheres becomes comparable to or greater than d. As such, the sphere does not behave as a point dipole anymore. Similar to the intermediate near-field regime, the power of d becomes material dependent and increases with increasing the size of the sphere. As shown in Fig. 5.2, the energy density and its distance dependence eventually approach those for a semi-infinite medium in the extreme near field (d^{-2} for metals and d^{-3} for dielectrics and semiconductors [1]).

The spectral energy density emitted by a SiC sphere in the extreme near-field, intermediate near-field, and far-field regimes is shown in Fig. 5.3(a) to 5.3(c), respectively, for various size parameters ranging from 0.002 to 5. Spheres with sizes smaller than or comparable to the wavelength can support LSPh modes when $\mathrm{Re}[\varepsilon] \approx -(l+1)/l$, where $l = 1, 2, 3, \ldots$ is the order of the mode [34]. The excitation of LSPhs increases thermal emission resonantly resulting in sharp peaks in the energy density. The peaks in the energy density spectra of Fig. 3 are labeled with the order of the associated LSPh modes. As seen from Figs. 5.3(a) and 5.3(b), at a given near-field distance, the order of the excited LSPh modes increases from l = 1 (dipole mode) to $l \to \infty$ (surface phonon-polariton mode of a semi-infinite medium) as the size parameter increases from X = 0.002 to X = 5. Also, the higher-order modes become more dominant in the

energy density spectra as X increases. However, in the far-field regime [Fig. 5.3(c)], the dipole mode dominates the energy density regardless of the size when $X \leq 1$ (i.e., when the sphere is smaller or comparable to the wavelength). When $X > 1$, the LSPh peaks are suppressed and broadened due to the retardation effects [35,36]. In addition to the LSPh modes, large electrical losses (i.e., large values of $\mathrm{Im}[\varepsilon]$) can result in peaks in the energy density when the sphere size is comparable to or larger than the wavelength. The spectral energy density for the Si and W spheres does not show any peaks and mostly follows the spectrum of a blackbody.

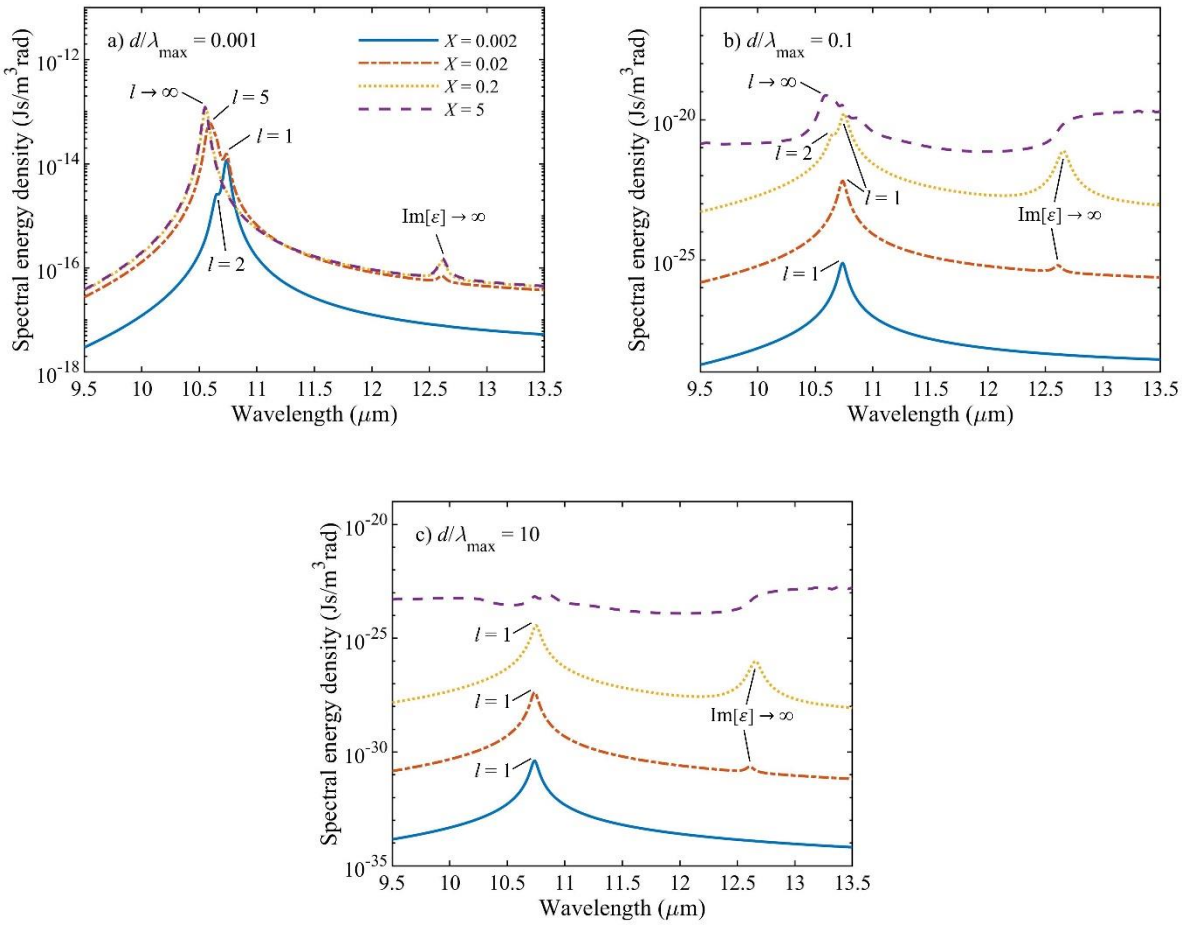

Figure 5.3 – Spectral energy density emitted by a SiC sphere with various size parameters in the (a) extreme near-field ($\frac{d}{\lambda_{max}} = 0.001$), (b) intermediate near-field ($\frac{d}{\lambda_{max}} = 0.1$), and (c) far-field ($\frac{d}{\lambda_{max}} = 10$) regimes.

5.5. Spatial Coherence

The formalism developed in Sec. 5.3 is used to study the spatial coherence of thermal radiation by a single sphere for various materials, observation distances, and size parameters. The correlation function matrix, $\ddot{\mathbf{W}}$, is calculated for two points [$\mathbf{r}_1 = (r_1, \theta_1, \varphi_1)$ and $\mathbf{r}_2 = (r_2, \theta_2, \varphi_2)$] along the radial direction, i.e., when $\theta_1 = \theta_2 = \theta$ and $\varphi_1 = \varphi_2 = \varphi$ [see the inset of Fig. 5.4(a)] as well as along the polar direction, i.e., when $r_1 = r_2 = r$ and $\varphi_1 = \varphi_2 = \varphi$ [see the inset of Fig. 5.8(a)]. The spatial correlation of thermal emission is calculated at three observation distances ($d = r_1 - a$) of $\frac{d}{\lambda_{\max}} = 0.001$ (located in the extreme near field), $\frac{d}{\lambda_{\max}} = 0.1$ (located in the intermediate near field), and $\frac{d}{\lambda_{\max}} = 10$ (located in the far field). While point $\mathbf{r}_1$ is fixed at one of these observation locations, the distance of point $\mathbf{r}_2$ from $\mathbf{r}_1$ is increased until the correlation function drops to negligible values. The components of the correlation function are normalized by their values at $\mathbf{r}_1 = \mathbf{r}_2$. The correlation function is first calculated for a wavelength of λ = 11 μm at which localized surface phonons (LSPhs) are not excited. Then, the effect of the LSPhs on the coherence of thermal emission is discussed.

5.5.1. Spatial Correlation along Radial Direction

Spatial correlation along the radial direction is studied in this subsection. Because of the spherical symmetry in this case, any arbitrary value can be assigned to θ and φ. In our calculations, $\theta = \frac{\pi}{2}$ and $\varphi = 0$ are selected [see the inset of Fig. 5.4(a)]. It should also be mentioned that $W_{\theta\theta}$ and $W_{\varphi\varphi}$ are equal due to spherical symmetry.

Figure 5.4 shows the diagonal components of the spatial correlation function in the extreme near-field regime. Figure 5.4(a) compares radial (W_{rr}) and polar ($W_{\theta\theta}$) components of the correlation function for

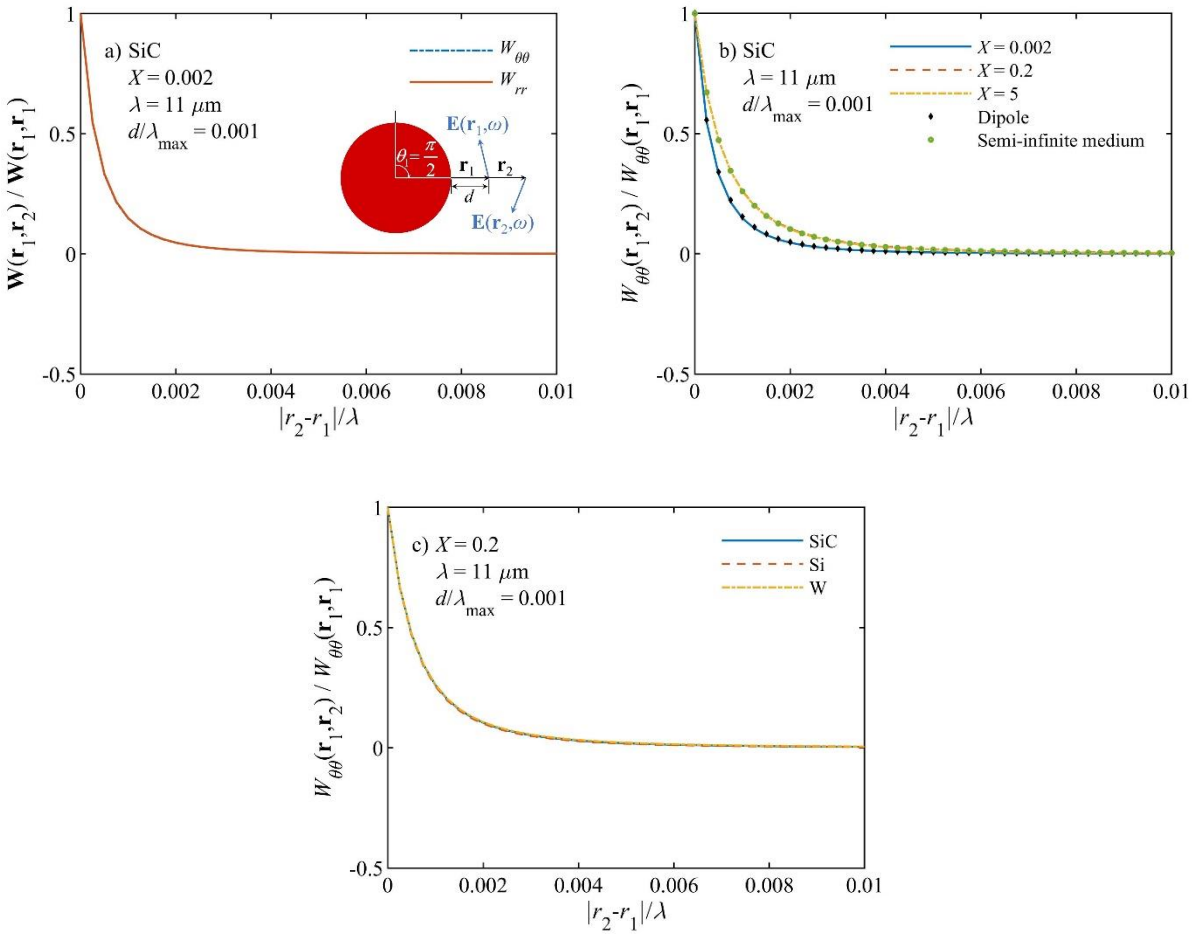

Figure 5.4 – Normalized correlation function along the radial axis in the extreme near-field regime ($\frac{d}{\lambda_{\max}}$ = 0.001) versus $\frac{|r_2 - r_1|}{\lambda}$ at λ = 11 μm. (a) Normalized $W_{\theta\theta}$ and W_{rr} for a SiC sphere with X = 0.002. (b) Normalized $W_{\theta\theta}$ for SiC spheres with various size parameters. (c) Normalized $W_{\theta\theta}$ for SiC, Si, and W spheres with X = 0.2.

a SiC sphere with X = 0.002. The radial and polar components are the same, and both exhibit an extremely short spatial correlation length in the extreme near field such that they decay rapidly within a distance of about 0.002λ. The equality of $W_{\theta\theta}$ and W_{rr} are also observed for X = 0.2 and 5 (the results are not shown). The polar component ($W_{\theta\theta}$) for a SiC sphere is compared for various size parameters in

Fig. 5.4(b). In this region, the correlation function of the SiC sphere with X = 0.002 is similar to that of a dipole. The SiC spheres with X = 0.2 and 5 show larger correlation lengths compared to the sphere with X = 0.002. The correlation function for these two size parameters converge to the one for a semi-infinite medium in the extreme near field. Still, the spatial correlation length for spheres with X = 0.2 and 5 is limited to a small fraction of wavelength ($\sim 0.006\lambda$) in the extreme near field. The polar component of correlation function for a sphere with X = 0.2 is compared for different materials in Fig. 5.4(c). As seen from this figure, the spatial coherence is material independent. To summarize, the correlation length at the extreme near-field distances from the sphere is very short (a few thousandths of a wavelength), slightly increases with the size of the sphere, and does not depend on the material.

Figure 5.5 shows the normalized correlation function in the intermediate near field. In this regime, the polar component of the correlation function shows a longer spatial correlation length than the radial component for a SiC sphere with X = 0.002, as shown in Fig. 5.5(a). The same behavior is observed for X = 0.2 and 5 (the results are not shown). Also, the length of coherence in this case is on the order of $\sim 0.1\lambda$ which is much longer than that in the extreme near field. Similar to the extreme near-field region, the spatial correlation for the sphere with X = 0.002 in the intermediate near field is similar to the one for a dipole. However, the enhancement of spatial correlation with increasing the size parameter is more significant in the intermediate near field than in the extreme near field [Fig. 5.5(b)], such that the spatial coherence for SiC spheres with X = 5 extends to distances on the order of a wavelength ($\sim \lambda$). Also, Fig. 5(c) shows that Si and SiC spheres with X = 0.2 exhibit the same spatial coherence in the intermediate near field, while the correlation function decays more rapidly for a W sphere. To summarize, in the intermediate near field, the correlation length is significantly longer than that in the extreme near field (between two and three orders of magnitude depending on the size parameter). Additionally, the spatial correlation is material dependent, and it increases with increasing the size of the sphere.

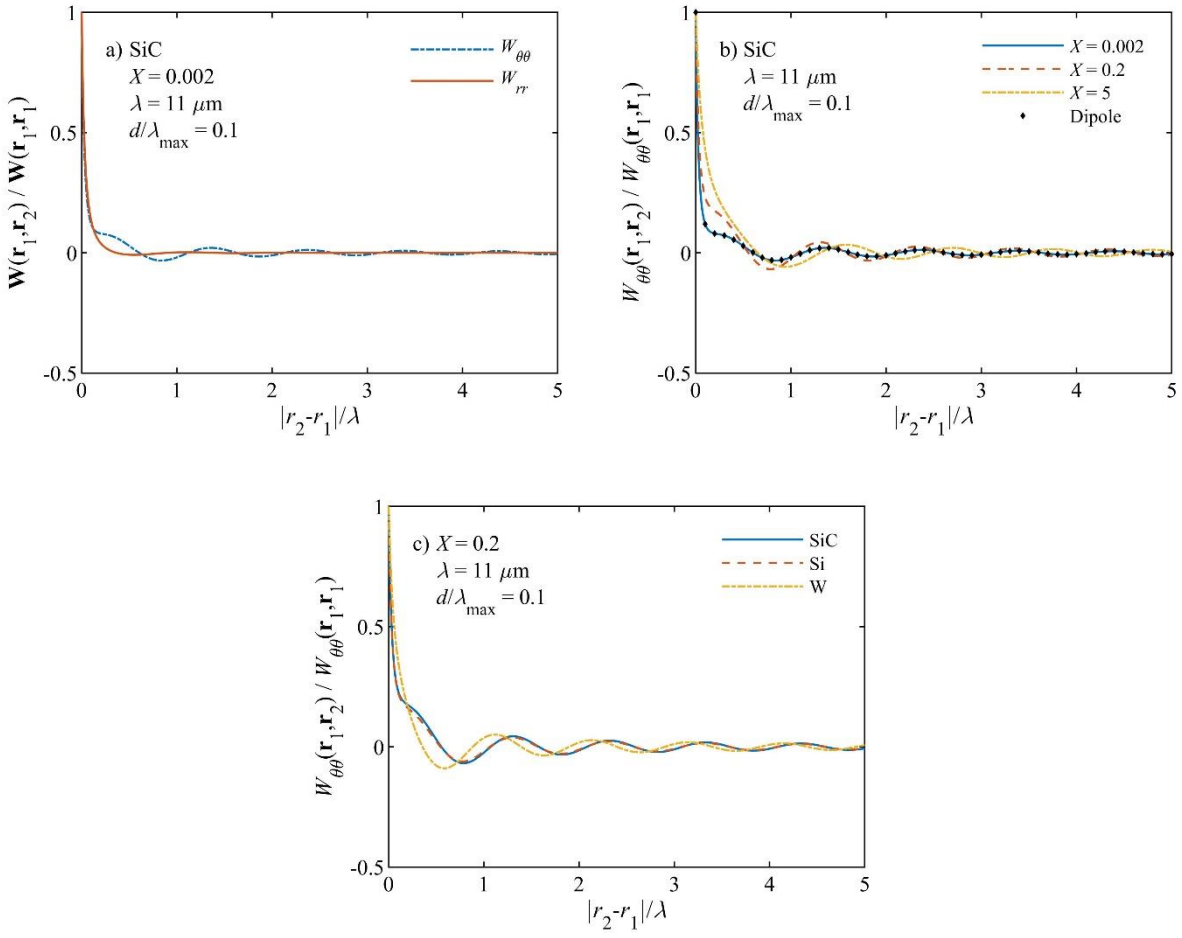

Figure 5.5 – Same as Fig. 5.4 for the intermediate near-field regime ($\frac{d}{\lambda_{\max}} = 0.1$).

The normalized correlation function in the far-field regime is plotted in Fig. 5.6. As illustrated in Fig. 5.6(a), the polar component of the correlation function is larger than the radial component. Also, the coherence length of thermal radiation is significantly larger than that in the intermediate and extreme near fields, such that it extends to distances on the order of 10λ. In addition, the spatial correlation agrees with the dipole approximation in the far field and does not vary with size parameter [Fig. 5.6(b)] and material [Fig. 5.6(c)].

To quantify the distance up to which the thermal field is correlated, the correlation length is calculated. The correlation length is defined as [16]

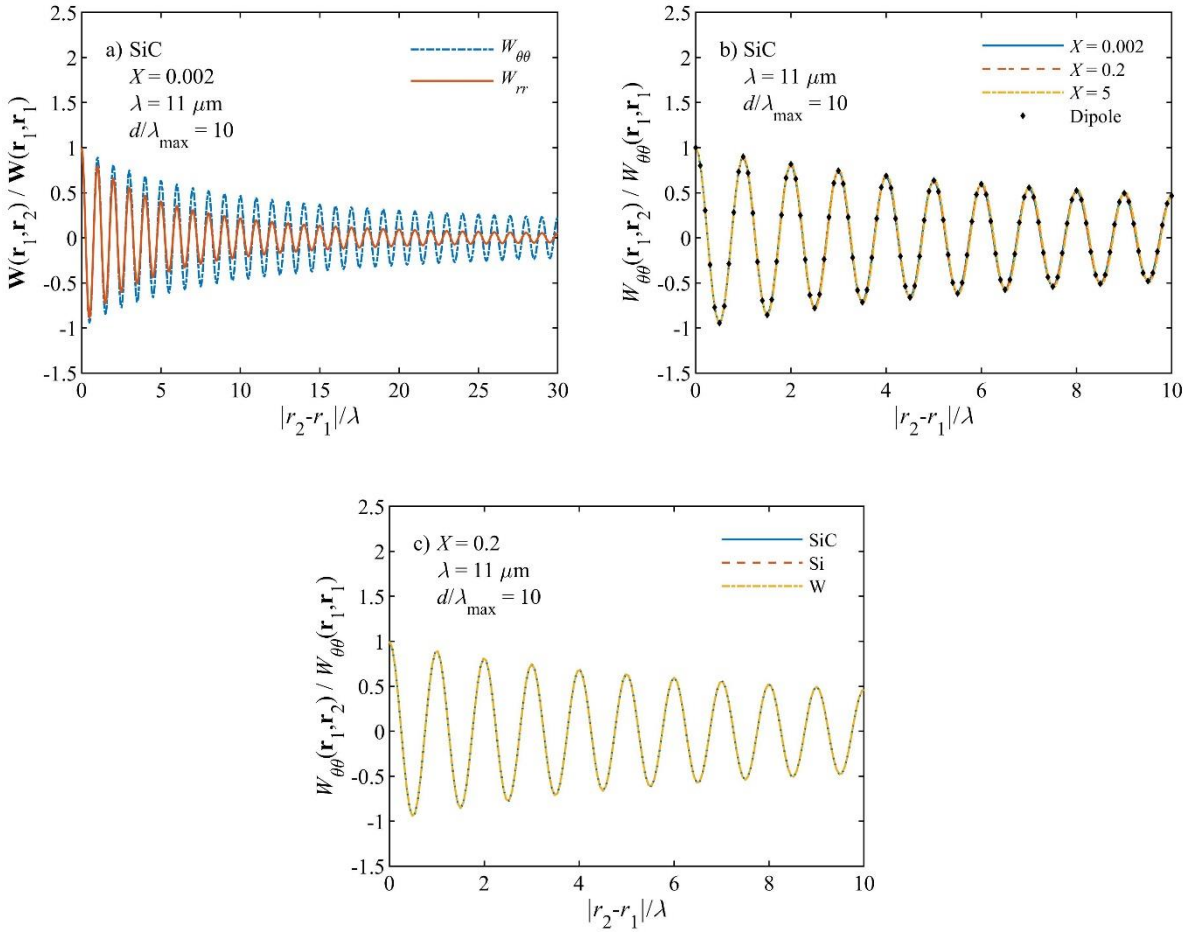

Figure 5.6 – Same as Fig. 5.4 for the far-field regime ($\frac{d}{\lambda_{\max}} = 10$).

$$L_{cor} = \frac{2\int_0^{\infty} \left| Tr\left(\overleftrightarrow{\mathbf{W}}(\mathbf{r}_1, \mathbf{r}_2, \omega)\right)\right|^2 dx}{\left| Tr\left(\overleftrightarrow{\mathbf{W}}(\mathbf{r}_1, \mathbf{r}_1, \omega)\right)\right|^2} \tag{5.20}$$

where $x = |r_2 - r_1|$. The correlation length normalized by the wavelength is calculated for a SiC sphere with different size parameters in the three regimes and is plotted versus wavelength in Fig. 5.7. It is observed that the correlation length significantly increases (by several orders of magnitude) with increasing the observation distance from the sphere for all size parameters. In addition, the correlation length monotonically decreases with the wavelength in the three regimes and for all size parameters except for a few wavelengths at which the correlation length has local minima and maxima. The

wavelengths associated with LSPhs and large electrical losses, which result in enhanced thermal emission as shown in Figs. 5.3(a)-5.3(c), are marked in Figs. 5.7(a)-5.7(d). It can be seen that the excitation of the dipolar LSPhs (l = 1) of the sphere does not affect the correlation length while the presence of the multipolar LSPhs ($l > 1$) reduces the spatial correlation in the extreme and intermediate near fields. With increasing the size parameter, the correlation length in the extreme and intermediate near field converges to that for a semi-infinite medium. Furthermore, the modes resulting from large losses ($\mathrm{Im}[\varepsilon] \to \infty$) in the sphere increase the correlation length of the thermal field.

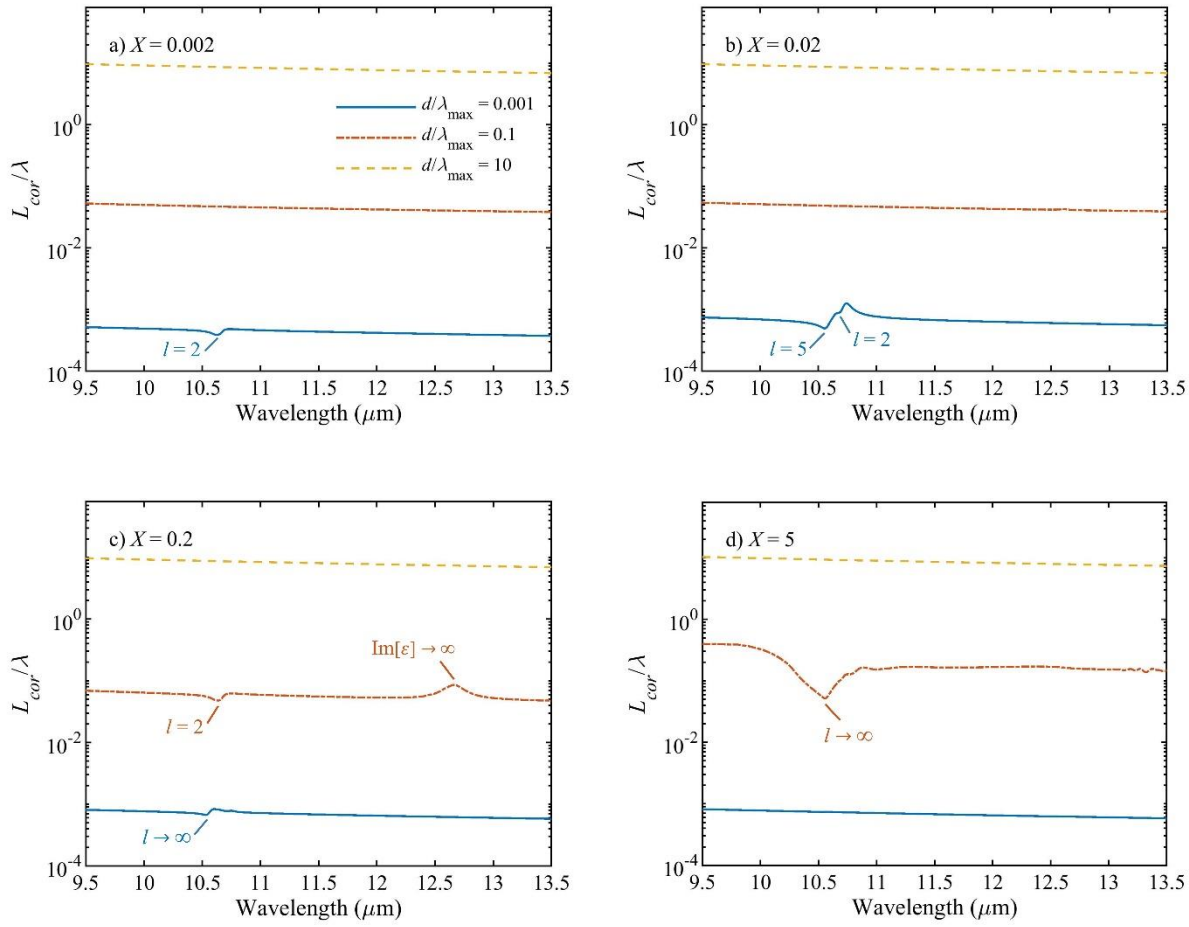

Figure 5.7 – Normalized correlation length versus wavelength for a SiC sphere with (a) X = 0.002, (b) X = 0.02, (c) X = 0.2, and (d) X = 5.

5.5.2. Spatial Correlation along Polar Direction

Spatial correlation along the polar direction is studied in this subsection. In this case, points $\mathbf{r}_1$ and $\mathbf{r}_2$ are located at the same radial distance and azimuthal angle (i.e., $r_1 = r_2 = r$ and $\varphi_1 = \varphi_2 = \varphi$) but have different polar angles [see the inset of Fig. 5.8(a)]. In the calculations, $\theta_1 = \frac{\pi}{2}$ and $\varphi = 0$, and three different values of r located in the extreme near-field, intermediate near-field, and far-field regimes are considered.

The normalized correlation function at an extreme near-field distance of $\frac{d}{\lambda_{\max}} = 0.001$ is plotted versus $\frac{|\theta_2 - \theta_1|}{\pi}$ in Fig. 5.8. Figure 5.8(a) shows the diagonal components of the spatial correlation function for a SiC sphere with X = 0.002. As seen from this figure, the azimuthal component of the correlation function ($W_{\varphi\varphi}$) exhibits strong spatial coherence for all values of $\frac{|\theta_2 - \theta_1|}{\pi}$, while the radial ($W_{rr}$) and polar ($W_{\theta\theta}$) components decrease slowly with $\frac{|\theta_2 - \theta_1|}{\pi}$ and become negligible at $\frac{|\theta_2 - \theta_1|}{\pi} = 0.5$. The effect of size parameter on $W_{\theta\theta}$ at the extreme near field is shown in Fig. 5.8(b). It is seen that $W_{\theta\theta}$ decreases significantly with increasing the size of the sphere, such that it vanishes for the sphere with X = 5 within a separation angle ($|\theta_2 - \theta_1|$) of only about 0.01π. The same size dependence is observed for W_{rr} and $W_{\varphi\varphi}$ (the results are not shown). Figure 5.8(c) compares $W_{\theta\theta}$ for SiC, Si, and W spheres with X = 0.2. This figure shows that the correlation function in the extreme near field does not depend on the material of the sphere. In summary, the spatial correlation in the extreme near field decreases rapidly with increasing the size parameter and is material independent.

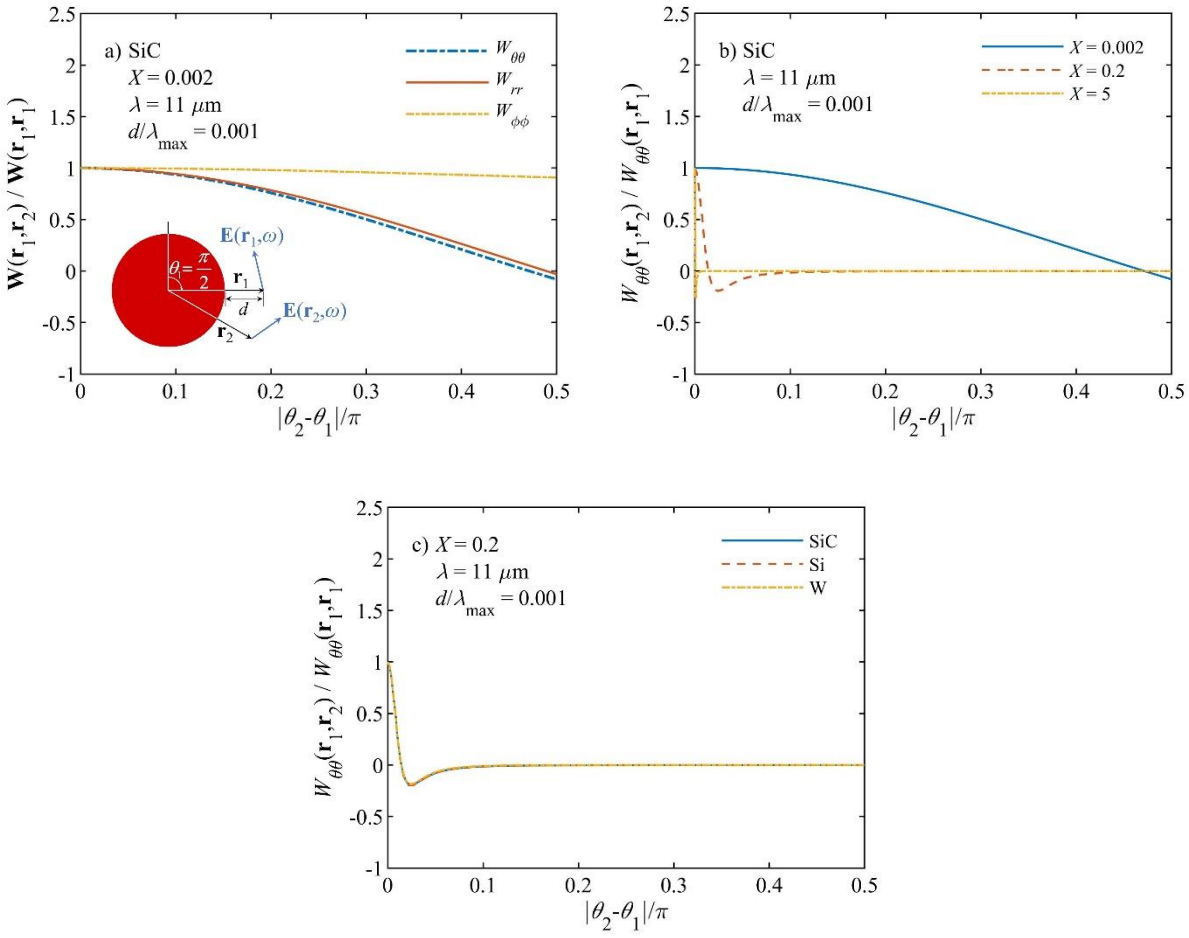

Figure 5.8 – Normalized correlation function along the polar direction in the extreme near-field regime ($\frac{d}{\lambda_{\max}} = 0.001$) versus $\frac{|\theta_2 - \theta_1|}{\pi}$ at λ = 11 μm. (a) Normalized $W_{\theta\theta}$, W_{rr} and $W_{\varphi\varphi}$ for a SiC sphere with X = 0.002. (b) Normalized $W_{\theta\theta}$ for SiC spheres with various size parameters. (c) Normalized $W_{\theta\theta}$ for SiC, Si, and W spheres with X = 0.2.

The spatial coherence shows similar behavior in the intermediate near-field ($\frac{d}{\lambda_{\max}} = 0.1$) and far-field ($\frac{d}{\lambda_{\max}} = 10$) regimes as shown in Figs. 5.9 and 5.10, respectively. As seen from Figs. 5.9(a) and 5.10(a), $W_{\varphi\varphi}$ is equal to unity at all separation angles, while W_{rr} and $W_{\theta\theta}$ (which are equal) slowly decrease to

zero when $\frac{|\theta_2 - \theta_1|}{\pi}$ = 0.5. The size dependence of spatial coherence in these two regimes is studied using Fig. 5.9(b) and 5.10(b), respectively. Unlike in the extreme near-field regime, the spatial coherence of the SiC sphere does not drastically decrease by increasing the size parameter in the intermediate near-field and far-field regimes. Figures 5.9(c) and 5.10(c) compare the spatial correlation for a sphere with X = 0.2 made of SiC, Si, and W. The correlation function for the SiC sphere is very close to that for the Si sphere, and it decreases from 1 at $\frac{|\theta_2 - \theta_1|}{\pi} = 0$ to 0 at $\frac{|\theta_2 - \theta_1|}{\pi} = 0.5$. The W sphere shows a remarkably stronger spatial coherence along the polar angle, such that the spatial correlation for the W sphere is almost equal to 1 for all values of $\frac{|\theta_2 - \theta_1|}{\pi}$. To summarize, the spatial correlation at the intermediate near-field and far-field distances is greater than that in the extreme near field, and it is material dependent.

Analogous to the length of correlation, we define a correlation angle for the spatial coherence as

$$\Theta_{cor} = \frac{2\int_0^{\pi/2} \left| Tr\left(\ddot{\mathbf{W}}(\mathbf{r}_1, \mathbf{r}_2, \omega)\right)\right|^2 dx}{\left| Tr\left(\ddot{\mathbf{W}}(\mathbf{r}_1, \mathbf{r}_1, \omega)\right)\right|^2} \tag{5.21}$$

where x is defined as $x = |\theta_2 - \theta_1|$. The correlation angle is plotted versus wavelength for SiC spheres with X = 0.002, 0.02, 0.2, and 5 in Figs. 5.11(a) to 5.11(d), respectively. The wavelengths at which energy density has peaks due to the excitation of LSPhs or the presence of large losses is marked in Figs. 5.11(a)-5.11(d). It can be seen that the effect of LSPhs and large losses on the correlation angle is the same as that on the correlation length along the radial direction. While the dipolar LSPhs (l = 1) do not significantly affect the correlation angle, the multipolar LSPhs ($l > 1$) reduce the spatial correlation in the extreme and intermediate near-field regimes. Additionally, the modes due to the large losses in the sphere ($\mathrm{Im}[\varepsilon] \to \infty$) increase the correlation angle in the intermediate near field.

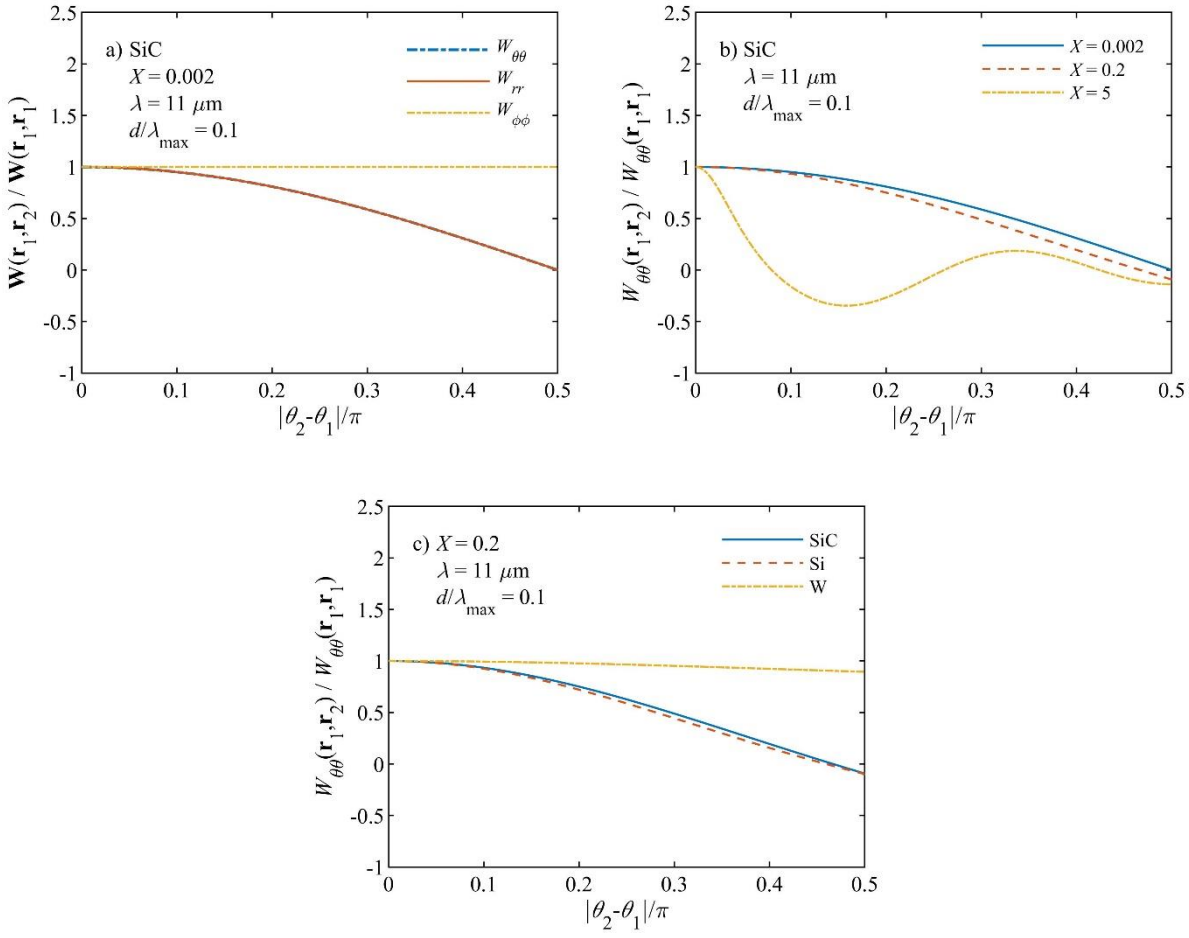

Figure 5.9 – Same as Fig. 5.8 for the intermediate near-field regime ($\frac{d}{\lambda_{\max}} = 0.1$).

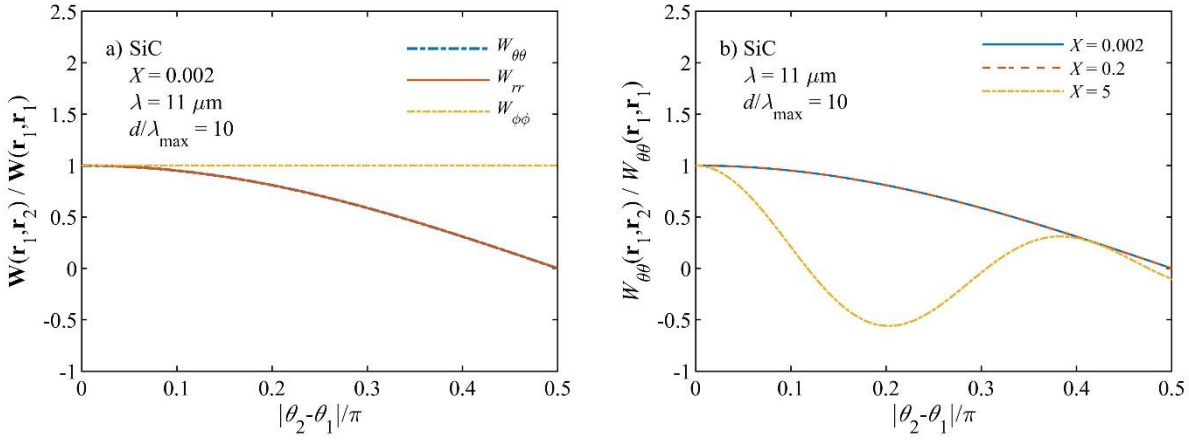

Figure 5.10 – Same as Fig. 5.8 for the far-field regime ($\frac{d}{\lambda_{\max}} = 10$).

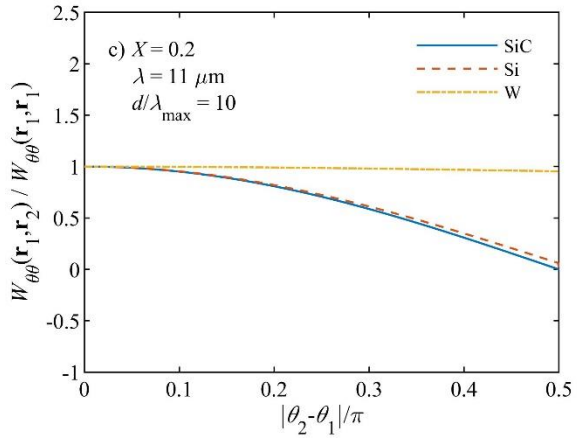

Figure 5.10 (contd.) – Same as Fig. 5.8 for the far-field regime ($\frac{d}{\lambda_{max}} = 10$).

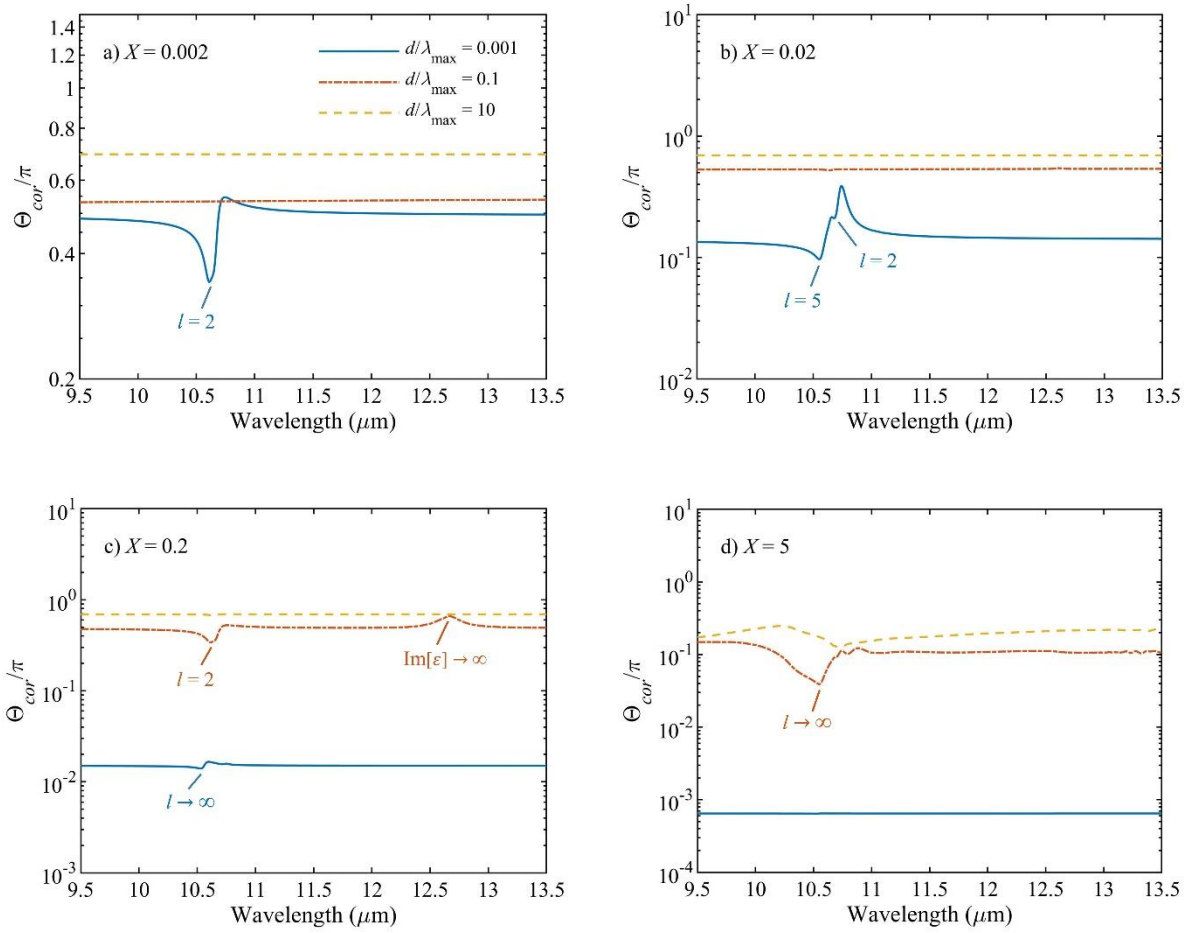

Figure 5.11 – Normalized correlation angle versus wavelength for a SiC sphere with (a) $X = 0.002$, (b) $X = 0.02$, (c) $X = 0.2$, and (d) $X = 5$.

5.6. Conclusions

The spectrum and spatial coherence of thermal emission by a homogeneous and isothermal sphere were analyzed in the extreme near-field, intermediate near-field, and far-field regimes. The energy density and correlation function of a sphere with an arbitrary size parameter and material were formulated using fluctuational electrodynamics. The energy density and spatial coherence along the radial and polar directions were studied for SiC, Si, and W spheres with X ranging from 0.002 to 5. It was shown that the energy density follows a power law of d^{-2} in the far field regardless of the size and material of the sphere. In the near-field regime, the energy density is governed by a power law of d^{-6} when $X \ll 1$ and $\frac{d}{a} \gg 1$ (dipole approximation is valid). The power of d in the near field increases with increasing X and decreasing $\frac{d}{a}$ until it eventually converges to that for a semi-infinite medium (between $d^{-0.5}$ and $d^{-3.5}$ depending on material and the near-field regime). It was also shown that the correlation length in the radial direction increases by several orders of magnitude from $\sim 0.001\lambda$ in the extreme near field to $\sim 0.1\lambda$ and $\sim \lambda$ in the intermediate near field and far field, respectively. The correlation angle in the extreme near field is strongly size dependent varying from 0.5π to 0.001π when X increases from 0.002 to 5. In the intermediate near-field and far-field regimes, the correlation angle has an order of magnitude of $\sim 0.1\pi$. It was demonstrated that the multipolar LSPhs reduce the spatial coherence along both radial and polar directions in the extreme and intermediate near-field regimes, whereas the dipolar LSPhs do not have any impacts on the spatial coherence. The spectral and spatial properties of thermal emission by a sphere are of great importance since spheres are the building blocks for many man-made materials.

5.7. Acknowledgment

The authors acknowledge support from the National Science Foundation under Grant No. CBET-1804360.

5.8. References

[1] C. Henkel, K. Joulain, R. Carminati and J. J. Greffet, Opt. Commun., 186, 57 (2000).

[2] M. Kreiter, J. Oster, R. Sambles, S. Herminghaus, S. Mittler-Neher and W. Knoll, Opt. Commun. 168, 117 (1999).

[3] J. J. Greffet, R. Carminati, K. Joulain, J. P. Mulet, S. Mainguy and Y. Chen, Nature 416, 61 (2002).

[4] O. G. Kollyukh, A. I. Liptuga, V. Morozhenko and V. I. Pipa, Opt. Commun. 225, 349 (2003).

[5] F. Marquier, K. Joulain, J. P. Mulet, R. Carminati, J. J. Greffet, and Y. Chen, Phys. Rev. B 69, 155412 (2004).

[6] P. Ben-Abdallah, J. Opt. Soc. Am. A, 21, 1368 (2004).

[7] M. Laroche, C. Arnold, F. Marquier, R. Carminati, J. J. Greffet, S. Collin, N. Bardou and J. L. Pelouard, Opt. Lett. 30, 2623 (2005).

[8] I. Celanovic, D. Perreault and J. Kassakian, Phys. Rev. B 72, 075127 (2005).

[9] B. J. Lee, C. J. Fu and Z. M. Zhang, Appl. Phys. Lett. 87, 071904 (2005).

[10] M. Laroche, R. Carminati and J.J. Greffet, Phys. Rev. Lett. 96, 123903 (2006).

[11] J. J. Greffet and C. Henkel, Contemp. Phys. 48, 183 (2007).

[12] S. M. Rytov, Y. A. Kravtsov and V. Tatarskii, *Principles of Statistical Radiophysics 3: Elements of Random Fields* (Springer, New York, 1989).

[13] R. Carminati and J.J. Greffet, Phys. Rev. Lett. 82, 1660, (1999).

[14] K. Joulain, J. P. Mulet, F. Marquier, R. Carminati and J. J. Greffet, Surf. Sci. Rep. 57, 59 (2005).

[15] C. Henkel and K. Joulain, Appl. Phys. B 84, 61 (2006).

[16] W. T. Lau, J. T. Shen, G. Veronis and S. Fan, Phys. Rev. E 76, 016601 (2007).

[17] K. Joulain and C. Henkel, Appl. Phys. B 93, 151 (2008).

[18] Y. Guo and Z. Jacob, J. Appl. Phys. 115, 234306 (2014).

[19] V. Yannopapas and N. V. Vitanov, Phys. Rev. Lett. 99, 053901 (2007).

[20] S. J. Petersen, S. Basu, B. Raeymaekers and M. Francoeur, J. Quant. Spectrosc. Radiat. Transfer 129, 277 (2013).

[21] S. J. Petersen, S. Basu, B. Raeymaekers and M. Francoeur, Photonics Nanostruct.: Fundam. Appl. 11, 167 (2013).

[22] A. Ghanekar, L. Lin, J. Su, H. Sun and Y. Zheng, 23, Opt. Express A1129 (2015).

[23] A. Ghanekar, L. Lin and Y. Zheng, Opt. Express 24, A868 (2016).

[24] G. W. Kattawar and M. Eisner, Appl. Opt. 9, 2685 (1970).

[25] M. Krüger, T. Emig and M. Kardar, Phys. Rev. Lett. 106, 210404 (2011).

[26] M. Krüger, G. Bimonte, T. Emig and M. Kardar, Phys. Rev. B 86, 115423 (2012).

[27] K. L. Nguyen, O. Merchiers and P. O. Chapuis, Appl. Phys. Lett. 112, 111906 (2018).

[28] L. Mandel and E. Wolf, *Optical Coherence and Quantum Optics* (Cambridge University Press, Cambridge, 1995).

[29] E. Wolf, *Introduction to the Theory of Coherence and Polarization of Light* (Cambridge University Press, Cambridge, 2007).

[30] C. F. Bohren and D. R. Huffman, *Absorption and Scattering of Light by Small Particles* (Wiley, New York, 1998).

[31] K. Zhang and D. Li, *Electromagnetic Theory for Microwaves and Optoelectronics* (Springer, New York, 2008).

[32] S. Enoch and N. Bonod, *Plasmonics: From Basics to Advanced Topics* (Springer, New York, 2012).

[33] G. Domingues, S. Volz, K. Joulain and J. J. Greffet, Phys. Rev. Lett. 94, 085901 (2005).

[34] A. V. Zayats and I. I. Smolyaninov, J. Opt. A: Pure Appl. Opt. 5, S16 (2003).

[35] M. L. Brongersma and P. G. Kik, *Surface Plasmon Nanophotonics* (Springer, New York, 2007).

[36] S. A. Maier, *Plasmonics: Fundamentals and Applications* (Springer, New York, 2007).

CHAPTER 6

THE QUANTUM CONFINEMENT EFFECT ON THE SPECTRUM OF NEAR-FIELD THERMAL RADIATION BY QUANTUM DOTS

This chapter has been reproduced from a previous publication in Journal of Applied Physics: *S. Zare and S. Edalatpour, J. Appl. Phys.* ***130****, 015108 (2021).*

6.1. Abstract

The quantum confinement effect on the spectrum of near-field thermal radiation by periodic and random arrays of quantum dots (QDs) is investigated. The local density of states (LDOS) thermally emitted by QD arrays made of three lead chalcogenides, namely, lead sulfide, lead selenide, and lead telluride, is computed at a near-field distance from the arrays. The dielectric function of the QDs is extracted from their absorption spectra by utilizing an optimization technique. The thermal discrete dipole approximation is used for computing the LDOS. It is shown that the peak wavenumber of near-field LDOS emitted by periodic arrays of lead chalcogenide QDs can be significantly modulated (up to 4490 cm^{-1}) by varying the size of the dots. The LDOS is proportional to the imaginary part of the QDs' polarizability which peaks at the bandgap energy of the QDs. The bandgap energy of the QDs (and thus the LDOS peak) is significantly affected by the quantum confinement effect which is size-dependent. While the magnitude of thermal radiation by random arrays of QDs can be different from the periodic arrays with the same filling factor by up to ±26%, the LDOS spectrum and peak location are the same for both periodic and random arrays. The peak wavenumber of near-field radiative heat transfer between the QD arrays is also strongly affected by quantum confinement in the QDs, and thus it can be tuned by changing the size of the QDs.

6.2. Introduction

Thermal radiation at sub-wavelength distances from an emitting medium, which is referred to as the near-field thermal radiation, can exceed the far-field blackbody limit by several orders of magnitude and be quasi-monochromatic [1]. Due to these unique properties, near-field thermal radiation has attracted significant attention for many promising applications in imaging [2-7], energy conversion using near-field

thermophotovoltaic (TPV) devices [8-24], nanomanufacturing [25-30], thermal management of electronic devices [31-33], and thermal rectification [34-46]. Near-field applications such as near-field TPV power generation and thermal rectification require tuning the spectrum of near-field thermal radiation. One mechanism that has been widely explored for customizing the near-field spectra is engineering the emitting medium at the sub-wavelength scale. Thermal radiation of these engineered materials, known as metamaterials, significantly differ from those of the corresponding bulk materials and can be tuned by modifying the geometry and size of the sub-wavelength features. A variety of metamaterials, such as periodic gratings [47-67], photonic crystals [68-74], hyperbolic metamaterials [75-104], nanoporous metamaterials [53,57,105-108], and double-negative metamaterials [101,109-133], have been proposed for tuning the near-field spectra. The spectrum of near-field thermal radiation by gratings can be tuned by varying the material properties and the geometry of the grating pattern [47-67]. Depending on the geometry and material properties, various modes such as transverse magnetic (TM) and transverse electric (TE) guided modes [52,55], spoof surface polaritons [52,55], hyperbolic modes [54], and magnetic polaritons [56] can be excited in gratings, resulting in near-field radiative properties different from those of the bulk material. Photonic crystals [68-74] are sub-wavelength periodic structures engineered to have a band gap that forbids propagation of a certain frequency range of thermal radiation. This property has been capitalized on for frequency-selective near-field thermal emission. Different mechanisms such as increased contribution from frustrated total internal reflection modes [73], band-folding effect [72], surface Bloch waves coupling [69], and the resonant leaky modes [70] can contribute to the near-field thermal emission depending on the geometry and material properties of the photonic crystal. Hyperbolic metamaterials [75-104] are anisotropic materials with metallic behavior (negative permittivity) in one direction and dielectric behavior (positive permittivity) in other directions. Thermal radiation by hyperbolic metamaterials shows a broadband enhancement due to the contribution of electromagnetic waves with very large wavevectors. Nanoporous materials [53,57,105-108] are anisotropic materials which can support a surface mode in addition to the one supported by the isotropic bulk material. The spectral location of the surface modes can be tuned by varying the filling fraction of the pores. Double-

negative metamaterials [101,109-133] have sub-wavelength inhomogeneities that are arranged in repeating patterns with a sub-wavelength periodicity. These metamaterials support both TM- and TE-polarized surface modes. The TE-polarized surface modes, which are not supported by most natural materials, cause an additional peak in the spectrum of near-field thermal radiation. Fabricating thermal metamaterials usually requires advanced, costly and time-consuming manufacturing techniques.

Another less explored but promising mechanism for tuning the spectrum of near-field thermal radiation is modulating the electronic structure of the emitter by capitalizing on the quantum confinement effect. The quantum confinement effect arises when the size of the emitter becomes comparable to the atomic length scales at least in one dimension. Quantum dots (QDs) are an example of these quantum-sized emitters which experience quantum confinement in three dimensions. They are quasi-spherical nanocrystals composed of tens to a few thousand atoms [134]. Because their dimensions are comparable to or smaller than the Bohr exciton radius, the electronic structure of QDs becomes quantized in the form of an ensemble of discrete energy levels. This quantization of energy levels results in modification of the bandgap and electromagnetic properties of the QDs compared to the bulk material in which energy levels are continuous [134].

The level of the quantum confinement depends on the size of the QDs [135]. As the size of the QDs decreases, the energy levels become more distant, and the bandgap increases. As such, the bandgap and electromagnetic properties of the QDs can be modulated by changing the size of the quantum dots. The size-dependent electromagnetic properties of quantum materials present an opportunity for designing thermal emitters with desired near-field emission spectra. In addition, QDs can be manufactured in bulk quantities and with high quality and size monodispersity using cost-efficient, solution-based techniques [136]. The opportunity for tuning the spectrum of near-field thermal radiation by capitalizing on the quantum confinement effect has not been explored. In this paper, we compute the near-field thermal emission spectra of QD arrays and show that the spectral location of the peak of thermal radiation can be tuned over a wide wavenumber range by changing the size of the QDs.

6.3. Problem Definition and Methods

A schematic of the problem under consideration is shown in Fig. 6.1. A periodic array of QDs with diameter *D* and temperature *T* is emitting into the free space. The QDs in the array are located on a rectangular grid with a pitch size of *L*. The LDOS thermally emitted at an observation distance *d* above the array and along the central axis of the QDs is to be calculated. Arrays of three lead chalcogenides QDs, namely lead sulfide (PbS), lead selenide (PbSe), and lead telluride (PbTe) QDs, are selected for this study. The Bohr exciton radii of lead chalcogenides are large (~18 nm for PbS [137], ~46 nm for PbSe [138], and ~150 nm for PbTe [139]), and therefore strong quantum confinement can be observed even for relatively large QDs of these materials. This allows tuning the spectral location of the peak of thermal emission over a wide range of wavenumbers. The bandgap of lead chalcogenides QDs is located in the wavenumber range of 5000-10000 cm^{-1} [140-144], which can be thermally excited. Lead chalcogenides QDs are more suitable for high-temperature emitters. For low temperate applications, mercury chalcogenides QDs [145] can be considered.

The electromagnetic (and thus thermal radiative) properties of QDs are determined from their dielectric function, ε, which is dependent on the size of the QDs. The size-dependent dielectric function of the QDs can be extracted from their measured absorbance spectra [140,141,143] by utilizing the Maxwell-Garnett effective medium theory (EMT) and the Kramers-Kronig (KK) relation [146]. The absorption spectra of dilute solutions (filling fractions of ~10^{-3} – 10^{-5}) of lead chalcogenides quantum dots in a transparent solvent have been measured using spectroscopy techniques [140,141,143]. The solvent for PbS and PbTe QDs is tetrachloroethylene (C_2Cl_4), while carbon tetrachloride (CCl_4) has been used for the PbSe QDs. For dilute solutions of QDs, the volume fraction of the QDs is very low and thus the absorption coefficient, α_λ, of the solution can be related to the dielectric function of the QDs using the Maxwell-Garnett EMT as [147]:

$$\alpha_\lambda = \frac{18\pi}{\lambda} \frac{n_s^3}{\left(\varepsilon' + 2n_s^2\right)^2 + \varepsilon''^2} \varepsilon'' \tag{6.1}$$

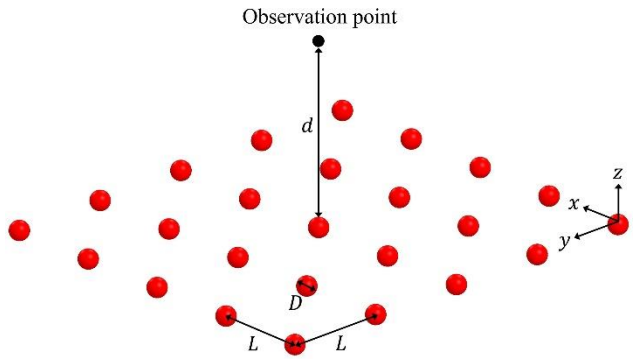

Figure 6.1 – A periodic array of QDs with diameter *D* is thermally emitting into the free space. The array has a pitch *L* along the *x*- and *y*-directions. The LDOS at an observation point located at a distance *d* above the array and along the central axis of the QDs is of interest.

where λ is the wavelength, n_s is the solvent refractive index (1.53 for C_2Cl_4 [148] and 1.46 for CCl_4 [148]), and ε' and ε'' are the real and imaginary parts of the dielectric function of the QDs, respectively. The measured absorbance spectra have arbitrary units, and therefore do not directly provide the magnitude of the absorption coefficient, α_λ. The magnitude of α_λ is determined from the measured absorption spectra using the following procedure. It has been experimentally observed that the quantum confinement effect in the lead chalcogenide QDs is negligible at wavelengths below 400 nm [149]. As such, the dielectric function of the lead chalcogenide QDs for wavelengths shorter than 400 nm is equal to that of the bulk. This allows calculating α_λ of the QD solutions in the spectral range of 0 – 400 nm using the dielectric function of the bulk and Eq. (6.1) [140,141]. For wavelengths longer than 400 nm, first the absorbance spectra are normalized by their value at λ = 400 nm. Then, the normalized spectra are multiplied by the absorption coefficient at 400 nm, $\alpha_{\lambda=400nm}$, as found using Eq. (6.1) and the dielectric function of the bulk, to obtain α_λ for $\lambda > 400$ nm.

Equation (6.1) provides a relation between α_λ and the dielectric function of the QDs, ε. However, the knowledge of α_λ is not sufficient for finding ε as there are two unknowns, namely ε' and ε'', in Eq.

(6.1). A relation between ε' and ε'' can be established via the KK relation. The KK relation provides an equation for determining ε' at a given wavelength when ε'' is known for all other wavelengths. To use the KK relation, first a wavelength interval between 0 and an upper limit, λ_{max}, is selected. The upper limit is selected such that α_λ is negligible for $\lambda > \lambda_{max}$. When α_λ is very small, ε'' is negligible and it does not contribute to ε'. The wavelength interval between 0 and λ_{max} is then discretized into N_λ equal subintervals of length $\Delta\lambda$. The wavelength subintervals are small enough such that the peaks and dips in the absorbance coefficient are captured in the discretized data. Finally, the discretized KK relation is used to relate the real part of the dielectric function at a given wavelength λ_j (i.e., $\varepsilon'(\lambda_j)$) to the imaginary part of the dielectric function at all other wavelengths (i.e, $\varepsilon''(\lambda_k)$, where $k = 1, 2, \ldots, N_\lambda+1$ and $k \neq j$) as [146]:

$$\varepsilon'\left(\lambda_j\right) = \varepsilon_\infty + \frac{2}{\pi}\sum_{\substack{k=1 \\ k\neq j}}^{N_\lambda+1} \frac{\lambda_j^2 \Delta\lambda}{\lambda_k\left(\lambda_j^2 - \lambda_k^2\right)} \varepsilon''\left(\lambda_k\right) \tag{6.2}$$

where $N_\lambda+1$ is the number of discretized wavelengths, and ε_∞ is the high-frequency dielectric function which equals 1.5 for PbSe [150] and 1.7 for PbS [151] and PbTe [152].

The real and imaginary parts of the dielectric function of the QDs are found using Eqs. (6.1) and (6.2) and by utilizing an optimization technique. A block diagram of the optimization technique is shown in Fig. 6.2. The optimization process starts with an initial guess for the imaginary part of the dielectric function of QDs, ε'', at all discretized wavelengths. Then, the real part of the dielectric function, ε', at a given wavelength λ_j ($j = 1, 2, \ldots, N_\lambda+1$), is computed from the imaginary part at all other wavelengths, λ_k ($k = 1, 2, \ldots, N_\lambda+1, k \neq j$), using the KK relation [Eq. (6.2)]. Using the initial guess for ε'' and the computed ε', the absorption coefficients at the discretized wavelengths, α_{λ_j} is estimated by Eq. (6.1). The total error involved in estimating α_λ is defined as the summation of the squared difference of the measured ($\alpha_{\lambda_j,meas}$) and computed ($\alpha_{\lambda_j,comp}$) absorption coefficients over the discretized wavelengths, i.e.,

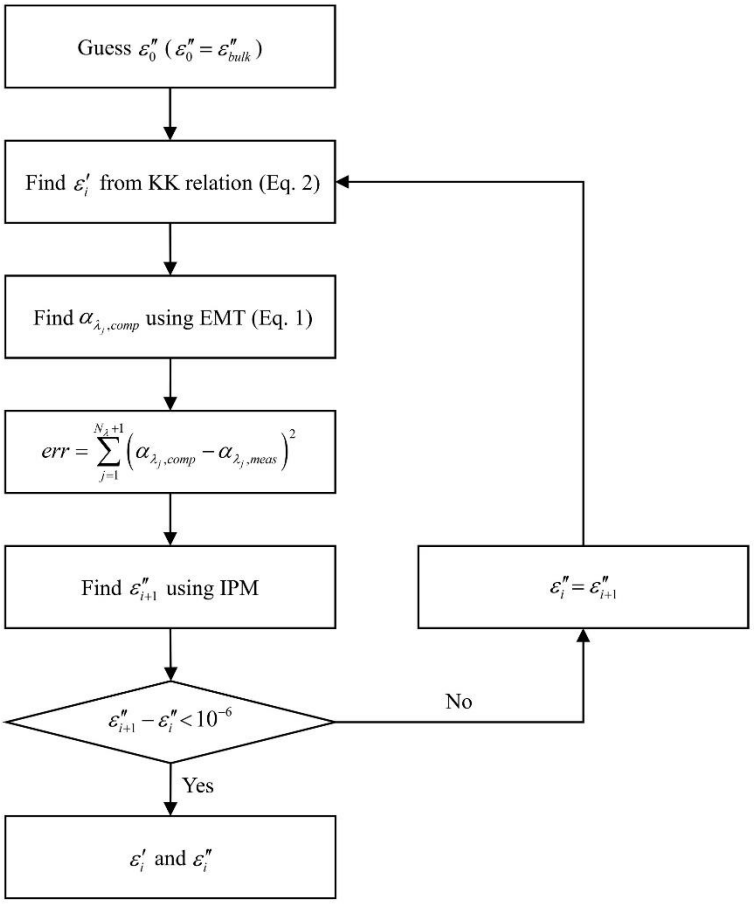

Figure 6.2 – A block diagram of the technique used for extracting the dielectric function of the QDs from their absorption coefficient. ε_m' and ε_m'' ($m = i, i+1$) refer to the real and imaginary parts of the dielectric function of the QDs in iteration m, respectively.

$$err = \sum_{j=1}^{N_\lambda+1}\left(\alpha_{\lambda_j,comp} - \alpha_{\lambda_j,meas}\right)^2 \tag{6.3}$$

Based on the error found from Eq. (6.3), ε'' is corrected for all discretized wavelengths. Then, ε' and α_λ are reevaluated in another iteration until the difference between ε'' in two consecutive iterations becomes less than 10^{-6} for all discretized wavelengths. To implement this optimization process, MATLAB's built-in *fmincon* function, which is a constrained nonlinear and multivariable minimization function, is utilized in which the interior-point method (IPM) is used for correcting ε'' in each iteration.

The objective function of *fmincon* is the total error defined by Eq. (6.3), while the decision variables are the imaginary parts of the dielectric function ε'' at the discretized wavelengths.

Once the size-dependent dielectric function of the QDs is found, the local density of states (LDOS) thermally emitted by a periodic array of QDs at a near-field observation distance from the array is computed using the periodic thermal discrete dipole approximation (T-DDA) [153]. In the periodic T-DDA, the unit cell of the array (one quantum dot in this study) is discretized into cubical sub-volumes with sizes much smaller than the wavelength, the observation distance, and the interdot spacing. In this case, the electric field within each sub-volume can be assumed as uniform (i.e., the sub-volumes behave as electric point dipoles) [153]. Then, the electric (magnetic) Green's function, $\mathbf{g}_{i,o}^{E(H)}$, representing the electric (magnetic) field generated in the unit-cell sub-volumes due to a point source at the observation location is obtained by solving a discretized form of Maxwell's equations as [153]:

$$\frac{1}{\alpha_i} V_i \varepsilon_0 \left(\varepsilon_i - 1\right) \mathbf{g}_{i,o}^{\gamma} - k_0^2 \sum_{j=1}^{N} V_j \left(\varepsilon_j - 1\right) \mathbf{G}_{i,j}^{0E,P} \cdot \mathbf{g}_{j,o}^{\gamma} = \mathbf{G}_{i,o}^{0\gamma,P} \ , \ \gamma = E \text{ or } H, \ i = 1, 2, \ldots, N \tag{6.4}$$

where α_i, V_i and ε_i are the polarizability, volume and dielectric function of sub-volume *i*, respectively, ε_0 is the free-space permittivity, k_0 is the magnitude of the wavevector in the free space, subscript *o* refers to the observation point, and $\mathbf{G}_{k,l}^{0E(H),P}$ is the electric (magnetic) periodic Greens function between points *k* and *l* in the free space [153]. It should be noted that the Greens function $\mathbf{g}_{i,o}^{E(H)}$ is wavevector-dependent, and thus Eq. (6.4) should be solved for all wavevectors in the Brillouin zone (i.e., wavevectors between $-\pi/L$ and π/L). The Green's functions for the replica (*m*, *n*) of sub-volume *i* in the unit cell can be found using $\mathbf{g}_{i,o}^{E(H)}$ as [153]:

$$\mathbf{g}_{imn,o}^{\gamma} = \mathbf{g}_{i,o}^{\gamma} e^{iL\left(mk_x + nk_y\right)}, \ m, n = 0, \pm 1, \pm 2, \ldots \tag{6.5}$$

Then, the total electric (magnetic) Greens function between replica (*m*, *n*) of sub-volume *i* and the observation point *o*, $\mathbf{G}_{imn,o}^{E(H)}$, can be found from the wavevector-dependent electric (magnetic) Greens functions as:

$$\mathbf{G}_{imn,o}^{\gamma} = \frac{L^2}{4\pi^2}\int_{-\pi/L}^{\pi/L}\int_{-\pi/L}^{\pi/L}\mathbf{g}_{imn,o}^{\gamma}\left(k_x,k_y\right)dk_y dk_x \text{ , } \gamma = E \text{ or } H \tag{6.6}$$

Finally, the spectral LDOS emitted by the array at the observation distance, ρ_ω, is found using the total electric and magnetic Greens functions computed using Eq. (6.6) as:

$$\rho_\omega = \frac{2k_0^2}{\pi\omega}\sum_{i=1}^{N}V_i\varepsilon_i''\sum_{m=0}^{N_k}\sum_{n=0}^{N_k}Trace\left[k_0^2\mathbf{G}_{imn,o}^{E}\otimes\mathbf{G}_{imn,o}^{E}+\mathbf{G}_{imn,o}^{H}\otimes\mathbf{G}_{imn,o}^{H}\right] \tag{6.7}$$

where ω is the angular frequency, *N* is the number of sub-volumes used for discretizing the unit cell of the array, $\otimes$ shows the outer product, and N_k is the number of wavevectors used for discretizing the Brillouin zone.

6.4. Results and Discussion

The dielectric function of PbS, PbSe, and PbTe QDs with various diameters *D* ranging from 3.3 nm to 6.8 nm is extracted from their absorption spectra using the optimization technique described in Sec. 6.3 (see Fig. 6.2). Several initial guesses, including ε'' of the bulk material (ε_{bulk}''), a constant (over wavelength) ε'' equal to ε_{bulk}'' at λ = 400 nm, and a ε'' inversely proportional to λ as $\varepsilon''\left(\lambda\right)=\frac{400\,\text{nm}}{\lambda\left(\text{in nm}\right)}\varepsilon_{bulk}''\left(400\,\text{nm}\right)$, are used for the decision variable when running the *fmincon* function. All initial guesses result in the same dielectric function for QDs. However, a faster convergence is achieved when ε'' of the bulk material is used as the initial guess. The ε'' of the bulk materials is obtained from literature [150-152].

As an example, the real and imaginary parts of the dielectric function of PbSe QDs are shown in Figs. 6.3(a) and 6.3(b), respectively. The dielectric function of a bulk of PbSe [150] is also shown in Fig. 6.3 for comparison. As it is seen from Fig. 6.3, ε'' of PbSe QDs has a peak in the wavenumber range of 5000 cm^{-1} – 10000 cm^{-1} (depending on the diameter of the QDs) which does not exist in ε'' of the bulk. The

imaginary part of the dielectric function represents absorption by the material. The dominant absorption mechanism in bulk lead chalcogenides (which are semiconducting materials) in this range of wavenumbers is the intrinsic absorption, i.e., the transition of electrons from the valence band to the conduction band due to absorption of photons with energy equal to or greater than the bandgap energy [154]. For this reason, ε'' of bulk lead chalcogenides abruptly increases at the bandgap energy (~2250 cm^{-1} for PbSe) above which photons can generate electron-hole pairs. Unlike bulk lead chalcogenides, ε'' of the QDs is negligible for wavenumbers slightly larger than the bandgap causing a peak in ε'' at the bandgap energy. Quantum dots have negligible ε'' above the bandgap energy since their energy levels are discrete due to the quantum confinement effect. As such, photons with energy slightly higher than the bandgap are less likely to be absorbed as their energy needs to exactly match the difference between two energy levels in the valence and conduction bands. This causes ε'' of the QDs to peak at the bandgap energy of the QDs. The bandgap energy of the QDs is strongly dependent on their size and so is the peak of their ε''. The peak of ε'' of the QDs significantly shifts toward smaller wavelengths as the diameter of the QDs increases. It is seen from Fig. 6.3(a) that ε' increases to a maximum value around the wavenumber of the peak of ε'' and then rapidly drops. This phenomenon is known as the anomalous dispersion [155].

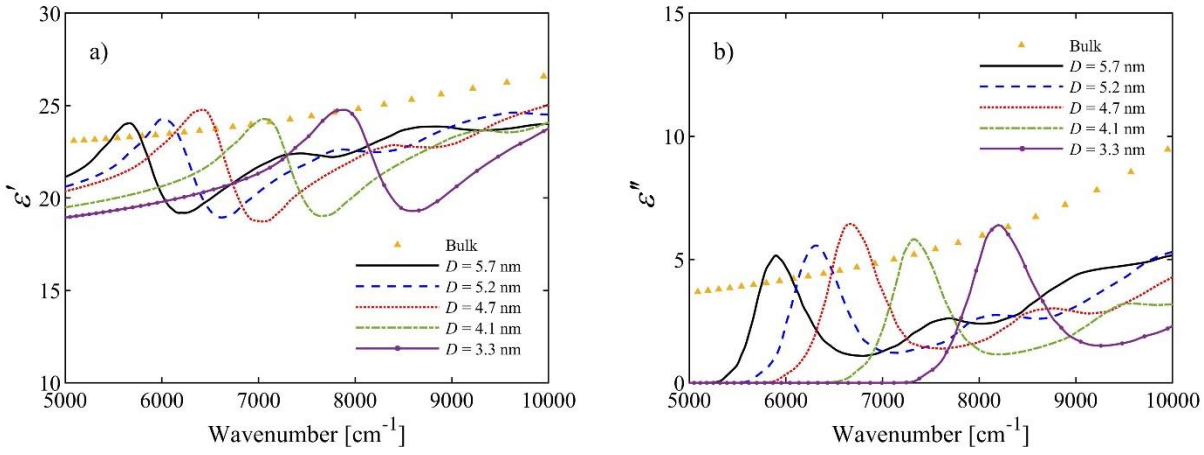

Figure 6.3 – The (a) real and the (b) imaginary parts of the size-dependent dielectric function of PbSe QDs in comparison with the dielectric function of a bulk of PbSe. The QDs have a diameter of *D*.

Using the extracted dielectric functions, the spectral LDOS due to thermal radiation of periodic arrays of PbS, PbSe, and PbTe QDs is computed at an observation distance *d* of 50 nm. The QDs in the arrays are separated by a distance of 4*D* in both *x*- and *y*-directions (i.e., the array pitch is *L* = 5*D*). Since the diameter of the QDs is much smaller than the wavelength, the observation distance and the interdot spacing, there is no need to discretize the QDs into smaller sub-volumes. The calculated LDOS spectra for PbS, PbSe, and PbTe QDs are shown in Figs. 6.4(a), 6.4(b), and 6.4(c), respectively. It is seen from Fig. 6.4 that the LDOS of the QD arrays has a peak whose spectral location strongly depends on the diameter of the QDs. The peak in the PbS spectrum is located at 5714 cm^{-1} when *D* = 6.8 nm. As *D* decreases, the spectral location of the peak shifts greatly toward higher frequencies such that the peak wavenumber reaches 10204 cm^{-1} (a shift of 4490 cm^{-1}) when *D* decreases by only 3.1 nm (i.e., when *D* = 3.7 nm). Similar size-dependent spectra are observed for periodic arrays of PbSe and PbTe QDs. The peak location of the LDOS thermally emitted by the PbSe (PbTe) QD arrays shifts from 5952 cm^{-1} (5682 cm^{-1}) for a diameter of 5.7 nm (6.7 nm) to 8265 cm^{-1} (6969 cm^{-1}) for a diameter of 3.3 nm (4.9 nm). The peaks observed in the LDOS spectra can be explained by considering the fact that thermal radiation by the QDs is proportional to the imaginary part of their electric polarizability given by the Clausius–Mossotti relation as $\alpha'' = \frac{3\pi D^3 \varepsilon''}{2|\varepsilon + 2|^2}$. It is seen that α'' is directly proportional to the imaginary part of the dielectric function, ε'', which represents absorption by the QDs. As discussed before, ε'' peaks at the bandgap energy of the QDs (see Fig. 6.3). As such, α'' and LDOS also exhibit a peak at the bandgap energy of the QDs. The bandgap energy of the QDs is strongly dependent on their diameter and so is the peak of thermal LDOS. The smaller the QDs, the larger the quantum confinement and the bandgap. As such, the peak of LDOS blue shifts significantly as QDs become smaller.

It should be noted that changing the pitch (or the filling factor) of the array mostly affects the magnitude of the LDOS rather than the spectral location of its peak. For example, the LDOS spectra for two arrays of 5.7-nm PbSe QDs with pitches of 5*D* (*f* = 0.021) and 6*D* (*f* = 0.015) are compared in Fig. 6.5. The

magnitude of the LDOS for a pitch of 6*D* is about 30% less than that for a pitch of 5*D* throughout the considered wavenumber range. The reduction in the magnitude of the LDOS for the array with $L = 6D$ is due to the smaller density of QDs in this array. The wavenumber of the LDOS peak, however, remains unchanged with increasing the array pitch from 5*D* to 6*D*. It should be noted that the coupling between neighboring QDs is negligible for both arrays with $L = 5D$ and $L = 6D$ due to the large interdot spacing. The coupling between neighboring QDs, which becomes significant for very dense arrays (where the interdot spacing << *D*), does not change the spectral location of the peak LDOS.

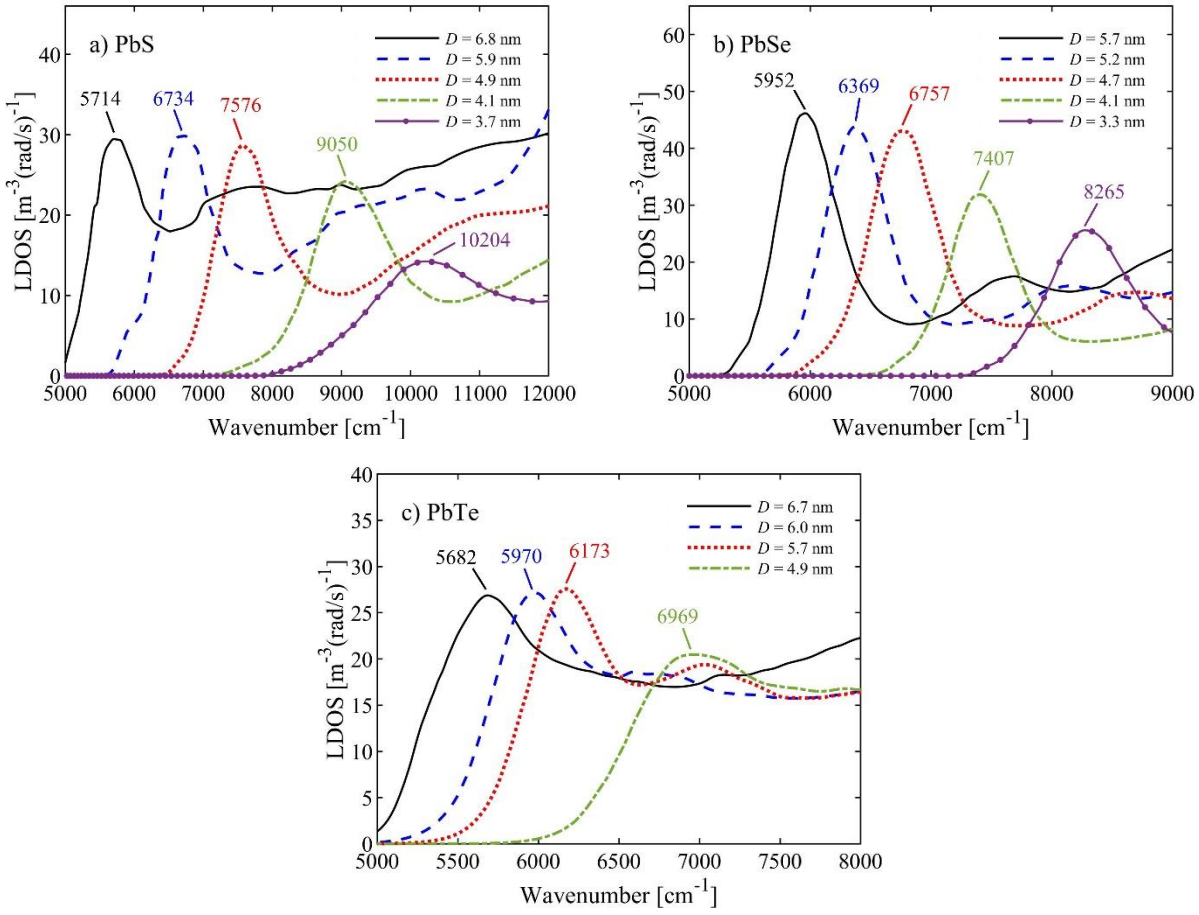

Figure 6.4 – Spectral LDOS thermally emitted by periodic arrays of (a) PbS, (b) PbSe, and (c) PbTe QDs with various diameters *D* at an observation distance of $d = 50$ nm above the array along the central axis of the QDs. The array pitch is 5*D*.

The effect of increasing the number of QD layers in the array on the magnitude and the spectrum of the LDOS is also studied. The LDOS thermally emitted by an array made of N_L layers of PbSe QDs (see the inset of Fig. 6.6) is shown in Fig. 6.6 for N_L ranging from 1 to 20. The QDs have a diameter of D = 5.7 nm, while the pitch size of the QD layers and the interlayer spacing are fixed at 5D. The LDOS is calculated at an observation distance of d = 50 nm above the top layer. It can be seen from Fig. 6.6 that adding QD layers to the array increases the magnitude of the emitted LDOS. The contribution of additional layers to the emitted LDOS decreases with increasing N_L such that increasing N_L beyond 10 does not affect the LDOS anymore. The magnitude of the total (spectrally integrated over a wavenumber range of 5000 – 9000 cm^{-1}) LDOS for N_L = 10 is 33.1% larger than that for an array with N_L = 1. The spectrum of the LDOS and the wavenumber of the LDOS peak, however, remains unchanged as additional layers are added to the array.

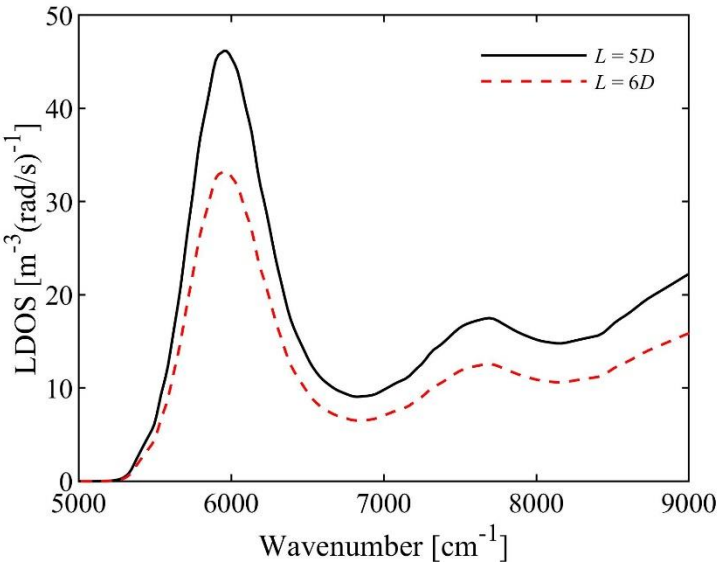

Figure 6.5 – The effect of array pitch on the thermally emitted LDOS. The spectral LDOS is calculated for periodic arrays of PbSe quantum dots with a diameter of D = 5.7 nm and pitches of L = 5D and L = 6D at an observation distance of d = 50 nm.

It should be noted that the peak of near-field radiative heat transfer between two identical arrays of QDs can also be strongly tuned by changing the diameter of the QDs. The peak of thermal radiation by the emitting array is located at the same wavenumber as the peak of absorption by the receiving array (both are located around the bandgap energy of the QDs). As such, the near-field radiative heat transfer between the two arrays also peaks around the bandgap energy of the QDs. As an example, near-field radiative heat flux between two periodic arrays of PbSe QDs with a pitch size of 5D separated by a gap of d = 50 nm is computed using the T-DDA for three different QD diameters. The emitting array is at 1200 K, while the receiving array is kept at 300 K. The near-field radiative heat flux between the two arrays is shown in Fig. 6.7 for three QD diameters of 4.7 nm, 5.2 nm, and 5.7 nm. The peak of near-field radiative heat transfer shifts significantly from 6725 cm^{-1} to 5925 cm^{-1}, when D slightly increases only from 4.7 nm to 5.7 nm.

Quantum dots can be fabricated in large quantities using cost-effective solution-based methods. The solution-based fabrication techniques result in random, rather than periodic, arrays of QDs. To study how the magnitude and spectrum of thermal radiation by random arrays are different from the periodic ones, the thermal LDOS for 100 random monolayer arrays is modeled using the non-periodic T-DDA [156]. The PbSe QDs with a diameter of 5.7 nm are considered for this study. The number of QDs in the random arrays is selected such that the filling factor of these arrays is the same as that of a periodic array with L = 6D (i.e., f = 0.015). Similar to the periodic array, a minimum interdot spacing of 5D is assumed between the QDs. The LDOS is calculated at a distance of d = 50 nm above the array. Initially, the LDOS is calculated for a 5L by 5L random array of QDs. Then, the array size is increased until no considerable change in the LDOS calculated at the distance of d = 50 nm is observed. An array size of 20L by 20L is found to be sufficient for modeling the LDOS at d = 50 nm. The spectral LDOS for the random arrays is compared with that for the periodic array in Fig. 6.8. As it is seen from this figure, the LDOS spectra and peak locations of the random arrays are similar to that for the periodic one. However, the magnitude of the LDOS fluctuates by 26% around its value for the periodic array. Figure 6.8 shows that the spectrum of near-field thermal radiation can be tuned using random arrays of QDs which can be fabricated in large quantities using cost-effective techniques.

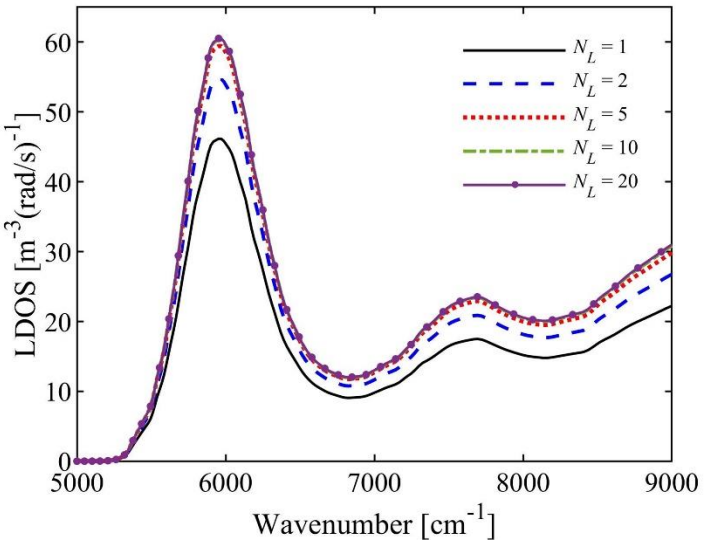

Figure 6.6 – The thermal LDOS emitted by N_L periodic layers of PbSe QDs with a diameter of D = 5.7 nm at an observation distance of d = 50 nm above the top layer. The pitch size of the periodic layers and the interlayer spacing are 5D.

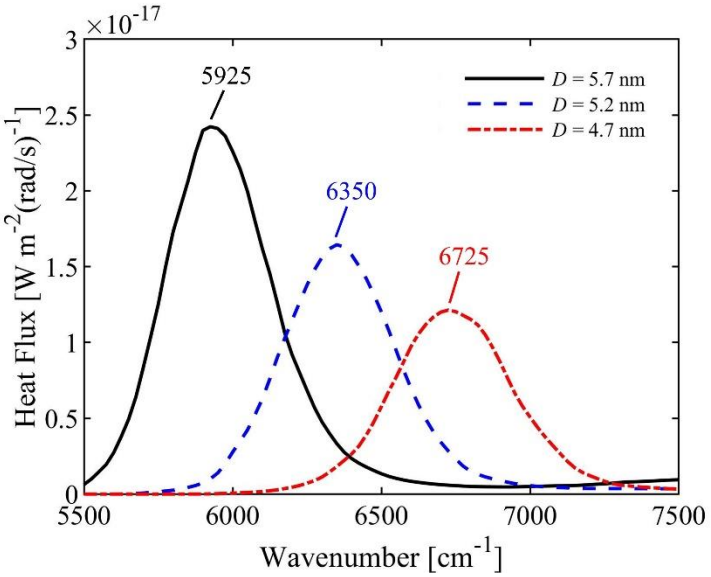

Figure 6.7 – Spectral heat flux between two periodic arrays of PbS QDs with various diameters D and an array pitch of 5D separated by a distance of 50 nm. The temperatures of the emitting and receiving arrays are 1200 K and 300 K, respectively.

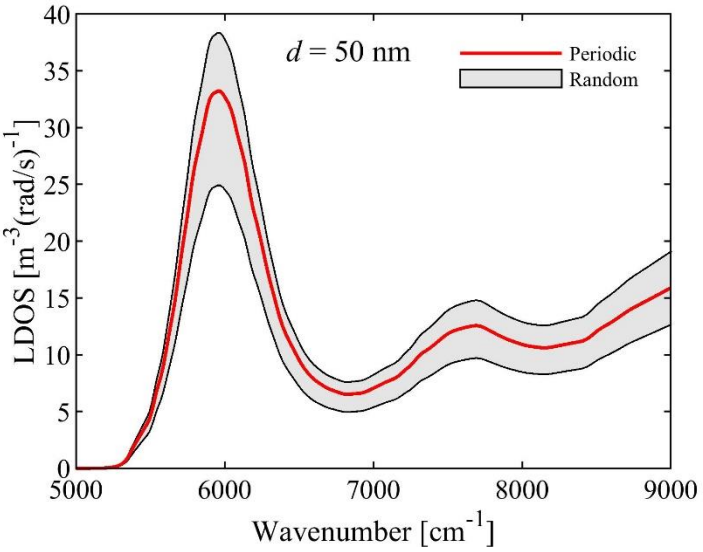

Figure 6.8 – Range of change in spectral LDOS thermally emitted by a randomly distributed array of PbSe quantum dots with a diameter of D = 5.7 nm and a filling factor of f = 0.015 relative to that emitted by a periodic array of the same D and f.

6.5. Conclusions

The thermally emitted LDOS by lead chalcogenide QD arrays at a near-field distance from the array as well as near-field radiative heat transfer between two identical lead chalcogenide QD arrays were calculated for various QD sizes using the T-DDA. The size-dependent dielectric function of the QDs was extracted from the measured absorption spectra found in the literature using the Maxwell-Garnett EMT, the KK relation and an optimization technique. It was shown that the near-field LDOS and heat flux have a peak around the bandgap energy of the QDs which strongly varies with the size of the QDs due to the quantum confinement effect. This peak is due to the large imaginary part of the polarizability of the QDs at the bandgap energy where interband transitions is the dominant absorption mechanism. This study shows that the spectrum of near-field thermal radiation can be tuned by capitalizing on the size-dependent quantum confinement effect.

6.6. Acknowledgment

This work is supported by the National Science Foundation under Grant No. CBET-1804360.

6.7. References

[1] K. Joulain, J. P. Mulet, F. Marquier, R. Carminati, and J. J. Greffet, Surf. Sci. Rep. 57, 59 (2005).

[2] Y. De Wilde, F. Formanek, R. Carminati, B. Gralak, P. A. Lemoine, K. Joulain, J. P. Mulet, Y. Chen, and J. J. Greffet, Nature 444, 740 (2006).

[3] Y. Kajihara, K. Kosaka, and S. Komiyama, Rev. Sci. Instrum. 81, 033706 (2010).

[4] A. C. Jones, and M. B. Raschke, Nano Lett. 12, 1475 (2012).

[5] H. A. Bechtel, E. A. Muller, R. L. Olmon, M. C. Martin, and M. B. Raschke, Proc. Natl. Acad. Sci. 111, 7191 (2014).

[6] X. Chen, D. Hu, R. Mescall, G. You, D. N. Basov, Q. Dai, and M. Liu, Adv. Mater. 31, 1804774 (2019).

[7] S. Labouesse, S. C. Johnson, H. A. Bechtel, M. B. Raschke, and R. Piestun, ACS Photonics 7, 3346 (2020).

[8] R. S. DiMatteo, P. Greiff, S. L. Finberg, K. A. Young-Waithe, H. K. H. Choy, M. M. Masaki, and C. G. Fonstad, Appl. Phys. Lett. 79, 1894 (2001).

[9] M. D. Whale and E. G. Cravalho, IEEE Trans. Energy Convers. 17, 130 (2002).

[10] A. Narayanaswamy and G. Chen, Appl. Phys. Lett. 82, 3544 (2003).

[11] M. Laroche, R. Carminati, and J. J. Greffet, J. Appl. Phys. 100, 63704 (2006).

[12] K. Park, S. Basu, W. P. King, and Z. M. Zhang, J. Quant. Spectrosc. Radiat. Transf. 109, 305 (2008).

[13] M. Francoeur, R. Vaillon, and M. P. Mengüç, M. P. IEEE Trans. Energy Convers. 26, 686 (2011).

[14] O. Ilic, M. Jablan, J. D. Joannopoulos, I. Celanovic, and M. Soljačić, Opt. Express 20, A366 (2012).

[15] M. P. Bernardi, O. Dupré, E. Blandre, P. O. Chapuis, R. Vaillon, and M. Francoeur, Sci. Rep. 5, 11626 (2015).

[16] S. Molesky and Z. Jacob, Phys. Rev. B 91, 205435 (2015).

[17] J. Z. J. Lau, V. N. S. Bong, and B. T. Wong, B. T. J. Quant. Spectrosc. Radiat. Transf. 171, 39 (2016).

[18] R. St-Gelais, G. R. Bhatt, L. Zhu, S. Fan, and M. Lipson, ACS Nano 11, 3001 (2017).

[19] N. Vongsoasup, M. Francoeur, and K. Hanamura, Int. J. Heat Mass Transfer 115, 326 (2017).

[20] A. Fiorino, L. Zhu, D. Thompson, R. Mittapally, P. Reddy, and E. Meyhofer, Nat. Nanotechnol. 13, 806 (2018).

[21] M. Lim, J. Song, J. Kim, S. S. Lee, I. Lee, and B. J. Lee, J. Quant. Spectrosc. Radiat. Transf. 210, 35 (2018).

[22] P. Sabbaghi, Y. Yang, J. Y. Chang, and L. Wang, J. Quant. Spectrosc. Radiat. Transf. 234, 108 (2019).

[23] G. R. Bhatt, B. Zhao, S. Roberts, I. Datta, A. Mohanty, T. Lin, J. M. Hartmann, R. St-Gelais, S. Fan and M. Lipson, Nat. Commun. 11, 2545 (2020).

[24] D. Milovich, J. Villa, E. Antolin, A. Datas, A. Marti, R. Vaillon, and M. Francoeur, J. Photonics Energy 10, 025503 (2020).

[25] H. J. Mamin, Appl. Phys. Lett. 69, 433 (1996).

[26] K. Wilder, C. F. Quate, D. Adderton, R. Bernstein, and V. Elings, Appl. Phys. Lett. 73, 2527 (1998).

[27] E. A. Hawes, J. T. Hastings, C. Crofcheck, and M. P. Mengüç, Opt. Lett. 33, 1383 (2008).

[28] V. L. Y. Loke, and M. P. Mengüç, JOSA A 27, 2293 (2010).

[29] Y. Wang, Z. Du, Y. Park, C. Chen, X. Zhang, and L. Pan, Opt. Lett. 40, 3918 (2015).

[30] J. Cui, J. Zhang, T. Barayavuga, X. Wang, X. He, L. Yang, H. Xie, X. Mei, and W. Wang, Integr. Ferroelectr. 179, 140 (2017).

[31] B. Guha, C. Otey, C. B. Poitras, S. Fan, and M. Lipson, Nano Lett. 12, 4546 (2012).

[32] K. Chen, P. Santhanam, and S. Fan, Phys. Rev. Appl. 6, 024014 (2016).

[33] L. Zhu, A. Fiorino, D. Thompson, R. Mittapally, E. Meyhofer, and P. Reddy, Nature 566, 239 (2019).

[34] C. R. Otey, W. T. Lau, and S. Fan, Phys. Rev. Lett. 104, 154301 (2010).

[35] S. Basu and M. Francoeur, Appl. Phys. Lett. 98, 113106 (2011).

[36] H. Iizuka and S. Fan, J. Appl. Phys. 112, 024304 (2012).

[37] L. P. Wang and Z. M. Zhang, Nanoscale Microscale Thermophys. Eng. 17, 337 (2013).

[38] Y. Yang, S. Basu, and L. Wang, Appl. Phys. Lett. 103, 163101 (2013).

[39] K. Joulain, Y. Ezzahri, J. Drevillon, B. Rousseau, and D. D. S. Meneses, Opt. Express 23, A1388 (2015).

[40] A. Ghanekar, J. Ji, and Y. Zheng, Appl. Phys. Lett. 109, 123106 (2016).

[41] Z. Zheng, X. Liu, A. Wang, and Y. Xuan, Int. J. Heat Mass Transfer 109, 63 (2017).

[42] A. Fiorino, D. Thompson, L. Zhu, R. Mittapally, S. A. Biehs, O. Bezencenet, N. El-Bondry, S. Bansropun, P. Ben-Abdallah, E. Meyhofer, and P. Reddy, ACS Nano 12, 5774 (2018).

[43] A. Ghanekar, Y. Tian, M. Ricci, S. Zhang, O. Gregory, and Y. Zheng, Opt. Express 26, A209 (2018).

[44] S. Wen, X. Liu, S. Cheng, Z. Wang, S. Zhang, and C. Dang, J. Quant. Spectrosc. Radiat. Transf. 234, 1 (2019).

[45] F. Chen, X. Liu, Y. Tian, and Y. Zheng, Adv. Eng. Mater. 23, 2000825 (2020).

[46] G. Xu, J. Sun, H. Mao, and T. Pan, Int. J. Therm. Sci. 149, 106179 (2020).

[47] S. A. Biehs, F. S. S. Rosa, and P. Ben-Abdallah, Appl. Phys. Lett. 98, 243102 (2011).

[48] R. Guérout, J. Lussange, F. S. S. Rosa, J. P. Hugonin, D. A. R. Dalvit, J. J. Greffet, A. Lambrecht, and S. Reynaud, Phys. Rev. B 85, 180301 (2012).

[49] J. Lussange, R. Guérout, F. S. S. Rosa, J. J. Greffet, A. Lambrecht, and S. Reynaud, Phys. Rev. B 86, 085432 (2012).

[50] X. L. Liu and Z. M. Zhang, Appl. Phys. Lett. 104, 251911 (2014).

[51] X. L. Liu, R. Z. Zhang, and Z. M. Zhang, Int. J. Heat Mass Transf. 73, 389 (2014).

[52] J. Dai, S. A. Dyakov, and M. Yan, Phys. Rev. B 92, 035419 (2015).

[53] A. Didari and M. P. Mengüç, Opt. Express 23, A1253 (2015).

[54] X. Liu, B. Zhao, and Z. M. Zhang, Phys. Rev. A 91, 062510 (2015).

[55] J. Dai, S. A. Dyakov, S. I. Bozhevolnyi, and M. Yan, Phys. Rev. B 94, 125431 (2016).

[56] Y. Yang and L. Wang, Phys. Rev. Lett. 117, 044301 (2016).

[57] V. Fernández-Hurtado, F. J. García-Vidal, S. Fan, and J. C. Cuevas, Phys. Rev. Lett. 118, 203901 (2017).

[58] K. Isobe, D. Hirashima, and K. Hanamura, Int. J. Heat Mass Transf. 115, 467 (2017).

[59] D. Lu, A. Das, and W. Park, Opt. Express 25, 12999 (2017).

[60] J. I. Watjen, X. L. Liu, B. Zhao, and Z. M. Zhang, J. Heat Transf. 139, 052704(2017).

[61] Y. Yang, P. Sabbaghi, and L. Wang, Int. J. Heat Mass Transf. 108, 851 (2017).

[62] H. Yu, D. Liu, Z. Yang, and Y. Duan, Sci. Rep. 7, 1 (2017).

[63] A. Didari, E. B. Elçioğlu, T. Okutucu-Özyurt, and M. P. Mengüç, J. Quant. Spectrosc. Radiat. Transf. 212, 120 (2018).

[64] J. Shen, X. Liu, H. He, W. Wu, and B. Liu, J. Quant. Spectrosc. Radiat. Transf. 211, 1 (2018).

[65] Y. H. Kan, C. Y. Zhao, and Z. M. Zhang, Phys. Rev. B 99, 035433 (2019).

[66] M. J. He, H. Qi, Y. T. Ren, Y. J. Zhao, and M. Antezza, Int. J. Heat Mass Transf. 150, 119305 (2020).

[67] F. R. Chen, G. An, and Z. G. Xu, J. Quant. Spectrosc. Radiat. Transf. 258, 107395 (2021).

[68] W. T. Lau, J. T. Shen, G. Veronis, S. Fan, and P. V. Braun, Appl. Phys. Lett. 92, 103106 (2008).

[69] P. Ben-Abdallah, K. Joulain, and A. Pryamikov, Appl. Phys. Lett. 96, 143117 (2010).

[70] A. Rodriguez, O. Ilic, P. Bermel, I. Celanovic, J. D. Joannopoulos, M. Soljačić, and S. Johnson Phys. Rev. Lett. 107, 114302 (2011).

[71] M. Tschikin, P. Ben-Abdallah, and S. A. Biehs, Phys. Lett. A 376, 3462 (2012).

[72] T. Inoue, T. Asano, and S. Noda, Phys. Rev. B 95, 125307 (2017).

[73] M. Elzouka, and S. Ndao, J. Quant. Spectrosc. Radiat. Transf. 204, 56 (2018).

[74] T. Inoue, T. Asano, and S. Noda, Opt. Express 26, 32074 (2018).

[75] S. A. Biehs and M. Tschikin, Phys. Rev. Lett. 109, 104301 (2012).

[76] Y. Guo, C. L. Cortes, S. Molesky, and Z. Jacob, Appl. Phys. Lett. 101, 131106 (2012).

[77] Y. Guo and Z. Jacob, Opt. Express 21, 15014 (2013).

[78] X. L. Liu, R. Z. Zhang, and Z. M. Zhang, Appl. Phys. Lett. 103, 213102 (2013).

[79] B. Liu and S. Shen, Phys. Rev. B 87, 115403 (2013).

[80] C. Simovski, S. Maslovski, I. Nefedov, and S. Tretyakov, Opt. Express 21, 14988 (2013).

[81] M. Tschikin, S. A. Biehs, R. Messina, and P. Ben-Abdallah, J. Opt. 15, 105101 (2013).

[82] T. J. Bright, X. L. Liu, and Z. M. Zhang, Opt. Express 22, A1112 (2014).

[83] S. Lang, M. Tschikin, S. A. Biehs, A. Y. Petrov, and M. Eich, Appl. Phys. Lett. 104, 121903 (2014).

[84] X. Liu, R. Z. Zhang, and Z. Zhang, ACS Photonics 1, 785 (2014).

[85] B. Liu, J. Shi, K. Liew, and S. Sheng, Opt. Commun. 314, 57 (2014).

[86] Y. Bai, Y. Jiang, and L. Liu, J. Quant. Spectrosc. Radiat. Transf. 158, 61 (2015).

[87] S. A. Biehs, S. Lang, A. Y. Petrov, M. Eich, and P. Ben-Abdallah, Phys. Rev. Lett. 115, 174301 (2015).

[88] J. Y. Chang, S. Basu, and L. Wang, J. Appl. Phys. 117, 054309 (2015).

[89] J. Y. Chang, Y. Yang, and L. Wang, Int. J. Heat Mass Transf. 87, 237 (2015).

[90] J. Liu and E. Narimanov, Phys. Rev. B 91, 041403 (2015).

[91] M. Tschikin, S. A. Biehs, P. Ben-Abdallah, S. Lang, A. Y. Petrov, and M. Eich, J. Quant. Spectrosc. Radiat. Transf. 158, 17 (2015).

[92] S. Jin, M. Lim, S. S. Lee, and B. J. Lee, Opt. Express 24, A635 (2016).

[93] R. Messina, P. Ben-Abdallah, B. Guizal, M. Antezza, and S. A. Biehs, Phys. Rev. B 94, 104301 (2016).

[94] S. A. Biehs, and P. Ben-Abdallah, Z. Naturforsch. A, 72, 115 (2017).

[95] T. Ikeda, K. Ito, and H. Iizuka, J. Appl. Phys. 121, 013106 (2017).

[96] K. Shi, F. Bao, and S. He, ACS Photonics 4, 971 (2017).

[97] B. Zhao, B. Guizal, Z. M. Zhang, S. Fan, and M. Antezza, Phys. Rev. B 95, 245437 (2017).

[98] L. Ge, Y. Cang, K. Gong, L. Zhou, D. Yu, and Y. Luo, AIP Adv. 8, 085321 (2018).

[99] Q. M. Zhao, T. B. Wang, D. J. Zhang, W. X. Liu, T.B. Yu, Q. H. Liao, and N. H. Liu, Chin. Phys. B 27, 094401 (2018).

[100] A. Ghanekar, Y. Tian, X. Liu, and Y. Zheng, J. Photonics Energy 9, 032706 (2019).

[101] J. Y. Chang, P. Sabbaghi, and L. Wang, Int. J. Heat Mass Transf. 158, 120023 (2020).

[102] W. Du, J. Yang, S. Zhang, N. Iqbal, Y. Dang, J. B. Xu, and Y. Ma, Nano Energy, 78, 105264 (2020).

[103] J. Song, Q. Cheng, L. Lu, B. Li, K. Zhou, B. Zhang, Z. Luo, X. Zhou, Phys. Rev. Appl. 13, 024054 (2020).

[104] X. Wu, and C. Fu, J. Quant. Spectrosc. Radiat. Transf. 258, 107337 (2021).

[105] S. A. Biehs, P. Ben-Abdallah, F. S. S. Rosa, K. Joulain, and J. J. Greffet, Opt. Express 19, A1088 (2011).

[106] E. Y. Santiago, J. E. Perez-Rodriguez, and R. Esquivel-Sirvent, J. Phys. Chem. C 121, 12392 (2017).

[107] T. Zhou, T. B. Wang, Q. H. Liao, J. T. Liu, T. B. Yu, and N. H. Liu, Phys. Lett. A 381, 1976 (2017).

[108] H. Yu, Y. Duan, and Z. Yang, Int. J. Heat Mass Transf. 123, 67 (2018).

[109] K. Joulain and J. Drevillon, Phys. Rev. B 81, 165119 (2010).

[110] S. Basu M. Francoeur, Appl. Phys. Lett. 99, 143107 (2011).

[111] M. Francoeur, S. Basu, and S. J. Petersen, Opt. Express 19, 18774 (2011).

[112] Z. Zheng and Y. Xuan, Int. J. Heat Mass Transf. 54, 1101 (2011).

[113] Z. Zheng and Y. Xuan, Chi. Sci. Bull. 56, 2312 (2011).

[114] L. Cui, Y. Huang, and J. Wang, J. Appl. Phys. 112, 084309 (2012).

[115] S. Basu and L. Wang, Appl. Phys. Lett. 102, 053101 (2013).

[116] L. Cui, Y. Huang, J. Wang, and K. Y. Zhu, Appl. Phys. Lett. 102, 053106 (2013).

[117] S. J. Petersen, S. Basu, and M. Francoeur, Photonics Nanostructures: Fundam. Appl. 11, 167 (2013).

[118] S. J. Petersen, S. Basu, B. Raeymaekers, and M. Francoeur, J. Quant. Spectrosc. Radiat. Transf. 129, 277 (2013).

[119] S. Basu and M. Francoeur, Opt. Lett. 39, 1266 (2014).

[120] D. Drosdoff, A. D. Phan, and L. M. Woods, Adv. Opt. Mater. 2, 1038 (2014).

[121] H. Iizuka and S. Fan, J. Quant. Spectrosc. Radiat. Transf. 148, 156 (2014).

[122] Y. Bai, Y. Jiang, and L. Liu, J. Phys. D: Appl. Phys. 47, 445304 (2014).

[123] Y. Bai, Y. Jiang, and L. Liu, J. Quant. Spectrosc. Radiat. Transf. 158, 36 (2015).

[124] S. Basu, Y. Yang, and L. Wang, Appl. Phys. Lett. 106, 033106 (2015).

[125] A. Didari and M. P. Mengüç, Opt. Express 23, A547 (2015).

[126] A. Ghanekar, L. Lin, J. Su, H. Sun, and Y. Zheng, Opt. Express 23, A1129 (2015).

[127] N. Zhou and X. Xu, J. Quant. Spectrosc. Radiat. Transf. 167, 156 (2015).

[128] A. Ghanekar, L. Lin, and Y. Zheng, Opt. Express 24, A868 (2016).

[129] A. Didari, M. P. Mengüç, J. Quant. Spectrosc. Radiat. Transf. 197, 95 (2017).

[130] A. Ghanekar, Y. Tian, S. Zhang, Y. Cui, and Y. Zheng, Materials 10, 885 (2017).

[131] Q. Zhao, T. Zhou, T. Wang, W. Liu, J. Liu, T. Yu, Q. Liao, and N. Liu, J. Phys. D: Appl. Phys. 50, 145101 (2017).

[132] K. Isobe and K. Hanamura, Int. J. Heat Mass Transf. 134, 807 (2019).

[133] Y. Taniguchi, K. Isobe, and K. Hanamura, Appl. Therm. Eng. 183, 116041 (2021).

[134] G. Schmid, Nanoparticles: from theory to application (John Wiley & Sons, Inc., Hoboken, NJ, 2011).

[135] H. V. Demir, and S. V. Gaponenko, Applied nanophotonics (Cambridge University Press, New York, NY, 2018).

[136] A. R. Kirmani, J. M. Luther, M. Abolhasani, and A. Amassian, ACS Energy Lett. 5, 3069 (2020).

[137] W. Ma, J. M. Luther, H. Zheng, Y. Wu, and A. P. Alivisatos, Nano Lett. 9, 1699 (2009).

[138] F. W. Wise, Acc. Chem. Res. 33, 773 (2000).

[139] J. E. Murphy, M. C. Beard, A. G. Norman, S. P. Ahrenkiel, J. C. Johnson, P. Yu, O. I. Mićić, R. J. Ellingson, and A. J. Nozik, J. Am. Chem. Soc. 128, 3241 (2006).

[140] I. Moreels, K. Lambert, D. De Muynck, F. Vanhaecke, D. Poelman, J. C. Martins, G. Allan, and Z. Hens, Chem. Mater. 19, 6101 (2007).

[141] I. Moreels, K. Lambert, D. Smeets, D. De Muynck, T. Nollet, J. C. Martins, F. Vanhaecke, A. Vantomme, C. Delerue, G. Allan, Z. Hens, ACS Nano 3, 3023 (2009).

[142] L. Yan, X. Shen, Y. Zhang, T. Zhang, X. Zhang, Y. Feng, J. Yin, J. Zhao, and W. W. William, RSC Adv. 5, 54109 (2015).

[143] J. L. Peters, J. de Wit, and D. Vanmaekelbergh, Chem. Mater. 31, 1672 (2019).

[144] Y. Xia, S. Liu, K. Wang, X. Yang, L. Lian, Z. Zhang, J. He, G. Liang, S. Wang, M. Tan, H. Song, D. Zhang, J. Gao, J. Tang, M. C. Beard, and J. Zhang, Adv. Funct. Mater. 30, 1907379 (2020).

[145] E. Lhuillier, and P. Guyot-Sionnest, IEEE J. Sel. Top. Quantum Electron. 23, 1 (2017).

[146] I. Moreels, G. Allan, B. De Geyter, L. Wirtz, C. Delerue, and Z. Hens, Phys. Rev. B 81, 235319 (2010).

[147] D. Ricard, M. Ghanassi, and M. C. Schanne-Klein, Opt. Commun. 108, 311 (1994).

[148] H. H. Marvin, Phys. Rev. Series I 34, 161 (1912).

[149] I. Moreels, and Z. Hens, Small 4, 1866 (2008).

[150] N. Suzuki, K. Sawai, and S. Adachi, J. Appl. Phys. 77, 1249 (1995).

[151] H. Kanazawa and S. Adachi, J. Appl. Phys. 83, 5997 (1998).

[152] N. Suzuki and S. Adachi, Jpn. J. Appl. Phys. 33, 193 (1994).

[153] S. Edalatpour, Phys. Rev. E 99, 063308 (2019).

[154] M. S. Dresselhaus, Solid State Physics, Part II: Optical Properties of Solids (Massachusetts Institute of Technology, Cambridge, MA, 2001).

[155] F. Wooten, Optical Properties of Solids (Academic Press, Cambridge, MA, 2013).

[156] S. Edalatpour, M. Čuma, T. Trueax, R. Backman, and M. Francoeur, Phys. Rev. E 91, 063307 (2015).

CHAPTER 7

CONCLUSIONS AND RECOMMENDATIONS

This dissertation studies tuning the spectrum of near-field thermal radiation using metamaterials, which are proposed for designing materials with radiative properties desirable for near-field thermal radiation applications. The main results and contributions of this research as well as some recommendations for future works are discussed hereafter.

7.1. Experimental Demonstration of Tuning the Spectrum of Near-Field Thermal Radiation Using Metamaterials

In this dissertation, a new simple and robust technique was established for measuring the near-field thermal radiation spectra. In this technique, the evanescent waves present at near-field distances from the emitting medium are coupled to a high-refractive-index internal reflection element (IRE). The coupled waves, which become propagating inside the IRE, are guided to an FTIR spectrometer where the spectrum of thermally emitted waves is recorded. As described in Chapter 2, this spectroscopy technique was shown to be capable of capturing the peaks in the near-field thermal radiation spectra due to the thermal excitation of resonant surface modes in quartz and silica as well as frustrated modes in PTFE. Moreover, the first experimental demonstration of broadband near-field thermal emission of hyperbolic modes from a uniaxial anisotropic medium, namely hexagonal boron nitride, was provided using this spectroscopy technique. The measured spectra were shown to be in great agreement with those predicted using the framework of fluctuational electrodynamics.

The implemented technique was used in this dissertation to experimentally investigate the spectrum of near-field thermal radiation from metamaterials, as described in Chapter 3. For this purpose, two periodic arrays of frustum-shaped 6H-SiC nanopillars with nanoscale interpillar spacings were fabricated on a 6H-SiC substrate, and the near-field spectra were measured. It was experimentally demonstrated that thermal emission of localized surface phonons (LSPhs) in the Reststrahlen band of 6H-SiC causes narrow peaks in the near-field spectrum. The peaks due to thermal emission of longitudinal monopole as well as

transverse dipole, quadrupole, and octupole were measured in the near-field thermal radiation spectra of the fabricated samples. Moreover, it was demonstrated that the spectral locations of the LSPh peaks in the near-field spectra of the nanopillar arrays vary with the height of the nanopillars, experimentally demonstrating that the near-field spectra can be tuned by engineering the materials at the sub-wavelength scale.

The experimental setup presented in this dissertation can be modified in future studies to capture a wider range of evanescent waves in the recorded near-field spectrum. In its current form, the setup is guiding the waves with k_ρ between $\sin(20.4°)n_1k_0$ and $\sin(69.6°)n_1k_0$ to an FTIR spectrometer. This limitation is due to the geometry of the IRE used in the setup, which has a trapezoidal cross-section with a beveled side of a fixed angle of 45°. The range of waves guided to the FTIR spectrometer can be expanded to include waves with $0 < k_\rho < n_1k_0$ by utilizing a hemispherical IRE in the setup instead of a trapezoidal IRE.

The spectroscopy technique established in this dissertation can be used in future studies to investigate the spectrum of near-field thermal radiation by other metamaterials proposed for tuning the near-field spectrum. Also, theoretical and numerical models should be developed to predict the redshifts in the near-field spectra of metamaterials measured using this technique and find the exact spectral location of near-field resonances, which are of great importance for near-field thermal radiation applications.

7.2. Prediction of the Spectrum of Near-Field Thermal Radiation in Nanowires and Nanospheres

The validity of the effective medium theory (EMT), which is commonly used for modeling thermal radiation by nanostructures, was examined for predicting near-field thermal radiation by nanowire arrays in Chapter 4. The results predicted by the Maxwell-Garnett (MG) and Bruggeman (BR) EMTs were compared with those obtained from a numerically exact method, namely the thermal discrete dipole approximation (T-DDA), for arrays of nanowires made of quartz and indium tin oxide (ITO). It was shown that the MG EMT agrees well with T-DDA for ITO nanowires. However, neither of the EMTs were capable of accurately estimating the magnitude and spectrum of near-field energy density for a

quartz nanowire array, which supports LSPhs. The conditions at which the EMTs agree the best with the exact numerical results were quantified for the quartz array and the shortcoming of the EMTs in accurate prediction of near-field thermal radiation in the lateral direction was also demonstrated. Since metamaterials made of polaritonic materials supporting LSPhs in the infrared region of the spectrum are of great interest for near-field thermal radiation, it is recommended that exact numerical methods are utilized to design the desired emitters for near-field thermal radiation applications.

In Chapter 5, analytical expressions were developed for predicting the energy density and spatial correlation function of thermal emission by spherical particles. Using the developed expressions, the spectral and total energy density at near-field and far-field distances from a single sphere was studied for various materials and sizes. The power laws governing the dependence of energy density on the observation distance, *d*, were also extracted in the near-field and far-field regimes. It was shown that the far-field energy density follows a power law of d^{-2} regardless of the sphere size. In the near-field regime, however, it was shown that the energy density is governed by a power law of d^{-6} when $X \ll 1$ and $\frac{d}{a} \gg 1$ (where *X* and *a* are the size parameter and radius of the sphere, respectively). The power of *d* in the near-field regime increases with increasing *X* and decreasing $\frac{d}{a}$ until it converges to that for a semi-infinite medium. Furthermore, it was shown that the near-field thermal radiation by polaritonic materials, such as SiC, is dominated by spectral peaks due to thermal excitation of LSPhs. It was also demonstrated that the spectral location of the dominant LSPh in a spherical particle can be tuned by varying the sphere size. In addition, the spatial coherence of thermal field emitted by a sphere was studied in radial and polar directions, and the effect of LSPhs on the correlation length and angle was discussed. It was shown that the spatial correlation length of the thermally emitted waves from a sphere varies by several orders of magnitude (between ~0.001λ and ~λ) when the observation distance changes from the extreme near-field regime to the far-field regime. These spectral and spatial properties of thermal radiation by a sphere can be of great interest for designing emitters that exhibit spectrally-selective

thermal emission and different spatial coherence in radial and polar directions. Studying the spectrum and spatial coherence of near-field thermal emission from periodic and random arrays of spherical nanoparticles of polaritonic materials, which is the configuration used in practice, is recommended for future studies.

7.3. Near-Field Thermal Radiation by Quantum Dots

Finally, the possibility of tailoring the spectrum of near-field thermal radiation by capitalizing on quantum confinement effect in emitters with a quantum size was explored in Chapter 6. For this purpose, the near-field thermal radiation spectra for periodic and random arrays of quantum dots (QDs) made of three lead chalcogenides, namely PbSe, PbS, and PbTe, were calculated using the T-DDA. The dielectric functions of the lead-chalcogenide QDs with various diameters ranging from 3.3 to 6.8 nm were extracted from their absorption spectra. It was shown that the near-field thermal radiation spectrum for QD arrays peaks around the bandgap of the QDs. The peak location can be significantly (by up to ~4500 cm^{-1}) tuned with varying the diameter of QDs due to the size dependence of the bandgap in QDs. The size dependence and spectral tunability of near-field thermal radiation by QDs were observed for both periodic and random arrays. As QDs can be manufactured in bulk quantities using solution-based techniques, the size-dependent near-field radiation by QD arrays offers a new, cost-efficient approach to engineering the spectrum of near-field thermal radiation. While the results presented in this dissertation provide a theoretical prediction, a next step in this project would be to experimentally demonstrate tuning the near-field spectra predicted for QD emitters. Closely-packed QD arrays can be fabricated using solution-based techniques and the spectroscopy technique presented in Chapter 2 can be utilized to measure the spectrum of near-field thermal radiation by QD arrays. Besides lead chalcogenides, QDs made of mercury chalcogenides (HgS, HgSe, and HgTe) and silver selenide (Ag_2Se) are promising candidates for exploring the potential of QDs as tunable thermal emitters. The bandgaps of these materials are in the infrared region of the electromagnetic spectrum, where can be thermally emitted.

BIBLIOGRAPHY

A. Babuty, K. Joulain, P.-O. Chapuis, J.-J. Greffet, and Y. De Wilde, Phys. Rev. Lett. 110, 146103 (2013).

Y. Bai, Y. Jiang, and L. Liu, J. Phys. D: Appl. Phys. 47, 445304 (2014).

Y. Bai, Y. Jiang, and L. Liu, J. Quant. Spectrosc. Radiat. Transf. 158, 61 (2015).

Y. Bai, Y. Jiang, and L. Liu, J. Quant. Spectrosc. Radiat. Transf. 158, 36 (2015).

C.A. Balanis, Advanced Engineering Electromagnetics 2nd ed. (John Wiley & Sons, Inc., New Jersey, 2012).

S. Basu and M. Francoeur, Appl. Phys. Lett. 98, 113106 (2011).

S. Basu and M. Francoeur, Appl. Phys. Lett. 99, 143107 (2011).

S. Basu and M. Francoeur, Opt. Lett. 39, 1266 (2014).

S. Basu and L. Wang, Appl. Phys. Lett. 102, 053101 (2013).

S. Basu, Y. Yang, and L. Wang, Appl. Phys. Lett. 106, 033106 (2015).

H. A. Bechtel, E. A. Muller, R. L. Olmon, M. C. Martin, and M. B. Raschke, Proc. Natl. Acad. Sci. 111, 7191 (2014).

P. Ben-Abdallah, J. Opt. Soc. Am. A, 21, 1368 (2004).

P. Ben-Abdallah, K. Joulain, and A. Pryamikov, Appl. Phys. Lett. 96, 143117 (2010).

M. P. Bernardi, O. Dupré, E. Blandre, P.-O. Chapuis, R. Vaillon, and M. Francoeur, Sci. Rep. 5, 11626 (2015).

M. P. Bernardi, D. Milovich, and M. Francoeur, Nat. Commun. 7, 12900 (2016).

G. R. Bhatt, B. Zhao, S. Roberts, I. Datta, A. Mohanty, T. Lin, J. M. Hartmann, R. St-Gelais, S. Fan and M. Lipson, Nat. Commun. 11, 2545 (2020).

S. A. Biehs and P. Ben-Abdallah, Zeitschrift für Naturforschung A 72, 115 (2016).

S. A. Biehs, P. Ben-Abdallah, F. S. S. Rosa, K. Joulain, and J. J. Greffet, Opt. Express 19, A1088 (2011).

S. A. Biehs, S. Lang, A. Y. Petrov, M. Eich, and P. Ben-Abdallah, Phys. Rev. Lett. 115, 174301 (2015).

S. A. Biehs, F. S. S. Rosa, and P. Ben-Abdallah, Appl. Phys. Lett. 98, 243102 (2011).

S. A. Biehs, M. Tschikin, and P. Ben-Abdallah, Phys. Rev. Lett. 109, 104301 (2012).

C. F. Bohren and D. R. Huffman, *Absorption and Scattering of Light by Small Particles* (Wiley, New York, 1998).

T. J. Bright, X. L. Liu, and Z. M. Zhang, Opt. Express 22, A1112 (2014).

M. L. Brongersma and P. G. Kik, *Surface Plasmon Nanophotonics* (Springer, New York, 2007).

D. A. G. Bruggeman, Ann. Phys. (Leipzig) 24, 636 (1935).

Y. Cai, L. Zhang, Q. Zeng, L. Cheng, and Y. Xu, Solid State Commun. 141, 262 (2007).

R. Carminati and J.J. Greffet, Phys. Rev. Lett. 82, 1660, (1999).

I. Celanovic, D. Perreault and J. Kassakian, Phys. Rev. B 72, 075127 (2005).

J. Y. Chang, S. Basu and L. Wang, J. Appl. Phys. 117, 054309 (2015).

J. Y. Chang, P. Sabbaghi, and L. Wang, Int. J. Heat Mass Transf. 158, 120023 (2020).

J. Y. Chang , P. Sabbaghi, Y. S. Weng, Y. B. Chen and L. Wang, J. Heat Transfer 142(7) (2020).

J. Y. Chang, Y. Yang and L. Wang, Int. Int. J. Heat Mass. Transf. 87, 237 (2015).

F. Chen, X. Liu, Y. Tian, and Y. Zheng, Adv. Eng. Mater. 23, 2000825 (2020).

F. R. Chen, G. An, and Z. G. Xu, J. Quant. Spectrosc. Radiat. Transf. 258, 107395 (2021).

K. Chen, P. Santhanam, and S. Fan, Phys. Rev. Appl. 6, 024014 (2016).

X. Chen, D. Hu, R. Mescall, G. You, D. N. Basov, Q. Dai, and M. Liu, Adv. Mater. 31, 1804774 (2019).

T. C. Choy, Effective Medium Theory: Principles and Applications 2nd ed. (Oxford University Press, New York, 2016).

J. Cui, J. Zhang, T. Barayavuga, X. Wang, X. He, L. Yang, H. Xie, X. Mei, and W. Wang, Integr. Ferroelectr. 179, 140 (2017).

L. Cui, Y. Huang, and J. Wang, J. Appl. Phys. 112, 084309 (2012).

L. Cui, Y. Huang, J. Wang, and K. Y. Zhu, Appl. Phys. Lett. 102, 053106 (2013).

L. Cui, W. Jeong, V. Fernández-Hurtado, J. Feist, F. J. García-Vidal, J. C. Cuevas, E. Meyhofer, and P. Reddy, Nat. Commun. 8, 14479 (2017).

G. D'Aguanno, N. Mattiucci, A. Alù, C. Argyropoulos, J. V. Foreman, and M. J. Bloemer, Opt. Express 20, 9784 (2012).

J. Dai, S. A. Dyakov, S. Bozhevolnyi, and M. Yan, Phys. Rev. B 94, 125431 (2016).

J. Dai, S. A. Dyakov, and M. Yan, Phys. Rev. B 92, 035419 (2015).

Y. De Wilde, F. Formanek, R. Carminati, B. Gralak, P. A. Lemoine, K. Joulain, J. P. Mulet, Y. Chen, and J. J. Greffet, Nature 444, 740 (2006).

H. V. Demir, and S. V. Gaponenko, Applied nanophotonics (Cambridge University Press, New York, NY, 2018).

A. Didari, E. Elçioğlu, T. Okutucu-Özyurt, M. Mengüç, J. Quant. Spectrosc. Radiat. Transf. 212, 120 (2018).

A. Didari and M. P. Mengüç, J Quant. Spectrosc. Radiat. Transf. 197, 95 (2017).

A. Didari and M. P. Mengüç, Opt. Express 23, A547 (2015).

A. Didari and M. P. Mengüç, Opt. Express 23, A1253 (2015).

R. DiMatteo, P. Greiff, S. Finberg, K. Young-Waithe, H. Choy, M. Masaki, and C. Fonstad, Appl. Phys. Lett. 79, 1894 (2001).

G. Domingues, S. Volz, K. Joulain and J. J. Greffet, Phys. Rev. Lett. 94, 085901 (2005).

M. S. Dresselhaus, Solid State Physics, Part II: Optical Properties of Solids (Massachusetts Institute of Technology, Cambridge, MA, 2001).

D. Drosdoff, A. D. Phan, and L. M. Woods, Adv. Opt. Mater. 2, 1038 (2014).

W. Du, J. Yang, S. Zhang, N. Iqbal, Y. Dang, J. B. Xu, and Y. Ma, Nano Energy, 78, 105264 (2020).

S. A. Dyakov, J. Dai, M. Yan, and M. Qiu, J. Phys. D: Appl. Phys. 48, 305104 (2015).

S. Edalatpour, Phys. Rev. E 99, 063308 (2019).

S. Edalatpour, M. Čuma, T. Trueax, R. Backman, and M. Francoeur, Phys. Rev. E 91, 063307 (2015).

S. Edalatpour and M. Francoeur, J. Quant. Spectrosc. Radiat. Transfer 133, 364 (2014).

S. Edalatpour, V. Hatamipour, and M. Francoeur, Phys. Rev. B 99, 165401 (2019).

M. Elzouka and S. Ndao, J. Quant. Spectrosc. Radiat. Transf. 204, 56 (2018).

M. Elzouka and S. Ndao, Sci. Rep. 7, 44901 (2018).

S. Enoch and N. Bonod, *Plasmonics: From Basics to Advanced Topics* (Springer, New York, 2012).

V. Fernández-Hurtado, F. García-Vidal, S. Fan, and J. Cuevas, Phys. Rev. Lett. 118, 203901 (2017).

A. Fiorino, D. Thompson, L. Zhu, R. Mittapally, S. Biehs, O. Bezencenet, N. El-Bondry, S. Bansropun, P. Ben-Abdallah, E. Meyhofer, and P. Reddy, ACS Nano 12, 5774 (2018).

A. Fiorino, L. Zhu, D. Thompson, R. Mittapally, P. Reddy, and E. Meyhofer, Nat. Nanotechnol. 13, 806 (2018).

S. Foteinopoulou, G. Devarapu, G. Subramania, S. Krishna, D. Wasserman, Nanophotonics 8, 2129 (2019).

M. Francoeur, S. Basu, and S. Petersen, Optics Express 19, 18774 (2011).

M. Francoeur, M. P. Menguc and R. Vaillon, J. Phys. D: Appl. Phys. 43, 075501 (2010).

M. Francoeur, M. P. Mengüç, and R. Vaillon, J. Quant. Spectrosc. Radiat. Transf. 110, 2002 (2009).

M. Francoeur, R. Vaillon, and M. P. Mengüç, IEEE Trans. Energy Convers. 26, 686 (2011).

L. Ge, Y. Cang, K. Gong, L. Zhou, D. Yu, and Y. Luo, AIP Adv. 8, 085321 (2018).

A. Ghanekar, J. Ji, and Y. Zheng, Appl. Phys. Lett. 109, 123106 (2016).

A. Ghanekar, L. Lin, J. Su, H. Sun and Y. Zheng, Opt. Express 23, A1129 (2015).

A. Ghanekar, L. Lin and Y. Zheng, Opt. Express 24, A868 (2016).

A. Ghanekar, Y. Tian, X. Liu, and Y. Zheng, J. Photonics Energy 9, 032706 (2019).

A. Ghanekar, Y. Tian, S. Zhang, Y. Cui, and Y. Zheng, Materials 10, 885 (2017).

A. Ghanekar, Y. Tian, M. Ricci, S. Zhang, O. Gregory, and Y. Zheng, Opt. Express 26, A209 (2018).

M. Ghashami, H. Geng, T. Kim, N. Iacopino, S. K. Cho, and K. Park, Phys. Rev. Lett. 120, 175901 (2018).

J. J. Greffet, R. Carminati, K. Joulain, J. P. Mulet, S. Mainguy and Y. Chen, Nature 416, 61 (2002).

J. J. Greffet and C. Henkel, Contemp. Phys. 48, 183 (2007).

R. Guérout, J. Lussange, F. Rosa, J. Hugonin, D. Dalvit, J. Greffet, A. Lambrecht, and S. Reynaud, Phys. Rev. B 85, 180301 (2012).

B. Guha, C. Otey, C. Poitras, S. Fan, and M. Lipson, Nano Lett. 12, 4546 (2012).

Y. Guo, C. L. Cortes, S. Molesky, and Z. Jacob, Appl. Phys. Lett. 101, 131106 (2012).

Y. Guo and Z. Jacob, J. Appl. Phys. 115, 234306 (2014).

Y. Guo and Z. Jacob, Opt. Express 21, 15014 (2013).

V. Hatamipour, S. Edalatpour, and M. Francoeur, Phys. Rev. Appl. 10, 54047 (2018).

E. A. Hawes, J. T. Hastings, C. Crofcheck, and M. P. Mengüç, Opt. Lett. 33, 1383 (2008).

M. J. He, H. Qi, Y. T. Ren, Y. J. Zhao, and M. Antezza, Int. J. Heat Mass Transf. 150, 119305 (2020).

C. Henkel and K. Joulain, Appl. Phys. B 84, 61 (2006).

C. Henkel, K. Joulain, R. Carminati and J. J. Greffet, Opt. Commun., 186, 57 (2000).

C. M. Herzinger, P. G. Snyder, B. Johs, and J. A. Woollam, J. Appl. Phys. 77, 1715 (1995).

X. J. Hong, J. W. Li, T. B. Wang, D. J. Zhang, W. X. Liu, Q. H., Liao, T. B. Yu and N. H. Liu, Jpn. J. Appl. Phys. 57, 045001 (2018).

J. R. Howell, M. P. Mengüç, K. Daun, and R. Siegel, Thermal Radiation Heat Transfer (CRC press, 2020).

L. Hu, A. Narayanaswamy, X. Chen, and G. Chen, Appl. Phys. Lett. 92, 133106 (2008).

X. Hu, T. Lo, A. Mancini, C. Gubbin, F. Martini, J. Zhang, Z. Gong, A. Politi, S. De Liberato, X. Zhang, D. Lei, S. A. Maier, Appl. Phys. Rev. 9, 021414 (2022).

J. Humlíček, R. Henn, and M. Cardona, Phys. Rev. B 61, 14554 (2000).

H. Iizuka and S. Fan, J. Appl. Phys. 112, 24304 (2012).

H. Iizuka and S. Fan, J. Quant. Spectrosc. Radiat. Transf. 148, 156 (2014).

H. Iizuka and S. Fan, Phys. Rev. Lett. 120, 063901 (2018).

T. Ijiro and N. Yamada, Appl. Phys. Lett. 106, 23103 (2015).

O. Ilic, M. Jablan, J. D. Joannopoulos, I. Celanovic, and M. Soljačić, Opt. Express 20, A366 (2012).

T. Ikeda, K. Ito, and H. Iizuka, J. Appl. Phys. 121, 013106 (2017).

T. Inoue, T. Asano, and S. Noda, Optics Express 26, 32074 (2018).

T. Inoue, T. Asano, and S. Noda, Phys. Rev. B 95, 125307 (2017).

K. Isobe and K. Hanamura, Int. J. Heat Mass Transf. 134, 807 (2019).

K. Isobe, D. Hirashima, and K. Hanamura, Int. J. Heat Mass Transf. 115, 467 (2017).

K. Ito, K. Nishikawa, H. Iizuka, and H. Toshiyoshi, Appl. Phys. Lett. 105, 253503 (2014).

K. Ito, K. Nishikawa, A. Miura, H. Toshiyoshi, and H. Iizuka, Nano Lett. 17, 4347 (2017).

J. D. Jackson, *Classical Electrodynamics, 3rd ed.* (John Wiley & Sons, New York, 1999).

A. Jarzembski, C. Shaskey, and K. Park, Front. Energy 12, 43 (2018).

S. Jin, M. Lim, S. S. Lee, and B. J. Lee, Opt. Express 24, A635 (2016).

A. C. Jones and M. B. Raschke, Nano Lett. 12, 1475 (2012).

K. Joulain and J. Drevillon, Phys. Rev. B 81, 165119 (2010).

K. Joulain, Y. Ezzahri, J. Drevillon, B. Rousseau, and D. D. S. Meneses, Opt. Express 23, A1388 (2015).

K. Joulain and C. Henkel, Appl. Phys. B 93, 151 (2008).

K. Joulain, J. P. Mulet, F. Marquier, R. Carminati, and J.-J. Greffet, Surf. Sci. Rep. 57, 59 (2005).

Y. Kan, C. Zhao, and Z. Zhang, Phys. Rev. B 99, 035433 (2019).

G. W. Kattawar and M. Eisner, Appl. Opt. 9, 2685 (1970).

Y. Kajihara, K. Kosaka, and S. Komiyama, Rev. Sci. Instrum. 81, 033706 (2010).

H. Kanazawa and S. Adachi, J. Appl. Phys. 83, 5997 (1998).

K. Kim, B. Song, V. Fernández-Hurtado, W. Lee, W. Jeong, L. Cui, D. Thompson, J. Feist, M. T. H. Reid, F. J. García-Vidal, and Others, Nature 528, 387 (2015).

A. R. Kirmani, J. M. Luther, M. Abolhasani, and A. Amassian, ACS Energy Lett. 5, 3069 (2020).

A. Kittel, W. Müller-Hirsch, J. Parisi, S.-A. Biehs, D. Reddig, and M. Holthaus, Phys. Rev. Lett. 95, 224301 (2005).

A. Kittel, U. F. Wischnath, J. Welker, O. Huth, F. Rueting, and S. A. Biehs, Appl. Phys. Lett. 93, 193109 (2008).

K. Kloppstech, N. Könne, S.-A. Biehs, A. W. Rodriguez, L. Worbes, D. Hellmann, and A. Kittel, Nat. Commun. 8, 14475 (2017).

O. G. Kollyukh, A. I. Liptuga, V. Morozhenko and V. I. Pipa, Opt. Commun. 225, 349 (2003).

E. H. Korte and A. Röseler, Anal. Bioanal. Chem. 382, 1987 (2005).

T. Kralik, P. Hanzelka, M. Zobac, V. Musilova, T. Fort, and M. Horak, Phys. Rev. Lett. 109, 224302 (2012).

M. Kreiter, J. Oster, R. Sambles, S. Herminghaus, S. Mittler-Neher and W. Knoll, Opt. Commun. 168, 117 (1999).

M. Krüger, G. Bimonte, T. Emig and M. Kardar, Phys. Rev. B 86, 115423 (2012).

M. Krüger, T. Emig and M. Kardar, Phys. Rev. Lett. 106, 210404 (2011).

S. Labouesse, S. C. Johnson, H. A. Bechtel, M. B. Raschke, and R. Piestun, ACS Photonics 7, 3346 (2020).

S. Landrieux, P. Ben-Abdallah, R. Messina, Appl. Phys. Lett. 120, 143502 (2022).

S. Lang, G. Sharma, S. Molesky, P. U. Kränzien, T. Jalas, Z. Jacob, A. Y. Petrov, and M. Eich, Sci. Rep. 7, 13916 (2017).

S. Lang, M. Tschikin, S. A. Biehs, A. Y. Petrov and M. Eich, Appl. Phys. Lett. 104, 121903 (2014).

M. Laroche, C. Arnold, F. Marquier, R. Carminati, J. J. Greffet, S. Collin, N. Bardou and J. L. Pelouard, Opt. Lett. 30, 2623 (2005).

M. Laroche, R. Carminati, and J.J. Greffet, J. Appl. Phys. 100, 63704 (2006).

M. Laroche, R. Carminati and J.J. Greffet, Phys. Rev. Lett. 96, 123903 (2006).

J. Z. J. Lau, V. N. S. Bong, and B. T. Wong, B. T. J. Quant. Spectrosc. Radiat. Transf. 171, 39 (2016).

W. T. Lau, J. T. Shen, G. Veronis and S. Fan, Phys. Rev. E 76, 016601 (2007).

W. T. Lau, J. T. Shen, G. Veronis, S. Fan, and P. V. Braun, Appl. Phys. Lett. 92, 103106 (2008).

B. J. Lee, C. J. Fu and Z. M. Zhang, Appl. Phys. Lett. 87, 071904 (2005).

E. Lhuillier, and P. Guyot-Sionnest, IEEE J. Sel. Top. Quantum Electron. 23, 1 (2017).

Likam Scientific Instruments Ltd., Waterfield, Epsom, Tadworth KT20 5LR, United Kingdom, www.linkam.co.uk.

M. Lim, S. S. Lee, and B. J. Lee, Phys. Rev. B 91, 195136 (2015).

M. Lim, J. Song, J. Kim, S. S. Lee, I. Lee, and B. J. Lee, J. Quant. Spectrosc. Radiat. Transf. 210, 35 (2018).

M. Lim, J. Song, S. S. Lee and B. J. Lee, Nat. Commun. 9, 4302 (2018).

B. Liu and S. Shen, Phys. Rev. B 87, 115403 (2013).

B. Liu, J. Shi, K. Liew, and S. Sheng, Opt. Commun. 314, 57 (2014).

J. Liu and E. Narimanov, Phys. Rev. B 91, 041403 (2015).

R. Liu, C. Zhou, Y. Zhang, Z. Cui, X. Wu, and H. Yi, Int. J. Extreme Manuf. 4, 032002 (2022).

X. L. Liu, T. J. Bright, and Z. M. Zhang, J. Heat Transfer 136, 092703 (2014).

X. L. Liu, L. P. Wang, and Z. M. Zhang, J. Heat Transf. 135, 061602 (2013).

X. L. Liu, R. Z. Zhang, and Z. M. Zhang, ACS Photonics 1, 785 (2014).

X. L. Liu, R. Z. Zhang, and Z. M. Zhang, Appl. Phys. Lett. 103, 213102 (2013).

X. L. Liu, R. Z. Zhang, and Z. M. Zhang, Int. J. Heat Mass Transf. 73, 389 (2014).

X. L. Liu and Z. M. Zhang, ACS Photonics 2, 1320 (2015).

X. L. Liu and Z. M. Zhang, Appl. Phys. Lett. 104, 251911 (2014).

X. L. Liu and Z. M. Zhang, Appl. Phys. Lett. 107, 143114 (2015).

X. L. Liu, B. Zhao and Z. M. Zhang, Phys. Rev. A 91, 062510 (2015).

V. L. Y. Loke, and M. P. Mengüç, JOSA A 27, 2293 (2010).

D. Lu, A. Das, and W. Park, Opt. Express 25, 12999 (2017).

C. Lucchesi, D. Cakiroglu, J. Perez, T. Taliercio, E. Tournié, P. Chapuis, and R. Vaillon, Nano Lett. 21, 4524 (2021).

J. Lussange, R. Guérout, F. S. S. Rosa, J. J. Greffet, A. Lambrecht, and S. Reynaud, Phys. Rev. B 86, 085432 (2012).

W. Ma, J. M. Luther, H. Zheng, Y. Wu, and A. P. Alivisatos, Nano Lett. 9, 1699 (2009).

S. A. Maier, *Plasmonics: Fundamentals and Applications* (Springer, New York, 2007).

H. J. Mamin, Appl. Phys. Lett. 69, 433 (1996).

A. Mancini, C. Gubbin, R. Berté, F. Martini, A. Politi, E. Cortés, Y. Li, S. De Liberato, and S. A. Maier, ACS Nano 14, 8508 (2020).

L. Mandel and E. Wolf, *Optical Coherence and Quantum Optics* (Cambridge University Press, Cambridge, 1995).

V. A. Markel, J. Opt. Soc. Am. A 33, 1244 (2016).

F. Marquier, K. Joulain, J. P. Mulet, R. Carminati, J. J. Greffet, and Y. Chen, Phys. Rev. B 69, 155412 (2004).

H. H. Marvin, Phys. Rev. Series I 34, 161 (1912).

J. C. Maxwell-Garnett, Philos. Trans. R. Soc. Lond. B 203, 385 (1904).

R. Messina, P. Ben-Abdallah, B. Guizal, M. Antezza, and S. A. Biehs, Phys. Rev. B 94, 104301 (2016).

D. Milovich, J. Villa, E. Antolin, A. Datas, A. Marti, R. Vaillon, and M. Francoeur, J. Photonics Energy 10, 025503 (2020).

M. S. Mirmoosa, F. Rüting, I. S. Nefedov and C. R. Simovski, J. Appl. Phys. 115, 234905 (2014).

R. Mittapally, B. Lee, L. Zhu, A. Reihani, J. W. Lim, D. Fan, S. R. Forrest, P. Reddy, and E. Meyhofer, Nat. Commun. 12, 4346(2021).

M. F. Modest, Fundamentals of Thermal Radiation (Academic Press, 2013).

S. Molesky and Z. Jacob, Phys. Rev. B 91, 205435 (2015).

I. Moreels, G. Allan, B. De Geyter, L. Wirtz, C. Delerue, and Z. Hens, Phys. Rev. B 81, 235319 (2010).

I. Moreels and Z. Hens, Small 4, 1866 (2008).

I. Moreels, K. Lambert, D. De Muynck, F. Vanhaecke, D. Poelman, J. C. Martins, G. Allan, and Z. Hens, Chem. Mater. 19, 6101 (2007).

I. Moreels, K. Lambert, D. Smeets, D. De Muynck, T. Nollet, J. C. Martins, F. Vanhaecke, A. Vantomme, C. Delerue, G. Allan, Z. Hens, ACS Nano 3, 3023 (2009).

S. Mukhopadhyay, A. Karumuri, and I. Barney, J. Phys. D: Appl. Phys. 42, 195503 (2009).

J. P. Mulet, K. Joulain, R. Carminati, and J.-J. Greffet, Microscale Thermophys. Eng. 6, 209 (2002).

J. E. Murphy, M. C. Beard, A. G. Norman, S. P. Ahrenkiel, J. C. Johnson, P. Yu, O. I. Mićić, R. J. Ellingson, and A. J. Nozik, J. Am. Chem. Soc. 128, 3241 (2006).

A. Narayanaswamy and G. Chen, Appl. Phys. Lett. 82, 3544 (2003).

K. L. Nguyen, O. Merchiers and P. O. Chapuis, Appl. Phys. Lett. 112, 111906 (2018).

B. T. O'Callahan, W. E. Lewis, A. C. Jones, and M. B. Raschke, Phys. Rev. B 89, 245446 (2014).

B. T. O'Callahan and M. B. Raschke, APL Photonics 2, 21301 (2017).

C. Otey, W. Lau, and S. Fan, Phys. Rev. Lett. 104, 154301 (2010).

R. S. Ottens, V. Quetschke, S. Wise, A. A. Alemi, R. Lundock, G. Mueller, D. H. Reitze, D. B. Tanner, and B. F. Whiting, Phys. Rev. Lett. 107, 14301 (2011).

E. D. Palik, *Handbook of Optical Constants of Solids* (Academic Press, 1997).

K. Park, S. Basu, W. P. King, and Z. M. Zhang, J. Quant. Spectrosc. Radiat. Transf. 109, 305 (2008).

F. Peragut, L. Cerruti, A. Baranov, J. P. Hugonin, T. Taliercio, Y. De Wilde, and J. J. Greffet, Optica 4, 1409 (2017).

J. E. Pérez-Rodríguez, G. Pirruccio and R. Esquivel-Sirvent, Phys. Status Solidi B 257, 1900498 (2020).

J. L. Peters, J. de Wit, and D. Vanmaekelbergh, Chem. Mater. 31, 1672 (2019).

S. J. Petersen, S. Basu, B. Raeymaekers and M. Francoeur, J. Quant. Spectrosc. Radiat. Transfer 129, 277 (2013).

S. J. Petersen, S. Basu, B. Raeymaekers and M. Francoeur, Photonics Nanostruct.: Fundam. Appl. 11, 167 (2013).

M. Planck, The Theory of Heat Radiation (Blakiston, 1914).

M. T. H. Reid, Computing the Photonic Local Density of States with SCUFF-LDOS http://homerreid.github.io/scuff-em-documentation/applications/scuff-ldos/scuff-ldos/.

M. T. H. Reid, Solving Electromagnetic Scattering Problems with SCUFF-SCATTER http://homerreid.github.io/scuff-em-documentation/applications/scuff-scatter/scuff-scatter/.

D. Ricard, M. Ghanassi, and M. C. Schanne-Klein, Opt. Commun. 108, 311 (1994).

A. Rodriguez, O. Ilic, P. Bermel, I. Celanovic, J. Joannopoulos, M. Soljačić, and S. Johnson, Phys. Rev. Lett. 107, 114302 (2011).

E. Rousseau, A. Siria, G. Jourdan, S. Volz, F. Comin, J. Chevrier, and J.-J. Greffet, Nat. Photonics 3, 514 (2009).

S. M. Rytov, Y. A. Kravtsov and V. Tatarskii, Principles of Statistical Radiophysics 3: Elements of Random Fields (Springer, New York, 1989).

P. Sabbaghi, Y. Yang, J. Y. Chang, and L. Wang, J. Quant. Spectrosc. Radiat. Transf. 234, 108 (2019).

E. Y. Santiago, J. E. Perez-Rodriguez, and R. Esquivel-Sirvent, J. Phys. Chem. C 121, 12392 (2017).

G. Schmid, Nanoparticles: from theory to application (John Wiley & Sons, Inc., Hoboken, NJ, 2011).

J. Shen, X. Liu, H. He, W. Wu, and B. Liu, J. Quant. Spectrosc. Radiat. Transf. 211, 1 (2018).

S. Shen, A. Mavrokefalos, P. Sambegoro, and G. Chen, Appl. Phys. Lett. 100, 233114 (2012).

S. Shen, A. Narayanaswamy, and G. Chen, Nano Lett. 9, 2909 (2009).

Z. Shen, H. Wu and H. Wang, Appl. Sci. 8, 2023 (2018).

P. Sheng, Introduction to Wave Scattering, Localization and Mesoscopic Phenomena 2 ed. (Springer, 2006).

J. Shi, P. Li, B. Liu, and S. Shen, Appl. Phys. Lett. 102, 183114 (2013).

K. Shi, F. Bao, and S. He, ACS Photonics 4, 971 (2017).

A. O. Silva and J. C. Costa, J. Microw. Optoelectron. Electromagn. Appl. 13, 10 (2014).

C. Simovski, S. Maslovski, I. Nefedov and S. Tretyakov, Opt. Express 21, 14988 (2013).

B. Song, Y. Ganjeh, S. Sadat, D. Thompson, A. Fiorino, V. Fernández-Hurtado, J. Feist, F. J. García-Vidal, J. C. Cuevas, P. Reddy, and Others, Nat. Nanotechnol. 10, 253 (2015).

B. Song, D. Thompson, A. Fiorino, Y. Ganjeh, P. Reddy, and E. Meyhofer, Nat. Nanotechnol. 11, 509 (2016).

J. Song, Q. Cheng, L. Lu, B. Li, K. Zhou, B. Zhang, Z. Luo, and X. Zhou, Phys. Rev. Appl. 13, 024054 (2020).

R. St-Gelais, G. R. Bhatt, L. Zhu, S. Fan, and M. Lipson, ACS Nano 11, 3001 (2017).

R. St-Gelais, L. Zhu, S. Fan, and M. Lipson, Nat. Nanotechnol. 11, 515 (2016).

C. Su and C. Fu, Int. J. Heat Mass Trans. 196, 123235 (2022).

N. Suzuki and S. Adachi, Jpn. J. Appl. Phys. 33, 193 (1994).

N. Suzuki, K. Sawai, and S. Adachi, J. Appl. Phys. 77, 1249 (1995).

C. T. Tai, *Dyadic Green Functions in Electromagnetic Theory*, 2nd ed. (IEEE Press, New York, 1994).

Y. Taniguchi, K. Isobe, and K. Hanamura, Appl. Therm. Eng. 183, 116041 (2021).

E. Tervo, E. Bagherisereshki, and Z. Zhang, Front. Energy 12, 5 (2018).

D. Thompson, L. Zhu, R. Mittapally, S. Sadat, Z. Xing, P. McArdle, M. M. Qazilbash, P. Reddy, and E. Meyhofer, Nature 561, 216 (2018).

T. E. Tiwald, J. A. Woollam, S. Zollner, J. Christiansen, R. B. Gregory, T. Wetteroth, S. R. Wilson, and A. R. Powell, Phys. Rev. B 60, 11464 (1999).

J. K. K. Tong, Photonic Engineering of Near-and Far-Field Radiative Heat Transfer, Massachusetts Institute of Technology, 2016.

L. Tsang, J. A. Kong, and K. H. Ding. Scattering of electromagnetic waves. (Wiley, New York, 2000).

L. Tsang, J. A. Kong, K. Ding and C. O. Ao, Scattering of Electromagnetic Waves: Numerical Simulations (John Wiley & Sons, Inc., New York, 2002).

M. Tschikin, P. Ben-Abdallah, and S. A. Biehs, Phys. Lett. A 376, 3462 (2012).

M. Tschikin, S. Biehs, P. Ben-Abdallah, S. Lang, A. Petrov, and M. Eich, J Quant. Spectrosc. Radiat. Transf. 158, 17 (2015).

M. Tschikin, S. A. Biehs, R. Messina, and P. Ben-Abdallah, J. Opt. 15, 105101 (2013).

P. J. Van Zwol, K. Joulain, P. Ben Abdallah, J.-J. Greffet, and J. Chevrier, Phys. Rev. B 83, 201404 (2011).

N. Vongsoasup, M. Francoeur, and K. Hanamura, Int. J. Heat Mass Transfer 115, 326 (2017).

H. Wang, X. Liu, L. Wang and Z. M. Zhang, Int. J. Therm. Sci. 65, 62 (2013).

H. Wang, D. Qi and H. Wu, J. Photonics Energy 9, 015501 (2019).

L. P. Wang and Z. M. Zhang, Nanoscale Microscale Thermophys. Eng. 17, 337 (2013).

T. Wang, P. Li, D. Chigrin, A. Giles, F. Bezares, O. Glembocki, J. Caldwell, and T. Taubner, ACS Photonics 4, 1753 (2017).

W. Wang and S. Mukhopadhyay, Carbon Trends 5, 100096 (2021).

X. J. Wang, J. L. Abell, Y-P. Zhao and Z. M. Zhang, Appl. Opt. 51, 1521 (2012).

Y. Wang, Z. Du, Y. Park, C. Chen, X. Zhang, and L. Pan, Opt. Lett. 40, 3918 (2015).

J. I. Watjen, X. Liu, B. Zhao, and Z. Zhang, J. Heat Transf. 139, 052704 (2017).

J. I. Watjen, B. Zhao, and Z. M. Zhang, Appl. Phys. Lett. 109, 203112 (2016).

S. Wen, X. Liu, S. Cheng, Z. Wang, S. Zhang, and C. Dang, J. Quant. Spectrosc. Radiat. Transf. 234, 1 (2019).

M. D. Whale and E. G. Cravalho, IEEE Trans. Energy Convers. 17, 130 (2002).

K. Wilder, C. F. Quate, D. Adderton, R. Bernstein, and V. Elings, Appl. Phys. Lett. 73, 2527 (1998).

U. F. Wischnath, J. Welker, M. Munzel, and A. Kittel, Rev. Sci. Instrum. 79, 73708 (2008).

F. W. Wise, Acc. Chem. Res. 33, 773 (2000).

E. Wolf, *Introduction to the Theory of Coherence and Polarization of Light* (Cambridge University Press, Cambridge, 2007).

J. A. Woollam Co., 645 M Street, Lincoln NE 68508 www.jawoollam.com.

F. Wooten, Optical Properties of Solids (Academic Press, Cambridge, MA, 2013).

L. Worbes, D. Hellmann, and A. Kittel, Phys. Rev. Lett. 110, 134302 (2013).

X. Wu, and C. Fu, J. Quant. Spectrosc. Radiat. Transf. 258, 107337 (2021).

Y. Xia, S. Liu, K. Wang, X. Yang, L. Lian, Z. Zhang, J. He, G. Liang, S. Wang, M. Tan, H. Song, D. Zhang, J. Gao, J. Tang, M. C. Beard, and J. Zhang, Adv. Funct. Mater. 30, 1907379 (2020).

G. Xu, J. Sun, H. Mao, and T. Pan, Int. J. Therm. Sci. 149, 106179 (2020).

L. Yan, X. Shen, Y. Zhang, T. Zhang, X. Zhang, Y. Feng, J. Yin, J. Zhao, and W. W. William, RSC Adv. 5, 54109 (2015).

J. Yang, W. Du, Y. Su, Y. Fu, S. Gong, S. He, and Y. Ma, Nat. Commun. 9, 4033 (2018).

Y. Yang, S. Basu, and L. Wang, Appl. Phys. Lett. 103, 163101 (2013).

Y. Yang, J. Y. Chang, P. Sabbaghi and L. Wang, J. Heat Transfer 139, 052701 (2017).

Y. Yang, P. Sabbaghi, and L. Wang, Int. J. Heat Mass Transf. 108, 851 (2017).

Y. Yang and L. Wang, Phys. Rev. Lett. 117, 044301 (2016).

V. Yannopapas and N. V. Vitanov, Phys. Rev. Lett. 99, 053901 (2007).

P. Yeh, *Optical Waves in Layered Media* (Wiley, Hoboken, 2005).

H. Yu, Y. Duan, and Z. Yang, Int. J. Heat Mass Transf. 123, 67 (2018).

H. Yu, D. Liu, Z. Yang, and Y. Duan, Sci. Rep. 7, 1026 (2017).

S. Zare and S. Edalatpour, Phys. Rev. B 101, 165424 (2020).

S. Zare, C. Tripp, and S. Edalatpour, Phys. Rev. B 100, 235450 (2019).

A. V. Zayats and I. I. Smolyaninov, J. Opt. A: Pure Appl. Opt. 5, S16 (2003).

K. Zhang and D. Li, *Electromagnetic Theory for Microwaves and Optoelectronics* (Springer, New York, 2008).

R. Z. Zhang, X. Liu and Z. M. Zhang, AIP Adv. 5, 053501 (2015).

W. B. Zhang, C. Y. Zhao and B. X. Wang, Phys. Rev. B 100, 075425 (2019).

Z. M. Zhang, Nano/Microscale Heat Transfer (McGraw-Hill, 2007).

X. Zhang and Y. Wu, Sci. Rep. 5, 7892 (2015).

B. Zhao, B. Guizal, Z. Zhang, S. Fan, and M. Antezza, Phys. Rev. B 95, 245437 (2017).

Q. Zhao, T. Zhou, T. Wang, W. Liu, J. Liu, T. Yu, Q. Liao, and N. Liu, J. Phys. D: Appl. Phys. 50, 145101 (2017).

Q. M. Zhao, T. B. Wang, D. J. Zhang, W. X. Liu, T.B. Yu, Q. H. Liao, and N. H. Liu, Chin. Phys. B 27, 094401 (2018).

Z. Zheng, X. Liu, A. Wang, and Y. Xuan, Int. J. Heat Mass Transf. 109, 63 (2017).

Z. Zheng and Y. Xuan, Chi. Sci. Bull. 56, 2312 (2011).

Z. Zheng and Y. Xuan, Int. J. Heat Mass Transf. 54, 1101 (2011).

N. Zhou and X. Xu, J Quant. Spectrosc. Radiat. Transf. 167, 156 (2015).

T. Zhou, T. B. Wang, Q. H. Liao, J. T. Liu, T. B. Yu, and N. H. Liu, Phys. Lett. A 381, 1976 (2017).

L. Zhu, A. Fiorino, D. Thompson, R. Mittapally, E. Meyhofer, and P. Reddy, Nature 566, 239 (2019).

APPENDICES

APPENDIX A

SUPPLEMENTAL MATERIALS FOR MEASUREMENT OF NEAR-FIELD THERMAL EMISSION SPECTRA USING AN INTERNAL REFLECTION ELEMENT

A.1. Parallel Component of the Wavevector for the Thermally Emitted Waves Exiting the IRE

In this section, we determine the parallel component of the wavevector, k_ρ, for the thermally emitted waves that can exit the IRE beveled ends and reach the FTIR spectrometer. In the following sub-sections, we analyze the interaction of the waves having wavevectors $k_\rho < k_0$, $k_0 < k_\rho < n_I k_0$, and $k_\rho > n_I k_0$ with the IRE to determine if they can exit the IRE.

A.1.1. Waves with $k_\rho < k_0$

The emitted waves with $k_\rho < k_0$ are propagative in both the air gap and the IRE. The propagation of these waves toward the IRE beveled ends is schematically shown in Fig. A.1(a). These waves arrive at the air-IRE interface with an angle of θ_0, which is between 0° and 90°, and partially transmit to the IRE [Fig. A.1(a)]. The transmitted waves make an angle of θ_1 with the surface normal that can be found by considering the conservation of the parallel-component of the wavevector (Snell's law) as:

$$\theta_1 = \sin^{-1}\left(\frac{\sin\theta_0}{n_I}\right) \tag{A.1}$$

In Eq. (A.1), n_I is the refractive index of the IRE which is equal to 2.4 for ZnSe. Since $0° < \theta_0 < 90°$, $0° < \theta_1 < \theta_{cr}$ where $\theta_{cr} = \sin^{-1}(1/n_I)$ is the critical angle for the air-IRE interface ($\theta_{cr} = 24.6°$ for a ZnSe IRE). After multiple reflections at the air-IRE interface, the propagative waves hit the IRE beveled ends at an angle of $\theta_2 = 90° - (\alpha + \theta_1)$, where α is the bevel angle of the IRE. Considering that $0° < \theta_1 < 24.6°$ and $\alpha = 45°$ in our experiments, the lower and upper limits for θ_2 are found as 20.4° and 45°, respectively. The waves with $\theta_2 \geq \theta_{cr} = 24.6°$ totally internally reflect at the beveled surface, while the waves with

$20.4° < \theta_2 < 24.6°$ exit the IRE. The waves exiting the IRE have a k_ρ in the range of sin(20.4°) $n_I k_0 < k_\rho < k_0$.

A.1.2. Waves with $k_0 < k_\rho < n_I k_0$

The interaction of the waves having k_ρ in the range of $k_0 < k_\rho < n_I k_0$ with the IRE is schematically shown in Fig. A.1(b). These waves are evanescent in the air but become propagative in the IRE [see Fig. A.1(b)]. The parallel component of the wavevector can be written as $k_\rho = n_I k_0 \sin\theta_1$. As such, the angle of propagation in the IRE is:

$$\theta_1 = \sin^{-1}\left(\frac{k_\rho}{n_I k_0}\right) \tag{A.2}$$

Using Eq. (A.2) and considering waves with $k_0 < k_\rho < n_I k_0$, it is found that $\theta_{cr} = 24.6° < \theta_1 < 90°$. Since $\theta_1 > \theta_{cr}$, these waves experience multiple total internal reflections at the air-IRE interfaces until they reach the beveled surface at angle θ_2. By a geometrical analysis, it can be shown that $\theta_2 = 90° - (\alpha + \theta_1)$ when $24.6° < \theta_1 < 45°$ and $\theta_2 = (\alpha + \theta_1) - 90°$ when $45° < \theta_1 < 90°$. Considering $\alpha = 45°$, the range of θ_2 for the former and latter cases is found to be $0 < \theta_2 < 20.4°$ and $0 < \theta_2 < 45°$, respectively. Since $\theta_2 < \theta_{cr} = 24.6°$ in the former case, all these waves can exit the beveled surface. These waves have a k_ρ in the range of $k_0 < k_\rho < \sin(45°) n_I k_0$. In the latter case, only the waves for which $0 < \theta_2 < \theta_{cr} = 24.6°$ can transmit to the air from the beveled surface. The parallel component of the wavevector for these waves varies in the range of $\sin(45°) n_I k_0 < k_\rho < \sin(69.6°) n_I k_0$. In total, the waves with $k_0 < k_\rho < \sin(69.6°) n_I k_0$ can exit the beveled side of the IRE and reach the FTIR spectrometer.

A.1.3. Waves with $k_\rho > n_I k_0$

The waves with $k_\rho > n_I k_0$ cannot propagate in the IRE as they are evanescent in both the air and the IRE. These waves do not exit from the IRE beveled surface.

To conclude, a thermally emitted wave can exit the IRE and be collected by the FTIR spectrometer if its parallel component of wavevector, k_ρ, is in the range of $\sin(20.4°) n_I k_0 < k_\rho < \sin(69.6°) n_I k_0$.

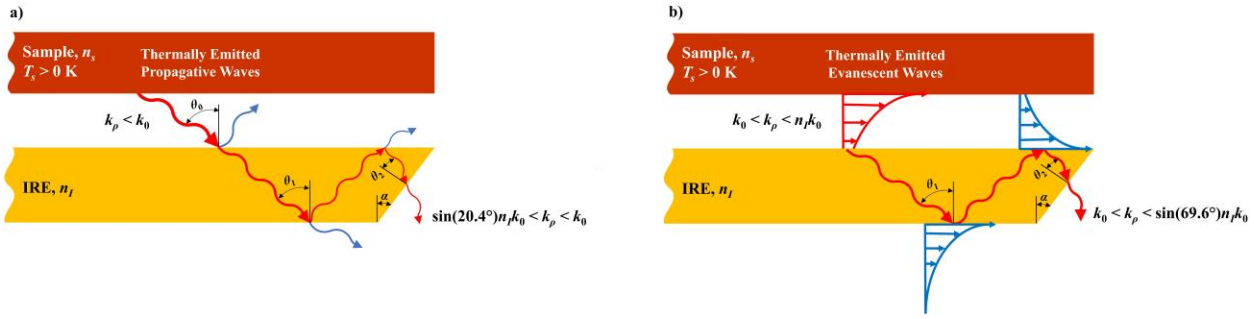

Figure A.1 – The interaction of the thermally emitted waves with $k_\rho < k_0$ and $k_0 < k_\rho < n_Ik_0$ with the IRE. (a) The waves with $k_\rho < k_0$ are propagative in both the air and the IRE. From these waves, those with $\sin(20.4°)\ n_Ik_0 < k_\rho < k_0$ exit the IRE. (b) The waves with $k_0 < k_\rho < n_Ik_0$ are evanescent in the air but propagative in the IRE. From these waves, those with $k_0 < k_\rho < \sin(69.6°)n_Ik_0$ exit the IRE.

The higher the refractive index of the IRE, the larger the number of modes that can exit the IRE. A ZnSe IRE with a refractive index of $n_I = 2.4$ is used in this study. Alternatively, silicon and germanium IREs with refractive indices of 3.4 and 4, respectively, can be used which increase the number of captured modes. Furthermore, if a hemispherical IRE instead of a trapezoidal one is used, all the modes with a k_ρ in the range of $k_0 < k_\rho < n_Ik_0$ can be measured.

It should also be mentioned that if the waves with $\sin(20.4°)n_Ik_0 < k_\rho < \sin(69.6°)n_Ik_0$ (which propagate in the IRE with an angle of $20.4° < \theta_1 < 69.6°$) directly impact the IRE beveled surface [see Fig. A.2(a)], they exit the IRE without coupling back to the sample. For a wave with a given propagation angle θ_1 and for the 2-mm thick IRE used in this study, this condition occurs when the wave is emitted by a segment of the sample located within $(2+2\tan\theta_1)$ mm of its edge [see Fig. A.2(b)]. This distance varies from 2.74 mm to 7.38 mm for the propagation angles of $20.4° < \theta_1 < 69.6°$. Additionally, the coupling of the thermal emission back to the sample can be avoided entirely by using a single-reflection ATR accessory (a multiple-reflection ATR accessory is used in this study). A single-reflection ATR accessory utilizes an IRE with triangular, rather than a trapezoidal, cross section [see Fig. A.2(c)]. In the case of a single-

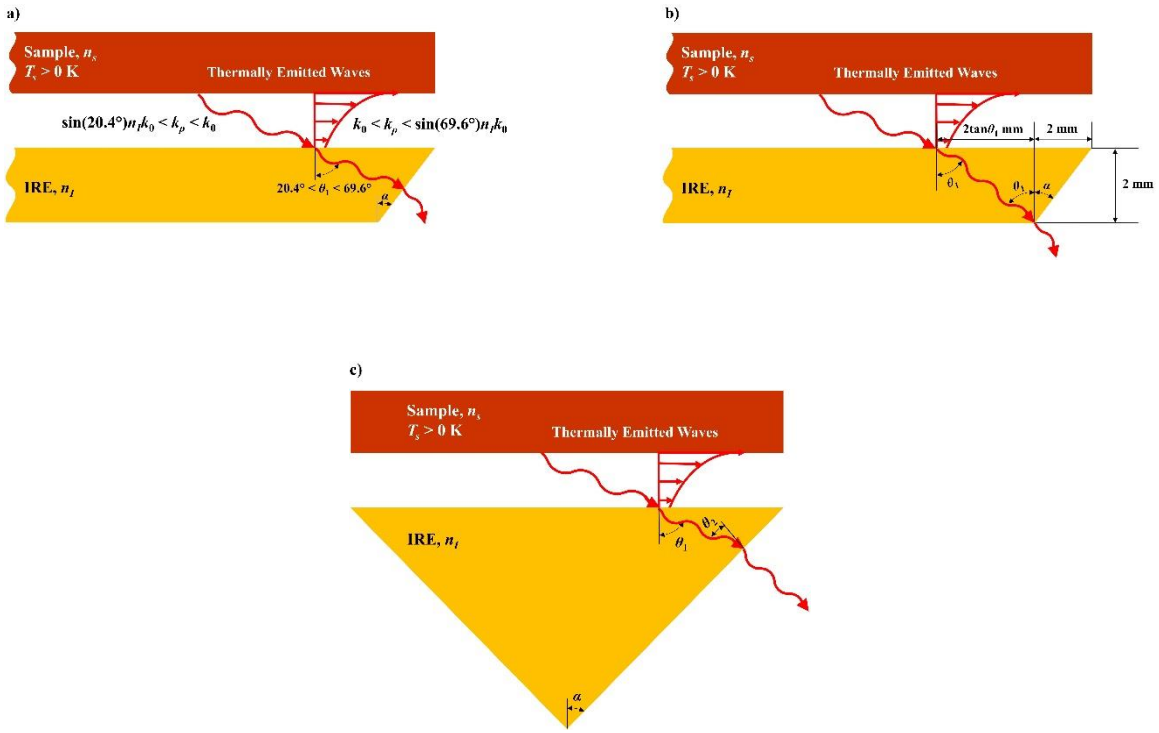

Figure A.2 – (a) If the waves with an angle of $20.4° < \theta_1 < 69.6°$ directly impact the IRE beveled surface, they exit the IRE without coupling back to the sample. (b) Thermally emitted waves by a segment of the sample located within $(2+2\tan\theta_1)$ mm of its edge exit the IRE without coupling back to the sample. (c) All of the waves with an angle of $20.4° < \theta_1 < 69.6°$ exit a triangular IRE without coupling back to the emitting sample.

reflection ATR accessory, all waves with an angle of $20.4° < \theta_1 < 69.6°$ exit the IRE without coupling back to the emitting sample.

A.2. Temperature of the Sample

The voltage supplied to the heater is adjusted such that the sample reaches a temperature of 160°C in the far-field measurements. If the same voltage is supplied in the near-field measurements, the sample temperature drops below 160°C due to the conductive heat transfer with the IRE. As such, the supplied voltage needs to be increased for near-field measurements. The sample temperature cannot be measured

in near-field experiments because the sample is in contact with the IRE. We increased the supplied voltage for near-field measurements until the ratio of the near-field and far-field spectra becomes flat at large wavenumbers where thermal emission is negligible due to the low energy of thermal oscillators. In spectroscopy, the spectral location of the peaks is of interest rather than the magnitude of thermal emission. Therefore, it is not required to have the exact same temperature for both near-field and far-field experiments. We experimentally verified that the spectral locations of the peaks are not affected by changing the supplied voltage in the near-field measurements.

A.3. Compensation for Background Thermal Emission, Wavenumber-Dependent Responsivity of the Photodetector, Absorption by Internal Parts of the ATR Accessory and the Ambient, and Modulation Efficiency of the FTIR Spectrometer

The intensity of the measured signal, I, can be written as:

$$I(\omega) = \beta(\omega)\left[I^{s}(\omega) + I^{bk}(\omega)\right] \tag{A.3}$$

where β is a frequency-dependent factor that accounts for the absorption by the internal components of the ATR accessory and the ambient gases, the modulation efficiency of the FTIR spectrometer, and the responsivity of the photodetector, I^{s} is the intensity of thermal emission by the sample, and I^{bk} is the intensity of the background thermal emission. The factor β varies with frequency, but it remains the same at a given frequency for all measurements.

To measure the ratio of near-field and far-field thermal emission by the sample, first the background thermal radiation is recorded. The background emission is measured by blocking thermal radiation by the sample from reaching the FTIR via placing a thick film of stainless steel (which is opaque in the infrared) at the exit of the ATR accessory. In this case, $I^{s} = 0$ and the measured signal, I, equals βI^{bk} [see Eq. (A.3)]. Then, the block is removed, and the signal is recorded for the cases where the sample is in contact (near-field) and at 1-mm distance (far-field) from the IRE. The intensity of total (spectrally-integrated) background thermal radiation is between 6 and 24 times (depending on the sample) smaller than that of near-field and far-field signals. Using Eq. (A.3), the intensity of the recorded signals can be written as:

$$I^{NF}(\omega)=\beta(\omega)\left[I^{s,NF}(\omega)+I^{bk}(\omega)\right] \tag{A.4-a}$$

$$I^{FF}(\omega)=\beta(\omega)\left[I^{s,FF}(\omega)+I^{bk}(\omega)\right] \tag{A.4-b}$$

where I^{NF} shows the intensity of the signal for the near-field measurement, I^{FF} shows the intensity of the signal for the far-field measurement, and $I^{s,NF}$ and $I^{s,FF}$ indicate the intensity of near-field and far-field thermal emission by the sample, respectively. The ratio $I^{s,NF}/I^{s,FF}$ is obtained by subtracting the background signal (βI^{bk}) from the near- and far-field signals (I^{NF} and I^{FF}, respectively) and taking the ratio of the reduced signals, i.e.,

$$\frac{I^{s,NF}}{I^{s,FF}}=\frac{I^{NF}(\omega)-\beta(\omega)I^{bk}(\omega)}{I^{FF}(\omega)-\beta(\omega)I^{bk}(\omega)} \tag{A.5}$$

A.4. Dielectric Functions of Quartz, Silica, Polytetrafluoroethylene, and Hexagonal Boron Nitride

The dielectric functions of quartz [2], silica [2], polytetrafluoroethylene (PTFE) [3], and hexagonal boron nitride (hBN) [4] are obtained from the experimental data in literature. The dielectric function of hBN in the parallel and perpendicular directions (relative to the optical axis) is written using the Lorentz oscillator model as $\varepsilon_s=\varepsilon_\infty\left(\omega^2-\omega_{LO}^2+i\Gamma\omega\right)\Big/\left(\omega^2-\omega_{TO}^2+i\Gamma\omega\right)$. The experimental oscillator parameters for parallel dielectric function are ε_∞ = 2.95, ω_{LO} = 830 cm^{-1}, ω_{TO} = 780 cm^{-1}, and Γ = 4 cm^{-1}, while for the perpendicular dielectric function they are ε_∞ = 4.87, ω_{LO} = 1610 cm^{-1}, ω_{TO} = 1370 cm^{-1}, and Γ = 5 cm^{-1} [4]. The dielectric functions of the samples are plotted versus the wavenumber in Fig. A.3.

A.5. Energy Density Emitted by an Anisotropic, Uniaxial Medium into the IRE

As discussed in Sec. A.1, the waves with a parallel component of wavevector, k_ρ, between sin(20.4°) n_1k_0 and sin(69.6°)n_1k_0 can exit the IRE and be captured by the FTIR spectrometer. The energy density of these waves in the IRE approximately models the measured spectrum. The energy density at distance Δ in the IRE can be obtained using the dyadic Green's functions for one-dimenisonal layered media and

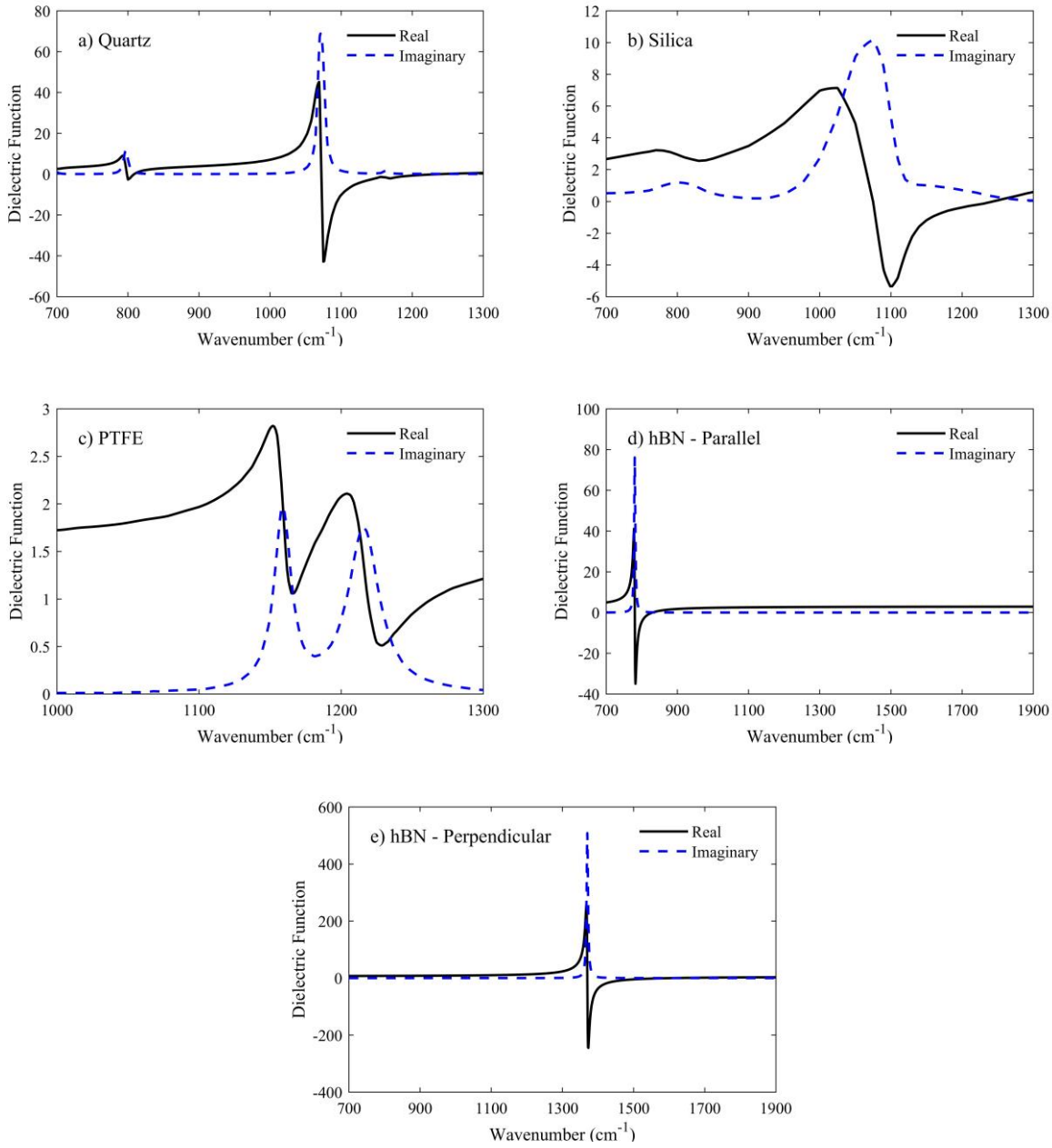

Figure A.3 – The dielectric functions of (a) quartz, (b) silica, (c) PTFE, and (d) and (e) hBN.

scattering matrix method. A schematic of the problem under consideration is shown in Fig. A.4. An anisotropic uniaxial sample with thickness t_s and temperature T_s is emitting thermal radiation. The anisotropic dielectric response of the sample is described using a frequency-dependent diagonal tensor as $\overline{\overline{\boldsymbol{\varepsilon}}}_s = \text{diag}\,[\,\varepsilon_{s,\perp}\,;\varepsilon_{s,\perp}\,;\varepsilon_{s,\parallel}\,]$, where $\varepsilon_{s,\perp}$ and $\varepsilon_{s,\parallel}$ are the dielectric functions of the sample perpendicular

and parallel to the optical axis (*z*-axis) of the sample. For isotropic samples (quartz, silica, and PTFE), $\varepsilon_{s,\parallel} = \varepsilon_{s,\perp} = \varepsilon_s$. An IRE with thickness t_I and dielectric function $\varepsilon_I = n_I^2$ which is transparent in the wavenumber range of interest (Im[ε_I] ≈ 0) is placed at distance *d* from the sample. Thermal emission by the IRE is negligible compared to that of the sample as it is transparent. The sample, IRE and free space are labeled as *s*, *I* and *v*, respectively. The objective is to find the energy density at distance Δ in the IRE.

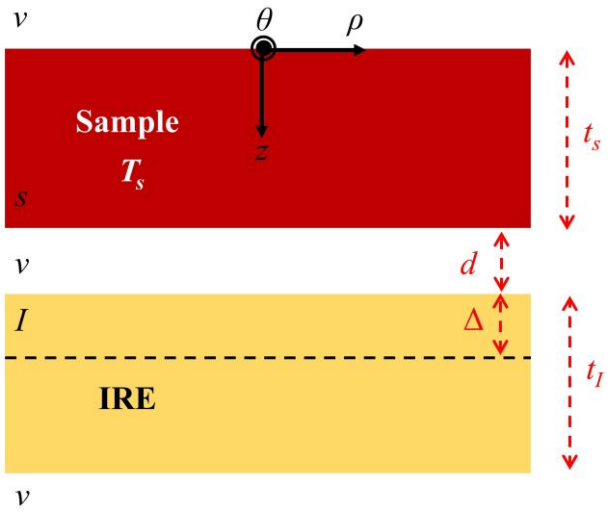

Figure A.4 – A Schematic of the problem under consideration. Energy density at distance Δ in the IRE due to thermal emission by the heated sample is desired.

The time-averaged spectral density in the IRE is given as [5]:

$$\left\langle u(\mathbf{r},\omega)\right\rangle = \frac{1}{4}\varepsilon_I\varepsilon_0 \mathrm{Trace}\left\langle \mathbf{E}(\mathbf{r},\omega)\otimes\mathbf{E}(\mathbf{r},\omega)\right\rangle + \frac{1}{4}\mu_0 \mathrm{Trace}\left\langle \mathbf{H}(\mathbf{r},\omega)\otimes\mathbf{H}(\mathbf{r},\omega)\right\rangle \quad \text{(A.6)}$$

where *u* is the energy density, ω is the angular frequency, **r** is the position at which the energy density is desired, < > represents the ensemble average, $\otimes$ is the outer product, ε_0 and μ_0 are the permittivity and permeability of the free space, respectively, and **E** and **H** are the electric and magnetic fields emitted by the heated sample, respectively. The electric and magnetic fields can be obtained using the electric and magnetic dyadic Green's functions, $\overline{\overline{\mathbf{G}}}^E$ and $\overline{\overline{\mathbf{G}}}^H$, and the thermally stochastic current $\mathbf{J}^{fl}$ as [6]:

$$\mathbf{E}(\mathbf{r},\omega) = i\omega\mu_0 \int_{V_s} \overline{\overline{\mathbf{G}}}^{E}(\mathbf{r},\mathbf{r}',\omega)\cdot\mathbf{J}^{fl}(\mathbf{r}',\omega)\,dV' \tag{A.7-a}$$

$$\mathbf{H}(\mathbf{r},\omega) = \int_{V_s} \overline{\overline{\mathbf{G}}}^{H}(\mathbf{r},\mathbf{r}',\omega)\cdot\mathbf{J}^{fl}(\mathbf{r}',\omega)\,dV' \tag{A.7-b}$$

where the integral is performed over the volume of the sample, V_s, where the fluctuating current is non-zero. The fluctuating current is given by the fluctuation-dissipation theorem as [7,8]:

$$\left\langle \mathbf{J}^{fl}(\mathbf{r}',\omega)\otimes\mathbf{J}^{fl}(\mathbf{r}'',\omega')\right\rangle = \frac{4}{\pi}\omega\varepsilon_0\,\mathrm{Im}\left[\overline{\overline{\boldsymbol{\varepsilon}}}_s\right]\Theta(\omega,T_s)\,\delta(\mathbf{r}'-\mathbf{r}'')\,\delta(\omega-\omega') \tag{A.8}$$

where Θ is the mean energy of an electromagnetic state [8]. By substituting Eqs. (A.7) and (A.8) into Eq. (A.6), the energy density can be written as:

$$\left\langle u(\mathbf{r},\omega)\right\rangle = \frac{k_0^2}{\pi\omega}\Theta(\omega,T)\int_{V_s}\mathrm{Trace}\Big[k_0^2\overline{\overline{\mathbf{G}}}^{E}(\mathbf{r},\mathbf{r}').\mathrm{Im}\left[\overline{\overline{\boldsymbol{\varepsilon}}}_s\right].\overline{\overline{\mathbf{G}}}^{E^\dagger}(\mathbf{r},\mathbf{r}') + \overline{\overline{\mathbf{G}}}^{H}(\mathbf{r},\mathbf{r}').\mathrm{Im}\left[\overline{\overline{\boldsymbol{\varepsilon}}}_s\right].\overline{\overline{\mathbf{G}}}^{H^\dagger}(\mathbf{r},\mathbf{r}')\Big]dV' \tag{A.9}$$

where superscript $\dagger$ indicates the Hermitian operator. The dyadic Green's functions can be expressed as an integral of plane waves using the Weyl representation as [9]:

$$\overline{\overline{\mathbf{G}}}^{E(H)}(\mathbf{r},\mathbf{r}') = \int_{-\infty}^{\infty}\overline{\overline{\mathbf{g}}}^{E(H)}(k_\rho,z,z',\omega)\,e^{ik_\rho(\mathbf{R}-\mathbf{R}')}d\mathbf{k}_\rho \tag{A.10}$$

where $\overline{\overline{\mathbf{g}}}^{E(H)}$ is the Weyl component of the electric (magnetic) dyadic Green's function, $\mathbf{k}_\rho$ is the parallel (to the surface) component of the wavevector, and $\mathbf{R}$ (z) and $\mathbf{R}'$ (z') are the parallel (perpendicular) components of the position vectors of the observation and source points, respectively. Substituting Eq. (A.10) into Eq. (A.9) and exploiting the azimuthal symmetry of the geometry, the energy density at distance Δ in the IRE due to the waves with k_ρ between sin(20.4°) $n_I k_0$ and sin(69.6°)$n_I k_0$ is written as:

$$\left\langle u(\Delta,\omega)\right\rangle = \frac{\Theta(\omega,T_s)\,\omega}{2c_0^2\pi^2}\int_{\sin(20.4°)n_Ik_0}^{\sin(69.6°)n_Ik_0}k_\rho\int_0^{t_s}\Big(k_I^2\mathrm{Trace}\Big[\overline{\overline{\mathbf{g}}}^{E}(k_\rho,\Delta,z',\omega)\cdot\mathrm{Im}\left[\overline{\overline{\boldsymbol{\varepsilon}}}_s\right]\cdot\overline{\overline{\mathbf{g}}}^{E^\dagger}(k_\rho,\Delta,z',\omega) + \overline{\overline{\mathbf{g}}}^{H}(k_\rho,\Delta,z',\omega)\cdot\mathrm{Im}\left[\overline{\overline{\boldsymbol{\varepsilon}}}_s\right].\overline{\overline{\mathbf{g}}}^{H^\dagger}(k_\rho,\Delta,z',\omega)\Big]\Big)dz'dk_\rho \tag{A.11}$$

The Weyl components of the electric and magnetic Green's functions can be written using the Sipe unit vectors as [10]:

$$\overline{\overline{\mathbf{g}}}^{E}\left(k_\rho,\Delta,z',\omega\right)=\frac{i}{2k_{z,s}^{TE}}\left(A_I^{TE}e^{ik_{z,I}\Delta-ik_{z,s}^{TE}z'}+B_I^{TE}e^{-ik_{z,I}\Delta-ik_{z,s}^{TE}z'}+C_I^{TE}e^{ik_{z,I}\Delta+ik_{z,s}^{TE}z'}+D_I^{TE}e^{-ik_{z,I}\Delta+ik_{z,s}^{TE}z'}\right)\hat{\mathbf{s}}\hat{\mathbf{s}}$$
$$+\frac{i}{2k_{z,s}^{TM}}\left(A_I^{TM}e^{ik_{z,I}\Delta-ik_{z,s}^{TM}z'}\hat{\mathbf{p}}_I^{+}\hat{\mathbf{p}}_s^{+}+B_I^{TM}e^{-ik_{z,I}\Delta-ik_{z,s}^{TM}z'}\hat{\mathbf{p}}_I^{-}\hat{\mathbf{p}}_s^{+}+C_I^{TM}e^{ik_{z,I}\Delta+ik_{z,s}^{TM}z'}\hat{\mathbf{p}}_I^{+}\hat{\mathbf{p}}_s^{-}+D_I^{TM}e^{-ik_{z,I}\Delta+ik_{z,s}^{TM}z'}\hat{\mathbf{p}}_I^{-}\hat{\mathbf{p}}_s^{-}\right)$$
(A.12-a)

$$\overline{\overline{\mathbf{g}}}^{H}\left(k_\rho,\Delta,z',\omega\right)=\frac{k_I}{2k_{z,s}^{TE}}\left(A_I^{TE}e^{ik_{z,I}\Delta-ik_{z,s}^{TE}z'}\hat{\mathbf{p}}_I^{+}\hat{\mathbf{s}}+B_I^{TE}e^{-ik_{z,I}\Delta-ik_{z,s}^{TE}z'}\hat{\mathbf{p}}_I^{-}\hat{\mathbf{s}}+C_I^{TE}e^{ik_{z,I}\Delta+ik_{z,s}^{TE}z'}\hat{\mathbf{p}}_I^{+}\hat{\mathbf{s}}+D_I^{TE}e^{-ik_{z,I}\Delta+ik_{z,s}^{TE}z'}\hat{\mathbf{p}}_I^{-}\hat{\mathbf{s}}\right)$$
$$-\frac{k_I}{2k_{z,s}^{TM}}\left(A_I^{TM}e^{ik_{z,I}\Delta-ik_{z,s}^{TM}z'}\hat{\mathbf{s}}\hat{\mathbf{p}}_s^{+}+B_I^{TM}e^{-ik_{z,I}\Delta-ik_{z,s}^{TM}z'}\hat{\mathbf{s}}\hat{\mathbf{p}}_s^{+}+C_I^{TM}e^{ik_{z,I}\Delta+ik_{z,s}^{TM}z'}\hat{\mathbf{s}}\hat{\mathbf{p}}_s^{-}+D_I^{TM}e^{-ik_{z,I}\Delta+ik_{z,s}^{TM}z'}\hat{\mathbf{s}}\hat{\mathbf{p}}_s^{-}\right)$$
(A.12-b)

In Eq. (A.12), superscript *TE* (*TM*) refers to the transverse electric (magnetic) polarization, and $\hat{\mathbf{s}}$ and $\hat{\mathbf{p}}_i^{\pm}$ are the Sipe unit vectors for TE- and TM-polarizations inside layer *i*, respectively. The Sipe unit vectors in the sample and the IRE are given by [10,11]:

$$\hat{\mathbf{s}}=-\hat{\boldsymbol{\theta}} \tag{A.13-a}$$

$$\hat{\mathbf{p}}_s^{\pm}=\frac{1}{k_s^{TE}}\left(\mp k_{z,s}^{TM}\hat{\boldsymbol{\rho}}+\frac{\varepsilon_{s,\perp}}{\varepsilon_{s,\parallel}}k_\rho\hat{\mathbf{z}}\right) \tag{A.13-b}$$

$$\hat{\mathbf{p}}_I^{\pm}=\frac{1}{k_I}\left(\mp k_{z,I}\hat{\boldsymbol{\rho}}+k_\rho\hat{\mathbf{z}}\right) \tag{A.13-c}$$

where $k_s^{TE}=\sqrt{\varepsilon_{s,\perp}}k_0$ is the magnitude of the TE-polarized wavevector in the sample and $k_{z,s}^{TM}=\sqrt{\varepsilon_{s,\perp}k_0^2-\frac{\varepsilon_{s,\perp}}{\varepsilon_{s,\parallel}}k_\rho^2}$ is the *z*-component of the TM-polarized wavevector in the sample.

The coefficients A_I^γ (B_I^γ) and C_I^γ (D_I^γ) are the amplitude of the γ-polarized (γ = *TE* or *TM*) waves in the IRE traveling toward the positive (negative) direction of the *z*-axis due to thermal sources emitting in

the positive and negative directions of the *z*-axis, respectively [10]. The coefficients A_I^γ , B_I^γ , C_I^γ and D_I^γ can be found using the scattering matrix method as [10]:

$$A_I^\gamma = \frac{t_{sv}^\gamma t_{vI}^\gamma e^{ik_{z,s}^\gamma t_s} e^{ik_{z,v}d}}{\left(1+r_{vs}^\gamma r_{sv}^\gamma e^{2ik_{z,s}^\gamma t_s}\right)\left(1+r_{vI}^\gamma r_{Iv}^\gamma e^{2ik_{z,I}t_I}\right)\left(1-R_s^\gamma R_I^\gamma e^{2ik_{z,v}^\gamma d}\right)} \tag{A.14-a}$$

$$B_I^\gamma = r_{Iv}^\gamma e^{2ik_{z,I}t_I} A_I^\gamma \tag{A.14-b}$$

$$C_I^\gamma = -r_{vs}^\gamma A_I^\gamma \tag{A.14-c}$$

$$D_I^\gamma = r_{Iv}^\gamma e^{2ik_{z,I}t_I} C_I^\gamma \tag{A.14-d}$$

where and r_{ij}^γ and t_{ij}^γ are the Fresnel reflection and transmission coefficients at the interface of layers *i* and *j* for γ-polarization, respectively, The Fresnel coefficients are given by [11]:

$$r_{ij}^{TE} = \frac{k_{z,i}^{TE} - k_{z,j}^{TE}}{k_{z,i}^{TE} + k_{z,j}^{TE}} \tag{A.15-a}$$

$$r_{ij}^{TM} = \frac{\varepsilon_{j,\perp} k_{z,i}^{TM} - \varepsilon_{i,\perp} k_{z,j}^{TM}}{\varepsilon_{j,\perp} k_{z,i}^{TM} + \varepsilon_{i,\perp} k_{z,j}^{TM}} \tag{A.15-b}$$

$$t_{ij}^{TE} = \frac{2k_{z,i}^{TE}}{k_{z,i}^{TE} + k_{z,j}^{TE}} \tag{A.15-c}$$

$$t_{ij}^{TM} = \frac{2\varepsilon_{j,\perp} k_{z,i}^{TM}}{\varepsilon_{j,\perp} k_{z,i}^{TM} + \varepsilon_{i,\perp} k_{z,j}^{TM}} \sqrt{\frac{\varepsilon_{i,\perp}}{\varepsilon_{j,\perp}}} \tag{A.15-d}$$

In Eq. (A.15), $k_{z,i}^{TE}$ is the *z*-component of the TE-polarized wave in the IRE and is given by $k_{z,i}^{TE} = \sqrt{\varepsilon_{i,\perp} k_0^2 - k_\rho^2}$. Note that for an isotropic sample $k_{z,i}^{TE} = k_{z,i}^{TM}$. In Eq. (A.14), R_j^γ represents the reflection coefficient of layer *j* in the free space for polarization state γ and is found as [12]:

$$R_j^\gamma = \frac{r_{vj}^\gamma + r_{jv}^\gamma e^{2ik_{z,j}^\gamma t_j}}{1+r_{vj}^\gamma r_{jv}^\gamma e^{2ik_{z,j}^\gamma t_j}} \tag{A.16}$$

A.6. Verification of the Existence of an Air Gap between the Sample and the IRE in the Experiments

In this section, we verify that an air gap exists between the IRE and the sample in our experiments. We compute the energy density in the middle of the IRE (Δ = 1 mm) due to the waves with k_ρ between $\sin(20.4°)\, n_I k_0$ and $\sin(69.6°) n_I k_0$ using Eq. (A.11) for two cases. In the first case, a gap of d = 200 nm is assumed between the sample and the IRE, while no gap (d = 0) is assumed in the second case. The quartz sample at a temperature of T_s = 160°C is considered.

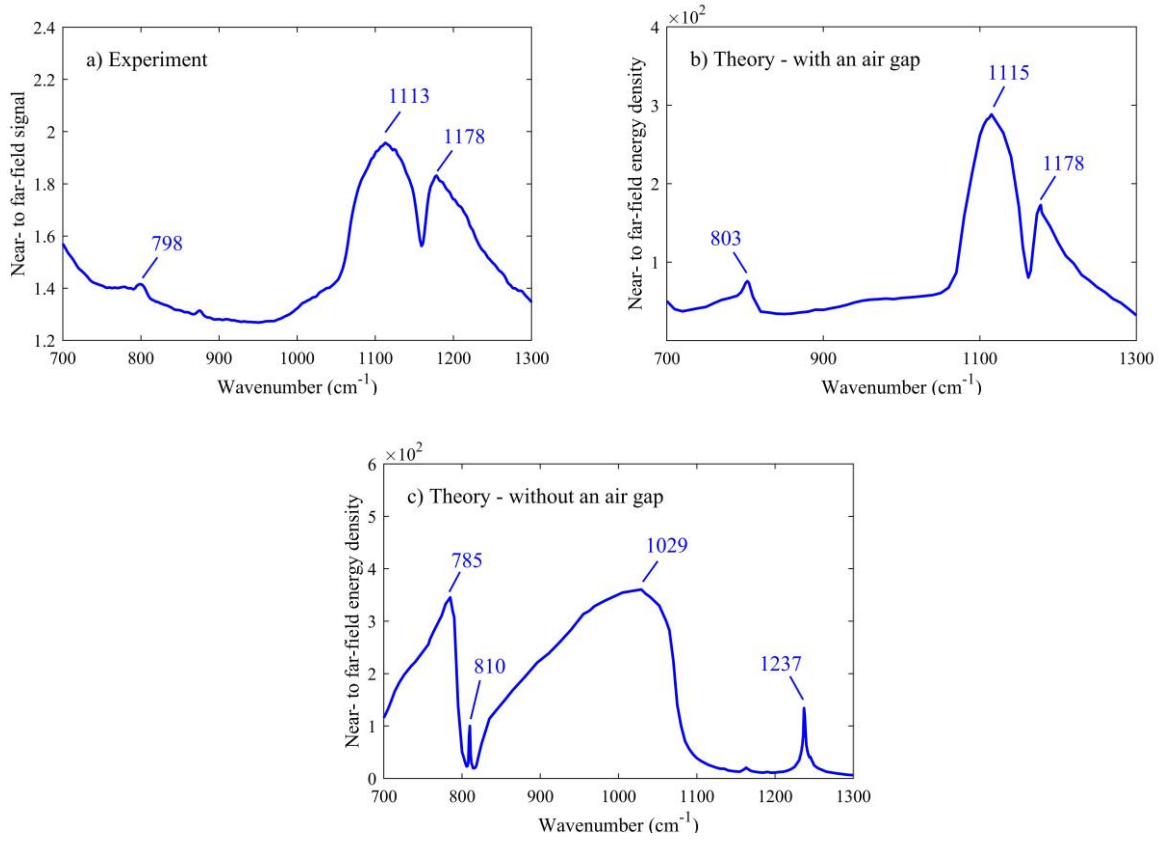

Figure A.5 – The ratio of near-field and far-field thermal spectra for quartz at 160°C. Panel (a) shows the measured spectrum, while the theoretical spectra at d = 200 nm and 0 are presented in Panels (b) and (c), respectively.

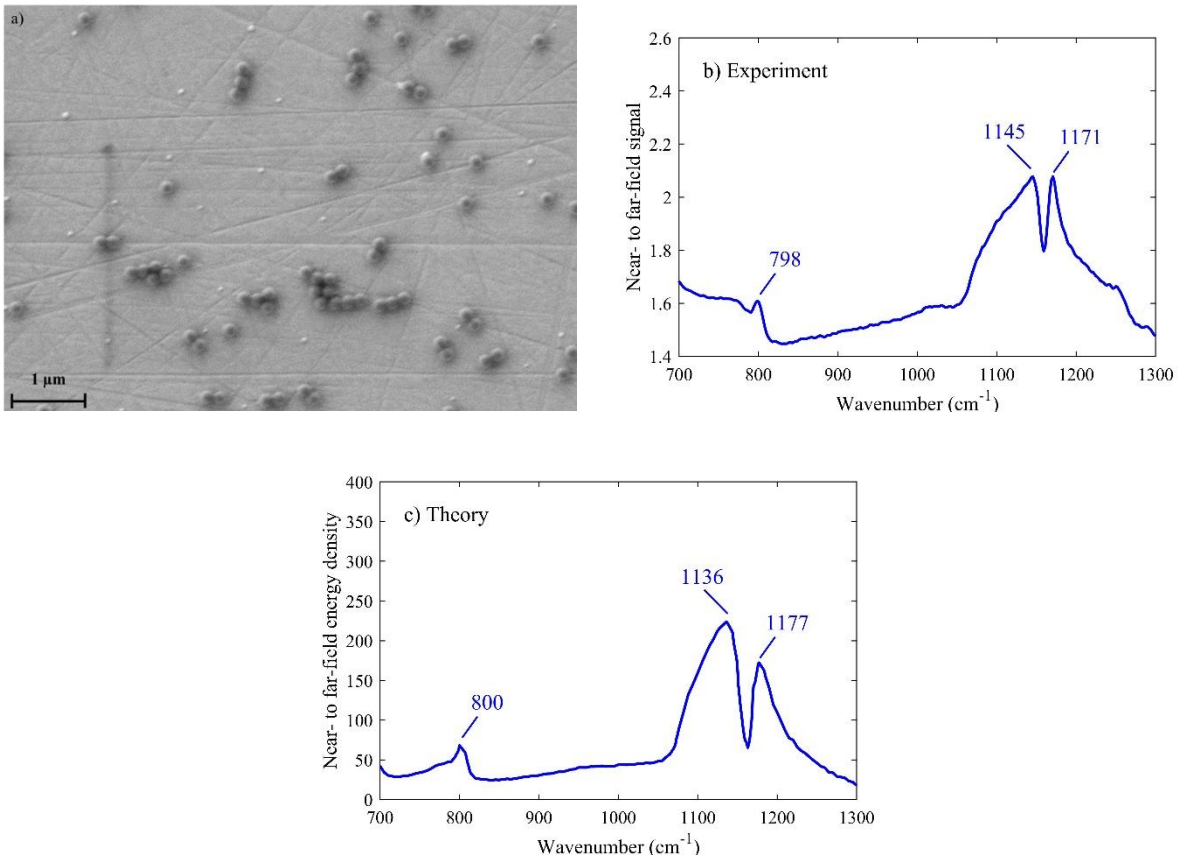

Figure A.6 – (a) An SEM image of the polystyrene nanoparticles of size 200 nm on the IRE surface. (b) The measured and (c) the theoretically-predicted thermal emission spectra of quartz in the presence of the polystyrene nanoparticles.

The computed spectra with d = 200 nm and 0 are compared with the measured spectrum in Fig. A.5. While the measured spectrum agrees well with the computed energy density at d = 200 nm, it is significantly different from that calculated for d = 0. This verifies that an air gap exists between the sample and the IRE when they are in contact.

A.7. Controlling the Air Gap between the Sample and the IRE

The air gap between the sample and the IRE can be adjusted by depositing polystyrene nanoparticles of a desired size on the IRE or the sample. The size of the air gap between the sample and the IRE is then equal to the diameter of the particles plus the surface roughness of the sample and the IRE. Very smooth

samples are required for near-field thermal radiation applications, and the IRE surface roughness is very small [a scanning electron microscope (SEM) image of the IRE surface is shown in Fig. A.6(a)]. In this case, the gap size is approximately equal to the diameter of the deposited nanoparticles. The total volume of the nanoparticles is small, and polystyrene is transparent in most of the infrared. As such, thermal emission by the nanoparticles is negligible compared to that of the sample. Also, only a small fraction of the IRE surface is covered with the nanoparticles (less than 5%). Therefore, the particles do not considerably change the dielectric environment between the sample and the IRE, and they do not cause significant scattering of thermally emitted electromagnetic waves.

To experimentally demonstrate that this gap-control mechanism can be used with the presented spectroscopy technique, polystyrene nanoparticles of size 200 nm are deposited on the IRE. The presence of the nanoparticles on the IRE surface is verified using an SEM image which is shown in Fig. A.6(a). The measured spectrum for quartz in the presence of the nanoparticles is shown in Fig. A.6(b). The near-field spectrum of quartz for a gap distance of 400 nm, equal to the surface roughness of the sample (200 nm) plus the size of the nanoparticle (200 nm), is also calculated using Eq. (2.1) and is shown in Fig. A.6(c). The experimental and theoretical spectra of quartz agree well, which shows that the polystyrene nanoparticles can be used for adjusting the air gap between the sample and the IRE.

A.8. References

[1] K. Joulain, J.-P. Mulet, F. Marquier, R. Carminati, and J.-J. Greffet, Surf. Sci. Rep. 57, 59 (2005).

[2] E. D. Palik, *Handbook of Optical Constants of Solids* (Academic Press, 1997).

[3] E. H. Korte and A. Röseler, Anal. Bioanal. Chem. 382, 1987 (2005).

[4] Y. Cai, L. Zhang, Q. Zeng, L. Cheng, and Y. Xu, Solid State Commun. 141, 262 (2007).

[5] J. D. Jackson, *Classical Electrodynamics, 3rd ed*. (John Wiley & Sons, New York, 1999).

[6] C. T. Tai, *Dyadic Green Functions in Electromagnetic Theory*, 2nd ed. (IEEE Press, New York, 1994).

[7] Y. A. K. S. M. Rytov and V. Tatarskii, Principles of Statistical Radiophysics 3: Elements of Random Fields (Springer, New York, 1989).

[8] S. Edalatpour, M. Čuma, T. Trueax, R. Backman, and M. Francoeur, Phys. Rev. E 91, 063307 (2015).

[9] L. Tsang, J. A. Kong, and K. H. Ding. Scattering of electromagnetic waves. (Wiley, New York, 2000).

[10] M. Francoeur, M. P. Mengüç, and R. Vaillon, J. Quant. Spectrosc. Radiat. Transf. 110, 2002 (2009).

[11] Y. Guo and Z. Jacob, J. Appl. Phys. 115, (2014).

[12] P. Yeh, *Optical Waves in Layered Media* (Wiley, Hoboken, 2005).

APPENDIX B

SUPPLEMENTAL MATERIALS FOR

PROBING NEAR-FIELD THERMAL EMISSION OF LOCALIZED SURFACE PHONONS FROM SILICON CARBIDE NANOPILLARS

B.1. Nanopillar Fabrication

To fabricate the SiC nanopillars, 6H-SiC <0001> wafers (MSE Supplies) with a thickness of 430 μm were cleaned using piranha solution and DI water. A 100-nm chromium layer was deposited to be used as a hard etch mask using RF sputtering at a rate of 2.6A/s. The wafer was diced into 1.2×1.2 cm^2 square chips after being coated in a protective layer of Shipley S1818 photoresist followed by photoresist stripping and another piranha cleaning step. Each chip was coated with a layer of maN-2403 negative-tone resist with a thickness of 300 nm. A Nanobeam Ltd. nB4 e-beam writer with an acceleration voltage of 80 kV and beam current of 31 nA was used to pattern a 1×1 cm^2 array of circles with a thickness, diameter, and spacing of 100 nm, 500 nm, 500 nm, respectively, into the resist. The pattern was developed in AZ 300 MIF developer and then rinsed with DI water. Then, the chromium circles were defined using inductively-coupled plasma reactive ion etching (ICP-RIE) in a Cl2/O2 plasma (Oxford PlasmaPro Cobra 100). Piranha solution was then used to remove the residual resist. The SiC nanopillars were defined by another ICP-RIE step using a SF6/O2 plasma with a pressure of 6 mtorr, a forward RIE power of 150 watts, and an ICP power of 1500 watts. The etch duration determined the height of the pillars. A commercial chromium etchant (Transene CR1A) was used to remove residual chromium hard mask at room temperature overnight. Finally, any residual surface oxides and/or particles were removed from nanopillars using 50:1 buffered oxide etch solution.

B.2. Near-Field Thermal Radiation Spectroscopy

The spectra of near-field thermal radiation are measured using an experimental technique utilizing an IRE for guiding the thermally-emitted evanescent waves to an FTIR spectrometer[43]. A schematic of the setup

used for implementing this spectroscopy technique is shown in Fig. B.1. A trapezoidal zinc selenide IRE (Harrick, EM2122) with a bevel angle of 45° and a refractive index of $n_I \approx 2.4$ is used in this setup. To maintain an air gap between the sample and the IRE, an array of 15×15 cylindrical gold nanopillars with a height of ~100 nm, diameter of ~4 μm, and spacing of ~620 μm are deposited on a 1×1 cm^2 area on one side of the ZnSe IRE. To deposit the gold pillars, a mask was designed with the L-edit program, and the resulting GDSII file was transferred to the RTS Mann Pattern Generator. The features (i.e., circles) from the GDSII file were stepped and exposed onto a mask blank (Nanofilm, HRC), consisting of a glass plate coated with an 80-nm chrome layer and a 530-nm positive photoresist layer. After exposure, the mask was developed in MIF300 developer, and the exposed layer (the areas around the circles) was wet-etched using chromium mask etchant (Transene, CE-5M). The mask was then cleaned with acetone, methanol, and isopropanol. Before depositing the posts, the ZnSe IRE was cleaned with acetone, methanol, and isopropanol and was dried in an oven at 120°C for 10 minutes. Then, it was coated with a layer of AZ nLOF 2020 photoresist, and was spun at 2500 RPM for 30 seconds using a Laurell resist spinner. Subsequently, it was heated for one minute at 110°C and allowed to cool down for about 10 minutes. The IRE and the mask were aligned using a Suss Microtec MA6 aligner, and were exposed to 365 nm UV light at 70 mJ/cm^2. After exposure, the IRE was heated again for one minute at 110°C for the post exposure image reversal bake, and then allowed to cool down for about 10 minutes. The unexposed circles were removed by dipping the IRE in a MIF300 developer.

The ZnSe IRE was then placed into an AJA International sputtering chamber. In the sputtering chamber, a layer of chrome was first deposited on the crystal to work as an adhesion for the gold posts. The deposition parameters were 120 Watts of DC power in 3.0 mTorr Argon resulting in a deposition rate of 0.7 Å/s for a total thickness of 20 nm. Immediately following the chrome deposition, a layer of gold was deposited on the crystal. The parameters for the gold deposition were 360 Watts of RF power in 3.0 mTorr of Argon which resulted in a deposition rate of 3.2 Å/s for a total height of 100 nm. The IRE was removed from the sputtering chamber after deposition and was dipped into AZ Kwik Strip photoresist

remover. The stripper and the IRE were placed inside of a 200 W ultrasonic bath at a temperature of 60°C to accelerate the removal of photoresist. The solvent and the IRE were kept in the bath overnight to ensure complete removal of the photoresists. Finally, the dimensions of the deposited gold posts were measured with a Tencor Alphastep 500 surface profilometer.

To capture the near-field radiation signal, the samples, heated to 150°C using a ceramic heater (Thorlabs, HT24S), are placed on the IRE (covered with the gold posts), and a 100-nm-thick air gap between the sample and the IRE is established. The evanescent waves with $k_\rho < n_1 k_0$ emitted from the heated sample are converted into propagating waves inside the IRE. The propagating waves inside the IRE experience total internal reflections at the flat surfaces of the IRE and travel inside the IRE toward the IRE beveled surfaces (see Fig. B.1). The waves with k_ρ in the range of $\sin(20.4°)n_1k_0 < k_\rho < \sin(69.6°)n_1k_0$ exit the beveled sides of the IRE and are guided to an FTIR spectrometer (ABB-Bomem MB1552E) using a multiple-reflection horizontal attenuated total reflection accessory (Harrick, HorizonTM). The FTIR spectrometer is equipped with a broadband mercury-cadmium-telluride detector (InfraRed Associates Inc.).

The measured near-field spectra of the fabricated samples are normalized by the far-field thermal emission from a carbon nanotube (CNT) sample at the same temperature as the nanopillar samples acting as a blackbody emitter. A distance of 1 mm is kept between the CNT sample and the IRE for the far-field blackbody measurements. The CNT sample is fabricated using floating catalyst chemical vapor deposition (CVD) of CNTs following the microwave plasma enhance CVD of a silica buffer layer [1,2], and consists of a 100-μm-thick layer of CNTs on a silicon wafer. To find the spectral, normal emissivity of the CNT sample, it was mounted on a Watlow Firerod cartridge heater and heated up to 150°C. The temperature of the sample is measured using a K-type thermocouple connected to a digital thermometer (OMEGA, HH-52). The signal due to thermal radiation by the sample at a normal (to the emitting surface of the sample) direction was collected by the mercury-cadmium-telluride detector (Thermo Fisher Scientific, MCT-A/CdTe) of a Fourier Transform Infrared (FTIR) spectrometer (Thermo Fisher Scientific, Nicolet iS50). The signal from a blackbody (ISDC, IR-563), at the same temperature as the

CNT sample, was also collected by the spectrometer. The background thermal radiation was recorded when the heater and blackbody were turned off, and it was subtracted from the signals collected for the CNT sample and the blackbody. Finally, the emissivity of the CNT sample was obtained by taking the ratio of the sample and blackbody signals (after the subtraction). Figure B.2 shows the measured emissivity for the CNT sample at different wavenumbers. As it is observed in Fig. B.2, the emissivity of the CNT sample varies between 0.968 and 0.995 in the wavenumber range of 750-1000 cm^{-1} considered in this study.

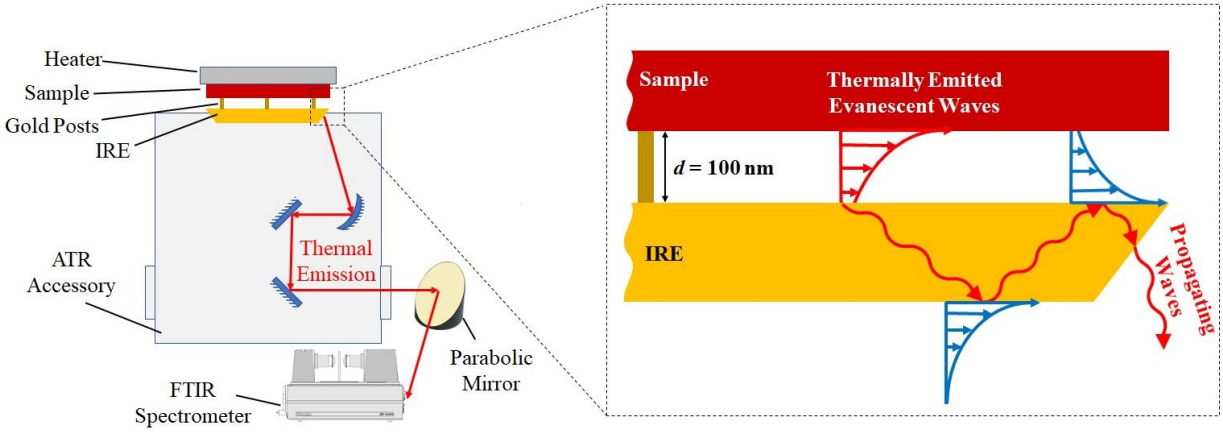

Figure B.1 - A schematic of the experimental setup used for near-field thermal radiation spectroscopy of the fabricated samples. A close-up view of the sample and IRE is also shown.

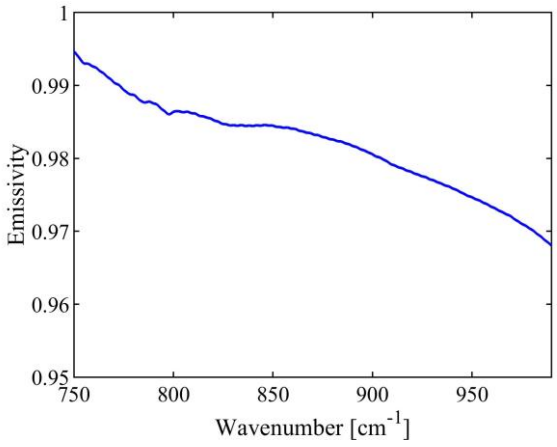

Figure B.2 – The spectral, normal emissivity of the CNT sample measured at 150°C.

B.3. Measuring the Dielectric Function of 6H-SiC using Ellipsometry

The ordinary and extraordinary complex dielectric functions of a single-side polished 6H-SiC c-plane (<0001>) substrate was measured using ellipsometry at a temperature of 200°C. For this purpose, the 6H-SiC substrate was mounted inside of a Linkam TSEL1000 high temperature stage [3] on a J. A. Woollam IR-VASE Mark II ellipsometer [4]. The measurements were performed in the range of 333-5900 cm^{-1} at a 50° angle of incidence. The collected data were modeled using a uniaxial anisotropic substrate model. The phonon modes for both ordinary (ε_o) and extraordinary (ε_e) dielectric responses were modeled using four asymmetric Lorentz oscillators, which account for coupling between modes [5]. Using a procedure similar to Tiwald et al. [6] and Herzinger et al. [7], various oscillator parameters were optimized to fit the model to the ellipsometric data. The measured ε_o and ε_e are plotted in Figs. B.3(a) and B.3(b), respectively.

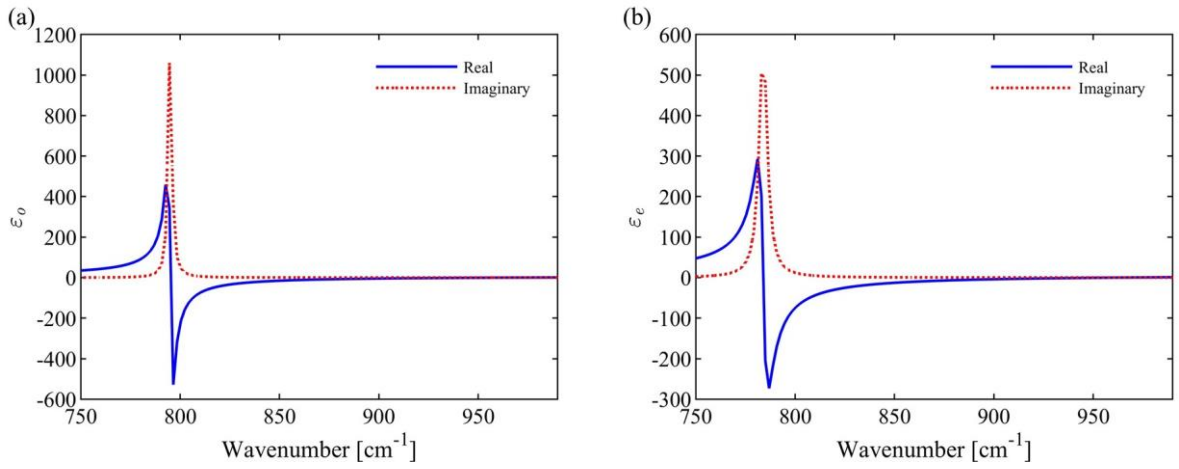

Figure B.3 - The (a) ordinary and (b) extraordinary dielectric functions of a 6H-SiC substrate measured using ellipsometry.

B.4. References

[1] S. Mukhopadhyay, A. Karumuri, and I. Barney, J. Phys. D: Appl. Phys. 42, 195503 (2009).

[2] W. Wang and S. Mukhopadhyay, Carbon Trends 5, 100096 (2021).

[3] Likam Scientific Instruments Ltd., Waterfield, Epsom, Tadworth KT20 5LR, United Kingdom, www.linkam.co.uk.

[4] J. A. Woollam Co., 645 M Street, Lincoln NE 68508 www.jawoollam.com.

[5] J. Humlíček, R. Henn, and M. Cardona, Phys. Rev. B 61, 14554 (2000).

[6] T. E. Tiwald, J. A. Woollam, S. Zollner, J. Christiansen, R. B. Gregory, T. Wetteroth, S. R. Wilson, and A. R. Powell, Phys. Rev. B 60, 11464 (1999).

[7] C. M. Herzinger, P. G. Snyder, B. Johs, and J. A. Woollam, J. Appl. Phys. 77, 1715 (1995).

BIOGRAPHY OF THE AUTHOR

Saman Zare was born in Mashhad, Iran, in 1991. He earned his Bachelor's degree in Mechanical Engineering with a concentration in Thermo Fluids from Ferdowsi University of Mashhad in 2012. Saman received an Elite Student Scholarship from Ferdowsi University of Mashhad to pursue his Master's studies in Mechanical Engineering with a concentration in Energy Conversion, from which he graduated in 2016. Saman also worked as Design and R&D Engineer for several years in multiple companies from 2012 to 2017. Later, he joined the Department of Mechanical Engineering at the University of Maine in August 2017. Saman is a candidate for the Doctor of Philosophy degree in Mechanical Engineering from the University of Maine and is expected to graduate in December 2022.